Title

Time- and Angle-resolved Photoemission Studies of Cuprate Superconductors

Author

Smallwood, Christopher Lee

Publication Date

2014

Peer reviewed|Thesis/dissertation

Time- and Angle-resolved Photoemission Studies of Cuprate Superconductors

by

Christopher Lee Smallwood

A dissertation submitted in partial satisfaction
of the requirements for the degree of

Doctor of Philosophy

in

Physics

in the

GRADUATE DIVISION

of the

UNIVERSITY OF CALIFORNIA, BERKELEY

Committee in charge:

Professor Alessandra Lanzara, Chair
Professor Joseph W. Orenstein
Professor Tanja Ćuk

Fall 2014

Time- and Angle-resolved Photoemission Studies of Cuprate Superconductors

by

Christopher Lee Smallwood

Abstract

Time- and Angle-resolved Photoemission Studies of Cuprate Superconductors

by

Christopher Lee Smallwood

Doctor of Philosophy in Physics

University of California, Berkeley

Professor Alessandra Lanzara, Chair

The origin of high-temperature superconductivity in cuprate ceramics is one of the great outstanding mysteries in physics. Discovered by Bednorz and Müller in 1986, the phenomenon has continued to both fascinate and baffle scientists for almost 30 years. At the heart of the cuprate problem lies the microscopic mechanism responsible for binding together Cooper pairs, which are a superconductor's lossless charge carriers. For most low-temperature superconductors, phonons are responsible, but Cooper pairs in the high-temperature superconductors may be bound together by magnetic interactions or even more exotic phenomena.

Although this most fundamental question remains unresolved, important insights continue to be gained in the field of high-temperature superconductivity, and many of them have originated from improved experimental methods and instrumentation. This thesis details progress in understanding the cuprate problem through the development and implementation of a high-resolution apparatus for conducting time- and angle-resolved photoemission spectroscopy (time-resolved ARPES). The technique works by using a near-infrared optical pump pulse to drive an electronic system out of equilibrium, and using an ultraviolet probe pulse to measure the subsequent dynamics of the nonequilibrium state using photoemission. Sub-picosecond time resolution is obtained by varying the path length of the pump pulse, and the net result is a movie of the relaxation dynamics of the band structure. Experimental results on the bi-layered cuprate superconductor $Bi_2Sr_2CaCu_2O_{8+\delta}$ (Bi2212) are presented and discussed in detail.

Content is organized into eight chapters. Chapter 1 gives an introduction and overview of superconductivity research. Chapter 2 summarizes basic theoretical underpinnings of the ARPES technique, and reviews analysis techniques that are relevant to ARPES and time-resolved ARPES as well as simple models of quasiparticle recombination. Chapter 3 contains a detailed overview of the time-resolved ARPES system constructed in the Lanzara research group. Chapters 4, 5, 6, and 7 present scientific results obtained using time-resolved ARPES to study Bi2212. Finally, conclusions and future directions are discussed in Chapter 8.

For Lindsey

Contents

List of Figures

List of Tables

Acknowledgments

A friend and fellow researcher once described the study of condensed matter as "cowboy physics," evoking a landscape of infinite surprise, maverick experiments, and rugged individualism. Indeed, new discoveries in the field often come from unexpected places, and a Nobel Prize seems to be within reach of almost anyone graced with enough luck, and willing to put in enough time and effort. Who would have thought, for example, that two-dimensional graphene—the darling of the next-generation semiconductor industry—would be first synthesized in 2004 by a process as simple as peeling Scotch tape off of pencil lead? And who would have predicted, in 1985, that the maximum known superconducting critical temperature would skyrocket to almost four times its previous value just one year later?

There is, however, one area in which the cowboy analogy grossly fails: no one in condensed matter physics (or in any branch of physics, for that matter) succeeds alone. Throughout my time in graduate school I have been incredibly blessed by the encouragement, support, and teachings of others.

I would like to first thank my advisor, Alessandra Lanzara, whose vision, tenacity, and unfailing devotion to new possibilities in physics have made the time-resolved ARPES project and my part within it possible. Donald Trump supposedly said, "As long as you're going to be thinking, anyway, think big." Alessandra certainly embodies this spirit, and the energy that she brings to the research group is infectious. I have learned a great deal about stretching my thoughts into larger ideas through working with her. Her guidance as an advisor has also taught me a great deal on about what it means to be a scientist on a day-by-day basis, and I am sure that both of these skill sets will continue to prove useful in the years to come.

I have also benefited tremendously from the other professors and staff scientists in and around Berkeley, particularly Joe Orenstein and Dung-Hai Lee, who patiently entertained hours of questions from me, and seeded experimental and theoretical ideas I would not have been able to come up with on my own. I am also grateful for discussions, experimental help, and advice from Robert Kaindl, Aaron Bostwick, Jonathan Denlinger, Jake Koralek, He Wang, Sung-Kwan Mo, Ashvin Vishwanath, Lex Kemper, and Tanja Cuk.

Additionally, I owe a huge debt of gratitude to various members of the support staff at Lawrence Berkeley Lab, particularly John Pepper, whose cryostat designs and ultrahigh vacuum and machining expertise are invaluable, and Todd Anderson and Derrick Crofoot, who have gone out of their way to help me navigate the many nuances of government purchase orders. On campus, a set of people who surely do not get thanked enough are the Berkeley Physics Department graduate student support staff, particularly Anne Takizawa, and Donna Sakima. Thank you so much!

None of the experimental results presented in this thesis would have been possible had it not been for the beautiful crystals of $Bi_2Sr_2CaCu_2O_{8+\delta}$ grown by Hiroshi Eisaki at the National Institute of Advanced Industrial Science and Technology in Japan. I have not yet had the chance to meet him in person, but I thank him profusely.

Among Lanzara Group members past and present, I am greatly indebted to Jeff Graf and Chris Jozwiak, who assembled much of the time-resolved ARPES experiment's current

infrastructure, pioneered the initial experiments on the system, and donated many hours teaching me about vacuum technology, lasers, data collection, analysis, programming, and writing. Daniel Garcia taught me impromptu lessons in superconductivity, versed me in the craft of ARPES, and entertained me with a great many stories of physicists gone by (some famous, some not-so-much). David Siegel is a brilliant mind, with whom I had the pleasure of exploring many ideas during preparations for various conferences. It has been a pleasure to work in parallel on time-resolved ARPES experiments with Wentao Zhang, an amazing scientist and an unfailingly gracious personality, who has taught me a great deal about the cuprates; and with Tristan Miller, whose sharp insights have clarified many concepts in my head, and whose blog only threatened to derail me from finishing the writing of this thesis once. Though our projects have been more tangentially related, it has also been a pleasure to work alongside Choonkyu Hwang, whose wizardry with graphene was inspiring; Kenny Gotlieb, whose perennial optimism is a joy and whose dogged work ethic is impressive; and Sebastien Lounis, whose entrepreneurial spirit has inspired new horizons in my thoughts on materials, and who has been a great friend both inside and outside the lab, particularly in the context of our adventures together with the *Berkeley Science Review*. It has also been a pleasure getting to know and work with the group's newer recruits, especially Greg Affeldt—who has saved me precious hours of sleep during some of our more ambitious experiments—but also Drew Latzke, Chiu-Yun Lin, and Ryo Mori; the visiting students, including Irene Lo Vecchio, Koshi Kurashima, Xiaozhu Yu, and Annemarie Kohl; and the undergraduates, including Reed Johnson, Allie Fero, Yuval Gannot, and Alex Nguyen.

I would like to thank the many friends I made both inside and outside of graduate school, without whom I might not have had the endurance to finish. Particularly noteworthy in context of this thesis are my partners in crime (in more ways than one, as it would turn out) in Building 2 and at the APS March Meeting: Stephen Wu and Jamie Hinton. You guys are awesome.

A large part of the reason I thought to apply to graduate school in the first place has to do with my undergraduate advisor, Ron Walsworth. Senior members of his research group, Irina Novikova (now at William & Mary), and David Phillips also deserve special thanks. Of course, in order to even have the chance to ever meet Ron, I had to have some excellent teachers in elementary school, middle school, and high school. Special thanks to Dayle Massey, Kathy DeFazio, Bill Davies, Stuart Welsh, and Buford Howell.

I thank my family: my brother, Greg Stallings, who put up with my teasing for so many years when we were younger and who has encouraged me in adulthood when not even I understood my research; my mother, Peggy Smallwood, who fostered a love of knowledge in the both of us from a young age; my father, Tom Smallwood, who pushed us both to be the best that we could be; and my extended family and in-laws, who remind me that there is value not just in what we do for a living, but in who we are and where we come from.

Thanks, also, to members of church families I have belonged to, both past and present. The PhD experience is in so many ways an exercise in faith, and I deeply appreciate the prayers and guidance.

Finally, most of all I would like to thank my wife, who has been there through it all,

who never fails to make me laugh, and whom I will love until the oceans lose their salt, until toddlers stop smearing spaghetti on their faces, and until supercurrents in temperature-controlled lead rings cease to flow. This is for you, Lindsey.

Chris Smallwood
August 5, 2014

Curriculum Vitæ

Christopher Lee Smallwood

Education

2014 University of California, Berkeley, CA, USA
Ph.D., Physics

2010 University of California, Berkeley, CA, USA
M.A., Physics

2005 Harvard University, Cambridge, MA, USA
A.B., Physics

Honors and Awards

2014 NIST National Research Council Postdoctoral Fellowship

2013 UC Berkeley Lars Commins Memorial Award in Experimental Physics

2009 NSF Graduate Research Fellowship Program, Honorable Mention

Publication Highlights

1. Tracking Cooper pairs in a cuprate superconductor by ultrafast angle-resolved photoemission. C. L. Smallwood, et al. **Science** 336, 1137 (2012)
   - Featured highlight in *Photonics Spectra* magazine, Aug. (2012)
   - Featured in "Ultrafast Spectroscopy of Quantum Materials," by Joseph Orenstein, *Physics Today*, Sept. (2012)
   - LBL Press Release: "A New Tool to Attack the Mysteries of High-Temperature Superconductivity," by Paul Preuss, June (2012)
2. An ultrafast angle-resolved photoemission apparatus for measuring complex materials. C. L. Smallwood, et al. **Review of Scientific Instruments** 83, 123904 (2012)
   - RSI Science Highlight
3. Nodal quasiparticle meltdown in ultrahigh-resolution pump-probe angle-resolved photoemission. J. Graf, C. Jozwiak, C. L. Smallwood, et al. **Nature Physics** 7, 805 (2011)

Publications - Complete List

1. C. L. Smallwood, W. Zhang, T. L. Miller, G. Affeldt, C. Jozwiak, K. Kurashima, H. Eisaki, D.-H. Lee, and A. Lanzara. Quasiparticle relaxation dynamics amid Dynamically Changing Band Topology in Bi2212. In preparation (2014)

2. W. Zhang, C. G. Hwang, C. L. Smallwood, T. L. Miller, G. Affeldt, K. Kurashima, C. Jozwiak, H. Eisaki, T. Adachi, Y. Koike, D.-H. Lee, and A. Lanzara. Ultrafast laser pumping of the electron-boson interaction and superconducting gap. Submitted (2014)
3. C. L. Smallwood, W. Zhang, T. L. Miller, C. Jozwiak, H. Eisaki, D.-H. Lee, and A. Lanzara. Time- and momentum-resolved gap dynamics in $Bi_2Sr_2CaCu_2O_{8+\delta}$. **Phys. Rev. B** 89, 115126 (2014)
4. A. Fero, C. L. Smallwood, G. Affeldt, and A. Lanzara. Impact of work function induced electric fields on laser-based angle-resolved photoemission spectroscopy. **J. Electron Specrosc. Relat. Phenom.**, in press (2014)
5. W. Zhang, C. L. Smallwood, C. Jozwiak, T. L. Miller, Y. Yoshida, H. Eisaki, D.-H. Lee, and A. Lanzara. Signatures of superconductivity and pseudogap formation in nonequilibrium nodal quasiparticles revealed by ultrafast angle-resolved photoemission. **Phys. Rev. B** 88, 245132 (2013)
6. C. L. Smallwood, C. Jozwiak, W. Zhang, and A. Lanzara. An ultrafast angle-resolved photoemission apparatus for measuring complex materials. **Rev. Sci. Instrum.** 83, 123904 (2012)
7. C. L. Smallwood, J. P. Hinton, C. Jozwiak, W. Zhang, J. D. Koralek, H. Eisaki, D.-H. Lee, J. Orenstein, and A. Lanzara. Tracking Cooper pairs in a cuprate superconductor by ultrafast angle-resolved photoemission. **Science** 336, 1137 (2012)
8. J. Graf, C. Jozwiak, C. L. Smallwood, H. Eisaki, R. A. Kaindl, D.-H. Lee, and A. Lanzara. Nodal quasiparticle meltdown in ultrahigh-resolution pump-probe angle-resolved photoemission. **Nat. Phys.** 7, 805 (2011)
9. J. Graf, S. Hellmann, C. Jozwiak, C. L. Smallwood, Z. Hussain, R. A. Kaindl, L. Kipp, K. Rossnagel, and A. Lanzara. Vacuum space charge effect in laser-based solid-state photoemission spectroscopy. **J. Appl. Phys.** 107, 014912 (2010)
10. F. Cane, D. Bear, D. F. Phillips, M. S. Rosen, C. L. Smallwood, R. E. Stoner, and R. L. Walsworth. Bound on Lorentz and CPT violating boost effects for the neutron. **Phys. Rev. Lett.** 93, 230801 (2004)

Invited Talks and Seminars

1. "Ultrafast electron dynamics of high-temperature superconductors." Santa Clara University, Apr. 2014
2. "Ultrafast momentum-resolved gap and quasiparticle dynamics in Bi2212." Gordon Research Seminar, Feb. 2014
3. "Ultrafast electron dynamics of high-temperature superconductors." Westmont College, Jan. 2014
4. "Non-equilibrium momentum-dependent dynamics of high-temperature superconductors." Molecular Foundry Facility Meeting, Jan. 2014

5. "Non-equilibrium momentum-dependent dynamics of high-temperature superconductors." SRI Conference, July 2013

Contributed Talks

1. "Signatures of phase transitions in nodal quasiparticles revealed by time-resolved photoemission." APS March Meeting, Mar. 2014
2. "Ultrafast momentum-resolved gap dynamics in Bi2212." APS March Meeting, Mar. 2014
3. "Gap dynamics in Bi2212 studied by time- and angle-resolved photoemission." APS March Meeting, Mar. 2013
4. "High-Tc superconductor studies with ultrafast ARPES," Poster presentation, Quantum Materials Program DOE Review, 2013
5. "Tracking cooper pairs in a cuprate superconductor: an ultrafast angle-resolved photoemission study. APS March Meeting, Mar. 2012
6. "High-Tc superconductor studies with ultrafast pump-probe angle-resolved photoemission." Poster presentation, Gordon Research Conference (Ultrafast phenomena in cooperative systems), Feb. 2012
7. "High resolution study of cuprate dynamics using time-resolved ARPES." APS March Meeting, Mar. 2011
8. "Probing dynamic excitations of complex materials by pump and probe photoemission spectroscopy." Poster presentation, UC Berkeley Physics Department, Oct. 2010
9. "Vacuum space charge effect in laser-based solid-state photoemission spectroscopy." APS March Meeting, Mar. 2010
10. "Probing dynamic excitations of complex materials by pump and probe photoemission spectroscopy." Poster Presentation, UC Berkeley Physics Department, Oct. 2009

Teaching Experience

2008 UC Berkeley: Graduate Student Instructor, Introductory Mechanics

2007 UC Berkeley: Graduate Student Instructor, Introductory Geometric & Physical Optics, Relativity and Quantum Physics

2005 Teach For America: Classroom Teacher, 5th Grade

Public Outreach

2012–2013 *Berkeley Science Review*: Editor/Contributing Author

2009–2012 KQED QUEST Community Science Blog: Contributing Author

2008–2011 Prison University Project: Volunteer Instructor/Volunteer tutor

Chapter 1

Introduction

> *I seem to have been only like a boy playing on the seashore, and diverting myself in now and then finding a smoother pebble or a prettier shell than ordinary, whilst the great ocean of truth lay all undiscovered before me.*
>
> — Isaac Newton[1]

The story of superconductivity is one of the great scientific epics of the 20th and 21st centuries. Originating with a single measurement at the University of Leiden in the Netherlands,[2] at the time of this writing the topic has crowned 11 Nobel laureates, is actively used or studied in research departments on every continent, and has inspired more than a half million scientific publications. Moreover, trends indicate that there are almost no signs of waning interest in the near or even intermediate future.

A superconductor is a material that undergoes a phase transition at low temperature into a peculiar state with two defining characteristics: (1) its electrical resistance drops perfectly to zero, and (2) it expels magnetic fields from its interior. From here, one can begin to understand why the phenomenon has driven so much interest across so many years.

First, superconductivity is delightfully strange. The phenomenon of zero resistance inspires thoughts of perpetual motion, and indeed, researchers have instigated flows of circulating electrical current in lead rings that have been measured to persist, without external drivers, for lifetimes that could be extrapolated out to 10 times the age of the Universe.[3] The tendency of superconductors to repel magnetic fields enables the controlled levitation of objects as large as even whole passenger trains.

Second, superconductivity is useful. Zero resistivity, in particular, has had an important impact in industry, for it enables the transport of extraordinary amounts of current through small spaces with practically no energy loss or heat generation. In turn, this has facilitated the development of modern magnetic resonance imaging (MRI), the construction of the

massively powerful magnets that are required for modern particle physics research, and a niche—but potentially growing—use of superconducting wires in the power grid.[4]

Finally, most abstractly, and perhaps most importantly from the point of view of science, superconductivity is among nature's most dramatic examples of a distinctly quantum-mechanical phenomenon that is also observable to the naked eye. Scientists have long sought to develop a microscopic understanding of the role of quantum mechanics in large ensembles Over the years the particular problem of superconductivity has proven to be a beguiling, frustrating, provocative, but ultimately exhilarating challenge. It is this final interest in superconductivity that has inspired the present work.

Below, I outline a brief history of the pioneering discovery of superconductivity, the major triumphs and discoveries that have come in the years since, and some of the important recent developments in photoemission and optical spectroscopy that have made the research summarized in the rest of this dissertation possible.

1.1 Historical background

1.1.1 "The Gentleman of absolute zero"

Materials exhibiting the phenomenon are fairly common: aluminum, mercury, tin, and niobium are all superconductors, for example. Yet, superconductivity went completely undiscovered until the early 1900s. The reason is that the effect typically only occurs in close proximity to a temperature of 0 K, in the hinterland of physical experience. This is where our story really begins. Superconductivity was born at the hands of the Dutch physicist Heike Kamerlingh Onnes. Driven, administratively savvy, and yet decidedly gracious toward his competitors, Kamerlingh Onnes became the first person to successfully manage to liquefy helium in 1908.[5] The achievement would shortly thereafter earn him a great deal of notoriety among the press as "the gentleman of absolute zero,"[6] and would ultimately lead (interestingly, with almost no reference to superconductivity) to his winning the 1913 Nobel Prize.

The critical discovery for superconductivity came during a series of experiments in 1911, when Kamerlingh Onnes and his collaborators undertook a study to investigate the DC electrical properties of mercury. At the time, there was an important intellectual debate between two prominent theories of the day about the low-temperature properties of metals. It was scientifically well-established that the electrical resistance of metals decreased with decreasing temperature, and it was understood that the source of this resistance could be found in the form of a decreasing scattering cross section between the electrons and the crystal's ions.[7] However, Lord Kelvin famously believed that this scattering decrease would also be accompanied by a decrease in electron mobility, and that the latter effect would ultimately win out over scattering. Thus, electrical resistance in any metal would approach

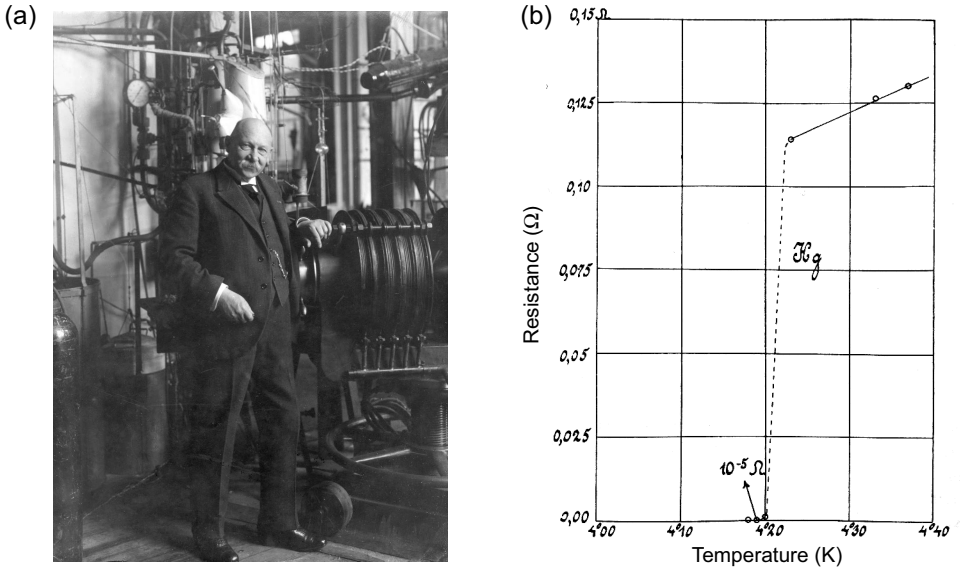

Figure 1.1. Heike Kamerlingh Onnes and the discovery of superconductivity. **(a)** Kamerlingh Onnes in his laboratory, circa 1911. **(b)** Early plot of the resistance of mercury as a function of temperature. From Ref. 2.

a minimum at some point, and should ultimately increase to infinity in the limit of zero temperature.

About the same time, however, inklings of quantum mechanical phenomena began to show up in low-temperature heat capacity measurements. A coherent theory of quantum mechanics was still some distance away, but both Kamerlingh Onnes and his Scottish contemporary, James Dewar, began to suspect that the dynamics of low-temperature electrons might not be as Kelvin expected. Dewar, in particular, was of the opinion that for very pure metals, the electrical resistivity might not diverge, but would rather descend smoothly to zero in the limit of zero temperature.[8] With the successful liquefaction of helium, Kamerlingh Onnes for the first time had an opportunity to put these ideas to the test.

Early measurements on platinum and gold seemed to confirm Kamerlingh Onnes' suspicions. Startlingly, however, when he and his collaborators turned their attention to mercury—which they chose because they could purify it with particular ease—Kamerlingh Onnes and his collaborators discovered what absolutely no one expected: at about 4 K, the resistance of mercury abruptly plummeted to zero. In the months and years that ensued, Kamerlingh Onnes discovered the same phenomenon in a variety of other materials, including lead and tin, and a new era of low-temperature physics was born.

1.1.2 Early progress

Progress was at first slow. Indeed, the search to develop a theory of superconductivity throughout the first part of the 20th century populated a veritable graveyard of failed theories, including attempts by Albert Einstein, Niels Bohr, Werner Heisenberg, and Max

Born.[9] In the mid-1950s the search to understand superconductivity led Richard Feynman down an extended rabbit hole that resulted in (according to him) "a big vacuum at that time" consisting of no significant results and only one cursory publication on the subject.[10] Part of the problem, particularly early on, was that only a select few experimentalists were even capable of witnessing superconductivity. Indeed, between 1911 and 1923, Kamerlingh Onnes' lab was the only place on Earth where liquid helium could successfully be generated.[5]

Other laboratories did eventually catch up, however, and a major experimental advance was achieved in the 1933 discovery of a superconductor's electric field expulsion by Meissner and Oschenfeld (for whom the effect is now named) in Germany.[11] It can be shown by ge-

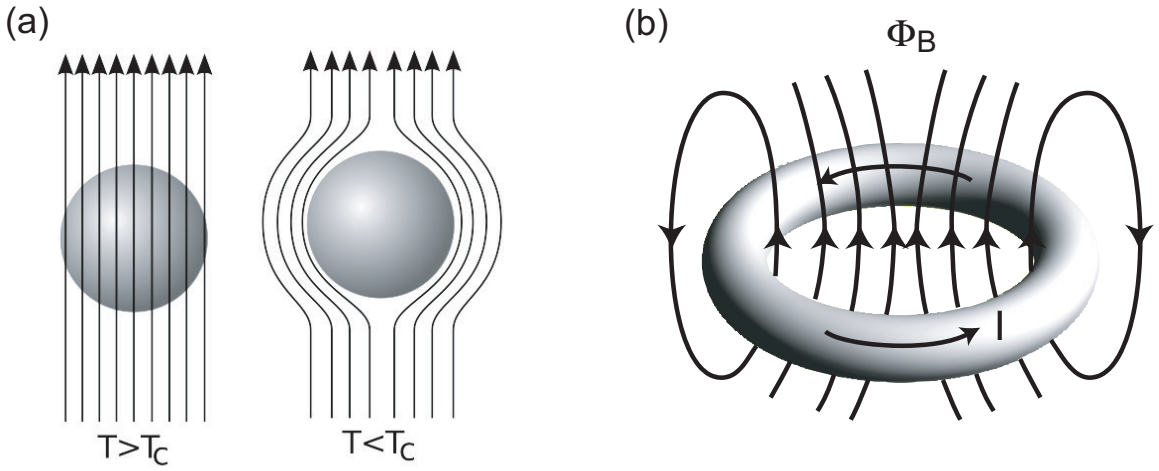

Figure 1.2. Schematic illustration of the Meissner effect. **(a)** Magnetic fields that are allowed to penetrate a superconductor above the critical temperature (T_c) are expelled when the temperature is decreased below T_c. **(b)** This property implies the existence of persistent currents (see text). After Refs. 12 and 13.

ometrical arguments involving multiply connected superconductors that the Meissner effect directly implies the existence of persistent currents, as shown by the illustration of a superconducting ring in Fig. 1.2(b). Because of the absence of magnetic monopoles, magnetic flux lines must be closed loops, which means that the flux lines encircling the current loop become permanently trapped. An immediate consequence, due to Faraday's law, is that it is impossible (without the active introduction of external magnetic fields) for there ever to be an electromotive force in the ring that would slow down the net flow of current.

Inspired by Meissner and Oschenfeld's discovery, the brothers Fritz and Heinz London developed the first phenomenologically correct description of a superconductor's electromagnetic properties in 1935.[14] In 1950 the Russian theorists Lev Landau and Vitaly Ginzburg teamed up to develop a description of superconductivity in terms of a complex order parameter, which in turn has stood a long test of time, proving itself to be particularly useful in describing the dynamics of spatially varying superconductivity. Still, the theory of superconductivity's biggest moment would be yet to come.

1.1.3 The triumph of BCS theory: 1957–1985

Finally, after 46 years a fantastically successful and truly microscopic theory emerged in 1957, developed by John Bardeen, Leon Cooper, and John Robert Schrieffer.[15] The essential components of this theory, which has come to be known as the BCS model, are that superconductivity develops in a material system through the creation of paired electrons, and that these electron "Cooper pairs" are bound together by sound waves.

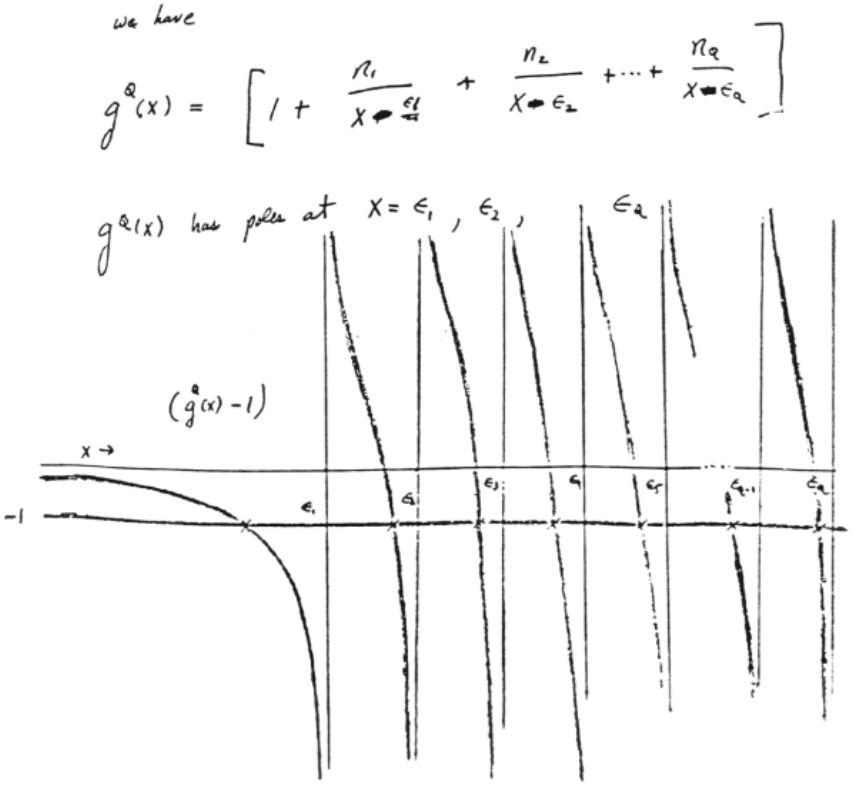

Figure 1.3. Notes that Cooper drafted in 1956, chronicling an early insight into the foundation of BCS theory. From Ref. 16.

Almost overnight, the BCS theory became widely accepted, in no small part because it both explained much of the new data that was beginning to emerge at the time, and because it gave rise to predictions that were almost immediately verified by new experiments. Among the most prominent of these was the successful BCS explanation of the isotope effect, which preceded the BCS theory by just a few short years,[17,18] and the prediction of an energy gap, of which heat capacity measurements before 1957 had been strongly suggestive,[19] and which would soon afterward be directly measurable through electron tunneling.[20]

The new theory also injected a great deal of interest in the field of condensed matter physics through its shear beauty. Philip Anderson has summed up the BCS theory as "the scientific love of my life," and used the new framework to inform new ideas with implications ranging from superconductivity in the presence of widespread presence of crystal defects, to the mechanism explaining the origin of mass in particle physics.[21] In the early 1960s, Brian

Josephson was able to improve upon the original BCS ideas in predicting new tunneling effects[22] that have in turn become the operative principle behind superconducting quantum interference devices (SQUIDs). Such devices are useful today in measuring magnetic fields down to the very quantum mechanical limit of sensitivity.

And then, for a time, interest began to die out. In 1969 R. D. parks wrote in the preface of the textbook *Superconductivity* that "during the preparation of this treatise one of the authors commented that it would be 'the last nail in the coffin [of superconductivity].' "[23] Another textbook on superconductivity by Michael Tinkham,[3] considered by many to be the single most valuable introduction to the subject in the literature today, went out of print for a time. Experimental progress flagged as well. Continued measurements and theoretical work failed to increase the maximum superconducting critical temperature by more than about a third of a degree per year, leading many to speculate on a fundamental "Max-T_c," which could not be exceeded for a given class of materials,[24] or perhaps for even any class of material. For a time it was believed that T_c could never be pushed above 30 K, permanently relegating superconductivity to the industrially expensive realm of low temperatures. These beliefs became so sufficiently ingrained that some some experimenters in industry who wished to continue the search for higher temperature superconductors even had to conceal their activities from their own bosses. Such was the case for Bednorz and Müller, who would play a starring role in the next chapter of the phenomenon.[25]

1.1.4 Discovery of the High-T_c cuprates

The field of superconductivity research may have appeared to strike a low point in the mid 1980s, but as it would turn out, superconductivity would explode into a condensed matter revolution with just a few short months. J. Georg Bednorz and K. Alexander Müller, working at the IBM Zurich Research Laboratory, had refused to believe in the max-T_c edict, and had heard about research indicating that the presence of strong electron-phonon coupling in strontium titanate (STO) could result, in certain cases, in superconductivity. Inspired by these works, they set about searching for other materials where Jahn-Teller distortions of the type seen in STO played a significant role, and they began to play around with doping in cuprate ceramics. In march of 1986, they published a fascinating result, indicating a superconducting critical temperature near 30 K in the material $La_{2-x}Ba_xCuO_4$.[26] Not only was this a higher critical temperature than any previously known material. It originated by doping a parent compound that was originally insulating.

Though the report was initially met with some skepticism, groups around the world very quickly began to be able to replicate the discovery, in Japan, in China, and in the U.S., perhaps most excitingly in a collaboration between the groups of C. W. Chu at the University of Houston and M. K. Wu at the University of Alabama in Huntsville, where it was demonstrated that the critical temperature of a closely related material, $YBa_2Cu_3O_{7-\delta}$, was as high as 92 K, significantly above the boiling point of liquid nitrogen.[27] By the beginning of 1987, the level of excitement had risen to such spectacular proportions that the American Physical Society decided to host a special workshop in February to showcase the new findings.

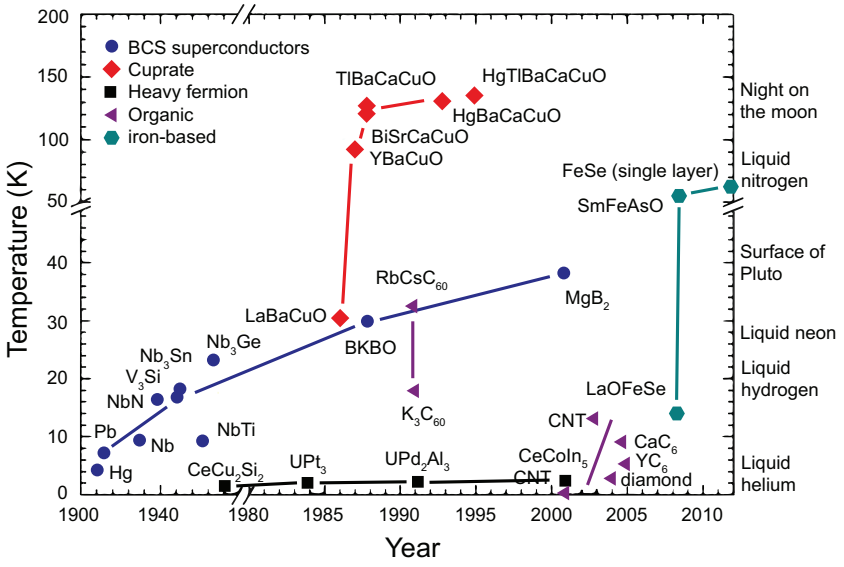

Figure 1.4. Discovery of prominent superconductors, with critical temperatures displayed as a function of time. After Ref. 31.

The event, packed with attendees from front to back, and projected using video feeds to several other venues, was about as rowdy as physics conferences tend to get, and would soon-thereafter be dubbed "the Woodstock of physics."

Since 1986, interest in the physics of new classes of high-temperature superconductors has held pace with the rise in T_c. First, there has been a burst of excitement from a technological perspective, for nitrogen is far less expensive to collect than helium, and the prospect of harnessing the properties of superconductors at temperatures that are (relatively) close to room temperature has sparked a great number of imaginative ideas.

From a scientific perspective, for the first time in a long time, the field has broken completely open, and it has now become evident that the BCS theory—though superb at describing low-temperature superconductors, may no longer be sufficient in describing high-T_c compounds. At present, there are several conflicting theories claiming to explain high-T_c, each seeming to disagree more loudly with the one that came before.[28,29] To make matters more interesting, in 2008, the field was invigorated by the discovery of a whole new class of high-T_c material, based on various layered structures containing iron, and only tangentially related to the cuprates in any aspect of its chemical composition.[30]

Despite this cacophony, the scientific community does seem to be in agreement on one thing: better and more sophisticated experiments are needed. At this point it is still too early to say definitively, but the recent coupling of ultrafast optical methods with photoemission spectroscopy—which is the subject of the rest of this dissertation—may help pave the way forward.

1.2 Quantitative models of superconductivity

The discovery of superconductivity, and more recently the discovery of high-temperature superconductivity, has sparked a tremendous amount of theoretical work. In order to put our own group's work into context, in the text that follows I briefly outline the basic formalism of ARPES, the Bardeen-Cooper-Schrieffer (BCS) theory of low-temperature superconductivity, and the current state of the High-T_c field in terms both of the phenomenological observations that fit within the classic BCS framework, and in terms of those that may not. Much of the theoretical content from this section is derived from the textbooks of Schrieffer,[32] Tinkham,[3] and Annett,[33] to which the reader is referred for further details.

1.2.1 London theory

As previously noted, an early enduring formalism for describing the physics of superconductivity was developed by Fritz and Heinz London in 1935,[14] The Londons' primary result, in Gaussian units, is given by

$$\mathbf{J} = -\frac{n_s q^2}{mc}\mathbf{A}, \tag{1.1}$$

where the current density $\mathbf{J}$ is expressed in terms of the vector potential $\mathbf{A}$, the constants e and m respectively correspond to an electron's charge and mass, c is the speed of light, and the constant n_s is a density that is interpreted in a modern framework as the superfluid density. To obtain this equation, the London brothers postulated that in a superconductor, Ohm's law should be replaced by an "acceleration equation" relating the $\mathbf{J}$ to the electric field $\mathbf{E}$:

$$\frac{d\mathbf{J}}{dt} = \frac{n_s e^2}{m}\mathbf{E}. \tag{1.2}$$

For $\mathbf{E} = 0$ this equation is cable of capturing a superconductor's persistent current. Taking the curl of Eq. (1.2) and applying Faraday's law gives $\nabla \times \dot{\mathbf{J}} = -(n_s q^2)/(mc)\dot{\mathbf{B}}$. However, the London brothers recognized that this led to solutions that were incompatible with the Meissner effect, so they postulated that the time derivatives could be removed in a superconductor without loss of generality, leading to

$$\nabla \times \mathbf{J} = -\frac{n_s e^2}{mc}\mathbf{B}. \tag{1.3}$$

Eqs. (1.2) and (1.3) are encapsulated in the condensed form of Eq. (1.1) by adopting the London gauge condition, which requires that $\nabla \cdot \mathbf{A} = 0$, that the normal component of $\mathbf{A}$ over the surface be related to any supercurrent through Eq. (1.1), and that $\mathbf{A} \to 0$ over the interior of bulk samples.[3]

The relationship between Eqs. (1.1)–(1.3) and the Meissner effect can be illustrated by taking the curl of Ampere's law and substituting in Eq. (1.3), leading to the equation

$$\nabla^2 \mathbf{B} = \frac{1}{\lambda_L^2}\mathbf{B}, \qquad \lambda_L \equiv \sqrt{\frac{mc^2}{4\pi e^2 n_s}}. \tag{1.4}$$

Evidently, magnetic fields must drop off exponentially inside a superconductor, with a characteristic penetration depth λ_L. This can be seen in an explicit example by considering the case of a uniform DC magnetic field applied parallel to the boundary of a semi-infinite superconductor, where the solution to Eq. (1.4) is given by

$$B_z(x) = B_0 e^{-x/\lambda_L}. \tag{1.5}$$

This length scale, widely known as the *London penetration depth*, is of great importance in the study of both low- and high-temperature superconductors.

1.2.2 The BCS theory

While the London formulation is remarkable for its simplicity and its immediate ability to explain much of the phenomenology of superconductivity, it was recognized from the theory's inception that a more complete theory was still needed. Ginzburg and Landau developed a significant improvement on the London theory in 1950.[34] However, a fully microscopic theory of superconductivity did not arrive until 46 years later, in 1957. The theory was developed by Bardeen, Cooper, and Schrieffer (BCS),[15] won them the Nobel Prize in Physics in 1972, and continues today as the universally accepted theory of superconductivity in low-temperature superconductors.[i] In a nutshell, BCS theory consists of the following tenets: that a continuous background of positive ions and negative electrons tends to screen out the Coulomb repulsion; that interactions between electrons and phonons can result in an attractive interaction between electrons; that this attractive interaction, no matter how weak, will result in the disintegration of the normal-state Fermi surface into a coherent many-body condensate of bound "Cooper pairs;" and that the physics behind all of this can be written down in a few brief equations.

It is widely believed that high-temperature superconductivity must involve physics beyond the simple BCS model because superconducting transition temperatures in excess of 40 K require vastly stronger coupling between electron pairs than BCS had originally assumed. Nevertheless many of the characteristic features of BCS theory are also seen in cuprate and pnictide superconductors, and in the absence of anything better, the language of the BCS theory persists in the discussion of all superconductors, no matter how exotic.

[i] I should note that it has been proven that Ginzburg-Landau theory becomes exactly equivalent to BCS theory in the vicinity of T_c.[35] In many cases (transport dynamics, for example), Ginzburg-Landau theory is even superior to the BCS theory because of its ease of application and its ability to incorporate spatial inhomogeneity. Nevertheless, I refrain from summarizing Ginzburg-Landau theory in this work because most ARPES observables are understood more cleanly by skipping straight to the BCS formalism.

1.2.2.1 Hamiltonian and ground state wavefunction

The basic Hamiltonian that undergirds all of BCS theory is

$$H = \sum_{\mathbf{k}s} \epsilon_{\mathbf{k}} n_{\mathbf{k}s} + \sum_{\mathbf{k},\mathbf{k}'} V_{\mathbf{k}\mathbf{k}'} b^\dagger_{\mathbf{k}} b_{\mathbf{k}'}, \qquad \left\{ \begin{array}{rcl} n_{\mathbf{k}s} & \equiv & c^\dagger_{\mathbf{k}s} c_{\mathbf{k}s} \\ b^\dagger_{\mathbf{k}} & \equiv & c^\dagger_{\mathbf{k}\uparrow} c^\dagger_{-\mathbf{k}\downarrow} \end{array} \right. \tag{1.6}$$

where the operators $c^\dagger$ and c correspond to electron creation and annihilation operators, $\mathbf{k}$ and s are momentum and spin quantum numbers, and $V_{\mathbf{k}\mathbf{k}'}$ is a pairing matrix element. Evidently, the Hamiltonian consists of two pieces: an on-site piece which takes the non-interacting energy of each electron into account, and a pairing interaction which scatters time-reversed pairs of electrons from one momentum state to another. It is the second piece which facilitates superconductivity and all of its associated properties.

Bardeen, Cooper, and Schrieffer made the brilliant discovery that the mean field ground state corresponding to the above Hamiltonian can be expressed as

$$|\phi_{BCS}\rangle = \prod_{\mathbf{k}} \left(u_{\mathbf{k}} + v_{\mathbf{k}} b^\dagger_{\mathbf{k}} \right) |0\rangle, \qquad \begin{array}{c} u^2_{\mathbf{k}} \\ v^2_{\mathbf{k}} \end{array} \equiv \frac{1}{2} \left(1 \pm \frac{\xi_{\mathbf{k}}}{\sqrt{\Delta^2_{\mathbf{k}} + \xi^2_{\mathbf{k}}}} \right), \tag{1.7}$$

where $|0\rangle$ is the normal state vacuum, the values $\xi_{\mathbf{k}}$ trace out the normal state energy spectrum relative to the chemical potential (i.e., $\xi_{\mathbf{k}} \equiv \epsilon_{\mathbf{k}} - \mu$), $b^\dagger_{\mathbf{k}}$ is as defined in Eq. (1.6), and the order parameter $\Delta_{\mathbf{k}}$ is implicitly defined (at zero temperature) by the attractive potential $V_{kk'}$ between electrons according to to the equation

$$\Delta_{\mathbf{k}} = -\sum_{\mathbf{k}'} V_{\mathbf{k}\mathbf{k}'} \frac{\Delta_{\mathbf{k}'}}{2\sqrt{\Delta^2_{\mathbf{k}'} + \xi^2_{\mathbf{k}}}}. \tag{1.8}$$

The BCS ground state wave function bears a striking resemblance to the bosonic coherent state wave function frequently used to describe laser radiation and Bose-Einstein condensates:[36]

$$|\{\alpha_{\mathbf{k}}\}\rangle = \prod_{\mathbf{k}} \exp\left(\alpha_{\mathbf{k}} a^\dagger_{\mathbf{k}} - \alpha^*_{\mathbf{k}} a_{\mathbf{k}} \right) |0\rangle = \prod_{\mathbf{k}} \left(1 + \alpha_{\mathbf{k}} a^\dagger_{\mathbf{k}} + ... \right) |0\rangle. \tag{1.9}$$

(The operators $a_{\mathbf{k}}$ and $a^\dagger_{\mathbf{k}}$ are boson creation and annihilation operators; $\alpha_{\mathbf{k}}$ and $\alpha^*_{\mathbf{k}}$ are constants.) This resemblance is no coincidence. Both states fit the broader definition of a *coherent state*, which exhibits a symmetric minimum uncertainty between particle number and phase. In fact many of the most interesting phenomena observed in superconductors, including persistent currents, quantized vorticity, and the Meissner and Josephson effects are a direct consequence of the underlying properties of coherent states, and similar effects are also observed in superfluid ^{4}He and the Bose-Einstein condensate (BEC) forms of a variety of dilute gasses, including the Rb and Na condensates for which the 2001 Nobel prize was awarded.

One should be careful about pushing the analogy too far, however. In a superconductor, the spacing between the two electrons in a Cooper pair is so large that the individual electrons

retain some of their fermionic character, and thus Cooper pairs *cannot* be regarded as true bosons. Early attempts to explain superconductivity as a Bose-Einstein condensate of paired electrons failed largely because of this subtlety. The excitation spectrum of a bosonic system is gapless, wheres the spectrum corresponding to superconductivity is not. The transition between this weakly-coupled BCS state and a true BEC, where the coupling between fermions is stronger, can be directly explored with magnetically or optically trapped systems of cold atoms, and is an important avenue of ongoing research. The BCS-BEC distinction is manifest in the above formalism through the fact that the operators b and $b^\dagger$ do not obey Bose-Einstein statistics, but are rather governed by the following commutation relations:

$$[b_{\mathbf{k}}, b^\dagger_{\mathbf{k}'}] = \delta_{\mathbf{k}\mathbf{k}'}\big(1 - (n_{\mathbf{k}} + n_{-\mathbf{k}})\big), \tag{1.10}$$

$$[b_{\mathbf{k}}, b_{\mathbf{k}'}] = [b^\dagger_{\mathbf{k}}, b^\dagger_{\mathbf{k}'}] = 0. \tag{1.11}$$

According to Schrieffer,[32] "perhaps it is simplest to view the 'pairon' operators $b_{\mathbf{k}}$ and $b^\dagger_{\mathbf{k}}$ as satisfying Bose-Einstein statistics for $k \neq k'$ and satisfying Pauli principle $b^{\dagger 2}_{\mathbf{k}} = 0 = b^2_{\mathbf{k}}$ for $\mathbf{k} = \mathbf{k}'$."

1.2.2.2 Solution by canonical transformation

Bardeen, Cooper, and Schrieffer originally derived the BCS ground state (Eq. (1.7)), as well as various thermodynamic and finite-temperature effects through a variational treatment of the Hamiltonian (1.6) and a trial ground state wavefunction. Contemporary derivations tend to follow a canonical transformation solution that was independently developed by Bogoliubov[37] and Valatin.[38] This canonical transformation method is here summarized to discuss the quasiparticle excitation spectrum and to lay groundwork for discussions of finite-temperature effects in Section 1.2.3.1. It has the advantage of explicitly introducing quasiparticle creation and annihilation operators.

After applying a mean-field approximation to equation (1.6) Bogoliubov found that the Hamiltonian could be diagonalized by the transformation[ii]

$$\gamma^\dagger_{\mathbf{k}0} = u^*_{\mathbf{k}} c^\dagger_{\mathbf{k}\uparrow} - v^*_{\mathbf{k}} c_{-\mathbf{k}\downarrow} \tag{1.12}$$

$$\gamma^\dagger_{\mathbf{k}1} = u^*_{\mathbf{k}} c^\dagger_{-\mathbf{k}\downarrow} + v^*_{\mathbf{k}} c_{\mathbf{k}\uparrow}. \tag{1.13}$$

resulting in the following Bogoliubov mean-field Hamiltonian:

$$H_M = \sum_{\mathbf{k}} E_{\mathbf{k}} \left(\gamma^\dagger_{\mathbf{k}0}\gamma_{\mathbf{k}0} + \gamma^\dagger_{\mathbf{k}1}\gamma_{\mathbf{k}1}\right) + \text{Constant}, \tag{1.14}$$

$$E_{\mathbf{k}} \equiv \sqrt{\Delta^2_{\mathbf{k}} + \xi^2_{\mathbf{k}}}. \tag{1.15}$$

The new operators $\{\gamma\}$ obey the same fermionic commutation rules as the original operators $\{c\}$, so they are true quasiparticle creation and annihilation operators. Because the Bogoliubov mean-field Hamiltonian is diagonal in these new operators, the quasiparticle excitation spectrum is directly given by $E_{\mathbf{k}}$.

[ii] Different texts use differing conventions in defining the Bogoliubov-Valatin transformation. I adopt the convention of Tinkham.[3]

We see as an immediate consequence that dropping a material into the superconducting state results in a quasiparticle excitation gap, with magnitude $|\Delta|$. The physical origin of this gap is that it corresponds to Cooper pair binding energy. When the temperature is very close to zero then the parameter $\Delta_{\mathbf{k}}$ approaches a constant ground state value, given by equation (1.8). In the presence of a finite population of quasiparticles, Eq. (1.8) must be generalized, so that now $\Delta_{\mathbf{k}}$ becomes temperature-dependent according to

$$\Delta_{\mathbf{k}} = -\sum_{\mathbf{k}'} V_{\mathbf{k}\mathbf{k}'} \frac{\Delta_{\mathbf{k}'}}{2E_{\mathbf{k}'}} \langle 1 - \gamma^{\dagger}_{\mathbf{k}'0}\gamma_{\mathbf{k}'0} - \gamma^{\dagger}_{\mathbf{k}'1}\gamma_{\mathbf{k}'1}\rangle. \tag{1.16}$$

This is a version of the BCS gap equation, discussed further in Section 1.2.3.

1.2.2.3 Coupling interaction

In the treatment thus far, very few requirements have been placed on the pairing interaction potential $V_{kk'}$. In fact, Cooper has shown that if we take the simple case of a uniformly negative $V(\omega_{\mathbf{k}})$ such that

$$V(\omega_{\mathbf{k}}) = \begin{cases} -V & \text{for} \quad \omega_{\mathbf{k}} < \omega_c \\ 0 & \text{for} \quad \omega_{\mathbf{k}} > \omega_c \end{cases} \tag{1.17}$$

(ω_c is a cutoff frequency), then *any* attractive interaction, no matter how small, is enough to destabilize the Fermi sea.[39] In its strictest sense, the BCS theory is a weak-coupling theory of superconductivity where precisely this form of coupling is assumed. Physically, the attractive interaction originates from phonons, which cause an attractive force between electrons in the low frequency regime as can be seen, for example, in the jellium model:[3]

$$V(\mathbf{q},\omega)_{ph} = \frac{4\pi e^2}{q^2 + k_s^2} \frac{\omega_{\mathbf{q}}^2}{\omega^2 - \omega_{\mathbf{q}}^2}, \tag{1.18}$$

where $\mathbf{q} = \mathbf{k} - \mathbf{k}'$ is the momentum difference between the interacting electrons, e is the electron charge, k_s is the Thomas-Fermi electronic screening wave vector, and ω_q is a characteristic phonon cutoff frequency. As long as $\omega < \omega_q$, this interaction will be negative. The physical origin of the attractive interaction is that the electron-phonon interaction causes positive ions to collect around an electron moving through the crystal lattice. Electrons move faster than the ions can react, and so a positive conglomeration of charge will trail this electron. In turn, other electrons are pulled toward the location where the first first electron was formerly located, resulting in a net attraction. Because of the delayed nature of this reaction, it is known as a retarded interaction.

For a sufficiently weak potential the specific functional shape of of the phonon interaction displayed in Eq. 1.18 is of no consequence, and an effective potential V can be defined in terms of the density of states at the Fermi level $N(0)$ and a dimensionless coupling constant λ according to

$$\lambda = N(0)V. \tag{1.19}$$

As previously shown in Section 2.1.3.5, the parameter λ is physically meaningful independently of superconductivity, and can in fact be directly characterized through analyses of band renormalization effects in ARPES data. It has been used to quantify the strength of the electron-phonon interaction in simple systems like molybdenum[40] and graphene,[41,42] as well as strongly correlated systems like the cuprate superconductors.[43]

For superconductors, knowing λ can also give information about the critical temperature. Solving the BCS gap equation (1.22) at T_c leads to

$$k_B T_c = 1.13\,\hbar\omega_c e^{-1/\lambda}. \tag{1.20}$$

For stronger coupling, McMillan has derived a formula that levels off to about 30 K for reasonably physical values.[24] For very strong coupling, one must employ the more powerful Eliashberg formalism.[44] In this case it can be shown that $T_c \sim \sqrt{\lambda}$.[45] Although this suggests in principle that T_c can increase without limit for phonon-mediated superconductivity, at some point one begins to fear for the structural integrity of the crystal lattice. However, ideas have been proposed for synthesizing high-temperature phonon-mediated superconductors using caged structures based on carbon.[46,47,48]

1.2.3 Physical predictions of the BCS theory

1.2.3.1 Energy gap and critical temperature

As mentioned in the previous section, an immediate consequence of Eq. (1.15) is that the quasiparticle spectrum is gapped, with gap magnitude given according to $|\Delta_{\mathbf{k}}|$. Physically, the magnitude $2|\Delta_{\mathbf{k}}|$ is the minimum energy required to split bound Cooper pairs into their respective components. An explicit temperature-dependent form of the gap equation can be obtained by recognizing that

$$\langle 1 - \gamma^\dagger_{k'0}\gamma_{k'0} - \gamma^\dagger_{k'1}\gamma_{k'1}\rangle = 1 - 2f(E_{\mathbf{k}}) = \tanh(\beta E_{\mathbf{k}}/2). \tag{1.21}$$

Additionally assuming the simple momentum-independent form given by Eq. (1.17) for V, and replacing the summation by an integral leads to

$$\frac{1}{N(0)V} = \int_0^{\hbar\omega_c} d\xi \frac{\tanh[\beta\sqrt{\xi^2+\Delta(T)^2}/2]}{\sqrt{\xi^2+\Delta(T)^2}}. \tag{1.22}$$

This is the most widely recognized form of the BCS gap equation. In the weak coupling approximation, it predicts a universal relationship

$$\Delta(0) = 1.764\,k_B T_c \tag{1.23}$$

between the maximal gap size and the superconducting critical temperature.

Historically, the energy gap was perhaps the single most important prediction of the BCS theory. Early measurements of this gap in the superconductors using electromagnetic

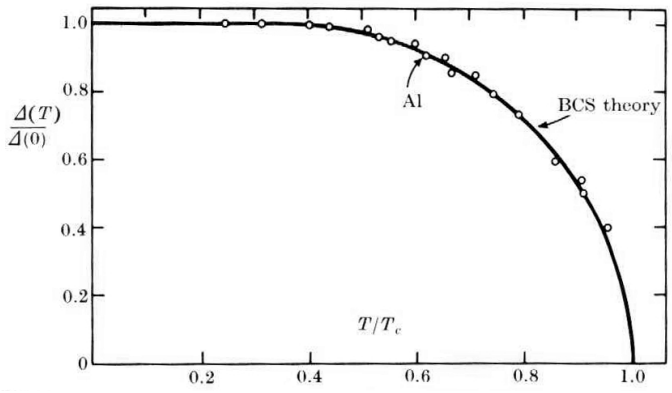

Figure 1.5. Solution to the BCS gap equation, and the temperature-dependent energy gap of aluminum as determined by electron tunneling. From Ref. 32.

absorption[49] and electron tunneling[20] served as both a strong validation of the BCS theory and a tell-tale sign that alternate theories, postulating a BEC framework for superconductivity,[50] were not likely to be correct. The basic validity of Eqs. (1.22) and (1.23) has now been broadly confirmed for many weakly coupled superconductors, including aluminum, niobium, tantalum, and tin.[51] Variations from Eq. (1.23) in more strongly coupled low-temperature superconductors like lead and mercury have clarified the influence of phonons on conventional superconductors.[32,51]

1.2.3.2 Quasiparticle excitations

Beyond the gap, the projection of Bogoliubov quasiparticles onto free-electron states reveals a quasiparticle spectrum where electrons and holes become increasingly mixed for electronic energies near the gap edge (as evident from the mixed electron and hole definitions of the Bogoliubov creation and annihilation operators in Eqs. (1.12) and (1.13)). Expressed in the language of Section 2.1.3 (do be discussed later on), the opening of a gap in BCS theory amounts to a self-energy correction given by[32,52]

$$\Sigma(\mathbf{k},\omega) = \frac{\Delta^2}{(\omega + i0^+) + \xi_{\mathbf{k}}}. \tag{1.24}$$

Substituting this into Dyson's equation and taking the imaginary part, one can show through a straightforward (albeit somewhat tedious) calculation that $A(\mathbf{k},\omega)$ is given by

$$A_{BCS}(\mathbf{k},\omega) = u_{\mathbf{k}}^2 \delta(\omega - E_{\mathbf{k}}) + v_{\mathbf{k}}^2 \delta(\omega + E_{\mathbf{k}}), \tag{1.25}$$

which is to say that the BCS self-energy splits solitary electron-like or hole-like spectral weight peaks in $A^{(0)}(\mathbf{k},\omega)$ into mixed states, as shown in Fig. 1.6. Although it is technically incorrect to think of these excited quasiparticles as true linear combinations of electrons and holes,[32] for certain purposes they can be thought of as such, and the effects have important implications for quasiparticle scattering properties.

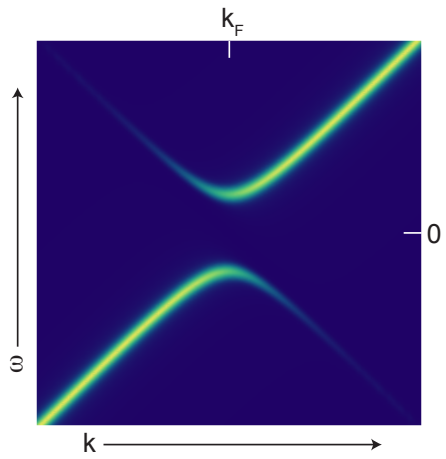

Figure 1.6. $A_{BCS}(\mathbf{k},\omega)$ for a linear bare band. The spectrum has been broadened slightly along the energy axis to illustrate delta-function weights.

1.2.3.3 Meissner effect

The Meissner effect can be derived in BCS theory by considering the momentum-space version of the electromagnetic perturbation Hamiltonian

$$H_1 = -\frac{e\hbar}{mc}\sum_{\mathbf{k},\mathbf{q}} \mathbf{k}\cdot\mathbf{a}(\mathbf{q})c^\dagger_{\mathbf{k}+\mathbf{q},s}c_{\mathbf{k},s} \tag{1.26}$$

and expanding out the creation and annihilation operators using the Bogoliubov transformation defined in Eqs. (1.12) and (1.13). The result for a static magnetic field upon calculating the current induced by the perturbation is[iii]

$$\mathbf{J}(\mathbf{r}) = -\frac{3c}{16\pi^2\xi_0\lambda_L(T)}\int \frac{\mathbf{R}[\mathbf{R}\cdot\mathbf{A}(\mathbf{r}')]}{R^4}J(R,T)d\mathbf{r}' \tag{1.27}$$

where $J(R,T)$ is a slowly varying function with temperature whose definition lies buried within the details of the BCS theory, but which is qualitatively similar to e^{-R/ξ_0}. The constant $\xi_0 \equiv \hbar v_F/\pi\Delta(0)$ is the BCS coherence length (not to be confused with $\xi_\mathbf{k}$ as identified in the previous sections!), and can be physically interpreted as the characteristic distance over which the the superconductor's superfluid density varies, or alternatively as the characteristic size of a Cooper pair, in real space at zero temperature. When $\mathbf{A}(\mathbf{r}')$ is constant over the range of $J(R,T)$, then Eq. (1.27) reduces to

$$\mathbf{J}(\mathbf{r}) = -\frac{c}{4\pi\lambda_L(T)}\mathbf{A}(\mathbf{r}), \tag{1.28}$$

which is exactly the London equation.

[iii] A derivation can be found in Refs. 3 and 15.

1.3 Beyond BCS: survey of cuprate phenomenology

It has become apparent that cuprate superconductors exhibit a great number of exotic characteristics not encapsulated within the simple BCS framework, including unconventional pairing symmetry, superconducting phase fluctuations, a poorly understood normal-state energy gap, and a phase diagram where superconductivity exists in close proximity to antiferromagnetism and various intertwined electronic phases. The 2008 discovery of high-temperature superconductivity in iron-based superconductors[30] added further intrigue to the situation, for there are many parallels between two classes of materials. In addition, the phase diagrams of both the cuprates and iron-based superconductors resemble the phase diagrams for a number of other superconductors that do not appear to fit well into the BCS framework, including heavy fermion compounds and various types of organic superconductors. The study of such "unconventional" superconductors has thus grown into a major research focus that extends well beyond high-T_c materials. Nevertheless, some basic tenets of the BCS theory have remained robust in the post-cuprate scientific understanding of superconductivity. In the final portion of this chapter, several defining characteristics of the cuprates that fall both within and beyond the scope of the BCS theory are reviewed.

1.3.1 BCS-like characteristics in the cuprates

Cooper pairs. Though theories postulating that superconductivity might arise from alternate schemes were briefly entertained in the immediate aftermath of the discovery of the cuprates,[53] it is by now well-established that the most fundamental tenet of the BCS theory—that electrons achieve macroscopic coherence by binding into Cooper pairs of charge $2e$—has remained intact in the post-cuprate world. Evidence for the the existence of Cooper pair picture is based on SQUID measurements,[54,55] where it has been shown that the fundamental flux quantum is $\Phi_0 = h/2e$ (see Fig. 1.7), as well as the Josephson effect.[56]

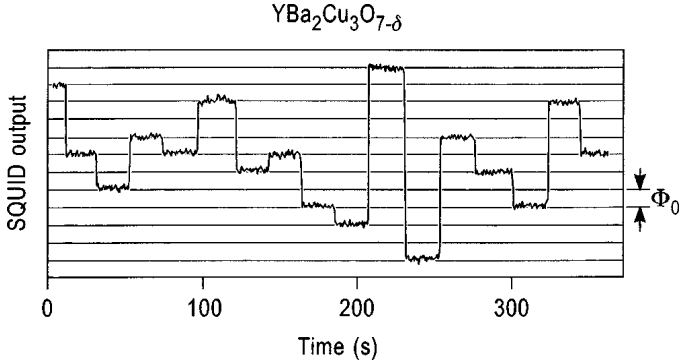

Figure 1.7. SQUID-based magnetic flux quantization measurement in superconducting $YB_2Cu_3O_{7-\delta}$, which provided early proof that superconducting charge carriers in the cuprates are pairs. After Ref. 54.

Singlet spin configuration. There is strong evidence, due to the Knight shift[57,58] and Andreev reflection[59,60] that the Cooper pairs in cuprates are bound in a singlet spin configuration, which is an implicit (although relaxable[33]) assumption in the BCS theory following from the expression (1.6) for $b^\dagger_{\mathbf{k}}$ in the BCS Hamiltonian.

Particle-hole mixing. Beyond proving that pairs form in singlet configuration, the demonstration of Andreev reflection in cuprates proves the existence of particle-hole mixing in the cuprates, for such processes would be impossible without mixing.[60] A complimentary verification of this phenomenon, measured by ARPES in the form of a quasiparticle peak that bends away from the chemical potential as it approaches $\mathbf{k}_F$, is displayed in Fig. 1.8. This, as well as subsequent studies[61,62] on both Bi2212 and Bi2223 have verified the basic functional form of the $u^2_{\mathbf{k}}$ and $v^2_{\mathbf{k}}$ coefficients as they appear in the BCS spectral function (Eq. (1.25)). However, as discussed later on, there is some evidence for particle-hole symmetry breaking in Pb-Bi2201, so the degree of particle-hole mixing near the Brillouin zone face may more complicated than Eq. (1.25) would indicate.

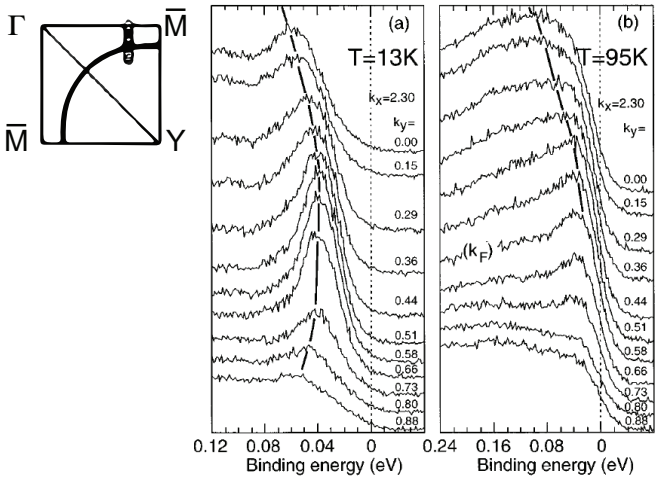

Figure 1.8. Verification of particle-hole mixing in Bi2212, as measured by ARPES. After Ref. 63.

1.3.2 Exotic properties of the cuprates

Unconventional pairing symmetry. Superconducting pairing symmetry refers to the group-theoretic properties of the gap parameter $\Delta_{\mathbf{k}}$ as determined after solving the BCS gap equation (Eq. (1.8)). In the simple BCS form it is assumed that $V_{\mathbf{kk}'}$ is negative and momentum-independent, so $\Delta_{\mathbf{k}}$ reduces to a constant. However, many other solutions are possible in the general case, including unconventional pairing symmetries where the gap changes sign depending on its location in k-space.[iv] In general, the solution for $\Delta_{\mathbf{k}}$ in

[iv] The term *unconventional pairing* historically refers to a pairing symmetry that is lower than the symmetry of the underlying crystal lattice.[3,33] Oddly enough, the iron-based superconductors, which are believed to

Eq. (1.8) can be rigorously expanded as a sum of basis functions $f_{\Gamma m}(\mathbf{k})$, classified in terms of the irreducible representations Γ of the superconductor's point group symmetry (see Ref. 33 for a more complete explanation). The spin configuration will restrict this summation to set of functions sharing even or odd parity, and in practice, basis functions originating from different symmetry representations will lead to such different values of T_c that only one family of functions is typically needed.[33] In the case of cuprates, the most relevant symmetry classification appears to be the B_{1g} representation of the D_{4h} point group, so that the gap parameter $\Delta_{\mathbf{k}}$ is given by[33,65,66]

$$\Delta_{\mathbf{k}} = \Delta_0 \left[\cos(k_x a) - \cos(k_y b)\right] + \Delta_0 B \left[\cos(2k_x a) - \cos(2k_y b)\right] + ... \tag{1.29}$$

This function has all of the same properties under rotations and reflections as the $d_{x^2-y^2}$ spherical harmonic, and for this reason it is often said that cuprates exhibit d-wave pairing symmetry, despite the fact that angular momentum is not a good quantum number. Given the normal-state Fermi surface, it is possible to use this gap function determine the shape of a bound Cooper pair in real space, using the equation[65,66]

$$\phi(\mathbf{x}_1 - \mathbf{x}_2) = \sum_{\mathbf{k}} \frac{\Delta_{\mathbf{k}}}{2E_{\mathbf{k}}} e^{i\mathbf{k}\cdot(\mathbf{x}_1 - \mathbf{x}_2)}. \tag{1.30}$$

Schematic diagrams of the d-wave order parameter, in k-space and in real space, are displayed in Fig. 1.9. Both the momentum-space gap function and real space correlation function

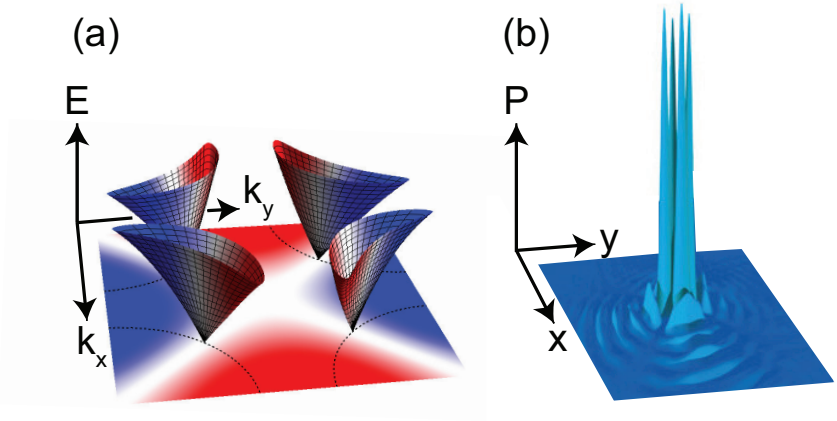

Figure 1.9. Visualization of a d-wave superconducting order parameter **(a)** in terms of the energy gap in k-space (color-coded to indicate the sign of $\Delta_{\mathbf{k}}$), and **(b)** in terms of a Cooper-pair correlation function in real space, defined as the probability of finding an electron at location (x, y) given its time-reversed partner at the origin. The plot in (b) is after Ref. 67.

exhibit nodal lines that extend radially outward from the origin along directions that are diagonal to the copper-oxide bonds.

predominantly have $s_{\pm}$ pairing, would actually be classified as conventional under this definition despite the parallels that connect them to cuprates. Largely for this reason, the term has been more recently redefined to include any gap parameter that has different signs in different regions of momentum space.[29,64] I adopt the latter interpretation.

The claim of $d_{x^2-y^2}$ pairing symmetry in the cuprates has been perhaps most strikingly verified through ARPES measurements of gap nodes along the Brillouin zone diagonals in cuprates,[68,69,70,71,72,73] and through phase-sensitive SQUID measurements,[74,75,65] but is also indicated by various other probes including measurements of the London penetration depth, specific heat, thermal conductivity, Raman scattering, nuclear magnetic resonance, and the nonlinear Meissner effect.[65] More recently, the cuprate pairing symmetry has also been confirmed in a phase-sensitive manner by scanning tunneling spectroscopy,[76] where it has been shown that the nontrivial coherence factors imposed by d-wave symmetry allow one to selectively enhance or reduce the scattering rates between certain portions of momentum space through exposing a cuprate sample to magnetic fields. It is worth noting, however, that there in very underdoped cuprates there have been recent reports of nodeless superconductivity,[73,77,78] which would require a more complex pairing symmetry than the lowest-order $d_{x^2-y^2}$ form.

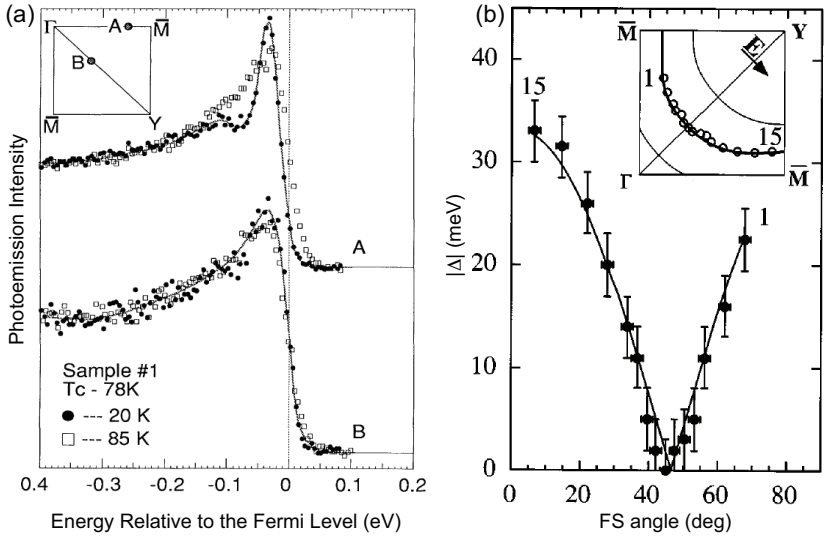

Figure 1.10. Early ARPES measurements of gap anisotropy in Bi2212. After Refs. 68 (panel (a)) and 69 (panel (b)).

Pseudogap. Not long after the discovery of the d-wave gap in the superconducting state of the cuprates, ARPES measurements discovered what appears to be an excitation gap even above the superconducting critical temperature.[79,80] Pioneering ARPES experiments cryptically dubbed this new phenomenon as a "pseudogap,"[80] which is a term borrowed from descriptions of NMR measurements[81,82] where it reflected an early belief that the phenomenon was perhaps not a true gap, but rather a partial suppression in the density of states. ARPES measurements indicate that at least for certain directions in momentum space, the pseudogap is as real as the superconducting gap. Nevertheless, the pseudogap terminology persists into the present day, perhaps aptly reflecting the field's corresponding vague understanding of the phenomenon's underlying physics. The current debate surrounding the pseudogap is considered by many to be one of the most important discussions in the physics of cuprates, perhaps second only to the question of the superconducting pairing mechanism.

Key characteristics of the pseudogap are the following: (1) It becomes largest near half-filling, and steadily decreases in magnitude with increased hole doping. Correspondingly, the pseudogap onset temperature T^* is highest at low doping and steadily decreases with increased hole doping until it eventually appears to merge with the superconducting critical temperature T_c somewhere near $p = 0.22$.[73,83] (2) Only a finite portion of the normal-state Fermi surface is gapped in the pseudogap state. This breaks up the normal-state Fermi surface into four apparently discontinuous "Fermi arcs," which appear to lengthen with increased hole doping or temperature, and which are extremely difficult to understand from a theoretical standpoint. (3) As a corollary to point (2), where the pseudogap does exist in momentum space, its largest magnitude is at the Brillouin zone face. This has lead many to conclude that the pseudogap shares the superconducting gap's d-wave symmetry, although the assertion is under debate. (4) It is difficult to identify T^* precisely. Whereas the opening of most excitation gaps accompanies phase transition, where well-defined singularities show up in various thermodynamic observables, this appears not to be the case for the pseudogap. In fact thermodynamic signatures of the pseudogap have only very recently been confirmed.[84]

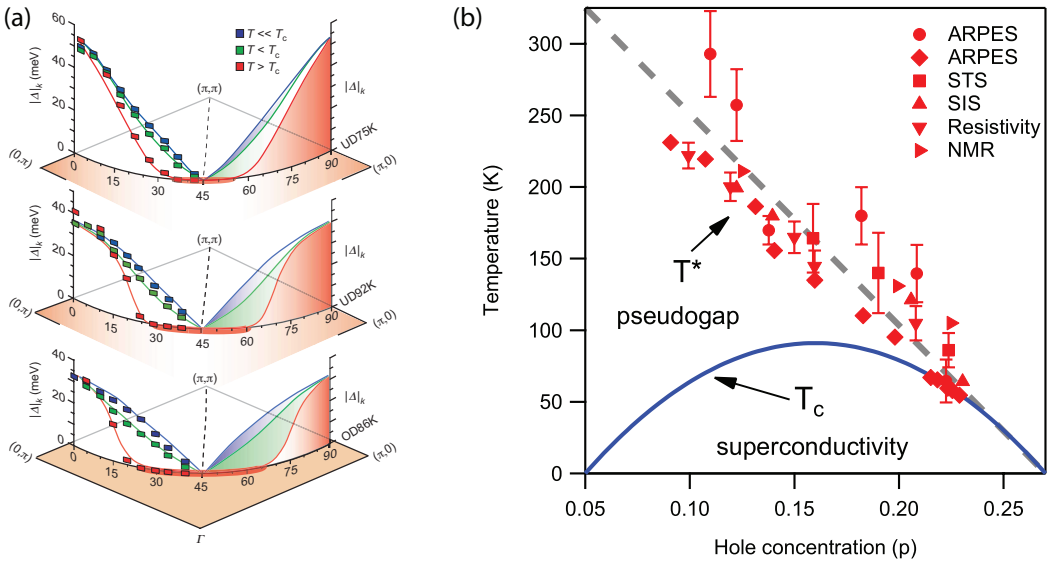

Figure 1.11. Phenomenology of the pseudogap. **(a)** Temperature- and momentum-dependent ARPES measurement of the gap magnitude for three different dopings of Bi2212. As shown by the red data points, the pseudogap state comes to a maximum at the Brillouin zone face and leaves (apparently) gapless Fermi arcs in the vicinity of the Brillouin zone diagonal. From Ref. 71. **(b)** Measurements of the doping and temperature dependence of T^*, aggregated from ARPES,[73,83] scanning tunneling spectroscopy (STS),[85] superconductor-insulator-superconductor (SIS) tunneling,[86,87] resistivity,[88] and NMR spin lattice relaxation[89] measurements.

Theories of the origin of the pseudogap in cuprates generally fall into one of two broad classifications. In the first classification, the pseudogap is explained by the substantial phase fluctuations that cuprates, particularly in the underdoped regime, are believed to exhibit. In such a scenario it is possible for electrons to bind into "pre-formed" pairs above T_c, which have not yet established the requisite level of phase coherence to result in superconductivity.

In the second classification, the pseudogap is related to a competing or intertwined phase that is completely different from superconductivity, tending for example toward the formation of a charge or spin density wave. Framed in this way, the question has often been distilled to whether or not the pseudogap is a "friend or foe" to superconductivity,[90] which could inform the synthesis of new materials with higher critical temperatures than we currently know about, or more desirable transport properties. In actuality, the question might not be so cleanly posed, for as we shall argue later on in Chapter 7, both effects likely play a role in shaping the pseudogap's existence. Specific evidence of phase fluctuations and competing phases in cuprates are discussed next.

Phase fluctuations. It was realized early on that cuprate superconductors are likely to be affected much more strongly by phase fluctuations than their low-temperature superconductors, and that these effects may put the cuprates into a regime where phase fluctuations, rather than the mean-field critical temperature, determine the superconducting critical temperature.[91] Perhaps the most compelling evidence to date for this scenario comes in the form of Nernst effect measurements, where evidence for superconducting vortices has been observed well above T_c, with a difference between the onset temperature for phase fluctuations and the superconducting critical temperature increasing in the underdoped regime.[92]

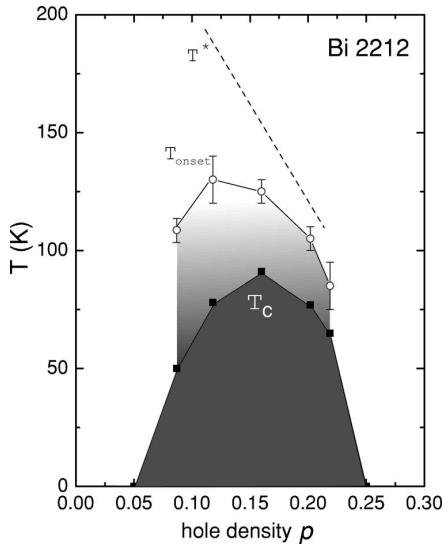

Figure 1.12. Nernst effect measurements of the onset of superconducting phase fluctuations above T_c in Bi2212. From Ref. 92.

For both of these reasons, many ARPES practitioners have taken the phase-fluctuation view in interpreting the pseudogap. Evidence for the phase fluctuation scenario in cuprates consists of the fact that the magnitude of the superconducting gap near the Brillouin zone face, as well as the shape of the spectrum, does not appear to significantly change across T_c,[93] and from the fact that some modeling approaches[94] and fitting methodologies[72] indicate that the onset of Fermi arcs near the Brillouin zone diagonals in the normal state may be an artifact caused by thermal broadening. There is some debate about this final point, as noted in the previous section.

Intertwined electronic ordered phases. Perhaps the most important recent progress in the study of cuprates has been the widespread establishment of intertwined electronic ordered phases, which exist in close proximity to or even simultaneously with superconductivity. Evidence for such phases, in the form of charge-density-wave stripes, was established as early as 1992 near $p = 0.125$ hole doping in LBCO, LSCO, and related cuprate compounds within the "lanthanum-214" crystal structure family.[95,96,97,98,99,100,101] Recently, however, a form of charge density wave has been observed through NMR[102] and x-ray scattering measurements.[103,104] The discovery not only established the prevalence of competing phases within a new class of cuprate crystal structures, but in doing so in YBCO, has established charge order in what is among the cleanest of cuprate materials.

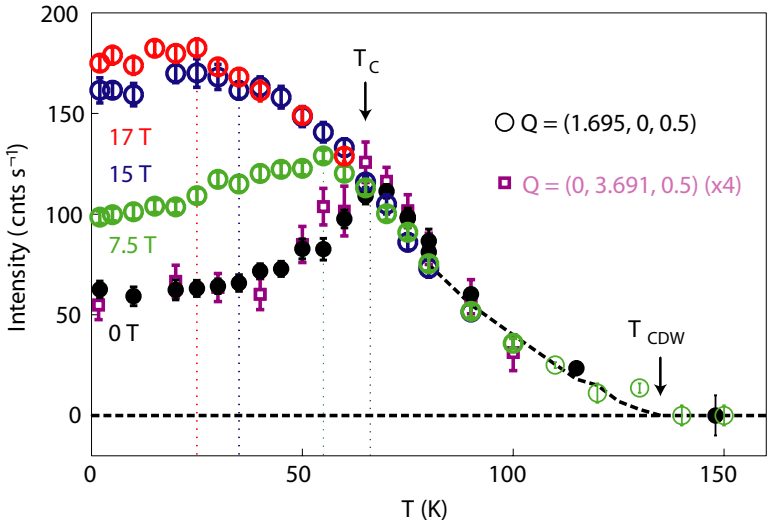

Figure 1.13. Charge density wave Bragg peak in YBCO as measured by x-ray diffraction. The cusp at T_c in the black data points, which indicates competition between the CDW and superconductivity, can be eliminated by the application of a large magnetic field as shown by the green, red and blue data points. From Ref. 104.

A flurry of experimental and theoretical work has followed. Evidence for charge-density-wave ordering tendencies in bismuth cuprates has been previously reported in STM measurements,[105] but recent combined STM, REXS, and ARPES measurements have now reported fortified claims of such ordering in both Bi2212[106] and Bi2201.[107] Theories being put forth by a number of researchers explaining the role that these intertwined phases might have in relation to superconductivity.[108,109,110,111] For ARPES, the evidence for charge-density-wave phases in cuprates may provide an alternate explanation for the pseudogap from phase fluctuations, and dovetails with recent evidence suggesting that the nodal and antinodal gap exhibit differing trends as a function of doping[73,112] and temperature[71] (though, as noted above, the latter claim is debated) and with the intriguing demonstration of particle-hole symmetry breaking in the antinodal quasiparticle spectra as extracted from lead-doped Bi2201.[113,114]

Proximity to antiferromagnetism. Cuprates exhibit an intriguingly intimate relationship with antiferromagnetism, for they only become superconducting after doping an antifer-

romagnetic parent compound with carriers. With the recent discovery of high-temperature superconductivity in iron-based superconductors, interest in this proximity has been greatly heightened, and in fact, very similar phase diagrams are observed in what is becoming an increasingly wide array of unconventional superconductors more generally, ranging from the cuprates, to iron-based superconductors, to heavy-fermion compounds, to organic superconductors. The appearance of superconductivity in close proximity to magnetic phenomena is extremely surprising from the point of view of BCS theory—external magnetic fields, for example, destroy superconductivity.

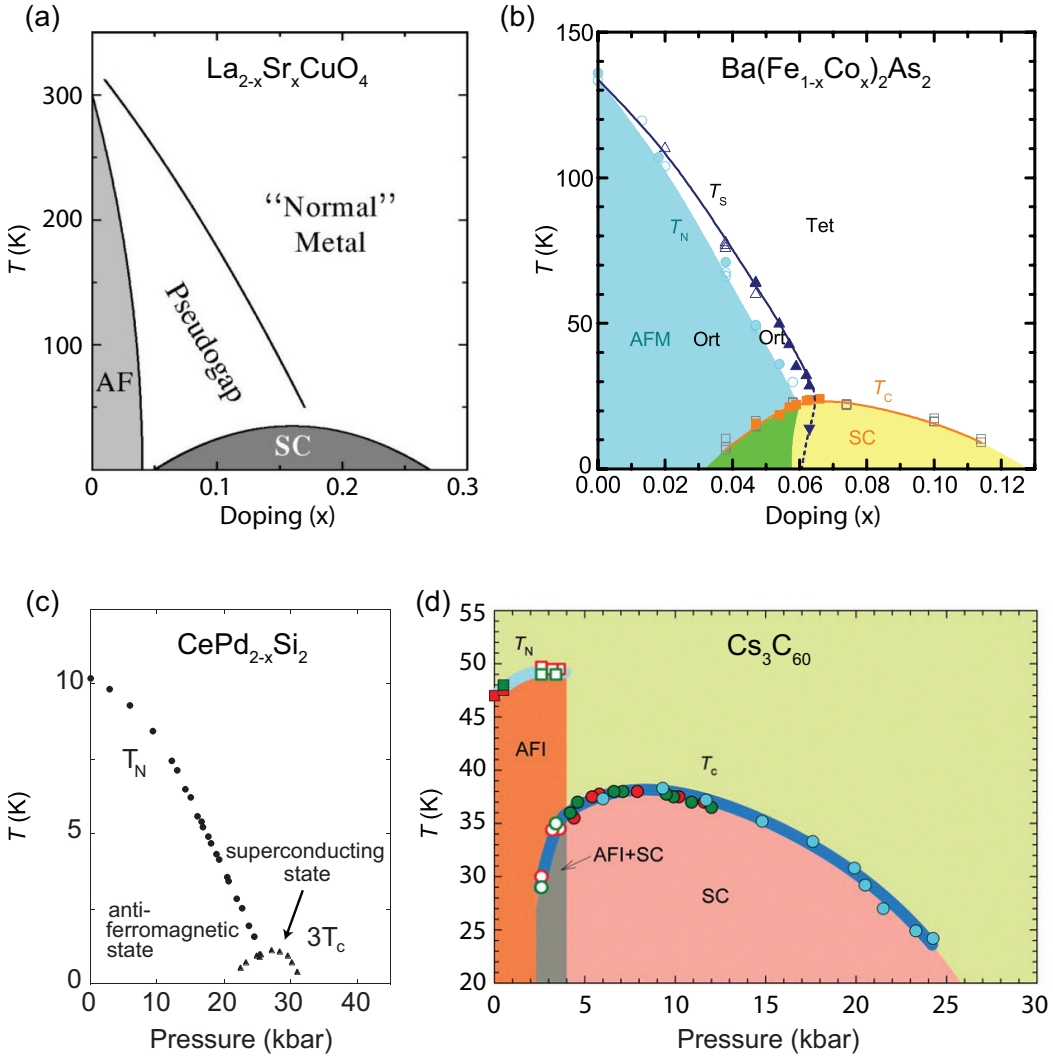

Figure 1.14. Comparison between the phase diagrams for **(a)** the cuprate superconductor $La_{2-x}S_xCuO_4$ and **(b)** the iron-based superconductor $Ba(Fe_{1-x}Co_x)_2As_2$ as a function of carrier concentration, as well as the phase diagrams for **(c)** the heavy fermion superconductor $CePd_{2-x}Si_2$ and **(d)** the organic superconductor A15-structured Cs_3C_{60} as a function of pressure. After Refs. 115, 116, 117, and 118.

Phonons. Finally, there is substantial evidence for strong electron-phonon coupling in the cuprate superconductors which, although reminiscent at first blush of the coupling interaction that drives low-temperature superconductivity, exhibits many exotic behaviors. In fact, one of the guiding principles that Bednorz and Müller followed in their discovery of $La_{2-x}Ba_xCuO_4$ was to search for materials with strong Jahn-Teller distortions.[26] There are many signatures for strong electron-phonon interactions in the cuprates, including Raman scattering measurements,[119] infrared spectroscopy,[120] and neutron scattering.[121] Perhaps the most straightforward evidence for electron-phonon coupling in recent times, however, appears through ARPES measurements of a prominent kink in the nodal electronic dispersion at a binding energy of 70 meV.[43] Measurements along the antinodal direction[122] reveal a similar feature that appears to reflect electron-phonon coupling, but which appears to be distinct, for it shifts to a binding energy of about 40 meV as the temperature is increased above T_c.

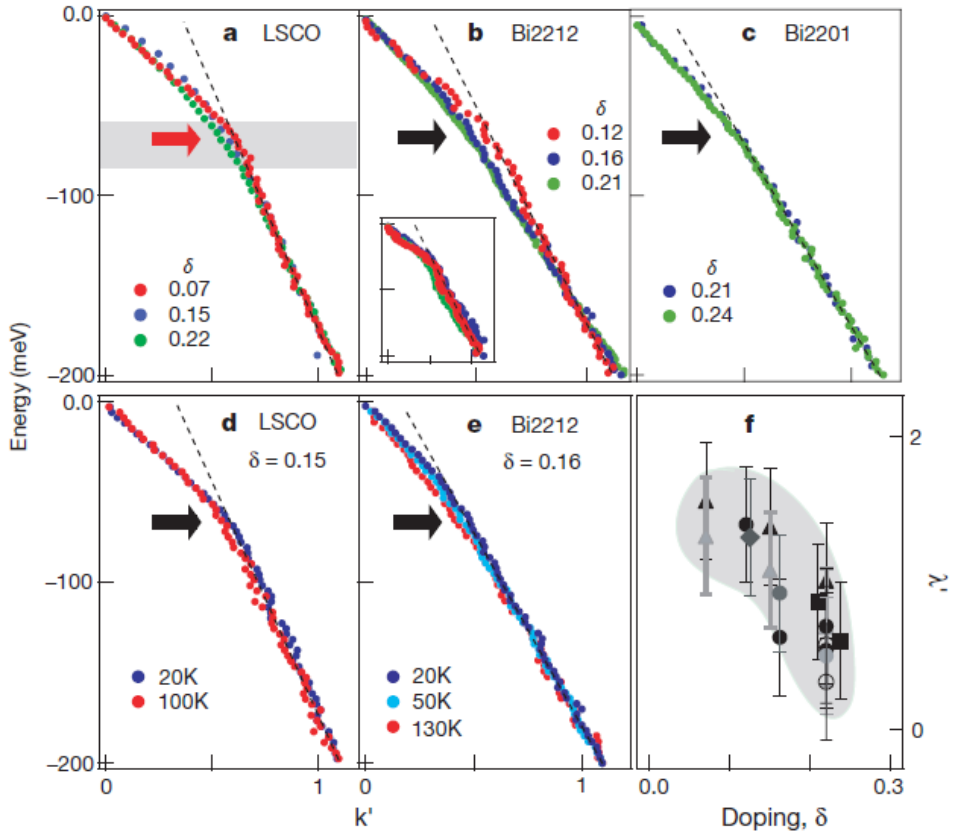

Figure 1.15. Evidence for widespread electron-phonon coupling in cuprate superconductors. **(a)**–**(e)** Nodal electronic dispersions in LSCO, Bi2212, and Bi2201. All dispersions exhibit a prominent electron-boson-coupling kink feature at 70 meV. **(f)** Doping-dependent coupling constant λ', defined by comparing the low- and high-binding energy slopes of the data displayed in (a)–(e). From Ref. 43.

1.4 Opportunities for time-resolved probes

We now come to the question of what do time-resolved methods have to offer? The answer is still in the making, but a number of possibilities are emerging.

With the cuprates in particular, there are a great many known interactions that all have similar energy scales, and yet which are different in their microscopic origin. The hope is that time-resolved techniques might be useful in disentangling these different interactions through projecting the interactions into a wider range of parameter space than would be available at equilibrium. In Chapter 4 we will demonstrate that quasiparticle relaxation rates exhibit a marked fluence and momentum dependence, for example, and explores the possibility that these differences in rates might lead to new insights in the pairing interaction or the interaction between superconductivity and intertwined phases. In Chapters 5 and 6 we will explore results that occur when the pump fluence is pushed beyond the threshold required for the destruction of superconductivity, thereby probing the dynamical interactions both between superconductivity and normal-state dynamics, and between superconductivity and between superconductivity and pseudogap dynamics. Finally, in Chapter 7 we demonstrate that time-resolved ARPES can be used to bring out signatures of changing interactions that are hard to disentangle by any other means. In particular, we will show that time-resolved ARPES is perhaps the only probe we are aware of that can simultaneously differentiate temperature scales for the pseudogap, phase fluctuations, and superconductivity in a single experiment, and furthermore that signatures appear along the nodal direction in momentum space, where neither superconductivity nor the pseudogap are normally identified.

Chapter 2

Analysis techniques

The text that follows summarizes the basic formalism of ARPES, as well as analysis techniques including recipes for characterizing momentum-dependent quasiparticle populations and superconducting band gaps. A discussion of quasiparticle relaxation models is also included with special emphasis on the Rothwarf-Taylor model, which is extensively used in interpreting the results presented in Chapters 4–7.

2.1 Theory of ARPES

Angle-resolved photoemission spectroscopy, or ARPES, is the experimental foundation on which all time-resolved ARPES systems are based. The basic scheme is a photon-in, electron-out scattering process employed employed to measure a flat, single-crystal sample maintained in ultrahigh vacuum (UHV) conditions. Photoelectron outgoing kinetic energies and exit angles are directly measured to obtain a picture of a material's electronic band structure. One can develop an intuitive understanding for ARPES by considering a non-interacting system, where the photoemission process is reduced to a one-particle problem. Translation symmetry is preserved along directions parallel to the sample surface, and consequently the parallel component of each electron's momentum is conserved (to within a reciprocal lattice vector) as electrons are ejected. In addition, for steady-state photoemission, the Hamiltonian is invariant under time evolution, which results in usual rules for energy conservation. Thus there exist simple relationships between photoelectron kinetic energies, exit angles, and the energy and momentum of electrons when they were still inside the crystal lattice, given by[123,124,115]

$$(E - \mu) = E_{kin} + \Phi_W - h\nu \tag{2.1}$$

$$\hbar k_{\parallel} = \sqrt{2m\,E_{kin}}\,\sin\theta, \tag{2.2}$$

where $\hbar k$ and E are the electronic crystal momentum and energy inside the sample, μ is the chemical potential (often identified in the literature as the Fermi energy E_F, although equality between the two quantities is strictly true only at $T = 0$), E_{kin} is photoelectron kinetic energy after leaving the sample, Φ_W is the work function, $h\nu$ is the incoming photon energy, $m = 9.11 \times 10^{-31}$ kg is the electronic mass in vacuum, and θ is the photoelectron exit angle relative to normal emission.

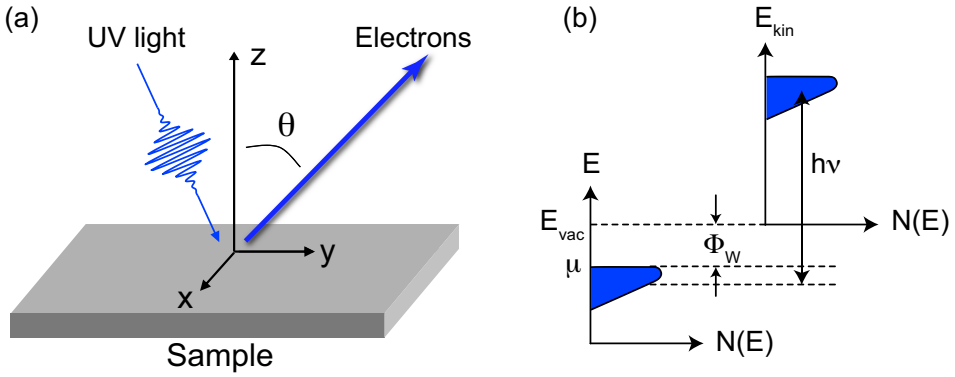

Figure 2.1. Schematic cartoon of the ARPES technique, **(a)** in real space, and **(b)** in terms of energy levels.

2.1.1 Theory of ARPES in the presence of interactions

For interacting systems, the physics of photoemission can be more accurately understood using Fermi's golden rule,

$$I = \sum_f \frac{2\pi}{\hbar} |\langle \psi_f^N | H_{int} | \psi_0^N \rangle|^2 \delta(E_f^N - E_0^N - h\nu), \tag{2.3}$$

where the energy- and momentum-resolved count rate I is expressed in terms of the matrix elements of an electromagnetic perturbation Hamiltonian H_{int} between $|\psi_0^N\rangle$ and $|\psi_f^N\rangle$, which are initial and final states of the N-particle system with respective energies E_0^N and E_f^N (at $T = 0$, for example, the state $|\psi_0^N\rangle$ corresponds to the N-particle ground state). Typically, one also makes two additional assumptions.[123,115,125] First, following the three-step model, it is assumed that the photoemission process can be divided into discrete events: (i) excitation of a photoelectron from the valence band high-energy states while still inside the crystal, (ii) transport of the photoelectron from the bulk to the sample surface, and (iii) photoelectron escape into the vacuum outside the crystal. Effects related to steps (ii) and (iii), which include inelastic scattering effects and photoelectron transition probability effects for crossing the sample surface, can therefore be isolated from the photoemission event (step (i)), and are often ignored or lumped into a background signal. Second, in what is termed the sudden approximation, it is usually assumed that steps (ii) and (iii) of the three-step model occur so quickly that the system can be approximated as responding instantaneously to the optical

perturbation, i.e., once a photoelectron is created, there is no subsequent interaction between it and the remaining system. Thus, the a photoelectron leaving the sample can be well-described as a plane wave.

Incorporating these approximations, we factorize the initial and final states in Eq. (2.3) as follows:

$$\begin{aligned} |\psi_f^N\rangle &\rightarrow |\psi_{E_{kin},m}^{\mathbf{k},N}\rangle = \mathcal{A}|\phi_{E_{kin}}^{\mathbf{k}}\rangle|\psi_m^{N-1}\rangle \\ |\psi_0^N\rangle &\rightarrow |\psi_0^{\mathbf{k},N}\rangle = \mathcal{A}|\phi_0^{\mathbf{k}}\rangle c_{\mathbf{k}}|\psi_0^N\rangle \end{aligned} \tag{2.4}$$

The final state $|\psi_f^N\rangle$ is described as the product of a one-electron plane wave state $|\phi_{E_{kin}}^{\mathbf{k}}\rangle$ and an $N-1$ particle state $|\psi_m^{N-1}\rangle$ corresponding to the electron population left behind. Because the total transition under the golden rule treatment is given the by summation over final states, this "remainder" state can be chosen to be an eigenfunction of the $N-1$ particle system and its index is accordingly changed to m, decoupling it from from the plane wave indices $\mathbf{k}$ and E_{kin}. The initial state $|\psi_0^N\rangle$ is also factorized into a one-electron orbital state and an $N-1$ electron remainder state (this amounts to an additional assumption beyond the three-step model and sudden approximation), though no assumptions are required regarding the shape of either wavefunction. In both the initial and final states, the operator $\mathcal{A}$ antisymmetrizes the product state to ensure compatibility with the Pauli exclusion principle.

Following Eqs. (2.4), the total perturbation matrix element can be separated into one-electron and overlap-integral components, $\langle\psi_f^{\mathbf{k}}|H_{int}|\psi_0^{\mathbf{k}}\rangle = \langle\phi_{E_{kin}}^{\mathbf{k}}|H_{int}|\phi_0^{\mathbf{k}}\rangle\langle\psi_m^{N-1}|c_{\mathbf{k}}|\psi_0^N\rangle$, so that Eq. (2.3) becomes[i]

$$\begin{aligned} I(\mathbf{k}, E_{kin}) = &\frac{2\pi}{\hbar}|\langle\phi_{E_{kin}}^{\mathbf{k}}|H_{int}|\phi_0^{\mathbf{k}}\rangle|^2 \\ &\times \sum_m |\langle\psi_m^{N-1}|c_{\mathbf{k}}|\psi_0^N\rangle|^2\, \delta(E_{kin} + \Phi_W + \mu + E_m^{N-1} - E_0^N - h\nu). \end{aligned} \tag{2.5}$$

The photoelectron contribution $E_{photo} = E_{kin} + \Phi_W + \mu$ to the energy eigenvalue $E_m^N = E_m^{N-1} + E_{photo}$ has also been explicitly written out in the delta function of the above equation to express the count rate I in terms of photoelectron kinetic energy E_{kin}. Finally, we can express Eq. (2.5) more suggestively by defining the quantity $\omega \equiv E_{kin} + \Phi_W - h\nu$, in analogy with $E - \mu$ in Eq. (2.1), to obtain

$$I(\mathbf{k}, \omega) = \underbrace{\frac{2\pi}{\hbar}|\langle\phi_{E_{kin}}^{\mathbf{k}}|H_{int}|\phi_0^{\mathbf{k}}\rangle|^2}_{I_0} \underbrace{\sum_m |\langle\psi_m^{N-1}|c_{\mathbf{k}}|\psi_0^N\rangle|^2 \delta(\omega + E_m^{N-1} - E_0^N)}_{A^-(\mathbf{k},\omega)}. \tag{2.6}$$

$$= I_0 \, A^-(\mathbf{k}, \omega) \tag{2.7}$$

The term I_0 encodes selection rules for photoemission transitions as a function of $\mathbf{k}$, ω, $h\nu$, and photon polarization. While experimentally important, it does not usually impart deep

[i] Energy conservation is imposed through the delta function in Eq. (2.5). Note that three-dimensional crystal momentum conservation is implicitly imposed for the sake of simplicity by defining the same value of $\mathbf{k}$ for the initial and final states in Eqs. (2.4). The condition can be relaxed to the imposition of parallel crystal momentum conservation only by generalizing $\mathcal{A}|\phi_0^{\mathbf{k}}\rangle c_{\mathbf{k}}|\psi_0^N\rangle$ to $\mathcal{A}|\phi_0^{\mathbf{k}'}\rangle c_{\mathbf{k}'}|\psi_0^N\rangle$ in Eq. (2.4), and by factoring out momentum-constraining delta functions or Lorentzians as appropriate and introducing a summation over initial states, as outlined in Ref. 123.

physical insights. The quantity $A^-(\mathbf{k},\omega)$, however, is very interesting. In the non-interacting case, the initial state $|\psi_0^N\rangle$ reduces to a product of one-electron Bloch states, as do the eigenstates $|\psi_m^{N-1}\rangle$, so that $m \to n, \mathbf{k}'$ (where $\mathbf{k}'$ corresponds to the crystal momentum of the removed electron). Thus, the overlap integral $\langle\psi_m^{N-1}|c_\mathbf{k}|\psi_0^N\rangle$ reduces to the delta function $\delta(\mathbf{k}-\mathbf{k}')$, and $A^-(\mathbf{k},\omega)$ traces out a series of delta functions centered at values of energy and momentum dictated by the conservation laws displayed in Eqs. (2.1) and (2.2). As we shall show in Section 2.1.3, in the more general case, $A^-(\mathbf{k},\omega)$ is intimately related to the single-particle spectral function $A(\mathbf{k},\omega)$, which is an important object from field theory that describes a material's band structure in the presence of electronic interactions. The ability of ARPES to measure $A(\mathbf{k},\omega)$ in such a direct manner is one of the main reasons why the technique is so useful. Indeed, over the past 20 years, ARPES has proven itself as perhaps the single most powerful technique in all of physics for experimentally accessing the dynamics of quantum materials.

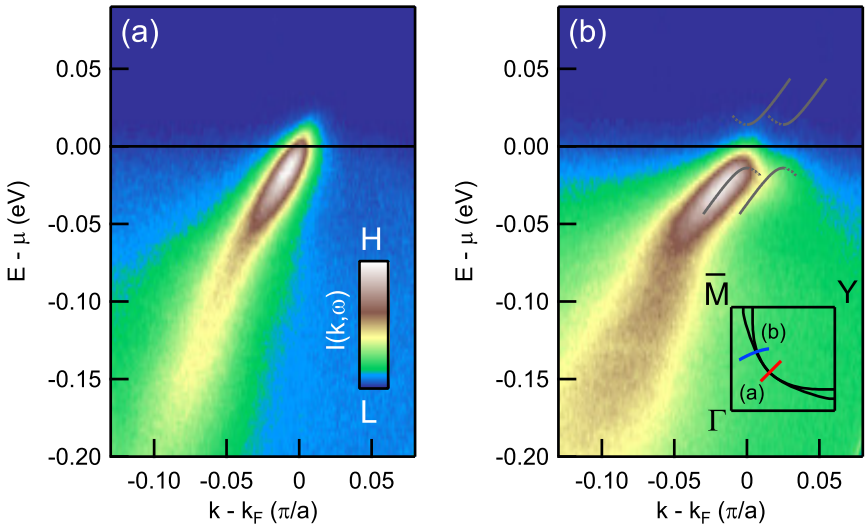

Figure 2.2. Typical measured ARPES dispersion spectra in the cuprate superconductor Bi2212 at low temperature, corresponding to two cuts through momentum space as indicated by the schematic in (b). The momentum wave vector k is expressed in units of π/a, where $a = 3.83$ Å is the Cu-O in-plane lattice constant.[126]

2.1.2 Experimental considerations

A number of experimental factors can separate an ARPES measurement from the true nature of band structure. First, as already alluded to in the previous section, momentum, energy, and polarization dependent variations in I_0 can make it difficult to accurately compare the intensities of one ARPES cut relative to another, and in cases may completely suppress the photoemission cross section.

Second, because the boundary between the crystal and vacuum breaks perpendicular translational symmetry, the perpendicular component of crystal momentum ($\hbar k_\perp$) is explic-

itly not conserved. In crystal structures with substantial c-axis dispersions, this results in a broadening of spectral bands that can make it hard to perform quantitative analyses of line shapes.[123,124] Fortunately, such problems are largely eliminated in two-dimensional systems like single-layer graphene or topological insulator surface states, and in layered crystal structures like the cuprate superconductors because c-axis dispersion is nearly or completely flat. In fact, non-conservation of $k_\perp$ in these two-dimensional cases may actually be a good thing, for it greatly simplifies the problem of locating desired points in the crystalline band structure. For example, in single-layer graphene[127] or the topological insulator bismuth selenide[128] the Dirac nodes can be located using a wide variety of photon energies. By contrast, in three-dimensional graphite[129] or Na_3Bi,[130] such nodes can only be located by carefully tuning both the photon energy and measurement angle to one of a much smaller subset of values.

Third, the photoelectron mean free path within a crystal is on the order of nanometers, classifying ARPES as a surface-sensitive technique. The effect is more severe at synchrotron photon energies (where the mean free path characteristically drops to $\approx$0.4 nm) than at laser photon energies (where the mean free path is characteristically $\approx$4 nm).[131] As above, this is irrelevant for true two-dimensional structures. However, features like surface reconstruction effects may be overly represented in ARPES measurements of layered materials like the cuprates.

Fourth, particularly at the low photon energies typical of laser-based ARPES systems, the work function Φ_W poses a significant additional complicating factor. At synchrotron photon energies, the work function is so much smaller than the photon energy that its precise value is largely irrelevant in Eqs. (2.1) and (2.2). At laser frequencies, by contrast, Φ_W is often equal to or even much greater than E_{kin}. Hence, it is imperative to be able to characterize it. It is occasionally noted that Φ_W is the work function corresponding to the analyzer, not the sample—the reason being that the analyzer cone and sample are both grounded, which sets up a contact potential between the two elements. In fact, the most influential contact potentials in an ARPES experiment are not those between the sample and the analyzer, but rather those occurring between the sample and the metallic puck on which the sample is mounted. Depending on the sample and puck material characteristics, empty space in the immediate vicinity of a sample may be subject to potential differences as large as 500 mV, over distances as small as a fraction of a millimeter. The specific geometry of the resulting electric fields does not alter Eq. (2.1), but it can—and does—significantly affect the angles θ at which photoelectrons enter the analyzer. The effect should not be ignored in laser ARPES measurements, and is discussed in greater detail in Chapter 3.

There is a silver lining to the contact potential effect in one sense. Because every electron, regardless of where it starts, will end up being measured by the same detector, photoelectrons at the chemical potential of every sample will be boosted to the same kinetic energy, given a fixed photon energy, by the time they make it to the analyzer cone regardless of differing sample, puck, and manipulator work functions. If the detection scheme is based on a hemispherical analyzer, it is therefore possible to quantify the chemical potential for a any material by comparing to a metallic reference like polycrystalline gold.

2.1.3 Field theory techniques

In a simplistic picture it is possible to understand and interpret ARPES data as an "energy-smeared" version of the simple non-interacting band structure picture. However, insight is greatly facilitated by adopting a field-theoretic perspective for the interpretation of $A^-(\mathbf{k},\omega)$. The reason is that a many-body description of nature is inherently built into the fabric of field theory, with particle creation and annihilation operators serving a fundamental purpose in even the simplest calculations. This section outlines some of the concepts from field theory that are most relevant to ARPES, starting with the one-electron Green function. An excellent expanded description of many of these ideas can be found in Chapter 5 of Ref. 32. The reader is referred to Ref. 132 for an exhaustive discussion of the role of field theory in condensed matter physics. Ref. 133 covers much of the same formalism from a high-energy physics perspective. The connection between Green functions and ARPES is also briefly discussed in Refs. 115, 123, and 125.

2.1.3.1 Green function approach to photoemission

The most relevant Green function for ARPES is the *one-electron Green function*, defined in the Heisenberg picture as

$$G_{\text{ret}}(r_1,t_1,r_2,t_2) \equiv -i\Theta(t_1-t_2)\langle\Omega|\{\psi(r_1,t_1),\psi^\dagger(r_2,t_2)\}|\Omega\rangle. \tag{2.8}$$

The states $|\Omega\rangle$ represent the interacting system's N-particle ground state, ψ and $\psi^\dagger$ respectively represent annihilation and creation operators. Spin degrees of freedom are ignored throughout this section for convenience, but could easily be incorporated by adding a quantum number subscript to ψ and $\psi^\dagger$. Eq. (2.8) is the retarded version of the one-electron Green function (hence the subscript) and represents just one of six closely related two-point correlation functions that are commonly used in field-theoretic approaches to solving many-body electron problems at zero temperature, and one of several relevant Green functions in the finite-temperature regime.[132] The retarded formulation is among the most physical of these as it obeys causality. Other formulations, such as the time-ordered propagator G_t that is extensively treated in Refs. 32 and 133, are useful in deriving the various theorems that are quoted below without proof.

If we assume time and translation invariance in Eq. (2.8) (as is commonly done despite the fact the latter is technically false in a solid) we find an equivalent description of the single particle Green function in terms of the spatial Fourier transform

$$G_{\text{ret}}(\mathbf{k},\tau) = -i\Theta(\tau)\langle\Omega|\{c_{\mathbf{k}}(\tau),c^\dagger_{\mathbf{k}}(0)\}|\Omega\rangle. \tag{2.9}$$

Physically, both the position and momentum representations of G describe the quantum mechanical probability amplitude for a particle originating at some point to propagate to some other point at later time $\tau = t_1 - t_2$. For example, the first term of the anticommutator in Eq. (2.8) is the probably amplitude for an electron starting in location r_2 at time t_2 to be found in a new location r_1 at time t_1. The second term of the anticommutator in Eq. (2.8) is the complex conjugate of the probably amplitude for a hole starting in location r_2 at time t_2 to be found in location r_1 at time t_1.

2.1.3.2 Non-interacting Fermi gas ($T = 0$)

The non-interacting Fermi gas provides an illustrative example of the physics encoded in the Green function formalism. The Hamiltonian is given by

$$H_0 = \sum_{\mathbf{k}} \epsilon_{\mathbf{k}} c^\dagger_{\mathbf{k}} c_{\mathbf{k}}, \tag{2.10}$$

where the values $\epsilon_{\mathbf{k}}$ correspond to the energies of individual non-interacting states, which are completely occupied below E_F and completely empty above E_F. For convenience we choose the non-interacting ground state energy to be 0. Under these circumstances, it is easy to show (based on the definition of Heisenberg picture operators in terms of Schrodinger picture operators) that $c_{\mathbf{k}}(\tau)$ and $c_{\mathbf{k}}(0)$ are related according to

$$c_{\mathbf{k}}(\tau) = c_{\mathbf{k}}(0) e^{-i\epsilon_{\mathbf{k}}\tau}. \tag{2.11}$$

If we substitute this into equation (2.9) we see that

$$\begin{aligned} G^{(0)}_{\text{ret}}(\mathbf{k}, \tau) &= -i\Theta(\tau) \left[\Theta(\epsilon_{\mathbf{k}} - E_F) - i\Theta(E_F - \epsilon_{\mathbf{k}})\right] e^{-i\epsilon_{\mathbf{k}}\tau} \\ &= -i\Theta(\tau) e^{-i\epsilon_{\mathbf{k}}\tau} \end{aligned} \tag{2.12}$$

For states both above and below the Fermi level, $G^{(0)}_{\text{ret}}$ is an oscillating function that begins at $\tau = 0$ and maintains the same amplitude out to $\tau = \infty$. In other words, electrons and holes added to the system remain in the same momentum state for all future times.

Another way to visualize this is by taking the time Fourier transform of $G^{(0)}_{\text{ret}}$,

$$G^{(0)}_{\text{ret}}(\mathbf{k}, E) = \frac{1}{E - \epsilon_{\mathbf{k}} + i0^+}, \tag{2.13}$$

where here and elsewhere 0^+ is an infinitesimal positive real number that is included to define a prescription for treating the function near its poles. Notice particularly that

$$\text{Im } G^{(0)}_{\text{ret}}(\mathbf{k}, E) = -\pi\delta(E - \epsilon_{\mathbf{k}}), \tag{2.14}$$

that is to say, the imaginary part of G_{ret} directly traces out the free Fermi gas band structure in delta functions. In fact, the imaginary part of G_{ret} gives information about a material's band structure even as interactions are turned on.

2.1.3.3 Green functions for an interacting system ($T = 0$)

As we turn on interactions between particles, the many body ground state $|\Omega\rangle$ is no longer an eigenstate of the annihilation and creation operators c and $c^\dagger$, and in consequence we can no longer expect $G_{\text{ret}}(\mathbf{k}, \tau)$ to maintain a constant amplitude as time winds forward or backward. In fact we will see, as we expect on physical grounds, that particles become limited to finite lifetimes.

A helpful way to visualize the interacting Green function is by writing out the time evolution of the field operators explicitly for Eq. (2.9) and judiciously inserting resolutions of the identity. Then $G_{\rm ret}(\mathbf{k},\tau)$ becomes

$$\begin{aligned} G_{\rm ret}(\mathbf{k},\tau) = &-i\Theta(\tau)\langle\Omega|e^{iE_0^N\tau}c_{\mathbf{k}}(0)e^{-iH\tau}\underbrace{\sum_m |\psi_m^{N+1}\rangle\langle\psi_m^{N+1}|}_{\text{identity}}c_{\mathbf{k}}^\dagger(0)|\Omega\rangle \\ &+ -i\Theta(\tau)\langle\Omega|c_{\mathbf{k}}^\dagger(0)e^{iH\tau}\underbrace{\sum_m |\psi_m^{N-1}\rangle\langle\psi_m^{N-1}|}_{\text{identity}}c_{\mathbf{k}}(0)e^{-iE_0^N\tau}|\Omega\rangle, \end{aligned} \tag{2.15}$$

$$\begin{aligned} G_{\rm ret}(\mathbf{k},\tau) = &-i\Theta(\tau)\sum_m\langle\Omega|c_{\mathbf{k}}(0)e^{-iH\tau}|\psi_m^{N+1}\rangle\langle\psi_m^{N+1}|c_{\mathbf{k}}^\dagger(0)|\Omega\rangle e^{iE_0^N\tau} \\ &+ -i\Theta(\tau)\sum_m\langle\Omega|c_{\mathbf{k}}^\dagger(0)e^{iH\tau}|\psi_m^{N-1}\rangle\langle\psi_m^{N-1}|c_{\mathbf{k}}(0)|\Omega\rangle e^{-iE_0^N\tau}, \end{aligned} \tag{2.16}$$

$$G_{\rm ret}(\mathbf{k},\tau) = -i\Theta(\tau)\sum_m |(c_{\mathbf{k}}^\dagger)_{m,0}|^2 e^{-i(E_m^{N+1}-E_0^N)\tau} - i\Theta(\tau)\sum_m |(c_{\mathbf{k}})_{m,0}|^2 e^{i(E_m^{N-1}-E_0^N)\tau}, \tag{2.17}$$

where the identity has been expressed in terms of the eigenstates $|\psi_m^{N+1}\rangle$ of the $N+1$ particle system with energies E_m^{N+1}, and in terms of the eigenstates $|\psi_m^{N-1}\rangle$ of the $N-1$ particle system with energies E_m^{N-1}. E_0^N is the N particle ground state energy. In the last step we have substituted the definitions

$$(c_{\mathbf{k}}^\dagger)_{m,0} \equiv \langle\psi_m^{N+1}|c_{\mathbf{k}}^\dagger(0)|\Omega\rangle, \qquad (c_{\mathbf{k}})_{m,0} \equiv \langle\psi_m^{N-1}|c_{\mathbf{k}}(0)|\Omega\rangle. \tag{2.18}$$

The notation can be clarified by defining $\pm\xi_m^{N\pm1} \equiv E_m^{N\pm1} - E_0^{N\pm1}$. Then $E_m^{N\pm1} - E_0^N = (E_m^{N\pm1} - E_0^{N\pm1}) + (E_0^{N\pm1} - E_0^N) = \pm\xi_m^{N\pm1} \pm \mu$, where μ is the chemical potential, and we can write equation (2.17) as

$$G_{\rm ret}(\mathbf{k},\tau) = -i\Theta(\tau)\sum_m |(c_{\mathbf{k}}^\dagger)_{m,0}|^2 e^{-i(\xi_m^{N+1}+\mu)\tau} - i\Theta(\tau)\sum_m |(c_{\mathbf{k}})_{m,0}|^2 e^{-i(\xi_m^{N-1}+\mu)\tau}. \tag{2.19}$$

Note that $\xi_m^{N+1} \geq 0$ and $\xi_m^{N-1} \leq 0$. We see by inspection of Eq. (2.19) that $\xi_m^{N\pm1} + \mu$ can be identified as the analogue of $\epsilon_{\mathbf{k}}$ in Eqs. (2.10)–(2.14) for the $N \pm 1$ particle system.

We now define the *spectral density function*:

$$A(\mathbf{k},\omega) \equiv \underbrace{\sum_m |(c_{\mathbf{k}}^\dagger)_{m,0}|^2\delta(\omega - \xi_m^{N+1})}_{A^+(\mathbf{k},\omega)} + \underbrace{\sum_m |(c_{\mathbf{k}})_{m,0}|^2\delta(\omega - \xi_m^{N-1})}_{A^-(\mathbf{k},\omega)}. \tag{2.20}$$

It is perhaps easiest to think of $A(\mathbf{k},\omega)$ a momentum-resolved density of states. By definition, the positive frequency component $A^+(\mathbf{k},\omega)$ delineates the probability distribution function that an electron of momentum $\mathbf{k}$ added to an interacting many body system will occupy any of the new $N+1$ particle system's energy eigenstates ξ_m^{N+1}. Likewise, the negative frequency component $A^-(\mathbf{k},\omega)$ is the probability distribution function that an electron of

final momentum $\mathbf{k}$ removed from an interacting many body system will leave a hole with energy eigenstate ξ_m^{N-1} in the remaining $N-1$ particle system. This latter piece is precisely the quantity measured by angle-resolved photoemission.

We can also use the functional form of $A(\mathbf{k},\omega)$ to compactly describe the frequency transformed version G:

$$G_{\text{ret}}(\mathbf{k},E) = \int_{-\infty}^{\infty} \frac{A(\mathbf{k},\omega)d\omega}{E-\omega-\mu+i0^+}. \tag{2.21}$$

This equation, known as the Källén-Lehmann spectral representation of $G_{\text{ret}}(\mathbf{k},E)$,[133,132] can be verified by performing the inverse Fourier transform and noting that equation (2.19) is recovered. Two facts are evident upon inspection of equation (2.21): (a) the full interacting G can be expressed as a simple weighted sum of various non-interacting Green functions G_0; and (b), the imaginary part of the Green function is, as in the non-interacting case, directly proportional to a solid's band structure:

$$\text{Im } G_{\text{ret}}(\mathbf{k},\omega+\mu) = -\pi A(\mathbf{k},\omega). \tag{2.22}$$

This remarkable property is caused by the unitarity of the operators $e^{\pm iH\tau}$ in Eq. (2.15),[133] and is closely related to the optical theorem in scattering theory.[133,134] Although in this thesis $A(\mathbf{k},\omega)$ is defined in terms of equation (2.20) to emphasize its physical significance, equation (2.22) is so simple and so well-established in the ARPES field that is occasionally invoked as an alternate spectral function definition.[125] $A(\mathbf{k},\omega)$ also obeys the following sum rule:

$$\int_{-\infty}^{\infty} A(\mathbf{k},\omega)d\omega = 1. \tag{2.23}$$

2.1.3.4 Finite temperature

Field-theoretic descriptions of ARPES can be generalized to finite temperature by incorporating Matsubara Green functions, as outlined by Mahan.[132] The most important differences between the above formalism and the finite-temperature regime are that $A^-(\mathbf{k},\omega)$ and $A^+(\mathbf{k},\omega)$ should be broadened across the chemical potential in Eq. (2.20), and can be expressed in terms of the Fermi-Dirac distribution function $f(\omega)$ as

$$A^-(\mathbf{k},\omega) \to A(\mathbf{k},\omega)f(\omega), \qquad A^+(\mathbf{k},\omega) \to A(\mathbf{k},\omega)[1-f(\omega)]. \tag{2.24}$$

In other words, at finite temperatures it becomes possible to remove electrons from the system even above the chemical potential (and likewise to add them back to the system below the chemical potential). This fact becomes useful later on in Section 2.2.2 when we discuss analysis techniques for characterizing superconducting band gaps.

2.1.3.5 Self-energy, and concrete electron interaction models

A useful theorem that we now state without proof is Dyson's equation,

$$G_{\text{ret}}(\mathbf{k},E) = \frac{1}{E-\epsilon_{\mathbf{k}}-\Sigma(\mathbf{k},E-\mu)}, \tag{2.25}$$

which states that the Green function for any interacting system can always be expressed as an infinite series expansion of the product of the non-interacting Green function $G^{(0)}_{\text{ret}}$ and an electronic self-energy term Σ. In general, the self-energy is an analytic complex function with real and imaginary parts, conventionally defined as $\Sigma(\mathbf{k},\omega) = \Sigma'(\mathbf{k},\omega) + i\Sigma''(\mathbf{k},\omega)$. Substituting Dyson's equation into Eq. (2.22) results in

$$A(\mathbf{k},\omega) = -\frac{1}{\pi}\frac{\Sigma''(\mathbf{k},\omega)}{\left(\omega - \xi_{\mathbf{k}} - \Sigma'(\mathbf{k},\omega)\right)^2 + \Sigma''(\mathbf{k},\omega)^2}, \tag{2.26}$$

where $\xi_{\mathbf{k}} \equiv \epsilon_{\mathbf{k}} - \mu$ is a reformulation of the bare band energy relative to the chemical potential. This form of $A(\mathbf{k},\omega)$ is frequently referenced in ARPES literature. We can see from Eq. (2.26) that the real part of the self energy causes a renormalization of the band structure, shifting the spectral weight maximum in $A(\mathbf{k},\omega)$ from $\xi_{\mathbf{k}}$ to $E_{\mathbf{k}}$, defined implicitly by the equation $E_{\mathbf{k}} = \xi_{\mathbf{k}} + \Sigma'(\mathbf{k}, E_{\mathbf{k}})$. The imaginary part results in a broadening of the band in accordance with the decrease in particle lifetime that the term represents.

Until this point, the Green function analysis has been exact, regardless of interaction strength, and has only required assumptions of time and translation invariance. To proceed further with useful theories of real systems, however, various approximations must be introduced to model the behavior of the self-energy Σ, for a given system. A few simple models, useful for capturing the basic phenomenology of electron-electron and electron-phonon interactions, are summarized below.

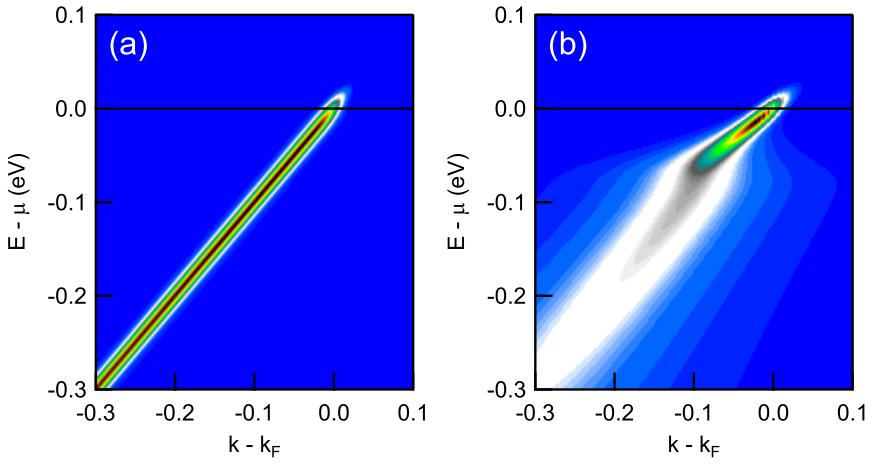

Figure 2.3. Simulations of ARPES spectral functions $A^{-}(\mathbf{k},\omega)$ for a normal metal with a linear bare band. **(a)** Non-interacting system. **(b)** System featuring electron-electron and electron-boson coupling interactions, such that the total self-energy is given by the sum of Eqs. (2.27) and (2.29), with $\omega_D = 70$ meV. Both simulations have been broadened slightly along the energy axis to simulate the effects of finite energy resolution and to illustrate delta-function weights.

Electron-electron self-energy. The most widely used functional form used to describe electron-electron interactions is the Fermi liquid self-energy, where it is assumed that $\Sigma(\mathbf{k},\omega)$

takes on the form[115,135]

$$\Sigma_{FL}(\omega) = \alpha\omega + i\beta\left[\omega^2 + (\pi k_B T)^2\right]. \tag{2.27}$$

The Fermi liquid's defining characteristics are the ω^2 and T^2 dependencies, which arise based on broadly applicable phase-space arguments,[135] and make Fermi liquid theory the starting approximation for most metallic systems. For cuprates, a slightly more applicable electronic self-energy may be the marginal Fermi liquid, invented by Chandra Varma, et al.[136] and defined according to

$$\Sigma_{MFL}(\omega) = \lambda_{MFL}\left[\omega \ln\frac{x}{\omega_c} - i\frac{\pi}{2}x\right], \tag{2.28}$$

where $x \approx \max(|\omega|, T)$, λ_{MFL} is a coupling constant, and ω_0 is an ultraviolet cutoff energy. Further discussion of these electronic self-energies and others may be found in Refs. 137 and 138.

Electron-phonon self-energy. The simplest self-energy model for capturing the interaction between electrons and phonons is the Einstein model at zero temperature, which treats the coupling between electrons and a single non-dispersive phonon mode at energy ω_0. In this case Σ is given by[139]

$$\Sigma_E(\omega) = -\frac{\lambda\,\omega_0}{2}\ln\left|\frac{\omega+\omega_0}{\omega-\omega_0}\right| - i\frac{\pi\lambda\,\omega_0}{2}\left|\Theta(\omega-\omega_0)\right|, \tag{2.29}$$

where λ is the electron-phonon coupling constant. The intuition behind the imaginary part of this expression is that low-energy quasiparticles are too close to the chemical potential to emit relatively high-energy phonons of energy ω_0, and therefore the spectrum remains infinitely sharp below ω_0. By contrast, for energies beyond the Einstein frequency, quasiparticles can decay by emitting phonons quite easily, and the inverse lifetime spikes upward to a finite value. The real part of the self-energy is obtained by Kramers-Kronig transformations, and reveals that low-energy electrons are slowed down by their interactions with the lattice.

A slightly more complicated but numerically better-behaved electron-phonon coupling function is the The Debye self-energy, which is derived from the coupling interactions between electrons and an acoustic phonon population. At zero temperature the Debye self-energy $\Sigma_D = \Sigma'_D + i\Sigma''_D$ is given by

$$\Sigma''_D(\omega) = \begin{cases} -|\lambda\pi\omega^3/(3\omega_D^2)| & \text{if } |\omega| < \omega_D \\ -\lambda\pi\omega_D/3 & \text{if } |\omega| > \omega_D \end{cases} \tag{2.30}$$

$$\Sigma'_D(\omega) = -\frac{\lambda\omega_D}{3}\left[\frac{\omega}{\omega_D} + \ln\left|\frac{\omega+\omega_D}{\omega-\omega_D}\right| + \left(\frac{\omega}{\omega_D}\right)^3 \ln\left|\frac{\omega^2-\omega_D^2}{\omega^2}\right|\right], \tag{2.31}$$

where the Debye energy ω_D serves a similar purpose to ω_0 in the Einstein model. In fact, the imaginary and real parts of this model look qualitatively similar to the Einstein model in general, and they have the same physical interpretation. In both the Einstein and Debye phonon models, it can be deduced that the coupling constant λ obeys the relation $\lambda = |\lim_{\omega\to 0}\partial_\omega\Sigma'(\omega)|$, which serves as a generalizable definition of λ for any electron-phonon self-energy.[139]

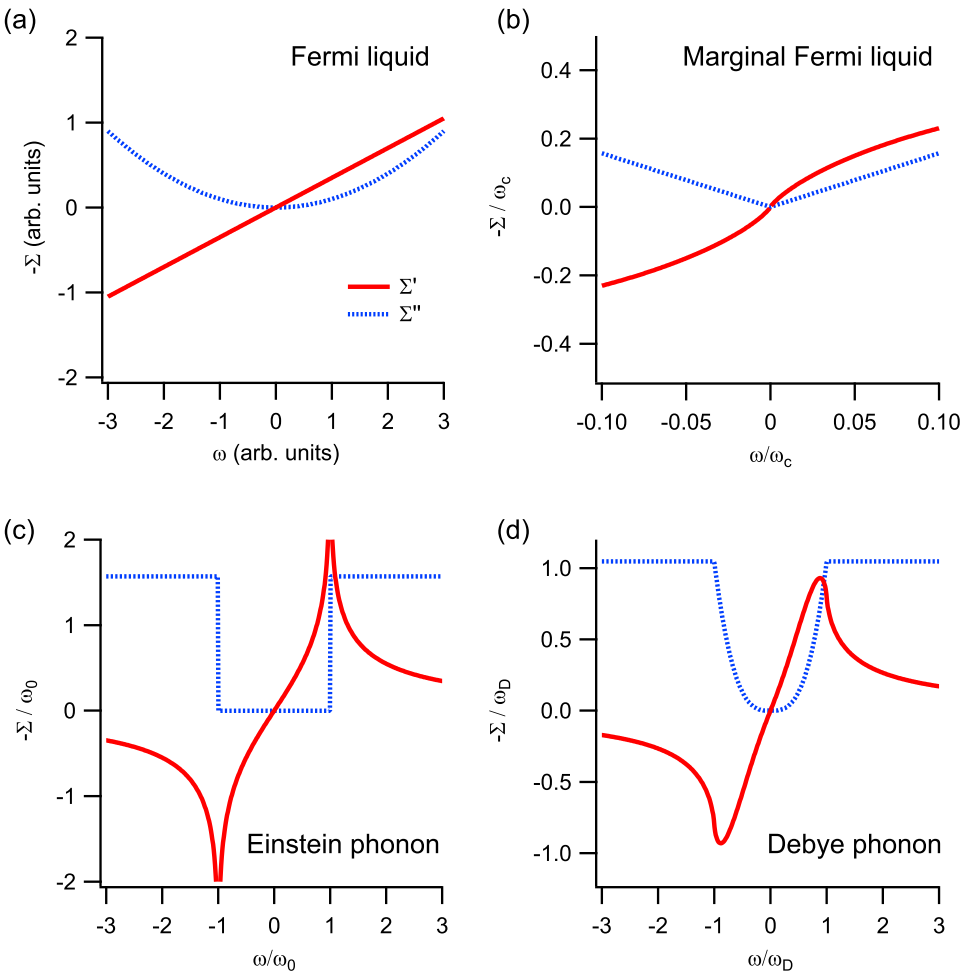

Figure 2.4. Simulated real and imaginary parts of electronic self-energy for a normal metal at $T = 0$. **(a)** and **(b)** correspond to models for electron-electron interactions, showing Fermi liquid and marginal Fermi liquid self-energies, respectively. **(c)** and **(d)** correspond to models for electron-phonon interactions, showing Einstein and Debye models, respectively. All models are drawn for a coupling constant $\lambda = 1$.

2.2 ARPES and time-resolved ARPES analysis

Having established a general theoretical background of ARPES and a survey of both conventional and unconventional superconductivity, we proceed to a discussion of analysis techniques relevant to understanding ARPES and time-resolved ARPES data on a practical level. Initial discussions include definitions and historical relevance of energy distribution curves (EDCs) and momentum distribution curves (MDCs), techniques for characterizing the superconducting gap, and techniques for extracting the physics of electron-boson coupling from the electronic band structure, which are equally relevant in discussions of static and time-resolved ARPES measurements. Following this, the Rothwarf-Taylor and two-temperature models of quasiparticle relaxation are discussed, which are specifically relevant to time-resolved experiments.

2.2.1 EDCs, MDCs, and delay curves

Modern ARPES systems have become extraordinarily sophisticated, possessing the ability to simultaneously acquire the energy dependence of $A(\mathbf{k}, \omega)$ as well as one (for hemispherical analyzers) or even two dimensions (for modern time-of-flight analyzers) of crystal momentum. In order to be able to make sense of all this data, it becomes helpful at times to restrict one's field of view to intensity as a function of one component of phase space only. This is part of the rationale behind the widespread use the terms "energy distribution curve" (EDC) and "momentum distribution curve" (MDC) in the ARPES literature. Essentially, EDCs correspond to ARPES intensity as a function of energy (with momentum or angle fixed), and MDCs correspond to ARPES intensity as a function of momentum (with energy fixed), as depicted in Fig. 2.5.

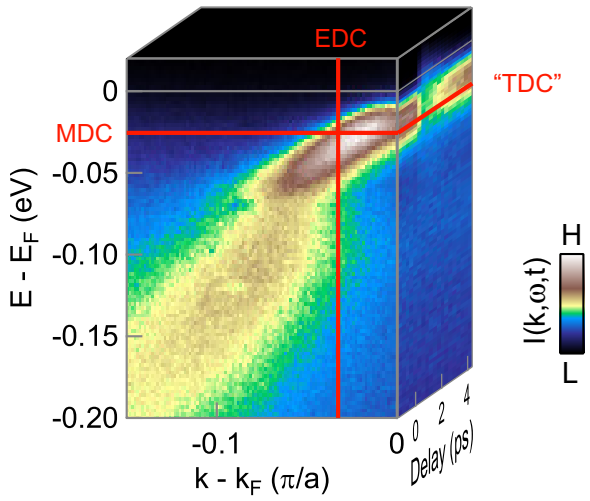

Figure 2.5. Energy distribution curve (EDC) and momentum distribution curve (MDC) definitions.

With the advent of time-resolved ARPES, the logical extension would be that an ARPES intensity curve plotted as a function of delay time should be called a "TDC." However, the term has not caught on, perhaps because there is a connection between the integrated area of an EDC or MDC and a probability distribution function (for EDCs this connection is made explicit by Eq. (2.23)); no such relation exists for the time dependence of ARPES intensity. Nevertheless, time-resolved ARPES intensity plotted as a function of delay time can be quite useful, and many such curves will be plotted later on in the analysis of Bi2212 presented in Chapters 4, 6, and 7. Typically such curves are simply referred to as "delay curves," and they are integrated across a finite window in energy and momentum space to improve signal-to-noise.

It is perhaps worth noting that there is some slight ambiguity in the literature with regard to the definition of EDCs, which has consequences in the interpretation of line shapes. Historically, ARPES data could only be acquired one angle at a time, so EDCs were defined as spectral intensity at constant angle, not necessarily constant momentum. Under these circumstances, some care should be taken in directly associating spectral widths lifetimes,

because the polar angle can play a role in artificially broadening or sharpening lineshapes.[140] The complication is largely bypassed with the advent of two- and three-dimensional analyzers because such a large quantity of data can be accumulated at once that there is no difficulty in numerically transforming the data from angle-space directly into momentum space using the conversion relations (2.1) and (2.2) before performing further analyses.

2.2.2 Superconducting gap characterization

One of the most important characteristics of an ARPES spectrum to analyze if one wishes to understand superconductivity is the momentum-dependent nature of the superconducting gap. Indeed, the measurement[68] of the gap's d-wave symmetry in superconducting Bi2212 was, and continues to be, one of the single most important contributions that ARPES practitioners have contributed to the high-T_c field. More recently, momentum- and temperature-dependent characterizations of the gap in the vicinity of the Brillouin zone face have led to important new information being revealed about the relationship between superconductivity, preformed Cooper pairs, and and/or intertwined electronic orders.[115,141,71,142,114,72] Two methods for characterizing the gap are summarized below: EDC symmetrization, and division by the Fermi-Dirac distribution function.

2.2.2.1 EDC symmetrization

The first challenge that must be overcome to extract the superconducting gap is the role of electron occupation (governed in equilibrium measurements by the Fermi-Dirac distribution function). This effect can artificially shift peak and leading edge positions in the underlying spectral function and can lead to mistaken gap characterizations if not treated appropriately. In equilibrium ARPES measurements, perhaps the most common way to remove the effect of the Fermi function is a methodology proposed by Norman, et al.,[52] known as EDC symmetrization. Under the symmetrization scheme, an EDC at the Fermi wave vector ($\mathbf{k}_F$) is reflected about the Fermi energy (E_F) and added to itself. Given an assumption of local particle-hole symmetry, at equilibrium this procedure removes the effect of the Fermi function, for if $A(\mathbf{k}_F, \omega) = A(\mathbf{k}_F, -\omega)$, then

$$I(\mathbf{k}_F, \omega) + I(\mathbf{k}_F, -\omega) = R * A(\mathbf{k}_F, \omega) f(\omega) + R * A(\mathbf{k}_F, -\omega) f(-\omega) \tag{2.32}$$

$$= R * \big(A(\mathbf{k}_F, \omega) f(\omega) + A(\mathbf{k}_F, \omega)[1 - f(\omega)] \big) \tag{2.33}$$

$$= R * A(\mathbf{k}_F, \omega). \tag{2.34}$$

The asterisk indicates convolution. One of the notable advantages of this technique is that symmetrization is only minimally affected by convolution, which is usually used to approximate the energy resolution. Thus, the energy resolution can be accounted for rather simply in a fit, by convolving a chosen fit function against a Gaussian resolution function and using the result to fit the data.

For time-resolved ARPES data, the nonequilibrium measured value $A^-(\mathbf{k},\omega)$ may no longer be thermal. However, the symmetrization approximation may still give meaningful results if $A^-(\mathbf{k},\omega)$ can be approximated by the product of some time-resolved spectral function $A(\mathbf{k},\omega,t)$ and an "anti-symmetric" distribution function $f^*(\omega)$ such that $f^*(\omega) = 1 - f^*(-\omega)$, which may or may not resemble a thermal function. In both the equilibrium and nonequilibrium case, local particle-hole symmetry must be assumed. This is not a problem for superconductivity, as particle-hole symmetry is built into almost any meaningful pairing interaction. However, such symmetry may break down under the influence of certain competing orders or normal-state effects.

2.2.2.2 Division by the Fermi-Dirac distribution function

An alternate method of extracting $A(\mathbf{k},\omega)$ from $A^-(\mathbf{k},\omega)$ comes from recognizing that in the thermal case the function $f(\omega)$ has the explicit form $f(\omega) = 1/(1+e^{\omega/k_BT})$: ideally, one can simply divide this function out of the data. Such methods were first used to characterize the normal-state electronic structure of Pb-Bi2201 in 2001.[143] More recently, it has been recognized that convolution (i.e., the effect of finite energy resolution) and multiplication by $f(\omega)$ do not commute, so numerical methods are often employed to "undo" the energy resolution before dividing by the Fermi function.[144,142] A demonstration of the Fermi division technique on momentum-dependent measurements of Bi2212 below and above the superconducting critical temperature $T_c = 91$ K is displayed in Fig. 2.6.

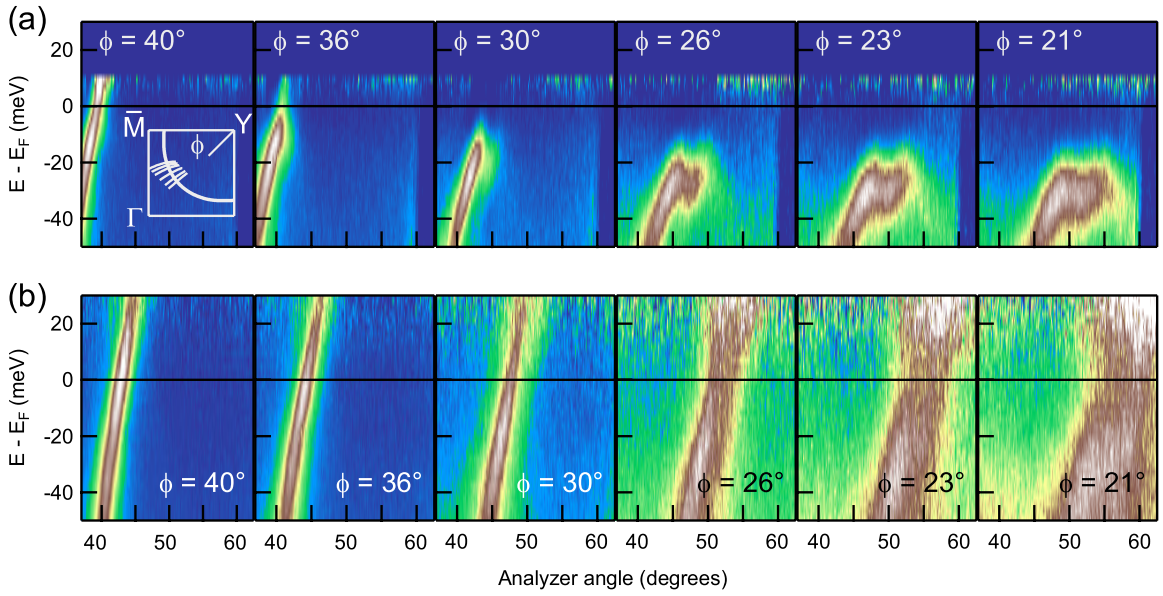

Figure 2.6. Equilibrium ARPES dispersions below and above $T_c = 91$ K, deconvolved[144,142] and divided by a Fermi function in order to extract $A(k,\omega)$ from the ARPES intensity, and to allow an examination of the band gap. **(a)** Low temperature dispersions ($T = 17.5$ K). The angle ϕ is defined as in the inset. **(b)** High temperature dispersions ($T = 100$ K). The onset of the pseudogap occurs at about $\phi = 28°$.

In the low-temperature data (Fig. 2.6(a)) a d-wave-symmetric gap is clearly visible, with a node at $\phi = 45°$ and maximal gap magnitude toward the Brillouin zone face. Figure 2.6(b) illustrates the phenomenology of the pseudogap. The band is continuous out to $\phi = 29°$, demonstrating the extent of the Fermi arc. Between $\phi = 29°$ and $\phi = 27°$ a gap becomes visible, and is unmistakable by $\phi = 26°$, in good agreement with measurements of the onset of the pseudogap in k-space based on synchrotron light.[71]

In the nonequilibrium case, gap characterization methods of this sort are only meaningful if the electronic distribution is closely approximated by a thermal distribution, and if the electronic temperature can be monitored in a time-resolved manner, for example by characterizing the Fermi edge width along the nodal direction in cuprates where there is no gap. Nevertheless, we have found that both symmetrization and Fermi-division give similar results for the evolution of the gap, as discussed later on in Chapter 5.

2.2.2.3 Gap fitting model

Once the gap has been disentangled from the Fermi-Dirac distribution function, it is necessary to extract the magnitude of the gap parameter $|\Delta|$ using an appropriate fit. We use the following,

$$A(k,\omega,t) \propto \text{Im}\left[\frac{1}{\omega - \xi(k) - \Sigma(k,\omega,t)}\right], \quad \Sigma(k,\omega,t) \equiv i\Gamma(t) + \frac{\Delta(t)^2}{\omega + \xi(k) + i\Gamma_0}, \qquad (2.35)$$

which is recognizable as the BCS spectral function (see Eq. (1.24)) except that the self-energy Σ_{BCS} has been phenomenologically broadened by adding the constants Γ and Γ_0. For an EDC extracted at the Fermi wave vector, $\xi(k) = 0$, and Γ_0 is typically negligible for the measurements we have characterized, reducing the fit parameters to $\Delta(t)$, Γ, and an overall proportionality constant. To improve fit quality and incorporate inelastic scattering an additional term $C_1|\omega|$ can be added to the model before convolving with the resolution function.

2.2.2.4 Other gap fitting characterization methods

Perhaps the simplest way to characterize an ARPES spectral gap is by examining the raw data to see whether or not there is a shift in the leading edge of spectra at the Fermi momentum. In general, this approach is plagued by systematic errors introduced through the distribution function and the finite energy resolution. However, up to a point, it is consistent with the more sophisticated techniques described above. Figure 2.8 shows raw and symmetrized EDCs at k_F, extracted from a time-resolved ARPES experiment on superconducting Bi2212. Notably, the symmetrized EDC fits are in good agreement with a simplistic analysis, shown in Fig. 2.8(c), where the gap shift is characterized by the leading edge of the EDC at k_F. A combined plot showing the gap fit results based on the symmetrized EDC fits and leading-edge analysis is shown in Fig. 2.8(d).

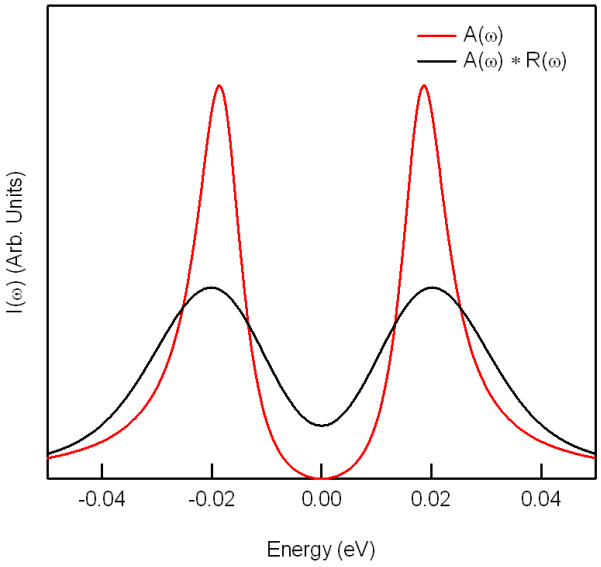

Figure 2.7. Graph of Eq. 2.35, as well as its convolution with a Gaussian resolution function $R(\omega)$ of FWHM = 20 meV.

Alternatively, the superconducting can be characterized after EDC symmetrization or Fermi-division by simply halving the energy difference between the positive and negative energy peaks. This characterization method is simple, but has drawbacks in that it is a noisier characterization technique than fitting to Eq. (2.35) because only a very few data points are sampled. Even with perfect statistics, the peak-to-peak characterization method may give systematically incorrect results if the underlying lineshapes are asymmetric and if energy resolution effects are at play. This is illustrated in Fig. 2.7, which shows a graph of Eq. (2.35) along with its convolution with a Gaussian function of FWHM = 20 meV. Because Eq. (2.35) has asymmetric quasiparticle peaks, the fitted gap size is slightly smaller than the maximum values of the resolution-convolved peaks would suggest.

Finally, we note that Reber et al.[72] have recently proposed an alternative fitting methodology to those described here, suggesting that robust gap measurements may result from integrating time-resolved ARPES spectra across momentum cuts intersecting the normal state Fermi surface, dividing by the spectrum along the node (which is conceptually similar to dividing by a Fermi function) and fitting the resultant spectra to the Dynes equation for electron tunneling,[145]

$$I(\omega) = \mathrm{Re}\,\frac{\omega - i\Gamma_{\mathrm{TDoS}}}{\sqrt{(\omega - i\Gamma_{\mathrm{TDoS}})^2 - \Delta^2}}. \tag{2.36}$$

This fit function phenomenologically broadens the BCS spectral function in a slightly different manner than does Eq. (2.35) while still using the same number of parameters (if Γ_0 is neglected in Eq. (2.35)), or perhaps even fewer parameters (if Γ_0 is not neglected). Though we have not employed this fitting methodology in the present work, it has been used to characterize band gaps in the iron-based superconductors,[146] and its use in cuprates has led to interesting proposals for the origin of the pseudogap.[72]

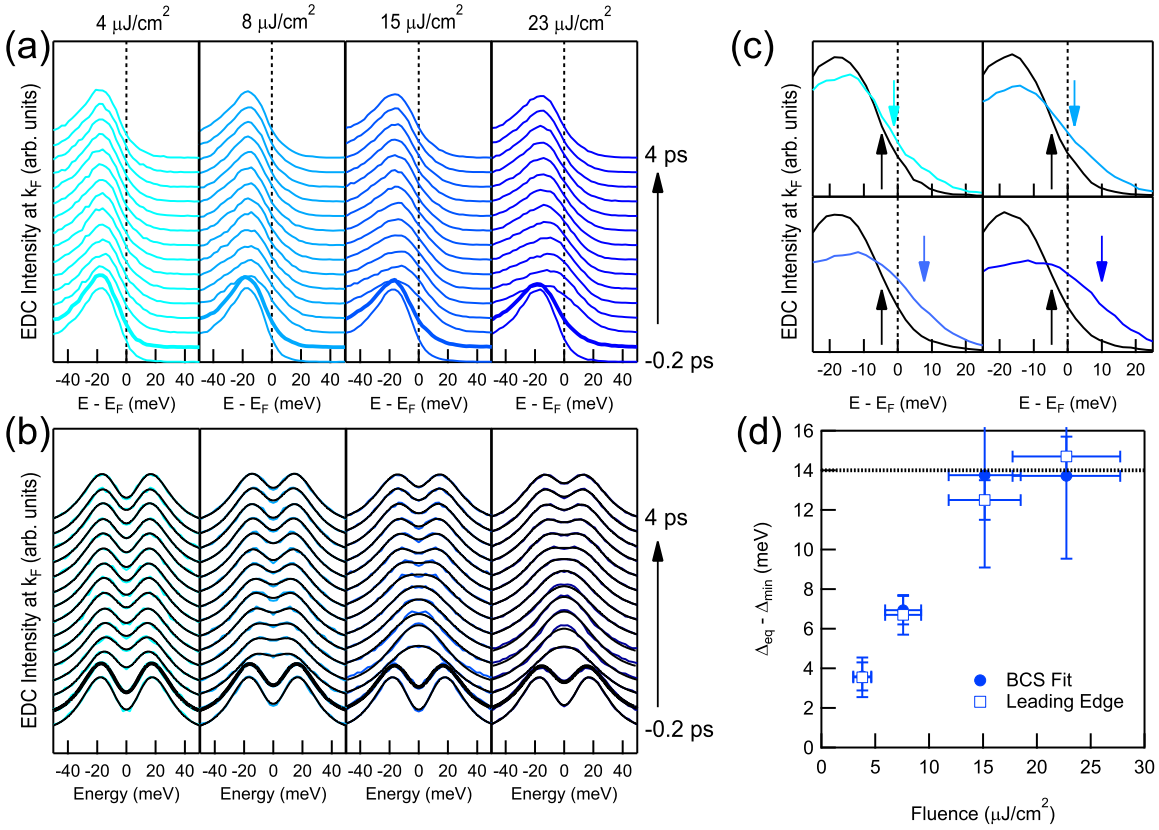

Figure 2.8. Comparison between leading-edge gap measurements and symmetrized EDC fitting methodology. **(a)** Raw EDCs at k_F between -1.1 ps and 4 ps, corresponding to fluences of 4, 8, 15, and 23 μJ/cm^2. Bold curves correspond to $t = 0$ ps. **(b)** Symmetrized EDCs, acquired by adding the data in (a) to its reflection across E_F. Black curves correspond to fits using Eqs. (2.35), convolved with a Gaussian resolution function. **(c)** Comparison between raw EDCs at equilibrium (in black) and those at 0.7 ps (in blue) for pump fluences of 4, 8, 15, and 23 μJ/cm^2, with colors indexed to the fluence values in panel (a). **(d)** Maximal gap shift ($\Delta_{eq} - \Delta_{min}$) versus pump fluence. Filled circles are the result of fitting to Eqs. (2.35). Open squares are from the leading-edge shift in the raw EDCs.

2.3 Quasiparticle relaxation models

Ultrafast optical techniques with time scales on the order of femtoseconds have only been a reality since the invention of the Ti:sapphire laser in 1982, but there has been considerable interest in quasiparticle relaxation rates in superconductors, and more generally in nonequilibrium superconductivity, since the 1960s. The final portion of this chapter gives an overview of the Rothwarf-Taylor model, which was developed to help understand these studies into non-equilibrium superconductivity. The two-temperature model and Keldysh contour formalism for discussing non-equilibrium superconductivity are also discussed.

2.3.1 Rothwarf-Taylor model

Perhaps the most common framework used to explain the relaxation dynamics of superconductors was developed by Rothwarf and Taylor in 1967.[147] Developed initially for s-wave superconductors, the primary simplification afforded by the model is that it is assumed that quasiparticles decay to the gap energy almost immediately after photoexcitation. In consequence, the full energy- and time-dependent spectral function may be replaced by a number density. Dynamics of quasiparticle decay into the superfluid state following this initial decay are governed by the coupled rate equations:

$$\dot{n} = I_0 + \gamma_{pc} N - R n^2 \tag{2.37}$$

$$\dot{N} = J_0 + R n^2/2 - \gamma_{pc} N/2 - \gamma_{esc}(N - N_T) \tag{2.38}$$

The first equation describes the response of quasiparticle density n. An initial photoexcitation pulse can rapidly boost the quasiparticle density through the first term, I_0. This may be modeled as a delta function or Gaussian, centered in time at $t = 0$. Following photoexcitation, $\dot{n}$ will decay proportionally to n^2 because quasiparticles decay into the superfluid by annihilating in pairs. As Cooper pairs condense, however, energy conservation dictates that bosons must be generated with energy equal to or greater than the gap energy. As many quasiparticles decay, bosons begin to break Cooper pairs apart again in a feedback process proportional to their own density N. The second equation describes the response of the coupled bosons, allowing for a direct excitation of bosons through J_0, and an external decay channel back to the equilibrium density N_T. The coefficients R, γ_{pc}, and γ_{esc} are constants.

2.3.1.1 Limiting cases

There is no generalized analytic solution to the Rothwarf-Taylor equations. In order to facilitate better visualization of equation dynamics, then, it becomes useful to examine a few limiting cases, as outlined below. Further discussion of the limiting forms of the Rothwarf-Taylor model can be found in Refs. 148 and 149.

Decoupled regime. At short times, if the coupling from bosons to quasiparticles is weak, or if bosons get drained off more rapidly than they are generated through Cooper pair formation (i.e., $\gamma_{pc} \ll \gamma_{esc}$), then the final term dominates in equation (2.37) and the equation decouples from its bosonic counterpart. This is perhaps the simplest limiting case of the Rothwarf-Taylor equations. In this "decoupled regime" it helps[148] to divide n and N into thermal and photoexcited pieces $n = n_T + n_{ex}$ and $N = N_T + N_{ex}$ such that $N_T\gamma_{pc} = Rn_T^2$. Equation (2.37) can be rewritten as $\dot{n}_{ex} = I_0 + \gamma_{pc}N_{ex} - Rn_{ex}^2 - 2Rn_Tn_{ex}$. Minimizing the influence of the feedback term in equation (2.37) amounts to setting the second term here to zero. The corresponding decoupled rate equation is $\dot{n}_{ex} = I_0 - Rn_{ex}^2 - 2Rn_Tn_{ex}$ or, if we allow ourselves to ignore the initial driving term I_0:

$$\dot{n}_{ex} = -R\left(n_{ex}^2 - 2n_Tn_{ex}\right). \tag{2.39}$$

This equation is exactly solvable and can be written, in terms of n_{ex}, as

$$\frac{1}{n_{ex}(t)} = \left(\frac{1}{2n_T} + \frac{1}{n_0}\right)e^{2n_TRt} - \frac{1}{2n_T} \tag{2.40}$$

where n_0 is an initial photoexcited quasiparticle population parameter determined indirectly through I_0. In the extreme case when the equilibrium temperature is zero (i.e. $n_T = 0$), Eq. (2.39) has a very simple solution, given by

$$n_{ex}^{-1}(t) = n(t)^{-1} = n_0^{-1} + Rt. \tag{2.41}$$

Eq. (2.41) is perhaps most familiar in the realm of chemistry, where it describes the kinetics of chemical reactions involving identical reactants merging to form a single product.[150] It is for this reason that this type of behavior is often referred to as "bimolecular" recombination in cuprates, despite the fact the constituent parts are actually electrons, and have little to do with actual molecules. At finite temperature, n_{ex} starts out dominated by bimolecular kinetics, but then evolves into an exponential decay as the photoexcited population fades into its thermal bath.

Bottleneck regime. An alternate limiting case occurs if equilibration between bosons and quasiparticles happens rapidly (i.e., $\gamma_{pc} \gg \gamma_{esc}$). Then the second and third terms of equations (2.37) and (2.38) nearly cancel as $\gamma_{pc}N \approx Rn^2$, resulting in a slower "bottlenecked" quasiparticle decay rate. It is useful under these conditions to define a variable s such that

$$s \equiv Rn^2 - \gamma_{pc}N. \tag{2.42}$$

Because of the bottleneck effect, s will be small, so $\dot{s}$ is essentially zero, leading to

$$\dot{s} = 2Rn\dot{n} - \gamma_{pc}\dot{N} \approx 0 \quad \Rightarrow \quad 2Rn\dot{n} \approx \gamma_{pc}\dot{N}. \tag{2.43}$$

In addition, since $\gamma_{esc} \ll \gamma_{pc}$, any product of γ_{esc}/γ_{pc} and s can be discarded. Substituting Eqs. (2.37), (2.43), and the relation $\gamma_{pc}N_T = Rn_T^2$ into Eq. (2.38) to get rid of N, $\dot{N}$, and N_T gives

$$\left(1 + \frac{4Rn}{\gamma_{pc}}\right)\dot{n} = -\frac{2\gamma_{esc}}{\gamma_{pc}}R\left(n^2 - n_T^2\right), \tag{2.44}$$

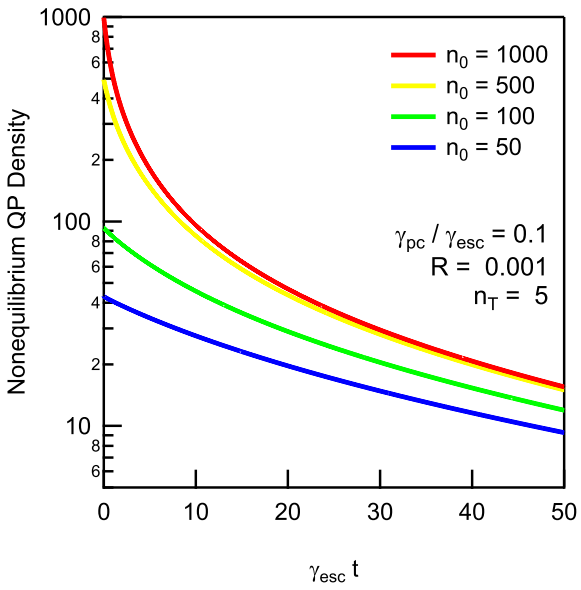

Figure 2.9. Rothwarf-Taylor simulated quasiparticle population recovery in the decoupled regime. The quasiparticle recovery rate is density-dependent, with the functional form of Eq. (2.40).

which amounts to the first-order expansion of the Rothwarf-Taylor equations in terms of s and γ_{esc}/γ_{pc}. If we again divide the quasiparticle population into photoexcited and thermal components, then Eq. (2.44) becomes

$$\left(1+\frac{4Rn_{ex}}{\gamma_{pc}}+\frac{4Rn_T}{\gamma_{pc}}\right)\dot{n}_{ex}=-\frac{2\gamma_{esc}}{\gamma_{pc}}R\left(n_{ex}^2+2n_Tn_{ex}\right). \tag{2.45}$$

If Rn_T/γ_{pc} is relatively large, then the final terms of the left-hand side of Eq. (2.45) dominate at all times. The quasiparticle population decays uniformly and in a nearly fluence-independent manner according to

$$n_{ex}(t)=\sqrt{n_T^2+\text{Const. }e^{-\gamma_{esc}t}}-n_T. \tag{2.46}$$

The phenomenon occurs in low-temperature superconductors,[151] but has also been observed and characterized in semiconductors under the guise of the "hot-phonon effect."[152] However, fluence-dependent behavior can occur in the bottleneck regime at long times if the temperature is sufficiently low and the energy gap is sufficiently large to make pair creation the fastest process in the problem. Mathematically, we require that $Rn_T \ll \gamma_{pc}/4$ in addition to the bottleneck assumption $\gamma_{esc} \ll \gamma_{pc}$. In this case, the total population of quasiparticles remains "small" throughout the bottlenecked time period (i.e., $R\,n(t) \ll \gamma_{pc}/4$ for all $t > 1/\gamma_{esc}$), the first term always dominates the left hand side of equation (2.45), and the dynamics reduce to

$$\dot{n}_{ex}=-\frac{2\gamma_{esc}}{\gamma_{pc}}R\left(n_{ex}^2+2n_Tn_{ex}\right). \tag{2.47}$$

At short times, the decay rate $\dot{n}_{ex}/n$ grows linearly with excitation fluence. At longer times,

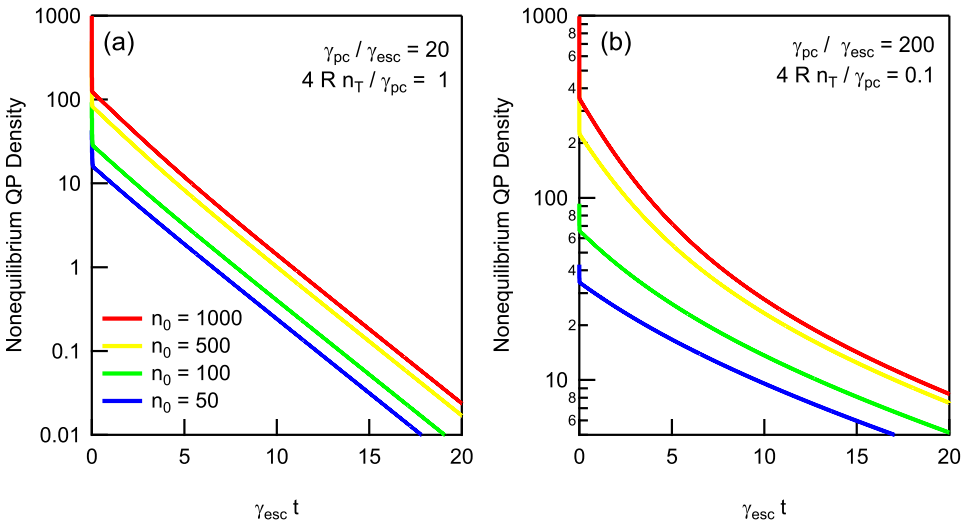

Figure 2.10. Rothwarf-Taylor simulated quasiparticle population recovery in the bottleneck regime. For both panels, $R = 1$ and $n_T = 5$. **(a)** Exponential regime ($4Rn/\gamma_{pc} \gg 1$). After quasiparticles and bosons equilibrate at short time, the quasiparticle recovery rate is nearly density-independent, with the functional form of Eq. (2.46). **(b)** Fluence-dependent regime ($4Rn_T/\gamma_{pc} < 1$). After quasiparticles and bosons equilibrate at short time, the quasiparticle recovery rate is density-dependent, with the functional form of Eq. (2.47).

the decay rate evolves into the constant $4(\gamma_{esc}/\gamma_{pc})Rn_T$. Curiously, these dynamics are completely identical to the dynamics in the case lacking a bottleneck (see Eq. (2.39)), except that the coefficient R on the right hand side of the equation has been renormalized by twice the phonon branching ratio γ_{esc}/γ_{pc}.

2.3.1.2 Probe penetration depth considerations

In Chapter 4 the Rothwarf-Taylor model is used to compare dynamics between a time-resolved optical measurement and time-resolved ARPES measurement of quasiparticle dynamics. In anticipation of that discussion, it is useful to briefly discuss the effects of finite probe penetration depth within in the context of the Rothwarf-Taylor model. The short-time limit of Eq. 2.41 is

$$\frac{n_{ex}(t)}{n_{ex}(0)} = 1 - R\, n_{ex}(0)\, t + O(t^2). \tag{2.48}$$

In the case of ARPES, 6 eV photons induce photoelectrons with a mean free path of 5 nm. This is well below the penetration depth of the 1.48 eV pump beam (100 nm), which means that only the surface of the material is probed. Furthermore, the initial photoexcited population $n_{ex}(0)$ vastly outweighs the thermal population n_T in the majority of cases. To a good approximation, then, initial decay rates as measured by time-resolved ARPES will correspond to the product $R\, n_{ex}(z = 0, t = 0)$.

In contrast, the optical reflectivity probe penetrates the same distance into the sample as

the pump, and therefore necessitates a more intricate analysis of spacial variation in $n_{ex}(z,t)$. The problem has been addressed by Gedik et al.,[148] who propose that the optical response should be modeled by inserting the solution of Eq. 2.41 into a weighted integral as follows:

$$\Delta R(t) = \frac{2\Delta R(0)\alpha}{n_0}\int_0^\infty dz\, e^{-\alpha z} n_{ex}(z,t), \quad n_{ex}(z,t) \equiv \frac{n_{ex}(0,0)e^{-\alpha z}}{1 + R n_{ex}(0,0)e^{-\alpha z} t} \tag{2.49}$$

$$= \frac{2\Delta R(0)}{\gamma_0 t}\left[1 - \frac{\ln(1+\gamma_0 t)}{\gamma_0 t}\right]. \tag{2.50}$$

The constant $\gamma_0 \equiv R\, n_{ex}(0,0)$ corresponds to the initial decay rate of quasiparticles at the surface. Finite temperature effects are ignored because $n_T \ll n_{ex}(0)$ (as noted above). In the short-time limit, the decay rate of this revised equation differs by a factor of 2/3 from its counterpart at the sample surface:

$$\frac{\Delta R(t)}{\Delta R(0)} = 1 - \frac{2}{3}\gamma_0\, t + O(t^2). \tag{2.51}$$

2.3.1.3 Momentum-Dependent Recombination

Finally, in order for the Rothwarf-Taylor model to better accommodate time-resolved measurements, it is useful to recast the model within a momentum-dependent framework. Eq. 2.39 becomes

$$\dot{n}_k = -n_k \int R_{kk'}\, n_{k'}\, d^2k' - n_k \int R_{kk'}\, n_{k'T}\, d^2k' - n_{kT} \int R_{kk'}\, n_{k'}\, d^2k' \tag{2.52}$$

where n_k is now the population of photoexcited quasiparticles at a given momentum k, $R_{kk'}$ is a recombination function related to the formation of Cooper pairs, and n_{kT} is the momentum-dependent population of thermal quasiparticles. The first term on the right corresponds to photoexcited quasiparticles recombining with other photoexcited quasiparticles. The second term corresponds to photoexcited quasiparticles at k recombining with thermal quasiparticles in other parts of the Brillouin zone. The final term corresponds to photoexcited quasiparticles in other parts of the Brillouin zone recombining with thermal quasiparticles at k. The integral in the second term is a constant, so the term does not contribute to any density or fluence dependence. The third term vanishes for all momenta except the nodal direction, and along the node it is small relative to the first term on the right for all but the lowest excitation densities. At short time, then, momentum-dependent recombination dynamics are dominated by the first term on the right.

In general, n_k is a function of the fluence F, and can thus be written as $n_k(F)$. Because n_k is the photoexcited quasiparticle population $n_k(0) = 0$. As a result, for small fluence $n_k(F)$ can be expanded to linear order in F as $n_k \approx \alpha_{k'} F$. Making this substitution to the integrand in the first term results in

$$\dot{n}_k \approx -n_k \int R_{kk'}\, n_{k'}\, d^2k' \approx -n_k \int R_{kk'}\, \alpha_{k'}\, F\, d^2k' \tag{2.53}$$

After pulling F outside of the integral and taking the derivative, the approximation finally reduces to

$$\gamma_{k0} \approx -F \int R_{kk'}\, \alpha_{k'}\, d^2k' \qquad \Rightarrow \qquad \frac{\partial \gamma_{k0}}{\partial F} \approx \int R_{kk'}\, \alpha_{k'}\, d^2k'. \tag{2.54}$$

2.3.2 Alternatives to the Rothwarf-Taylor model

2.3.2.1 Two-temperature model

An alternative to the Rothwarf-Taylor is the two-temperature model outlined perhaps most clearly by Allen in 1987.[153] Under this model, it is assumed that quasiparticles and bosons are able to exchange energy with other quasiparticles and bosons without necessarily needing to interact with each other, so that the overall system can be described by a single thermalized bath of quasiparticles at temperature T_e, and a separate thermalized bath of bosons at a distinct temperature T_p. Over time, the electron bath comes into equilibration with the phonon bath according to the equation

$$\frac{\partial T_e}{\partial t} = -\frac{6}{\pi k_B^2 T_e} \int_0^\infty d\Omega \alpha^2 F(\Omega) (\hbar\Omega)^2 \left[n(\Omega, T_e) - n(\Omega, T_p) \right] + I_0/C_e \tag{2.55}$$

where $\alpha^2 F(\Omega)$ is the Eliashberg coupling function related to the electron-boson coupling constant λ according to $\lambda = 2\int \Omega^{-1} \alpha^2 F(\Omega) d\Omega$, where $n(\Omega, T)$ is the Bose-Einstein distribution function $n(\Omega, T) \equiv 1/(e^{\Omega/k_B T} - 1)$, where I_0 accommodates the pump pulse, and where C_e is the electronic specific heat. Occasionally, to improve the fit quality, the two-temperature model is extended to include three or even more distinct baths of excitations (for example, to differentiate strongly-coupled phonons of energy 2Δ from the rest of the phonon bath in analogy to the hot phonons of the Rothwarf-Taylor model). It is particularly useful in describing quasiparticle relaxation processes in metals, but has been applied to Bi2212 in one time-resolved ARPES study.[154]

One particular advantage of analyzing ARPES data in connection with a two-temperature model is that for places where band structure is relatively featureless, ARPES spectra can be directly integrated across the momentum direction as a function of delay time to obtain measurements of the Fermi edge. Fitting this to a Fermi-Dirac distribution function gives a quantitative estimate of the absolute electronic temperature. By contrast, for all-optical techniques to use this method, absolute values of temperature cannot be extracted by any means, and the only meaningful information that can be extracted comes from decay rates.

In fact the ability to fit ARPES and time-resolved ARPES data to Fermi-Dirac distributions directly opens an important avenue of opportunities in ARPES and time-resolved ARPES. In Chapter 3 the technique will be used to quantify equilibrium heating. In Chapter 5 the technique will be used as an aid to quantify the nonequilibrium gap.

2.3.2.2 Keldysh contour approach

Finally, we note that beyond these simple models, the theory of non-equilibrium quasiparticle dynamics in metals and superconductors is rapidly developing as numerical modeling methods supercomputer processing capabilities become increasingly advanced. Although such theoretical work is beyond the scope of the analysis techniques used in this dissertation, comparisons between these theoretical studies time-resolved ARPES data are facilitating many new discussions and research directions. In particular, it is now possible to quantitatively model highly nonlinear effects—such as pump-induced Haldane multilayers in graphene,[155] Higgs modes in superconductors,[156] and effects reminiscent of the Wannier-Stark ladder in metals[157]—using the Keldysh contour formalism.

Chapter 3

Time-resolved ARPES

At this point, we come to the experimental technique at hand: time- and angle-resolved photoemission spectroscopy. The contents of this chapter include an overview of time-resolved ARPES, a brief description of the physics of Ti:sapphire lasers (which are key components that make many time-resolved ARPES systems possible), a detailed description of the Lanzara Group time-resolved ARPES setup, and finally, discussions of experimental considerations that are specific to the acquisition of time-resolved ARPES and laser-ARPES data.

3.1 The time-resolved ARPES technique

The chief difference between more traditional "static" ARPES and time-resolved ARPES is that in a traditional ARPES experiment, only one frequency of ultraviolet light is needed at a time, and it does not matter whether or not the light is pulsed. By contrast, in a time-resolved ARPES experiment, a crystalline material is irradiated by two laser pulses, of different frequencies, in rapid succession (see Fig. 3.1). These are commonly designated as "pump" and "probe" pulses. The pump pulse is typically in the infrared, and drives the sample's low energy electrons into a nonequilibrium state. The probe pulse—typically ultraviolet—photoemits electrons outside the sample, where they are measured using the techniques of traditional ARPES. Varying the time delay between pump and probe pulses makes it possible to see and analyze the time-dependent processes involved in the relaxation of these nonequilibrium electronic states.

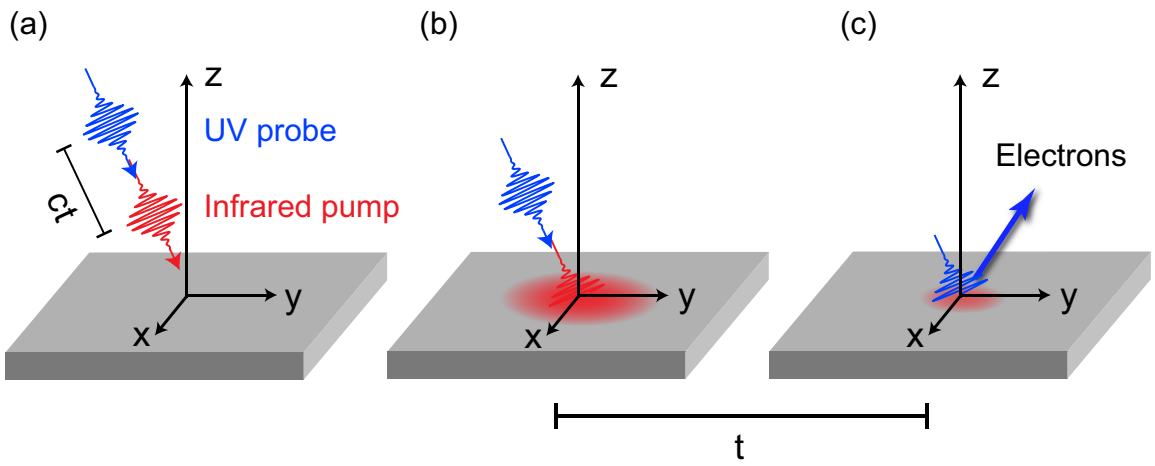

Figure 3.1. Illustration of the time-resolved ARPES technique. **(a)** Pump and probe pulses, separated by a distance ct, approach a sample. **(b)** The infrared pump pulse strikes the sample, creating a nonequilibrium quasiparticle population. **(c)** The ultraviolet probe pulse follows suit, ejecting photoelectrons from the nonequilibrium state at time t following photoexcitation.

3.2 Classes of time-resolved ARPES systems

Instruments used for time-resolved ARPES can be divided into three classes. At the smallest scale are systems based on solid-state lasers, where ultraviolet (UV) pulses suitable for photoemission are created using second-harmonic generation or sum-frequency generation in nonlinear crystals.[158,159,160,161,162] In comparison with larger-scale systems these setups have the advantage of low cost, adaptability, and exceptional momentum resolution due to the fact that they typically operate at low probe frequency. Solid-state systems are well-suited for measurements of electronic states near the first Brillouin zone's Γ point, for example the d-wave node in cuprate superconductors or the central Dirac cone in topological insulators. However, they become less practical for measurements at larger momenta because the maximum photon energy that can be reached using nonlinear crystals is 6–7 eV, and the sample must be rotated to increasingly oblique angles in order to access electronic states. Crystal momentum k, photon energy $h\nu$, the work function Φ_W, and photoelectron exit angle θ are related to each other by the relation $\hbar k_{||} = \sqrt{2m_e(h\nu - \Phi_W)}\sin\phi$, so there is an upper limit on the accessible momenta at a fixed photon energy.[123,163]

A second category of time-resolved ARPES experiments is based on high-harmonic generation (HHG) techniques.[164,165,166,167,168,169,170,171,172] As in the systems above, the fundamental beam for these types of systems is typically a solid-state laser. HHG sources circumvent the low photon energy problem by taking advantage of dramatic nonlinear processes which occur when a laser pulse is focused through an atomic gas[173,174] or reflected off of plasmonic mirrors.[175] Using the atomic gas method, HHG sources have been successfully used for time-resolved ARPES studies of charge density wave materials.[176,177] However, in existing systems good energy resolution is difficult to achieve using HHG techniques because atoms must be exposed to large electric fields in order to efficiently generate harmonics. Short pulses are an

effective way to manage this with finite laser power, but the frequency spread of such pulses must also be relatively broad due to the Fourier transform limit.

At the largest scale, time-resolved ARPES is being developed and proposed in conjunction with soft x-ray free electron laser (FEL) sources, which have only recently become an experimental reality.[178,179] In principle time-resolved ARPES based on FEL sources has great advantages including tunable photon energy, pulses of variable duration, a Fourier-transform-limited energy resolution, and the wide range of accessible momentum states. The technique has been demonstrated at the FLASH facility in Hamburg,[180] although the low repetition rates at current FELs are a severe restriction for ARPES because pulse intensities must also be kept low to minimize space charge effects.[181,182,183,184,185]

3.3 Ti:sapphire lasers

The experimental apparatus utilized for the reported research in this thesis falls into the first of the aforementioned classes, and is based on a Ti:sapphire laser system used in conjunction with nonlinear crystals and a hemispherical analyzer. To this end, we now proceed to a short discussion on the physics of Ti:sapphire lasers.

3.3.1 Principles of operation

A laser, in the most literal sense of the word, is an acronym that stands for light amplification by stimulated emission of radiation. Three fundamental components are required: an energy source (for Ti:sapphire oscillators, this turns out to be another laser), a gain medium (the Ti:sapphire crystal), and a mechanism for providing optical feedback (typically consisting of an array of mirrors arranged to produce an optical cavity). For a Ti:sapphire laser, the operative element of the gain medium is the collection of titanium atoms embedded within the sapphire structure, and the lasing mechanism for these atoms can be understood by approximating the crystal as a four-level system, schematically illustrated in Fig. 3.2.

When the external energy source is off, electrons tend toward the ground state ($|1\rangle$), as shown in Fig. 3.2(a). Turning the energy source on sets a series of transitions in motion between states $|1\rangle$ and $|2\rangle$. This results in an improvement in optical coherence; however, there is not usually any light amplification yet, for it is impossible to create a population inversion with a statistical ensemble of two-level systems.[i] Rather, lasing is achieved because of the presence of states $|3\rangle$ and $|4\rangle$, which interact with states $|1\rangle$ and $|2\rangle$ via non-radiative transitions. As shown in Fig. 3.2(c), electrons decay from state $|1\rangle$ to state $|2\rangle$, generating a substantial population inversion that can be directly witnessed by an incoming photon at energy $h\nu_{\text{laser}}$, the energy difference between states $|3\rangle$ and $|4\rangle$. Stimulated emission ensues shortly thereafter, amplifying the light to generate the laser output as shown in Fig. 3.2(d).

[i] There are, of course, exceptions that prove the rule. See Scully and Zubairy[36] for a discussion of lasing without inversion.

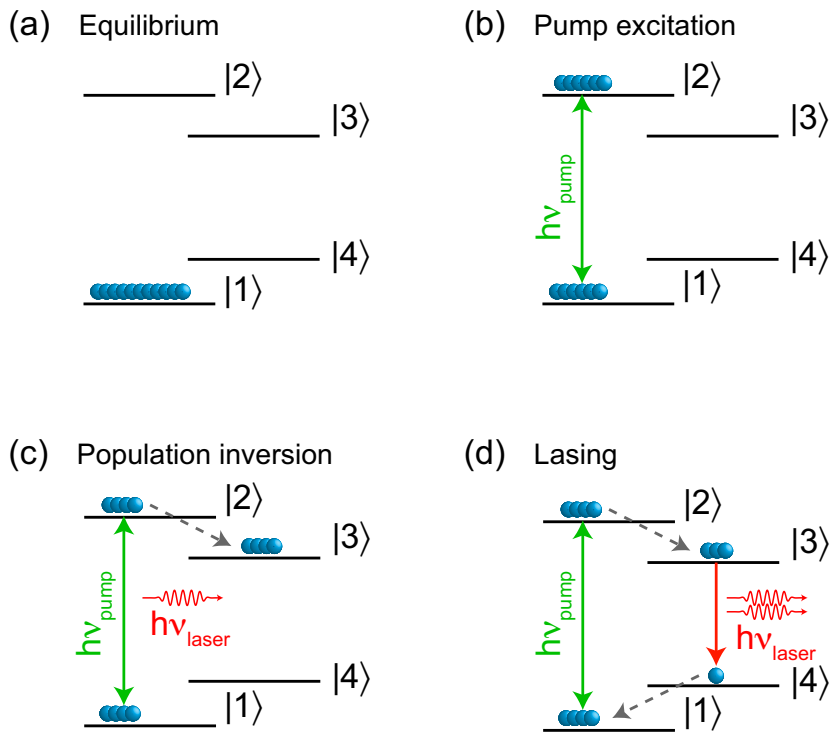

Figure 3.2. Energy level diagrams illustrating the generation of a population inversion and subsequent stimulated emission effects in a generic 4-level laser.

Thus far, principles discussed apply to a vast array of different types of lasers. Ti:sapphire lasers are special, however, in that they are capable of achieving not just coherent light, but light that comes in the form of pulses. Indeed, this is the only reason such lasers have any utility at all in pump-probe optical techniques. Ti:sapphire lasers achieve this through the optical Kerr effect (see Fig. 3.3), in which a material's refraction index is a function of electric field intensity. Because of this, pulsed light (where intense electric fields become increasingly bunched up into shorter time durations) can be focused differently from continuous-wave (cw) light using the appropriate optics, and can be filtered out of the laser signal through the use of a carefully tuned slit width (the technique is known as Kerr-lens mode locking). In modern Ti:sapphire lasers, engineers have now managed to hone this effect to the point where pulses less than 100 fs have become extremely common.

3.3.2 Figures of merit

Within this basic framework, a variety of pulsed lasers are now available on the market, each with their own advantages and disadvantages. A few of the more important figures of merit are summarized below.

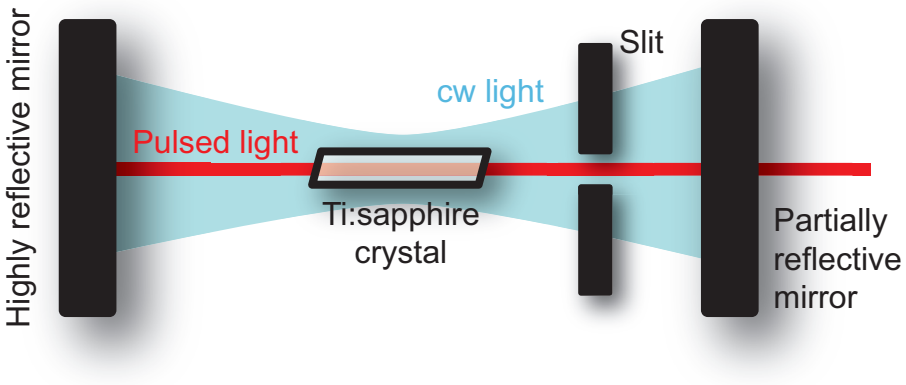

Figure 3.3. Kerr-lens modelocking in a Ti:sapphire laser. A beam from a pump laser (not shown) creates a population inversion in the Ti:sapphire crystal. Subsequent stimulated emission events result in highly coherent pulsed and cw beams, which are focused differently by the crystal. An adjustable slit is used to selectively amplify pulsed light and to suppress cw components.

Pulse energy. Not to be confused with the photon energy $h\nu$, this corresponds to the total amount of energy contained within a single laser pulse. Pulse energy is important because in a pump-probe experiment, very intense pulses are sometimes necessary to produce interesting nonlinear effects. In the system to be discussed, maximum pulse energies are typically in the neighborhood of 55 nJ.

Repetition rate. Repetition rate is the rate at which pulses are emitted by the laser. It is best if this can be adjusted, for different experiments often require different repetition-rate settings. If the repetition rate is too low, then either the signal-to-noise will be poor, or intense pulses will be necessary. However, in the latter case space charge (discussed later on) can become a serious issue. If the repetition rate is too high, the laser can result in an equilibrium heating of the sample. The optimal repetition rate, though typically in the neighborhood of 250 kHz–100 MHz, varies depending on the sample. To study the topological insulator Bi_2Se_3, for example, a pulse repetition rate of 80 MHz is sufficiently low under a wide variety of circumstances to measure a sample without suffering from adverse equilibrium heating effects[162] By contrast, the cuprate superconductor $Bi_2Sr_2CaCu_2O_{8+\delta}$ (Bi2212) measured at 20 K has a lower thermal conductivity,[186] and the repetition rate must often be greatly reduced—to less than 1 MHz—to minimize sample heating.[187,188,189]

Output power. This is already covered within the previous two figures of merit. Output power is given by the product of the repetition rate and pulse energy. To prevent heating in Bi2212 with a beam diameter of 100 μm, it is best if the output power can be kept below 3 mW.

Pulse duration. Pulse duration governs the fundamental timescale that an experiment is capable of measuring. Generally speaking, the shorter the pulse duration, the better. However, it should be recognized that the Heisenberg uncertainty principle sets a fundamental limit on the relationship between pulse duration and energy resolution, as discussed next.

Bandwidth (energy resolution). It is impossible to generate ultrashort pulses without the introduction of a finite frequency bandwidth, which figures into the total energy resolution of a time-resolved ARPES experiment. The relationship between the two quantities is given by

$$\sigma_{h\nu}\sigma_t \geq \frac{\hbar}{2} \qquad \Rightarrow \qquad \Delta h\nu \times \Delta t \geq 1.82 \text{ meV ps}, \tag{3.1}$$

where $\Delta h\nu$ and Δt correspond to the full-width half-maximum (FWHM) values of the bandwidth and pulse duration (assuming Gaussian pulse durations), respectively measured in meV and picoseconds. Thus, a 100-fs pulse cannot have a bandwidth smaller than 18.2 meV.

Frequency tunability. Ti:sapphire lasers are known for a broad range of frequency tunability within the near-infrared spectrum, which can be important for resonantly particular nonequilibrium modes. Tunability can be equivalently expressed in terms of wavelength or energy, which are related to each other according to

$$\lambda \times h\nu = hc \qquad \Rightarrow \qquad \lambda \times h\nu = 1240 \text{ nm eV}. \tag{3.2}$$

Unfortunately, in a time-resolved ARPES setup a substantial laser tunability can be tempered by the fact that the most common technique for generating photoemission light in a pump-probe ARPES experiment (and the technique currently employed by the Lanzara group) is by quadrupling the light. This limits the range of available pump frequencies because it is required that the probe beam frequency be sufficiently high to overcome the material work function. Pump beam tunability can be improved in a time-resolved ARPES setup by incorporating the use optical parametric amplifiers (OPAs) or optical parametric oscillators (OPOs) within a give setup.

Stability. Finally, stability is an extremely important, but difficult to quantify, figure of merit in a laser. Time-resolved experimental runs can run for days on end, so it is important to find a system that can operate with minimal maintenance.

3.4 Lanzara group experimental scheme

We now proceed to a more detailed description of the Lanzara group experimental apparatus. Figure 3.4 shows the system's schematic diagram.

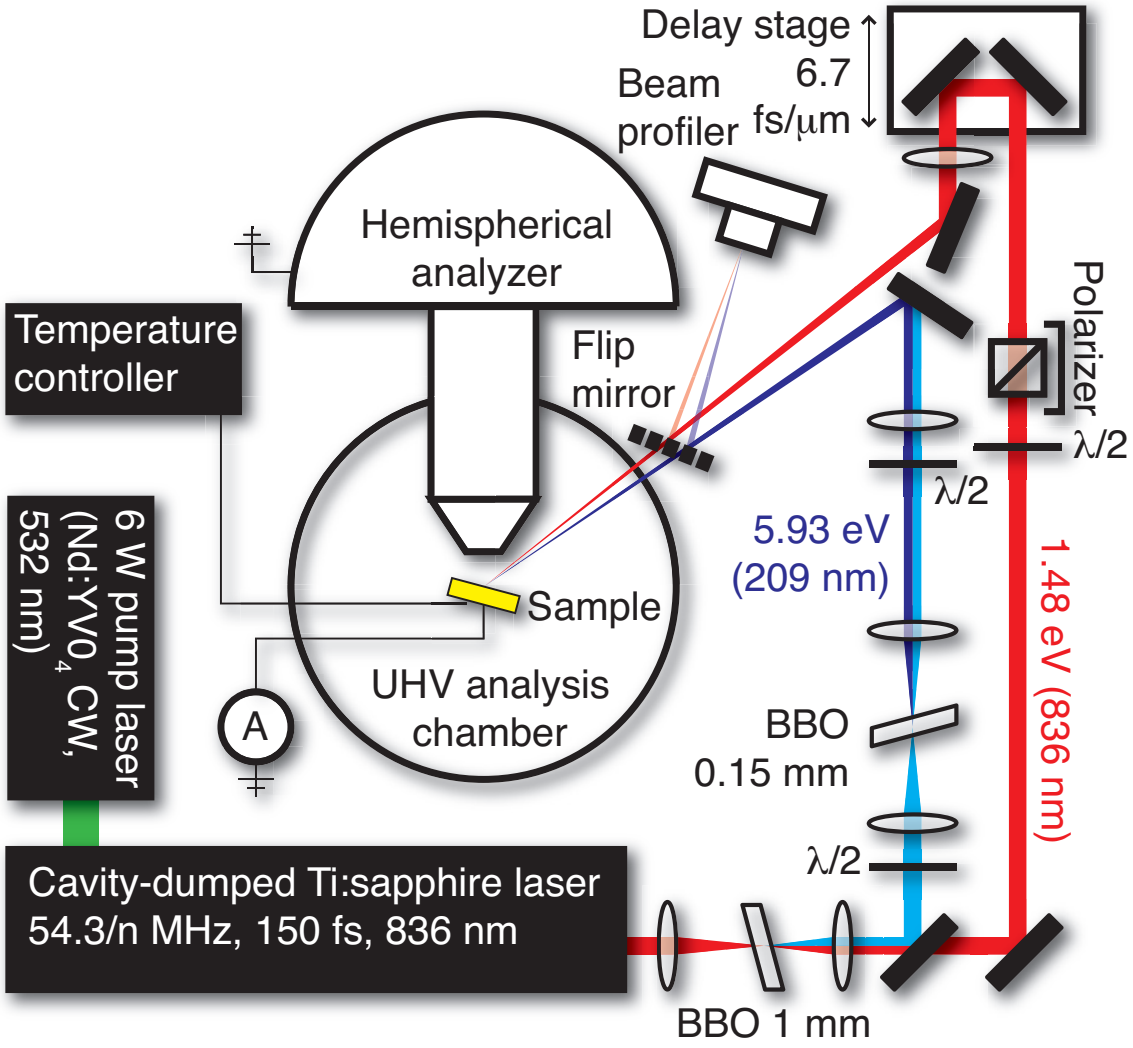

Figure 3.4. Schematic diagram of the experimental apparatus. From Ref. 190.

3.4.1 Light source

Laser pulses are generated using a mode-locked Ti:sapphire oscillator purchased commercially from Coherent Inc. (Mira 900), which is pumped with a 6 W frequency-doubled Nd:YVO_4 laser (Coherent Verdi V6). Through the use of a cavity dumper (APE PulseSwitch), the pulse repetition rate is adjustable and given by $54.3/n$ MHz, where n is any positive integer between 1 and 260,000 (typically set to 100 for cuprates). This repetition rate tunability is one of the system's main advantages.

At the oscillator output, pulses have a nominal duration of 150 fs. The output frequency may be adjusted between 700–980 nm, but is typically tuned near 836 nm ($h\nu = 1.48$ eV). We generate the ultraviolet probe beam (209 nm, $h\nu = 5.93$ eV) by frequency-quadrupling the oscillator output using type-I second harmonic generation in two β-barium borate (BBO) crystals of 1 mm and 0.15 mm thickness, arranged in series. Light which remains at the fundamental frequency after passing through the first BBO crystal is split off from the second harmonic using a dichroic mirror and is used for the pump beam. A variable time delay between pump and probe pulses is achieved to within 17 fs using a motorized translation stage (Newport ILS250PP, on-axis accuracy: ± 2.5 μm). The polarizations of the pump and probe beams can be freely adjusted.

3.4.2 Sample orientation

The sample is mounted on a copper puck (diameter 1") and placed inside an ultrahigh vacuum (UHV) analysis chamber (pressure maintained below 5×10^{-11} Torr) on a custom-built manipulator. The manipulator has 6 degrees of freedom (3 translational and 3 rotational) which allow the sample to be moved and rotated arbitrarily. Using liquid helium, the sample can be cooled to 15 K. A resistive heater mounted on the end of the cryostat allows us to vary the temperature anywhere between this lower limit and 450 K. The temperature is monitored using a silicon diode placed in thermal contact with the sample. The sample is electrically grounded through a picoammeter (Keithley 6485), which measures the sample photocurrent. The pump and probe beams pass into the chamber through a UV-grade fused silica window.

Because the pump and probe beams are at such different wavelengths, they must be aligned to the same spot on the sample using independent optics. This is accomplished with a 100 μm-diameter pinhole mounted on the manipulator below the sample. A phosphor-coated glass window on the far side of the chamber fluoresces when the pump or probe beam is centered through the pinhole. For the pump beam, which is more powerful than the probe, a power meter placed at the exit window is used to fine-tune the alignment. Probe beam alignment is fine-tuned by minimizing photoemission counts, which are stronger when the beam hits the edge of the pinhole than when it passes through the empty space in the pinhole center. To heighten the contrast in this effect, a layer of gold was deposited around the pinhole's edges.

3.4.3 Photoelectron detection

The energy and momentum of photoemitted electrons are measured using a hemispherical analyzer with a 2D imaging detector (SPECS Phoibos 150). Such analyzers offer high throughput for simultaneous two-dimensional data acquisition as a function of kinetic energy and momentum along one direction. Recent developments in time-of-flight systems have made them competitive with hemispherical analyzers in certain respects. Time-of-flight electron analyzers can have an advantage in experiments with unique detector requirements such as spin-resolved ARPES,[191] and progress has been made developing 3D time-of-flight analyzers that can simultaneously measure energy and two components of crystal momentum.[192,193] However, although they are improving, the time-sensitive detectors in these systems have limited maximum count rates in comparison with the 2D phosphor detectors used in hemispherical analyzers.

The angle between the center of the analyzer and incident laser beams is fixed at 55°. The analyzer is connected to the main chamber though a rotary seal which allows the slit to be oriented either vertically or horizontally. Measurements in this correspondence were collected with a horizontal slit in the lab frame.

3.5 Fluence considerations

A very important physical quantity in a time-resolved ARPES experiment is the fluence, defined as the average optical energy deposited on a sample surface per unit area. The reason is because fluence directly correlates to the initial density of excited quasiparticles. In our experiment, the fluence is adjusted by output power of the laser directly, and through the use of half-wave plates and polarizers (see Fig. 3.4 for optical element locations along the beam path).

3.5.1 Overall characterization

Assuming the pump and probe beams have Gaussian transverse spatial intensity profiles, the total average pump fluence will be given by

$$F_{ave} = G \times (1 - R) \times \frac{0.88\, E_{pu}}{\mathrm{FWHM}_{pu}^2 + \mathrm{FWHM}_{pr}^2}, \tag{3.3}$$

where E_{pu} is the pump pulse energy, where FWHM_{pu} and FWHM_{pr} are the pump and probe beam diameters as defined by the transverse intensity profile's full-width at half-maximum (FWHM), where the geometrical factor G accounts for spot size modification caused by the sample's angular orientation relative to the incoming beams, and where R is the sample reflectance. This equation is derived in Section 3.5.2 below, and is reasonable when the spot size of the probe is smaller than the spot size of the pump.

Several factors contribute to fluence uncertainty, including power meter measurement error, losses from the viewport windows, pump-probe misalignment, and inaccuracies in the pump and probe beam spot size measurements. We determined the combined fluence error according to the formula,

$$\left(\frac{\Delta F}{F}\right)^2 = \underbrace{\left(\frac{\Delta P}{P}\right)^2}_{\text{power meter}} + \underbrace{0.03^2}_{\text{windows}} + \underbrace{\left(\frac{A\,\delta}{\text{FWHM}_{pu}}\right)^2}_{\text{alignment}} + \underbrace{\frac{4\,\text{FWHM}_{pu}^2\,(\Delta\text{FWHM}_{pu})^2 + 4\,\text{FWHM}_{pr}^2\,(\Delta\text{FWHM}_{pr})^2}{\left(\text{FWHM}_{pu}^2 + \text{FWHM}_{pr}^2\right)^2}}_{\text{spot sizes}}, \tag{3.4}$$

where F is the fluence, P is the laser power, A is a proportionality factor, δ is the pump-probe spacial misalignment, and FWHM_{pu} and FWHM_{pr} are the respective pump and probe full-width half-maximum intensity values as in Eq. 3.3. The variables σ refer to the standard error of their respective subscripts. The specific way in which each of these sources contribute to the overall error is discussed in greater detail below. As a general rule, in the Lanzara group setup we have estimated 10% fractional power meter uncertainty, 3% fractional uncertainty due to window losses, 10% fractional uncertainty from pump-probe alignment, 10% uncertainty in the respective pump and probe FWHM values, and a typical pump-probe ratio of 2:1, which leads to a combined fractional fluence uncertainty of 22%.

3.5.2 Impact of spot size and alignment on fluence

We characterized the spot sizes of the pump and probe pulses using a CCD beam profiler (DataRay WinCamD-UCD12) and a flip mirror placed in front of the UHV analysis chamber. When raised, the flip mirror deflects the pump and probe beams toward the profiler, which is positioned to preserve the pump and probe path lengths and spot sizes. Measurements of the pump and probe beam sizes and shapes are displayed in Fig. 3.5. We fit the images to a two-dimensional Gaussian

$$f(x,y) = f_0 + A\exp\left[\frac{-1}{2(1-c^2)}\left(\left(\frac{x-x_0}{\sigma_x}\right)^2 + \left(\frac{y-y_0}{\sigma_y}\right)^2 - \frac{2\,c\,(x-x_0)(y-y_0)}{\sigma_x\sigma_y}\right)\right] \tag{3.5}$$

and extracted the mean full-width half-maximum (FWHM) beam diameter by the relation $\text{FWHM}^2 = 8\ln(2)\,\sigma_x\sigma_y\sqrt{1-c^2}$. In the instance shown the pump spot has a FWHM = 109 μm and the probe spot has a FWHM = 43 μm, giving a pump-probe width ratio of about 2:1. Such sizes and ratios are typical of this setup, and provide a good compromise between competing system needs: the pump beam must be focused tightly enough to drive

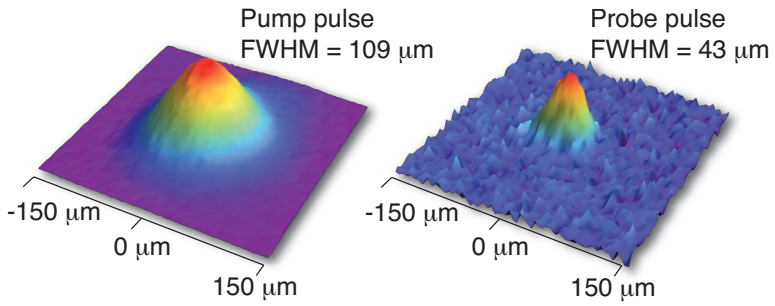

Figure 3.5. Transverse intensity profiles of the pump and probe pulses, experimentally determined by a CCD beam profiler. From Ref. 190.

the system far from equilibrium, but the probe beam should still be wide enough to prevent space charge effects from becoming prohibitive.

We were able to confirm the measurement of the pump beam's effective FWHM using the 100 μm-diameter pinhole. We measured the beam's power at the far end of the chamber both when the beam was focused through the pinhole, and when the pinhole was removed. We then calculated the FWHM by comparing this power ratio to the theoretical ratio between the volume of a complete Gaussian line shape and its central peak confined to a radius of 50 μm. For the pump spot in Fig. 3.4(b), the pinhole characterization gave a pump FWHM = 118 μm, agreeing within 8% to the CCD characterization.

The Gaussian-profile assumption readily lends itself to an analytic method of calculating both fluence and fluence uncertainty. The total average fluence is given by a weighted integral over the pump beam profile according to

$$F_{ave} = \frac{E_{pu}}{4\pi^2\sigma_{pu}^2\sigma_{pr}^2}\int_{-\infty}^{\infty} d^2x\, \exp\left[-\frac{|\boldsymbol{x}|^2}{2\sigma_{pu}^2}\right]\exp\left[-\frac{|\boldsymbol{x}-\boldsymbol{\delta}|^2}{2\sigma_{pr}^2}\right] \tag{3.6}$$

$$= \frac{E_{pu}}{2\pi(\sigma_{pu}^2+\sigma_{pr}^2)}\exp\left[-\frac{|\boldsymbol{\delta}|^2}{2(\sigma_{pu}^2+\sigma_{pr}^2)}\right]. \tag{3.7}$$

Here E_{pu} is the total pump pulse energy, σ_{pu} and σ_{pr} are the pump and probe widths ($1/\sqrt{e}$ intensity), and $\boldsymbol{\delta}$ is the spatial misalignment vector. For a perfectly aligned pump and probe beam the equation simplifies to

$$F_{ave} = \frac{0.88\,E_{pu}}{\mathrm{FWHM}_{pu}^2+\mathrm{FWHM}_{pr}^2} \tag{3.8}$$

where beam sizes have been recast in terms of FWHM diameters by substituting FWHM = $2\sigma\sqrt{2\ln(2)}$, and the numerical constant $0.88 = 4\ln(2)/\pi$. This proves the main portion of Eq. (3.3). The rightmost term in Eq. (3.4) follows from differentiating Eq. (3.8) with respect to FWHM_{pu} and FWHM_{pr}, and applying standard rules of error propagation.[194]

For a misaligned pump and probe Eq. (3.7) becomes

$$F_{ave} = \frac{0.88\, E_{pu}}{\mathrm{FWHM}_{pu}^2 + \mathrm{FWHM}_{pr}^2} \exp\left[-\frac{2.77\,|\boldsymbol{\delta}|^2}{(\mathrm{FWHM}_{pu}^2 + \mathrm{FWHM}_{pr}^2)}\right]. \tag{3.9}$$

which offers an avenue for characterizing the fluence uncertainty due to pump-probe mis-alignment. Pump-probe mis-alignment is the single greatest cause of random uncertainty between one fluence measurement and the next in the ultrafast ARPES experiment. According to equation (3.9) a misalignment of δ that is $0.2 \times FWHM_{pu}$ for a pump-probe ratio of 2:1 can result in an average incident fluence that differs from the $\delta = 0$ value by 8%.

3.5.3 Impact of geometry on fluence

While the formalism so far applies to pump and probe beams impinging upon a sample at normal incidence, an accurate calculation of the incident fluence also requires taking into account the oblique angle at which the pump and probe beams impinge upon the sample. For example, when the beam approaches a sample at an angle φ from normal incidence, it will spread into a spot that is larger by a factor of $1/\cos\varphi$. It can easily be shown that the average fluence is correspondingly reduced by $G = \cos\varphi$. In typical 6 eV laser ARPES data sets on Bi2212, the angle φ ranges between 0–35°, corresponding to a 0–20% decrease in fluence.

3.5.4 Impact of reflectance on fluence

Reflectance values can figure importantly into fluence calculations because light that reflects back from the sample can play no role in photoexcitation. In Bi2212 sample reflectance is typically quite low ($\approx 9\%$), which makes it necessary to incorporate fluence corrections for reflectance only when the pump beam impinges upon the sample from very oblique angles. However, we have corrected for these effects in the analysis performed in Chapters 5 and 6. The importance of taking reflectance into account increases significantly for the measurement of shinier samples, such as the topological insulator Bi_2Se_3 and many of the iron-based superconductors.

For Bi2212, reflectance values can be calibrated based on room-temperature measurements, as shown in Fig. 3.6. Reflectance at 836 nm depends on temperature only very weakly,[195] rendering low-temperature measurements unnecessary. Bi2212 is slightly birefringent between the Γ–Y and Γ–X orientations,[196] which results in two pairs of curves in Fig. 3.6. Because the typical sample orientation in a time-resolved ARPES experiment on Bi2212 does not diverge significantly from $E_{ab} \parallel \Gamma$–X, we have ignored the data for $E_{ab} \parallel \Gamma$–Y in our fluence calculations (E_{ab} corresponds to the projection of the linearly polarized pump pulse's electric field amplitude onto the ab-plane of the crystal). The solid lines in the figure are the result of fitting to the Fresnel equations[197] with a complex refractive index $\tilde{n}$, under the constraint that $\mathrm{Im}\,[\tilde{n}] = 0.5$. This corresponds to an absorption depth of

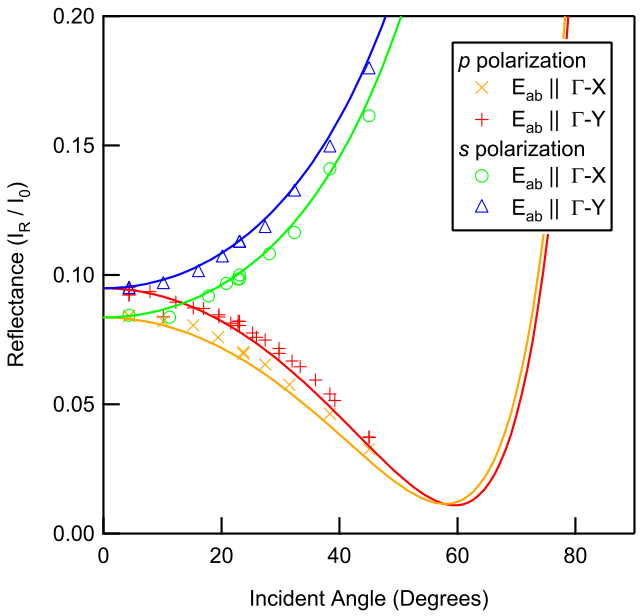

Figure 3.6. Reflectance of single-crystal Bi2212. Measurements were taken at room temperature and atmospheric pressure with 836 nm light. E_{ab} corresponds to the projection of the linearly polarized laser beam's electric field amplitude onto the ab-plane of the crystal. The solid curves are fits to the Fresnel equations under the constraint that $\mathrm{Im}\,[\tilde{n}] = 0.5$. For $E_{ab} \parallel \Gamma$–X, $\tilde{n} = (1.57, 0.5)$. For $E_{ab} \parallel \Gamma$–Y, $\tilde{n} = (1.67, 0.5)$.

133 nm, in adequate agreement with direct measurements of the absorption depth in the superconducting state.[151] For $E_{ab} \parallel \Gamma$–X, we estimate $\tilde{n} = (1.57, 0.5)$.

3.6 Time and energy resolution

Time and energy resolution are crucial figures of merit in any time-resolved ARPES experiment. While there are technological limitations on these quantities, they are also intrinsically linked by the Heisenberg uncertainty principle. Here we detail methods for characterizing time and energy resolution in the Lanzara group system, and outline the major contributing factors contributing to each.

3.6.1 Overall characterization

We estimated the system's time resolution by measuring polycrystalline gold far above the Fermi level ($E - E_F > 1$ eV) as shown in Fig. 3.7(a). At this energy the lifetimes of electronic states are expected to be brief with respect to the time resolution, so the duration of the time-resolved photoemission response primarily reflects the length of the pump and

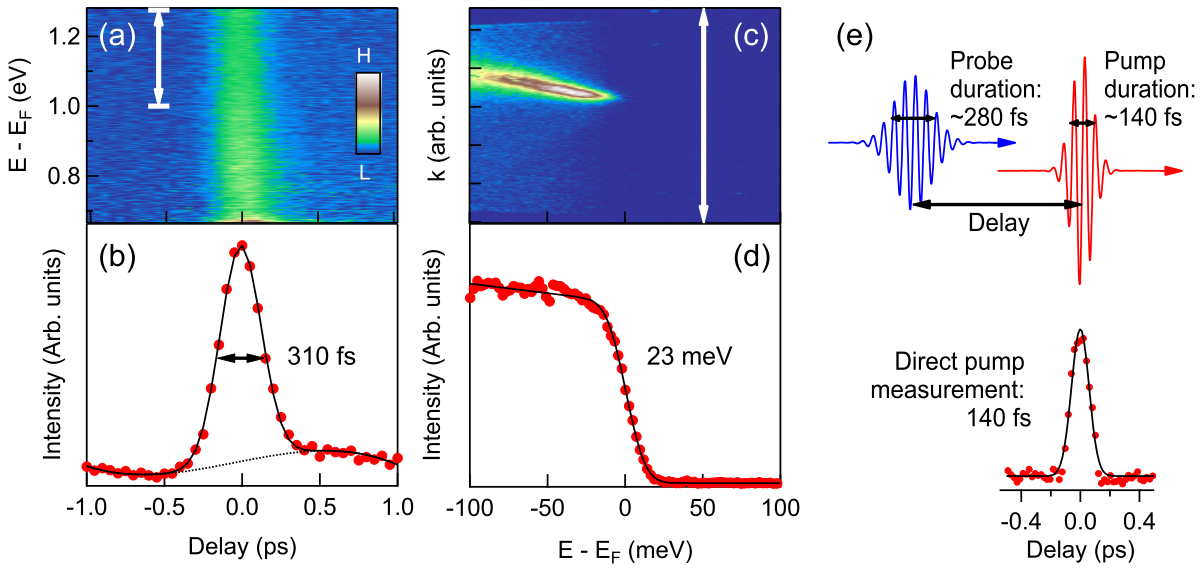

Figure 3.7. System time and energy resolution calibration methodology. **(a)** Photoemission intensity on polycrystalline gold. The image is normalized by the average intensity between -1 and -0.5 ps. **(b)** Intensity integral between the boundaries of the white double arrow shown in (a). A Gaussian fit with a polynomial background function is used to estimate pump-probe cross correlation. **(c)**–**(d)** Fermi edge measurement of Bi2212 at 16 K, extracted from a nodal cut in k-space where there is no superconducting gap. A complementary error function fit is used to calibrate the energy resolution. **(e)** Cartoon depicting pump and probe pulse durations, and direct measurement of pump pulse duration by frequency-resolved optical gating (FROG).

probe pulses themselves. The Fig. 3.7(e) cartoon illustrates the mechanics of the pump-probe measurement. As the delay stage alters the relative path lengths of pump and probe beams, the time delay changes between the two pulses. When the pulses are passed through each other, photoemission intensity at high energy spikes, generating a feature with a duration equal to the quadrature sum of the pump and probe beam durations. As shown in Fig. 3.7(b), the delay profile can be fit to a Gaussian of FWHM = 310 fs. This gives an estimate (actually an upper bound) of the cross-correlation between the pump and probe beams, which defines the system resolution. Assuming a 150 fs pump pulse, the estimated duration of the probe pulse is 280 fs.

The total energy resolution can be characterized by measuring the Fermi edge at low temperature of any sample with bands that cross the chemical potential. Figs. 3.7(c) and 3.7(d) show the Fermi edge of Bi2212 at 16 K, which was acquired by taking an angle-integrated measurement from a cut along the Γ-Y direction in k-space where there is no superconducting gap. Because the system resolution is significantly broader than the Fermi broadening, it dominates the line shape. An error function fit gives a resolution of 23 meV. After subtracting out the analyzer resolution (here 15 meV) this corresponds to a probe pulse energy uncertainty of 17 meV. A Fourier-transform-limited probe beam with such an energy spread would have a pulse duration of 110 fs. The extra broadening in the pulse length primarily results from imperfections in the second-harmonic generation processes (described

in further detail below). Additional factors, such as pulse chirp, air currents, and acoustic vibrations, may also be present.

3.6.2 Impact of second- and fourth-harmonic generation

Aside from the inherent time resolution of the Ti:sapphire pulses themselves, the single greatest factors influencing system time resolution are related to the BBO crystals used to generate the fourth-harmonic probe pulse light. To generate 6-eV light with system we send the laser beams through two successive frequency-doubling BBO arrangements (see Fig. 3.4). We use type-I phase matching, where two photons polarized along the ordinary axis are combined in the BBO crystal to produce a second-harmonic photon that is orthogonally polarized at an optimal phase-matching angle θ relative to the extraordinary axis.[ii] In practice, this means vertically polarized second-harmonic light is generated from the horizontally polarized fundamental, and that horizontally polarized fourth-harmonic light is generated from the vertically polarized second-harmonic beam.

A crucial element dictating the energy and time resolution of the outgoing pulse is the length of the BBO crystal. In particular, second-harmonic generation properties will significantly change depending on how the crystal length L compares to the quantity L_D^{SHG} defined[198]

$$L_D^{SHG} \equiv \frac{\tau_{p1}}{|\nu_2^{-1} - \nu_2^{-1}|}, \tag{3.10}$$

where τ_{p1} is the incoming pulse duration (FWHM) and ν_1 and ν_2 are respective group velocities of the fundamental and second-harmonic beams as they travel through the crystal.

In the limit $L \ll L_D^{SHG}$ the power of the second-harmonic pulse increases quadratically with both fundamental pulse intensity and BBO crystal length, which can be understood quantum mechanically by noting that it takes two fundamental-frequency photons to generate one second-harmonic photon. Because of the quadratic intensity dependence, for a Gaussian profile the up-conversion process results in a second-harmonic pulse that is shorter than the fundamental pulse by a factor of $\sqrt{2}$. The primary cost of choosing very short BBO crystals is a low second-harmonic generation conversion efficiency.

In contrast, as the length of the pulse approaches and begins to exceed L_D^{SHG}, conversion efficiency greatly increases, but the rules for up-conversion change, with a pulse duration that becomes increasingly longer with increasing BBO crystal length. The pulse duration eventually approaches a value given by the product $L \times |\nu_2^{-1} - \nu_2^{-1}|$. The physical origin of the increasing pulse duration is temporal walk-off between the fundamental and second-harmonic pulses. Curiously, a longer-length BBO crystal also places stricter restrictions on the frequencies of light that can be efficiently phase-matched and up-converted, resulting in improved energy resolution. Thus, in cases it can be advantageous to choose a longer BBO crystal.

[ii] A comprehensive introduction to the general phenomena associated with second-harmonic generation, with many details that I have glossed over, is given by Diels and Rudolph.[198]

λ (nm)	θ (°)	$\lvert\nu_2^{-1} - \nu_2^{-1}\rvert$ (fs/mm)
836	28.0	173
828	28.3	177
800	29.2	193
418	77.3	1214
414	80.8	1254
400	—	—

Table 3.1. Phase-matching angles and group velocity mismatch values for Type-I second-harmonic generation in BBO at selected wavelengths.[199]

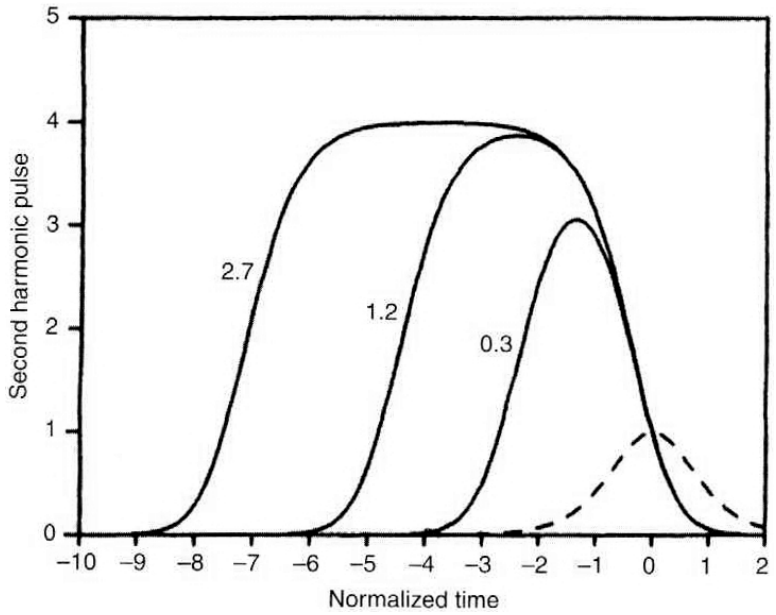

Figure 3.8. Second-harmonic pulse for different, normalized crystal lengths L/L_D^{SHG}, assuming a fundamental pulse with a hyperbolic secant intensity profile (dashed curve at right). From Ref. 198.

Beyond the role that the BBO crystals play in increasing the pulse duration of the second-harmonic beam, at very high conversion efficiencies passing the fundamental may result in a broadening of the fundamental pulse through third-order effects. This adversely affects time resolution because the remainder of the fundamental pulse is recycled after being passed through the first BBO crystal and deflected toward the sample to be used as the pump pulse.

For all of the experiments described in this dissertation, a 1-mm thickness BBO was used to convert from 836 nm to 418 nm, and a 0.15-mm thickness BBO was used to convert from 418 nm to 209 nm. System upgrades are underway to replace the first BBO with a BBO of 0.5-mm thickness, and to replace the second BBO with a BBO of 0.05-mm thickness.

3.6.3 Impact of the analyzer on energy resolution

The energy resolution is broadened by the inherent resolution of the hemispherical analyzer. The energy resolution, ΔE is given according to the equation[200]

$$\frac{\Delta E}{E_p} = A\frac{S}{R_0} + B\alpha^2, \tag{3.11}$$

where S and R_0 are as defined in Fig. 3.9,[iii] α is the angular variation of electrons passing through the entrance slit, and E_p, the pass energy, is the energy required for an electron to trace a circular route between the hemispherical electrodes at the mean radius R_0. Specific

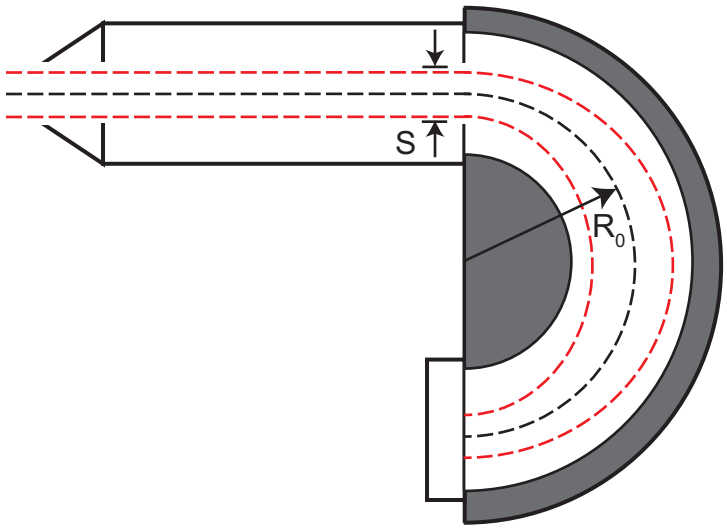

Figure 3.9. Schematic illustration of the origin of energy resolution in a hemispherical analyzer. The dashed black line is the path for an electron entering the analyzer at the pass energy and at the center of the entrance slit. The dashed red lines are paths for electrons entering the analyzer at the pass energy but at the top or bottom of the entrance slit.

values of A and B will vary depending on the quality of the analyzer, with typical values being $A \approx 1/2$ and $B \approx 1/4$.[201,202,200,203] In most cases the second term above is dominated by the first term due to the small spot size of the probe beam.

It would seem, based on Eq. (3.11) that the energy resolution contribution from the analyzer could be made arbitrarily small by minimizing S or E_p, both of which can be easily adjusted in modern analyzers. However, reducing either of these values also reduces electron throughput, thereby increasing the time it takes to acquire high-statistics data. In a time-resolved ARPES experiment, where we wish to explore vast regions of parameter space, such throughput is important. Since the energy resolution of the analyzer and the combined

[iii] There is some confusion about the definition of S in the literature, which originates from the fact that early hemispherical analyzers had slits at both the hemisphere entrance and exit locations, whereas in modern analyzers the exit slit has been replaced by a multi-channel plate. Here, S refers only to the entrance slit.

energy resolution from other sources add in quadrature, it makes sense to tune the slit and pass energy so that these are roughly equivalent. We typically adjust the entrance slit to 0.8 mm and set the pass energy to 5 eV, giving an analyzer resolution of about 15 meV.

3.6.4 Impact of space charge on energy resolution

Finally, the energy resolution is broadened by space charge. This effect originates from repulsive Coulomb forces that photoelectrons exert on each other when they pass in vacuum between the sample and the photoelectron detector, and results in a reduced kinetic energy for the lowest-energy photoelectrons, an increased kinetic energy for photoelectrons at the Fermi edge, and an overall smearing of the wave packet features. While potentially relevant in

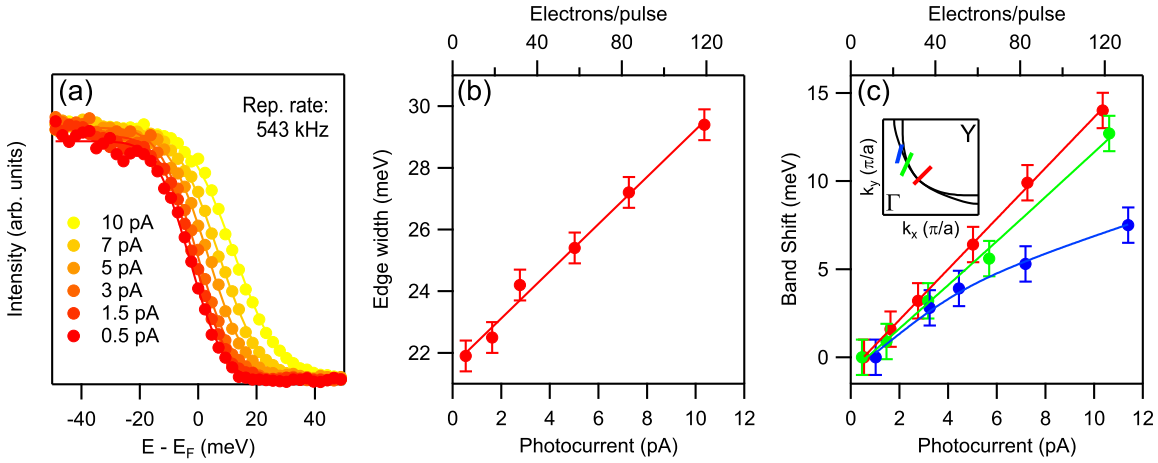

Figure 3.10. Space charge effects for Bi2212 under typical time-resolved ARPES experimental conditions. The probe pulse duration was ≈ 280 fs, the spot size was 46 μm, the pulse repetition rate was 543 kHz, and the temperature was 20 K. **(a)** Effect for angle-integrated EDCs along a G-Y k-space cut (see inset to (c)). **(b)** Edge width versus photocurrent, extracted by fitting the curves in (a) to a complementary error function, as in Ref. 183. **(c)** Leading edge shift versus photocurrent for three k-space cuts through the Bi2212 Fermi surface.

any ARPES experiment,[181,182,183,184] space charge is particularly important in time-resolved ARPES setups because of the short optical pulse durations, small spot sizes, and low electron kinetic energies typically involved.

Figure 3.10 shows space charge effects for typical experimental conditions used in collecting Bi2212 data. Energy-resolution broadening effects along Γ–Y become comparable to the background resolution (22 meV) when the photocurrent is increased beyond 10 pA (115 electrons/pulse). To minimize these effects, we typically acquire data with a photocurrent less than 5 pA (57 electrons/pulse). A visible upward shift in the Fermi edge also occurs, increasing with a typical rate of 1.4 meV/pA (0.12 meV/electron). While this latter effect is easily corrected by shifting the spectra downward in post-processing, care should be taken

to calibrate data acquired along different angles: The energy shift is angle-dependent,[183] as shown in Fig. 3.10(c).

3.7 Detector nonlinearity

Nonlinearity effects are common in electron spectrometers and have been characterized with photoemission on core levels.[204,205,206] The effects are also gaining awareness in the laser ARPES community,[72,189,190,207] where intense line shapes amidst low levels of background counts are common.

One of the advantages of the Lanzara group system is that the sample is connected to ground through a picoammeter, allowing for efficient characterization of detector nonlinearity. Fig. 3.11 shows the relationship between the incident probe power and the resulting photocurrent measured by the picoammeter. The pump beam was blocked as these mea-

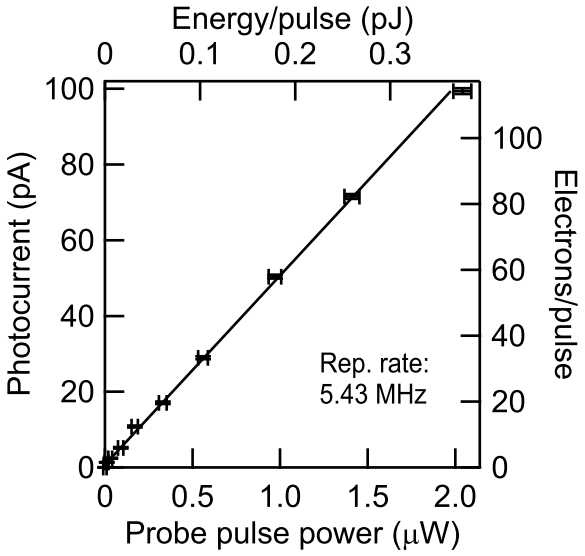

Figure 3.11. Sample photocurrent versus incident probe beam power. From Ref. 190.

surements were taken. As shown in the figure, the two variables are proportional to each other to within 1 pA (a best-fit line places the y-intercept at 0.7 ± 0.3 pA). This very linear relationship, which extends also to high probe powers,[183] is a strong indication that photocurrent and incident probe beam power reflect the true electron count rate, and spurious effects in the photocurrent or laser power, such as those potentially caused by space charge or image charges, are not evident.

Figure 3.12 illustrates a methodology for characterizing detector nonlinearity. Fig. 3.12(a) shows the relationship between photocurrent and nominal count rate, where the detector is used to measure a sample of polycrystalline gold. While the relationship is linear at the lowest count rates, there is a clear deviation from linearity at moderate count rates. The same effect

can be characterized directly in any material of interest. Data on optimally doped Bi2212 are shown as an example in Fig. 3.12(b). Because of a single crystal sample's momentum-resolved character, localized portions of the detector window must be characterized separately. The three curves represent high, middle, and low intensity portions of the spectrum. Given the same count rate, pixels at different locations on the detector still have similar nonlinear responses to each other. In consequence there exists a scaling relation wherein all the curves in Figs. 3.12(a) and 3.12(b) can be horizontally collapsed to one curve as shown in Fig. 3.12(c). The nonlinearity calibration curve is sample-independent, as expected of an effect originating from the detector.

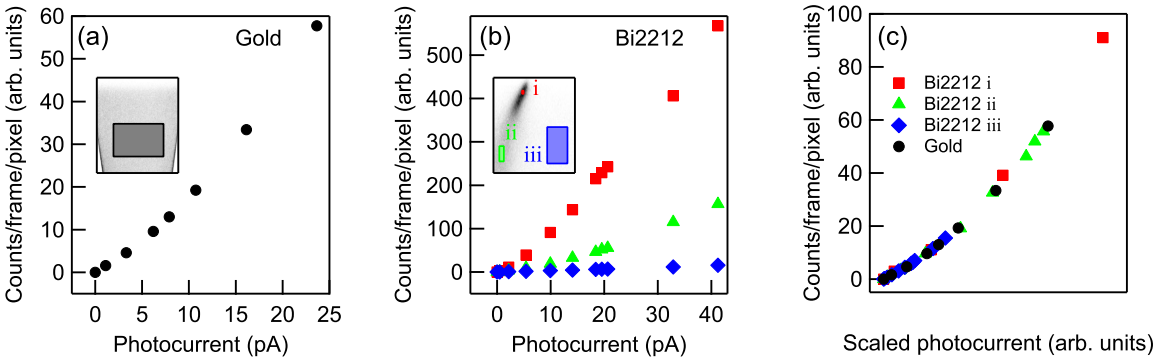

Figure 3.12. Detector nonlinearity calibration measurements. **(a)–(b)** Nominal detector counts measured by the hemispherical analyzer versus sample photocurrent. The measurements was acquired using a sample of polycrystalline gold (panel (a)) and single-crystal Bi2212 (panel (b)) and averaged over a finite region of the detector as shown in the panel insets. The three plots in (b) correspond to high, moderate, and low intensity portions of the detector image. **(c)** Universal nonlinearity curve, acquired by horizontally scaling the data from panels (a) and (b). From Ref. 190.

Once characterized, the nonlinearity curve can be inverted and applied to any set of data, minimizing nonlinearity effects. Fig. 3.13 shows a demonstration of the detector nonlinearity correction applied to a representative energy/momentum dispersion plot of Bi2212.

3.8 Contact potentials

Care must be taken in treating the effects of stray electric and magnetic fields in a time-resolved ARPES experiment, both of which have influences that become increasingly severe in the limit of low kinetic energy. Although magnetic forces can be greatly reduced by μ-metal shielding, electric forces are unavoidable, and must be understood and corrected computationally.

All of the experiments carried out with our laser ARPES setup employ samples mounted on pucks that are similar in style to Fig. 3.14. While the one-inch-diameter design is system-specific, the more general approach of mounting a sample onto a larger puck (consisting of

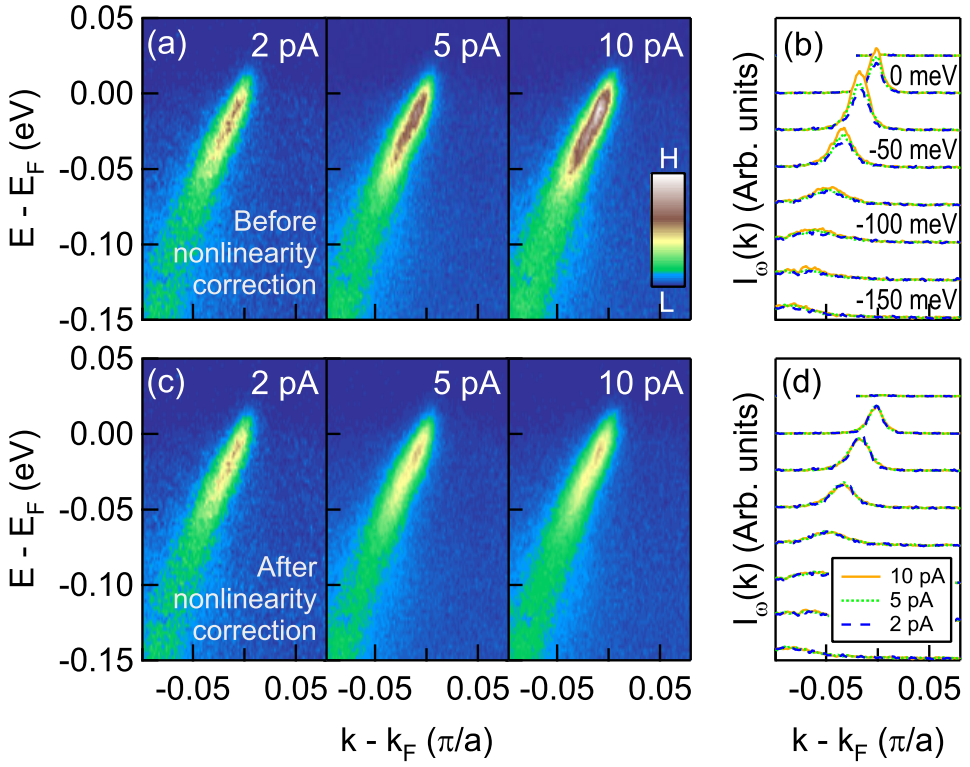

Figure 3.13. Effect of accounting for detector nonlinearity on cuprate data. Images show a nodal dispersion plot for optimally doped Bi2212 (T_c = 91 K) at 17 K. (a) Dispersion maps before applying the detector nonlinearity correction curve, corresponding to three different photocurrent values. Maps have been divided by the acquisition time and average photocurrent in order to allow for a direct intensity comparison. (b) Momentum distribution curves (MDCs) from the maps in (a) at selected energies. Curves are vertically offset for ease of viewing. (c–d) Dispersion maps and selected MDCs after applying the detector nonlinearity correction curve. From Ref. 190.

a different material than the sample) to facilitate efficient transport to and from the UHV analysis chamber is almost universally employed in ARPES systems at both low and high energy. Because the sample and surrounding puck are in electrical contact, their chemical potentials will equilibrate, resulting in a contact potential given by the difference in work function between the sample and puck. When this contact potential is comparable to typical photoelectron kinetic energies, the effect can dramatically influence the path of exiting photoelectrons.

As an order-of-magnitude example, it is useful to consider the case of a photoelectron exiting a sample with a kinetic energy of 2 eV, and assuming a 0.5 V contact potential between the sample and surrounding puck. Under these circumstances, it is reasonable to assume that the electron will be transversely accelerated through an electric potential of

Figure 3.14. Sample of Bi2212 mounted on a 1-inch copper puck.

perhaps 100 mV. Since in free space an electron is governed by the dispersion relation

$$E = \frac{p_\parallel^2}{2m} + \frac{p_\perp^2}{2m} = E_\parallel + E_\perp, \tag{3.12}$$

we can estimate that the electron's course will by altered by an angle

$$\theta = \tan^{-1}\left(\frac{p_\perp}{p_\parallel}\right) = \tan^{-1}\left(\sqrt{\frac{100\text{ meV}}{2\text{ eV}}}\right) = 13^\circ. \tag{3.13}$$

The above conditions closely mirror the physical conditions of an actual experiment. With a photon energy $h\nu = 5.93$ eV, photoelectron initial kinetic energies for Bi2212 are typically on the order of 2 eV. As shown in Table 3.2, typical contact potentials for Bi2212 mounted on copper, aluminum, or graphite pucks range from 0.1–0.5 V.

Material	Φ_W (eV)
Bi2212 (001)	4.01 ± 0.02
Al (polycr)	3.96 ± 0.06
Cu (polycr)	4.50 ± 0.03
Graphite (polycr)	(4.47 ± 0.01)

Table 3.2. Work functions for Bi2212, Al, Cu, and graphite, measured by photoemission.[208] Bi2212, Al, Cu were measured by biasing samples to -18 V. The value for graphite is inferred from a measurement on Bi2212 surrounded by graphite at zero bias. The measurements of Cu and Al are somewhat lower than the typical values in the literature,[209] which is likely explained by surface quality variations. From Ref. 208.

3.8.1 Modeling contact potential effects

Contact potential effects with the one-inch puck geometry can be modeled more rigorously by calculating electric potentials and trajectories for a point charge (simulating an

isolated photoelectron) placed in proximity to a circular conductor of radius r and potential V (simulating the sample), embedded within an infinite conducting plane at potential 0 (simulating the surrounding puck). The electric potential generated by this geometrical configuration is (quite literally[197]) a textbook example of an electrostatics problem with Dirichlet boundary conditions, and can be solved using the method of images to give

$$\varphi(x_\parallel, x_\perp) = \frac{V}{4\pi}\int_0^{r_0}\int_0^{2\pi}\frac{2x_\perp\rho}{(x_\parallel^2+\rho^2+x_\perp^2-2x_\parallel\rho\cos\phi)^{3/2}}d\phi\,d\rho \tag{3.14}$$

$$= \frac{2x_\perp V}{\pi}\int_0^{r_0}\frac{E\left(-\frac{4x_\parallel\rho}{x_\parallel^2-2x_\parallel\rho+\rho^2+x_\perp^2}\right)}{(x_\parallel^2+2x_\parallel\rho+\rho^2+x_\perp^2)\sqrt{x_\parallel^2-2x_\parallel\rho+\rho^2+x_\perp^2}}d\rho, \tag{3.15}$$

where $x_\parallel$ corresponds to the transverse distance from the sample center, $x_\perp$ corresponds to perpendicular distance from the sample surface, r_0 corresponds to the sample radius, V is the contact potential difference, and $E(k^2)$ is a complete elliptic integral of the second kind.

Figure 3.15 shows model geometry, as well as equipotentials and corresponding electric fields. Using SimIon 8.0 electron optics modeling software, it is also possible to generate

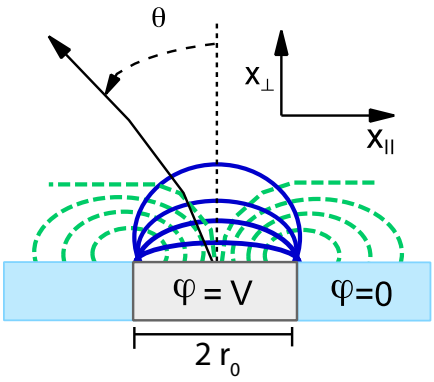

Figure 3.15. Model geometry for the circular-sample model described in the text, including a visualization of electric fields (green dashed lines) and equipotentials (solid blue lines) corresponding to Eq. (3.14). The arrow represents a possible electron trajectory. From Ref. 208.

increasingly realistic variations on this model, with square-shaped central conductors and/or structures placed far away from the sample designed to simulate additional components of the UHV chamber. However, the circular-sample approximation captures most of the essential physics.[208]

SimIon-generated model trajectories for the circular-sample model are displayed in Fig. 3.16 under the assumption of a positive contact potential V (realistic for Bi2212 mounted on copper or graphite), and reveal two overarching trends. First, photoelectrons are uniformly deflected away from normal emission, with final photoelectron exit angles that are increased relative to their initial values, as shown in Figs. 3.16(a) and 3.16(b). Second, photoelectron final angles exhibit a dependence on initial photoelectron position, with photoelectrons tending to be deflected away from the sample edges, as shown in Figs. 3.16(c)

and 3.16(d). It is worth noting that the overall deflection angles are about half as large as predicted from the order-of-magnitude estimate above, and that with the exception of effects very close to the sample edge, all effects are nearly linear.

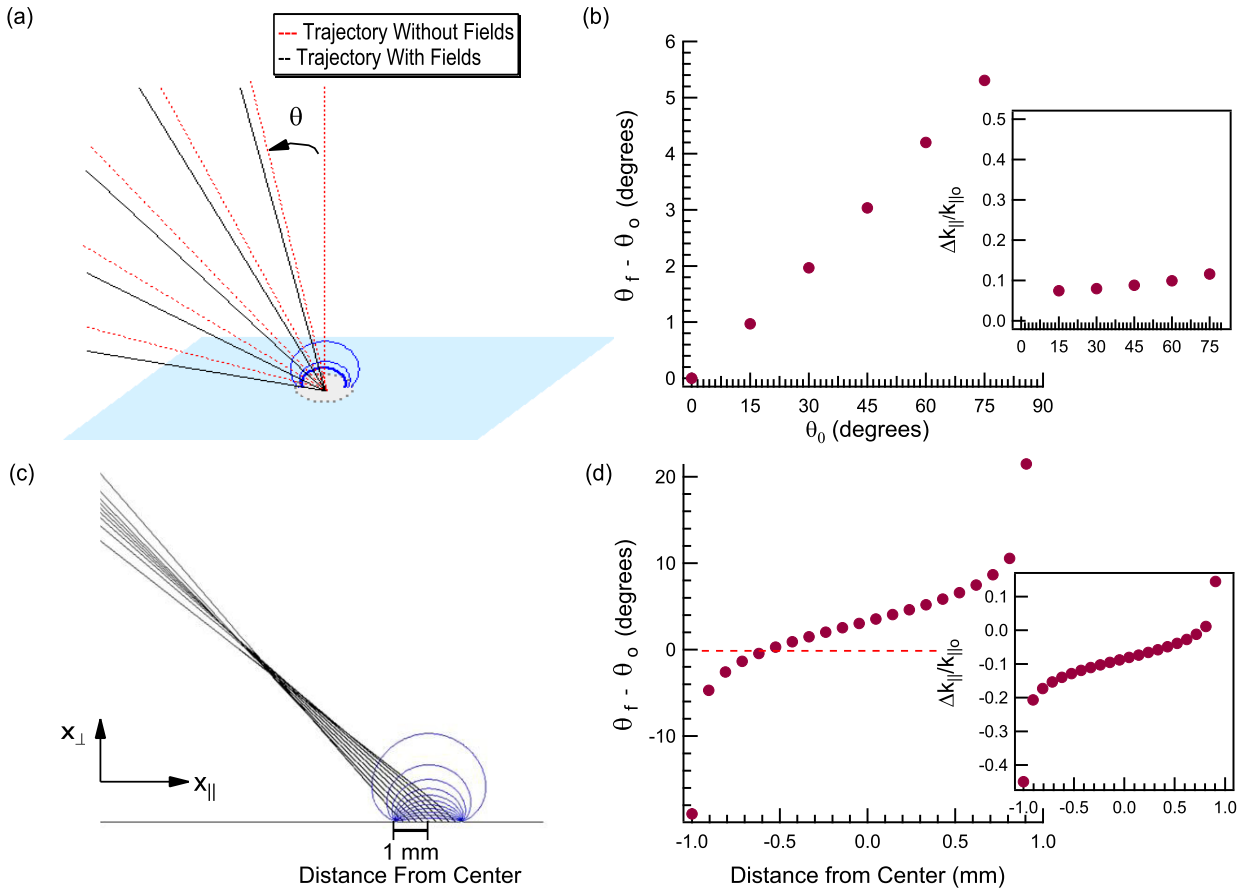

Figure 3.16. Simulations of contact potential effects on photoelectron trajectory. **(a)** Trajectory of electrons leaving the center of the sample at various angles with and without electric field effects, under a simulation where photoelectrons exit the sample with an initial kinetic energy of 2 eV. **(b)** The change in angle of electrons far from the sample versus exit angle. Inset: The relative change in parallel momentum $\Delta k_{||}/k_{||o}$ versus exit angle. **(c)** The trajectory of electrons leaving the sample at 45 degrees for various initial positions. **(d)** The change in angle of electrons leaving the sample at an initial angle of 45 degrees, versus initial photoelectron position across the sample diameter. Inset: The relative change in parallel momentum $\Delta k_{||}/k_{||o}$ versus position. From Ref. 208.

Direct comparisons between the model and physical data can be measured by characterizing spectra along the nodal direction in optimally doped Bi2212, as shown in Fig. 3.17. In the absence of contact potential effects, the Fermi momentum for this cut should occur at an angle of 37°,[208] which we have used as our value of θ_0 in the simulations. Samples mounted on three different pucks are are displayed, consisting of copper (simulated $V = 490$ mV), graphite (simulated $V = 460$ mV), and aluminum (simulated $V = -50$ mV). Contact

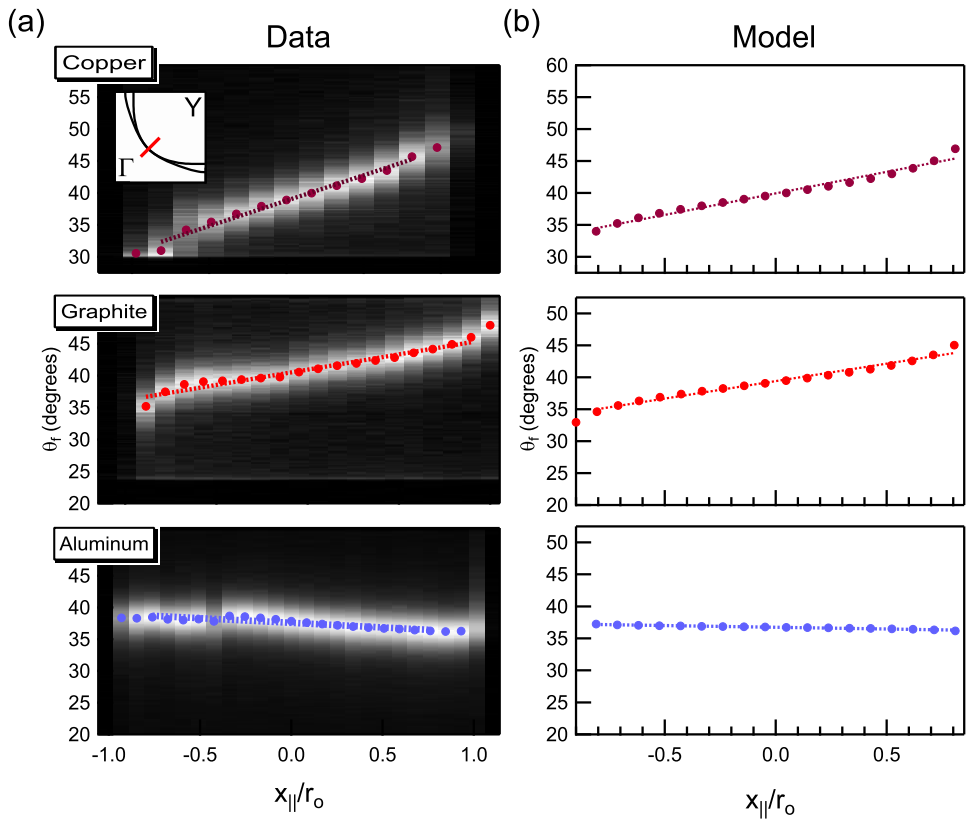

Figure 3.17. Comparison between contact potential simulations and ARPES data. **(a)** Raw image plots of ARPES intensity versus θ_f and $x_\parallel$ at E_F, corresponding to measurements of samples of Bi2212 mounted on copper, aluminum, and graphite pucks. Filled circles correspond to intensity maxima, extracted by Lorentzian MDC fits. **(b)** Simulated variation in θ_f versus $x_\parallel/r_0$. Dashed lines in (a) and(b) are linear fits to θ_f between $0.8r_0 < x_\parallel < 0.8r_0$. From Ref. 208.

potential effects were characterized by scanning the probe beam spot location along $x_\parallel$, from one edge of the sample to the other. There is good agreement between theory and experiment overall, with one exception being that the simulated results for the measurement on aluminum had to be uniformly shifted outward by 4 degrees in order to match the data.[208] The likely origin of this discrepancy is additional contact potential effects originating from the manipulator or analyzer entrance, which are coated in graphite.

3.8.2 Correcting contact potential effects

Because of the high degree of linearity in the contact potential effect, it is possible to make simple corrections to data on a material of interest by comparing to a known Fermi surface for the sample extracted from high-energy synchrotron measurements. Figure 3.18(a) shows a low-temperature (20 K) constant-energy map along the Γ–Y direction in Bi2212, which illustrates the necessity of making this correction, where data have been transformed

from angle-space to k-space assuming a work function of 4.38 eV. While measurements near

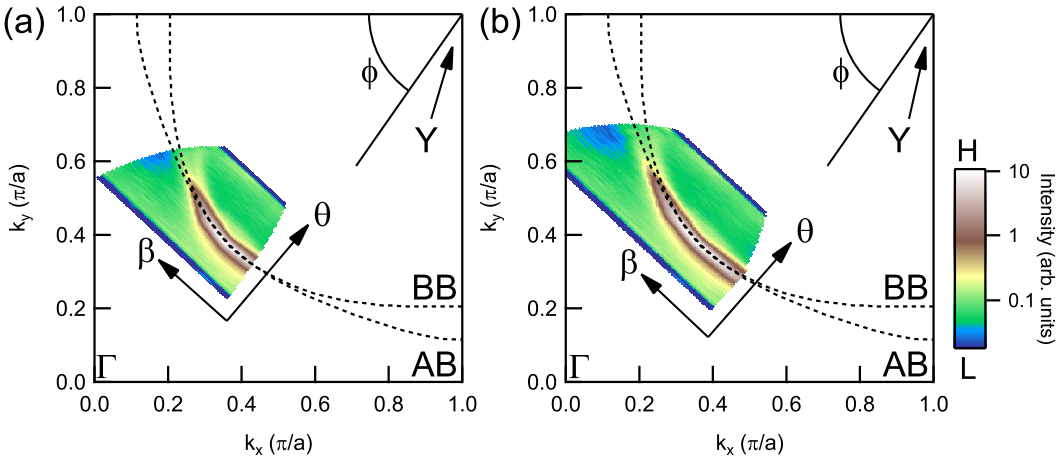

Figure 3.18. Momentum-space maps of equilibrium ARPES intensity at 20 K. The intensity has been integrated across an 18 meV window centered at E_F. The dotted lines correspond to the normal-state Fermi surface of the bonding band (BB) and antibonding band (AB) in optimally doped Bi2212, as distilled from a number of synchrotron measurements.[71,210,211,212] **(a)** No contact potential correction. **(b)** Contact potential correction with all values of β multiplied by 1.3.

the Brillouin zone diagonal are well-matched to the synchrotron Fermi surface, it is clear in Fig. 3.18(a) that the measured Fermi surface deviates from the true value toward the Brillouin zone face in a way that cannot be fixed by uniformly adjusting the work function parameter. However, multiplying all β values by 1.3 before converting from angle-space to k-space results in the map displayed in Fig. 3.18(b), which is in very good agreement with the synchrotron Fermi surface. Simulation results based on the model described in the previous section indicate that 1.3 is a reasonable stretching parameter, which arises from fact that the sample in this particular case is not quite aligned to the center of rotation for β. As a result, the probe beam traced a path from the bottom of the sample to the top of the sample as β was rotated.

Measurements of the superconducting gap for the corrected data in Fig. 3.18(b) confirm the validity of making the contact potential correction: measurements are in close agreement with widely accepted measurements in the literature. Figure 3.19 shows measurements of the superconducting gap characterized by fitting symmetrized EDCs extracted at k_F to Eqs. (2.35). The gray circles and squares respectively show a synchrotron measurement and 7 eV laser ARPES measurement of the superconducting gap for a similarly doped sample of Bi2212.[213]

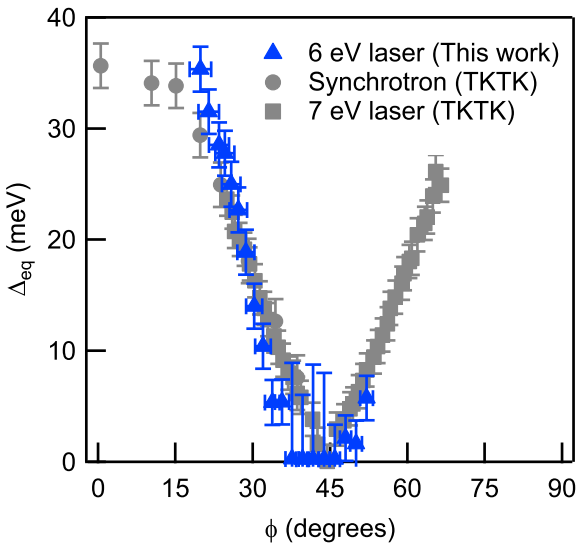

Figure 3.19. Equilibrium low-temperature gap in Bi2212, extracted by fitting symmetrized EDCs to Eqs. (2.35). Blue triangles are extracted from the sample studied in the present work. Gray circles and squares are from Refs. 71 and 213, shown for comparison. The angle ϕ is defined as in Fig. 3.18.

3.9 Sample heating

An important systematic source of uncertainty in time-resolved ARPES pump-induced residual sample heating, which is not detectable with the silicon diode described in Section 3.4.2 due to its localized nature, and which can potentially result in a conflation of pump-fluence-dependent effects with temperature-dependent effects. Bismuth cuprates are particularly sensitive to sample heating because c-axis thermal conductivity is relatively poor compared to other cuprates.[214]

As shown in Fig. 3.20, in the fluence range of 0–15 μJ/cm^2 with a pulse repetition rate of 543 kHz, pump-induced sample heating effects on Bi2212 are not large enough to result in any significant changes in quasiparticle recovery rates. This is important in validating the conclusions of many of the Chapters that follow.

In the limit of higher fluence, pump-induced heating can occur, and can be directly quantified using Fermi edge measurements along the nodal direction at negative delay time. Figure 3.21 shows that sample heating effects are typically restricted to a temperature increase $\Delta T < 20$ K up to a fluence of 21 μJ/cm^2 with a 543 kHz pulse repetition rate. The repetition rate can be lowered to keep heating effects at bay. It may alternatively be possible to reduce heating effects by mechanically establishing direct thermal contact between the puck and the sample's top layer, although we have not yet tested this hypothesis.

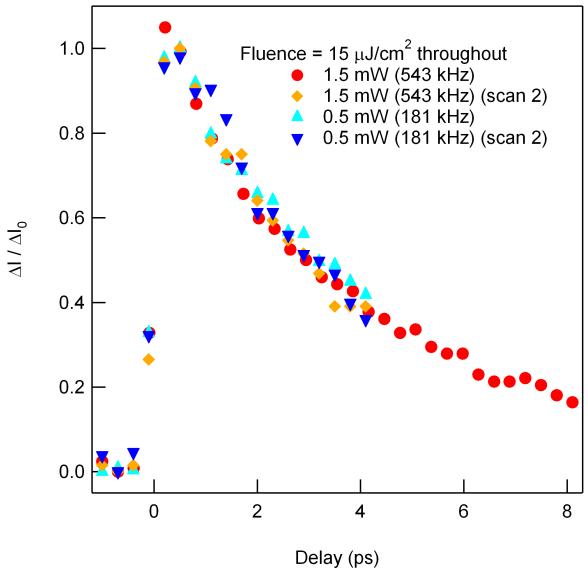

Figure 3.20. Dependence of spectral decay (nodal integrated ARPES intensity change above E_F versus delay) on laser repetition rate. Red circles and orange diamonds correspond to 543 kHz. Blue and cyan triangles correspond to 181 kHz. From Ref. 189.

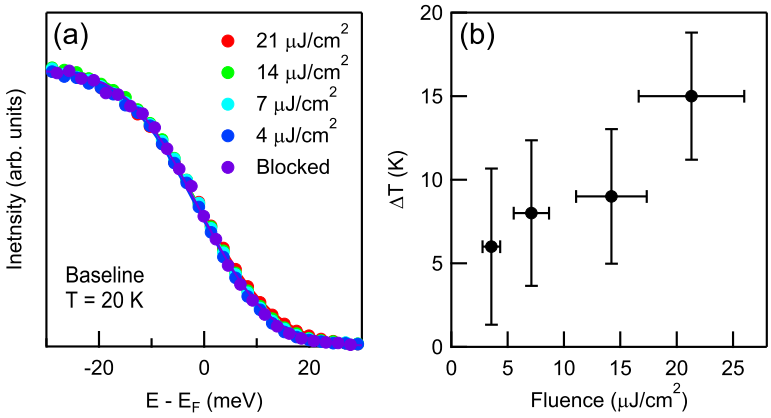

Figure 3.21. Pump-induced heating in Bi2212. **(a)** Fermi-edge width measurements along the nodal direction at negative delay time. The base temperature, when the pump was blocked, was 20 K. Fits correspond to resolution-convolved Fermi functions. **(b)** Residual heating ΔT, obtained by subtracting 20 K from the electronic temperatures extracted from (a).

Chapter 4

Quasiparticle dynamics in $Bi_2Sr_2CaCu_2O_{8+\delta}$ at low fluence

In chapters that follow, we present a series of results where time-resolved ARPES has been specifically used to study the dynamics of the cuprate superconductor $Bi_2Sr_2CaCu_2O_{8+\delta}$ (Bi2212). We begin with a combined time-resolved ARPES and time-resolved reflectivity measurement of the low-fluence (0–15 $\mu J/cm^2$) response of superconducting $Bi_2Sr_2CaCu_2O_{8+\delta}$. We have found under these circumstances that gap and quasiparticle population dynamics reveal marked dependencies on both excitation density and crystal momentum. Close to the *d*-wave nodes, the superconducting gap is sensitive to the pump intensity and Cooper pairs recombine slowly. Far from the nodes pumping affects the gap only weakly and recombination processes are faster. The results demonstrate a new window into the dynamical processes that govern quasiparticle recombination and gap formation in cuprates.

4.1 Introduction

The lifetime of Bogoliubov quasiparticles, the low energy excitations of a superconductor, contains a wealth of information pertinent to the origin of superconductivity in a given material.[32] This lifetime reflects two distinct processes: quasiparticle scattering and recombination. In the former, a quasiparticle scatters from one momentum state to another, conserving the fermionic particle number. Recombination, on the other hand, refers to interactions in which two quasiparticles annihilate. To conserve energy and momentum, recombination must involve emission of other excitations, for example phonons or magnons, to which the quasiparticles are strongly coupled. Measurement of quasiparticle recombination rates as a

function of their energy and momentum can, in principle, provide direct information about the interactions that induce Cooper pairing and superconductivity.[215] Only very recently, with the demonstration that angle-resolved photoemission spectroscopy (ARPES) can be performed with ultrashort laser pulse sources,[154,159,187,188,176,177,216] have measurements with the necessary energy, momentum, and time resolution become possible. We present the results of experiments that use synchronized laser pulses to perform time-resolved ARPES measurements of quasiparticle recombination and gap dynamics in the high-temperature superconductor $Bi_2Sr_2CaCu_2O_{8+\delta}$.

Time-resolved ARPES measurements were performed at 18 K on an optimally doped sample with a critical temperature (T_c) of 91 K. A transient state is created with an infrared laser pump pulse ($h\nu = 1.48$ eV) and measured via photoemission shortly thereafter, with a temporal resolution of 300 fs, using an ultraviolet probe pulse ($h\nu = 5.9$ eV). The experiment benefits from high momentum and energy resolution (0.003 Å^{-1} and 23 meV, respectively) and the ability to explore low pump fluences (2-15 $\mu\text{J/cm}^2$). Time-resolved reflectivity experiments were also performed using the same laser system as the ARPES experiment, also operating at a repetition rate of 543 kHz. Both pump and probe pulses were infrared and were focused onto a 54 μm spot on the sample. The pump delay was modulated using a rapid scan delay line operating at 20 Hz, with the pump amplitude modulated by a photo-elastic modulator (PEM) operating at 100 kHz. The reflected probe beam was detected by a silicon photodiode, which was output to a lock-in amplifier referenced to the PEM modulation.

Measurements were performed on different cleaves of the same sample, comprising four data sets. The data corresponding to a Fermi surface angle of $\phi = 27°$ in Figs. 2, 3, and 4 are from the first cleave. The data corresponding to $\phi = 32°$, $\phi = 38°$, and $\phi = 45°$ (cut 5) in Figs. 2, 3, and 4 are from the second cleave. The data corresponding to $\phi = 31°$ and $\phi = 45°$ (cut 6) in Figs. 1, 3, and 4 are from the third cleave. The time-resolved reflectivity data are from the fourth cleave.

4.2 Dispersion effects

Figure 4.1 shows typical equilibrium and transient ARPES dispersions ($t = -1$ ps and $t = 0.6$ ps respectively) for cuts along nodal and off-nodal directions in k-space. Here the time origin $t = 0$ coincides with the application of the pump pulse. The off-nodal cut has an equilibrium gap of 15 meV. In both cuts a well-defined kink (marked by arrows in panels (A-B) and (F-G))[43,122] separates sharply defined coherent dispersive features from poorly defined incoherent features, as also visible in the selected energy distribution curves (EDCs) shown in panels (D) and (I). The following changes are evident in the transient spectra: 1) a decrease of intensity below the Fermi level (E_F) and slight broadening in the coherent spectra (panels (C-E), and (H-J)), similar to a previous report for nodal quasiparticles[187] and mainly confined below the kink binding energies;[43,122] 2) an overall transfer of spectral weight across E_F (panels (C), (E), (H), and (J)), indicating the creation of transient quasiparticles; and

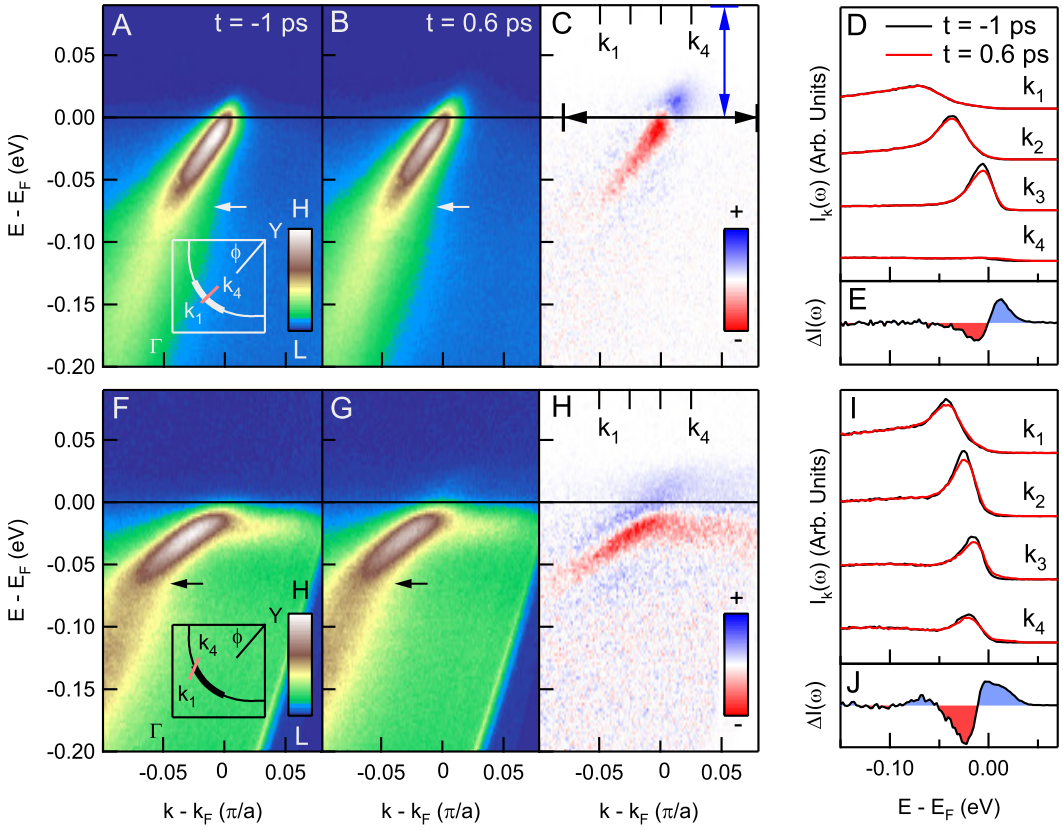

Figure 4.1. Typical ARPES dispersions before and after pumping for nodal ($\phi = 45°$) and gapped ($\phi = 31°$) regions of k-space. The incident pump fluence was 5 μJ/cm^2. **(A)** Equilibrium ($t = -1$ ps) and **(B)** transient ($t = 0.6$ ps) energy-momentum maps for the nodal state. Data are shown with identical color scales. The inset shows the location of the cut. The arrow marks the position of the dispersion kink. **(C)** Subtraction between (A) and (B). Blue indicates intensity gain, and red indicates intensity loss. **(D)** Energy distribution curves (EDCs) from k_1 to k_4 for equilibrium (in black) and transient (in red) states. EDCs are shifted vertically for ease of comparison. **(E)** Difference between transient and equilibrium EDCs, integrated across the double black arrow in panel (C). **(F–J)** Same as (A–E) but for a gapped (off-nodal) momentum cut. Spectra have been corrected for detector non-linearity. The diagonal line in the lower right portion of (F) and (G) is the edge of the detector. From Ref. 189.

3) a small shift of the spectral peak toward E_F in the off-nodal cut (panels (H) and (I)), indicating a partial closure of the superconducting gap.

4.3 Superconducting gap response

Figure 4.2 shows the temporal evolution of the superconducting gap in response to photoexcitation, as extracted from symmetrized EDCs at k_F, the Fermi wave vector.[52] Panels (A-B) and (C-D) correspond to two representative cuts at $\phi = 32°$ and $\phi = 27°$, respectively, with ϕ defined according to the inset of panel (E). These spectra indicate very different responses of the gap amplitude to photoexcitation for the two cuts. The gap is relatively insensitive to fluences below 5 μJ/cm^2 but 13 μJ/cm^2 induces a clear reduction in size. As shown in panel (E) the gap closer to the node decreases by 55% of its equilibrium magnitude, while the gap at $\phi = 27°$ decreases by only 20%. This may indicate different dynamics inside and outside the Fermi arc, which is reported to end rather abruptly at $\phi = 30°$ for samples of this doping,[112,71] although studies farther from the node are needed. Gap recovery rates are illustrated in Fig. 4.2F, where the curves from panel (E) have been inverted and rescaled by their maximum change. The initial recovery rate is slower for states closer to the node (0.9 ± 0.6 ps^{-1}) than for states farther from the node (1.3 ± 0.6 ps^{-1}), although the difference is within the error bar.

4.4 Quasiparticle dynamics

Figs. 4.3 and 4.4 show quasiparticle recombination dynamics. In this low fluence regime the gap is almost unchanged for most of the recovery process, so quasiparticle recombination is largely decoupled from gap dynamics. Fig. 4.3A–4.3C shows the temporal evolution of the above-E_F spectral change ΔI for representative nodal and off-nodal k-space cuts, where ΔI is defined by the integrated intensity change across the blue and black double arrows in Fig. 4.1C. The spectral change is nearly symmetric above and below E_F in this fluence regime, so we focus on the intensity above E_F because of its superior statistics and smaller background. Faster decay rates occur at higher fluences and off-nodal momenta, an effect which cannot be explained by equilibrium heating (see Section 3.9).

Figure 4.3D summarizes the dependence of quasiparticle recombination on fluence and momentum. The rate γ_0 is defined by fitting the decay curves at short times to the convolution of a Gaussian and decaying exponential.[217,148] In line with Figs. 4.3A–4.3C, two prominent decay rate trends are apparent: 1) fluence dependence, with faster initial decay rates γ_0 occurring at higher fluences; and 2) momentum dependence, with off-nodal decay rates increasing faster with fluence than those at the node. The first trend implies that intrinsic quasiparticle recombination processes are observed.[148,218] The second trend indicates that this recombination occurs more rapidly in off-nodal regions of k-space than

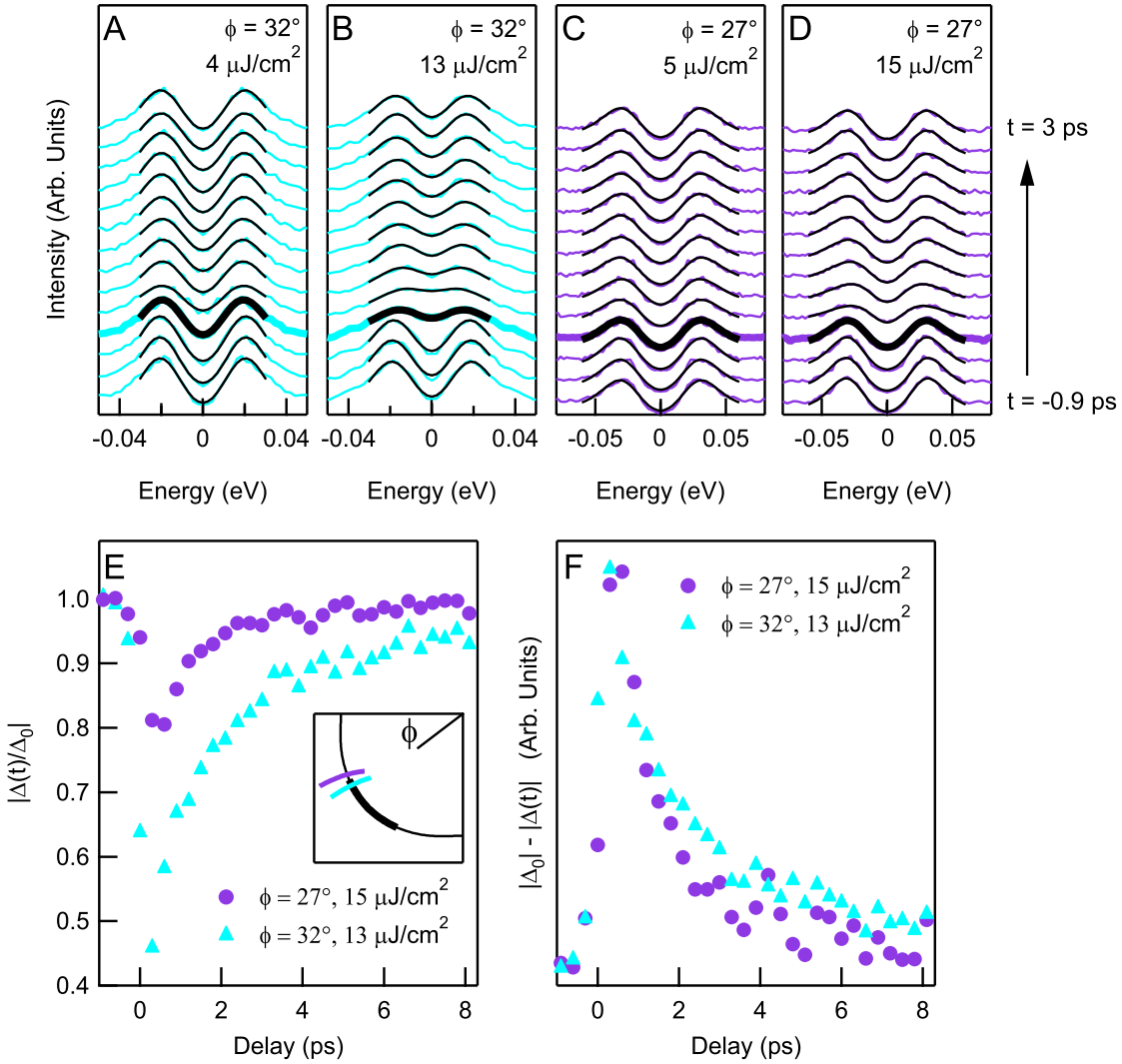

Figure 4.2. Evolution of the superconducting gap following pump excitation. Symmetrized EDCs at k_F for $\phi = 32°$ at low **(A)** and higher **(B)** fluence. The gap is obtained by fitting to a phenomenological model (see Section 2.2.2.3),[52] but can also be approximated by halving the distance between positive and negative peaks. Bold curves correspond to $t = 0$. **(C–D)** Analogous EDCs for a cut at $\phi = 27°$. **(E)** Gap magnitude normalized by its equilibrium value vs. pump-probe delay for momentum cuts at $\phi = 27°$ and $\phi = 32°$. **(F)** Gap magnitude, inverted and normalized by maximal change upon pumping in order to compare recovery rates. From Ref. 189.

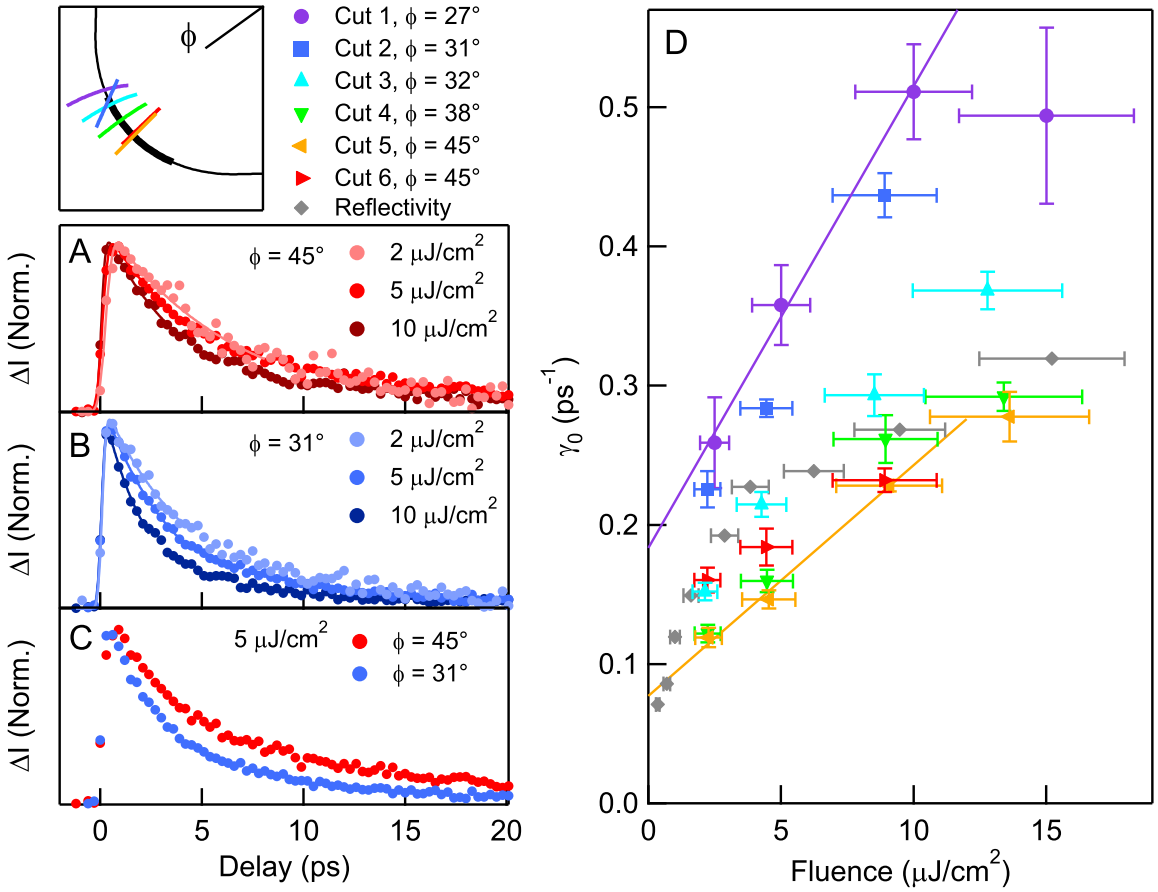

Figure 4.3. Quasiparticle recombination dynamics vs. pump fluence and crystal momentum. ARPES data correspond to intensity change above E_F (ΔI) as integrated between the blue and black double arrows in Fig. 4.1C. Time-resolved reflectivity rates correspond to fractional change in reflectivity. **(A)** Nodal decay curves at 2, 5, and 10 μJ/cm^2, normalized to the same amplitude. **(B)** Analogous off-nodal decay curves ($\phi = 31°$). **(C)** Overlay of nodal and off-nodal curves at the same fluence. **(D)** Initial decay rate γ_0 vs. fluence, obtained by fitting decay curves at short times (for $\Delta I(t) \gtrsim \Delta I_0/2$) to the convolution of a Gaussian and the function $f(t) = \Delta I_0 e^{-\gamma_0(t-t_0)}\Theta(t-t_0)$, where ΔI_0 and t_0 are additional fit parameters. Time-resolved reflectivity rates were multiplied by 3/2 in order to take the finite penetration depth of the optical probe into account (following Section 2.3.1.2). From Ref. 189.

at the node. The fluence dependence is also complementary to ultrafast studies using all-optical techniques, which report a dramatic decay rate fluence dependence, particularly in the low fluence regime,[217,148,219,218,220] and there is overall agreement between the ARPES results and a time-resolved reflectivity measurement taken on the same sample (gray circles in Fig. 4.3D). The decay rate measured by reflectivity is uniformly faster than nodal ARPES decay rates (cuts 5-6), but slower than the off-nodal rates (cuts 1-3), suggesting that optical spectroscopy provides an effective momentum-integrated average of the quasiparticle population. Interestingly, along both $\phi = 27°$ and $\phi = 32°$ directions quasiparticle decay rates are slower than the gap recovery rates in Fig. 4.2: compare 1.3 ± 0.4 ps^{-1} and 0.9 ± 0.6 ps^{-1} for the gap recovery vs. 0.49 ± 0.06 ps^{-1} and 0.37 ± 0.01 ps^{-1} for the intensity recovery. This indicates that the superconducting gap recovers well before the nonequilibrium quasiparticle population drops to zero. A potentially related effect occurs at equilibrium in the BCS model, where the gap becomes large for T only slightly below T_c. Finally, we note that the fluence and momentum dependencies reported here are in contrast to the findings of another time-resolved ARPES work,[188] where the quasiparticle recombination rate was reported to be independent of both fluence and momentum. The discrepancy might be explained by the higher fluences used in the previous work, which likely result in a complete closure of the superconducting gap, or by the coarser momentum and energy resolution compared to the present study.

4.5 Recombination model

As noted above, the fluence dependence of γ_0 means that ARPES decay rates are connected to intrinsic quasiparticle recombination processes. Time-resolved optical measurements indicate that the total (momentum-integrated) population of photoexcited quasiparticles $n_{ex}(t)$ can be described by a bimolecular rate equation,[148,218]

$$\frac{\dot{n}_{ex}}{n_{ex}} = -R\left(n_{ex} + 2n_T\right), \tag{4.1}$$

where R is a quasiparticle recombination constant, and n_T is the population of thermal quasiparticles. As discussed in Section 2.3.1, this is a special case of the Rothwarf-Taylor model of quasiparticle recombination,[147] which has been successfully used to model dynamics of both conventional and high-temperature superconductors.[221,148,219,218,149,222,223,220,224,225,226] The general model also incorporates negative feedback from "hot" bosons ($\hbar\omega \gtrsim 2\Delta$) that are created by the quasiparticle decay process. For low fluence and temperature the model reduces to Eq. 4.1 under both weak feedback and strong feedback (boson bottleneck) scenarios, which beget differing interpretations of the coefficient R.[148,149] In both approximations, however, bimolecular recombination is the active ingredient in fluence-dependent dynamics.

In contrast to time-resolved optics, ARPES measures the momentum-dependent nonequilibrium quasiparticle density $n_k(t)$. The short-time fluence-dependent recombination dynamics are given by

$$\frac{\dot{n}_k}{n_k} \approx -\int R_{kk'}\, n_{k'}\, d^2k', \tag{4.2}$$

where $R_{kk'}$ is a modified recombination coefficient for the interaction between quasiparticles at specific points k and k' in reciprocal space. A weighted average of $R_{kk'}$ over k' is given by $\partial\gamma_0/\partial F$, the rate of increase of the initial decay rate γ_0 with fluence (see Section 2.3.1.3). Figure 4.4 shows an analysis of $\partial\gamma_0/\partial F$ as calculated by fitting straight lines to the data in Fig. 4.3D for fluences $F < 12\ \mu\mathrm{J/cm}^2$. It is clear that $\partial\gamma_0/\partial F$ increases with decreasing Fermi surface angle ϕ, which means that the rate of recombination is enhanced as the quasiparticle momentum moves farther from the node.

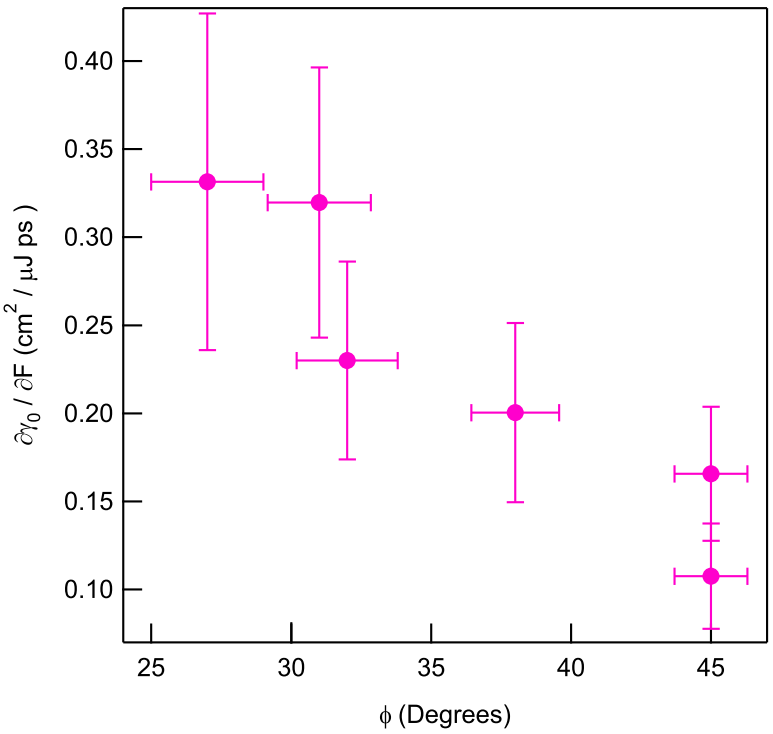

Figure 4.4. Initial rate of increase $\partial\gamma_0/\partial F$ as extracted from straight line fits to the data in Fig. 4.3D for fluence $F < 12\ \mu\mathrm{J/cm}^2$. The horizontal axis corresponds to the Fermi surface angle. From Ref. 189.

One potential scenario for the momentum dependence of the recombination rates is that with increasing distance from the node the quasiparticle energy and momentum approach resonance with charge or spin density wave fluctuations to which the electrons are strongly coupled. For example, a prominent neutron spin resonance is observed in $Bi_2Sr_2CaCu_2O_{8+\delta}$ along the (1,1) momentum vector.[227] Resonance between this mode and a quasiparticle pair would occur at a Fermi surface angle of about 12°, leading to the prediction of a peak in $\partial\gamma_0/\partial F$ at this Fermi surface angle. We believe that demonstrating that recombination can be mapped using time-resolved ARPES and observing its strong momentum dependence will further stimulate development of pulsed sources that are capable of reaching all the relevant regions of momentum space.

Chapter 5

Time- and momentum-resolved gap dynamics in $Bi_2Sr_2CaCu_2O_{8+\delta}$

Perhaps the most direct window into the dynamics of superconductivity can be found by monitoring the dynamics of the gap itself. As we show below, photoexcitation drives superconducting Bi2212 into a nonequilibrium pseudogap state: Near the Brillouin zone diagonal (inside the normal-state Fermi arc), the gap completely closes for a pump fluence beyond $F \approx 15$ μJ/cm^2; toward the Brillouin zone face (outside the Fermi arc), it remains open to at least 24 μJ/cm^2. This strongly anisotropic gap response may indicate multiple competing ordering tendencies in Bi2212. Despite these contrasts, the gap recovers with relatively momentum-independent dynamics at all probed momenta, which shows the persistent influence of superconductivity both inside and outside the Fermi arc.

5.1 Introduction

When a superconductor's electrons bind into Cooper pairs, they leave an energy gap in the electronic band structure that is strongly influenced by the strength, symmetry, and underlying character of the pairing mechanism within a given material.[3] In high-temperature cuprate superconductors the pairing mechanism remains a matter of considerable debate, and there has been great interest in characterizing the details of both the superconducting gap and the possibly related pseudogap. This latter gap exists in hole-doped cuprates at low carrier concentration near the Brillouin zone faces even above the superconducting critical temperature (T_c),[228,79,80] and leaves perplexing ungapped "Fermi arcs" near the Brillouin zone diagonals.[93]

Several experimental studies have reported evidence that the superconducting gap and

pseudogap are manifestations of intertwined yet separate charge ordering tendencies. For example, momentum-dependent gap measurements using angle-resolved photoemission spectroscopy (ARPES) indicate that the gap near the Brillouin zone face not only remains open above T_c, but exhibits peculiar structure at low and high temperature that is hard to explain in the context of superconductivity alone.[112,113,114] Specific evidence for a competing order, in the form of charge-density-wave stripes, has long been known to exist in $La_{2-x}Sr_xCuO_4$ and related lanthanum 214 compounds.[95,96,97,98,99,100,101] More recently, nuclear magnetic resonance[102] and x-ray scattering studies[103,104] have revealed that a charge density wave directly competes with superconductivity in underdoped $YBa_2Cu_3O_{6+x}$.

Here we use time-resolved ARPES to measure gap dynamics following the destruction of superconductivity by an ultrafast near-infrared laser pulse in nearly optimally doped Bi2212 (T_c = 91 K). The study expands upon previous time-resolved ARPES works on cuprates[154,187,188,189,229,230] and measurements in the previous chapters by providing gap measurements at a larger range of fluences than has previously been presented, by exploring a range of momentum space extending definitively beyond the normal-state Fermi arc, and by employing more advanced methods to characterize the nonequilibrium gap.

We report three primary findings. First, photoexcitation using a fluence (average optical energy deposited on a surface per unit area) greater than 15 μJ/cm^2 unambiguously drives the closure of the near-nodal gap, with a response time of 300–600 fs. Because the gap is a direct manifestation of the superconducting order parameter, this result constitutes one of the most detailed characterizations to date of a nonequilibrium phase transition involving the destruction of superconductivity. Second, we find significant momentum-dependent differences in gap sensitivity to photoexcitation: although the gap completely closes near the Brillouin zone diagonal, it remains open near the Brillouin zone face, establishing a transient pseudogap. Such momentum-dependent differences support the existence of two (or more) competing orders in the cuprates. Finally, we characterize gap recovery rates. In spite of the nonequilibrium gap shift's amplitude variation, recovery rates throughout the probed crystal momentum range are nearly momentum-independent. Thus, even in the presence of a competing-order scenario, the findings indicate that superconductivity continues to have a large influence on gap dynamics both inside and outside the Fermi arc region.

5.2 Experimental details

Data were acquired deep in the superconducting state at an equilibrium temperature of $T < 20$ K, measured using a silicon diode placed in thermal contact with the sample. The laser repetition rate was set to 543 kHz, ensuring that residual heating caused by the pump pulse was less than 20 K. We corrected for detector nonlinearity following the prescription of Ref. 190. Samples were grown using the traveling solvent floating zone method, and measured to be near optimal doping (T_c = 91 K). In all cases, samples were cleaved in situ in a vacuum chamber maintained at pressures below 5×10^{-11} Torr.

There is currently no established consensus on how best to characterize the nonequilib-

rium gap. At equilibrium, the band gap appears as a feature in the single-particle spectral function, $A(\mathbf{k},\omega)$, which is given in general terms by the sum of two constituent parts, $A^-(\mathbf{k},\omega)$ and $A^+(\mathbf{k},\omega)$, corresponding to electron removal and electron addition. ARPES measures only $A^-(\mathbf{k},\omega)$ because electrons are extracted from the sample rather than added to it.[i] Progress in analyzing the gap can be achieved using the identity[231]

$$A^-(\mathbf{k},\omega) = A(\mathbf{k},\omega)f(\omega), \tag{5.1}$$

which relates $A^-(\mathbf{k},\omega)$ to $A(\mathbf{k},\omega)$ through the Fermi-Dirac distribution function.

Out of equilibrium, $A^-(\mathbf{k},\omega)$ can be rigorously extended into the time-dependent form $A^-(\mathbf{k},\omega,t)$, provided that finite-duration pump and probe pulses are incorporated into the spectral function definition.[232] The relationship between $A^-(\mathbf{k},\omega,t)$ and the nonequilibrium gap is more complicated than a simple extension of Eq. 5.1 because the theoretical concept of temperature may no longer be well-defined.[233,157] Nevertheless, strategies borrowed from analyses commonly used at equilibrium can still provide insight. In the following, we characterize the nonequilibrium gap in superconducting Bi2212 following two complementary techniques: (i) dividing the data by a Fermi-Dirac distribution function corresponding to an assumed electronic temperature $T_e(t)$, and (ii) symmetrizing time-dependent energy distribution curves (EDCs: ARPES intensity at fixed momentum) at the Fermi wave vector (k_F). Gap characterization using EDC symmetrization, which can be analyzed with smaller statistical uncertainty than the Fermi division analysis, is then carried out to extract detailed fluence and momentum-dependent gap recovery dynamics.

5.3 Fermiology: Fermi-division analysis

To divide by an effective Fermi function, one must first extract a transient electronic temperature $T_e(t)$. This may be done by examining time-resolved spectra through a k-space cut intersecting one of the superconducting gap nodes, which occur along the Brillouin zone diagonals. As shown in Fig. 5.1, we fit momentum-integrated EDCs for a cut along the Γ–Y direction to the equation

$$I(E) = \left[\frac{C_0 + C_1(E-\mu_e)}{\exp\left(\frac{E-\mu_e}{k_B T_e}\right)+1} + C_2 + C_3 E\right] * R(E), \tag{5.2}$$

where T_e and μ_e are fit parameters, k_B is Boltzmann's constant, R is a Gaussian resolution function of FWHM = 23 meV, and the asterisk denotes convolution. The constants C_0, C_1, C_2, and C_3 allow the fit to account for an inelastic scattering background, for density-of-states variation, and for a linear background above E_F caused by higher-order photoemission processes and spurious camera noise.

[i] Inverse photoemission apparatuses exist, but at the time of this writing the energy resolutions of such systems exceed the magnitude of the superconducting gap in the cuprates, and no inverse photoemission experiment incorporates time-resolution.

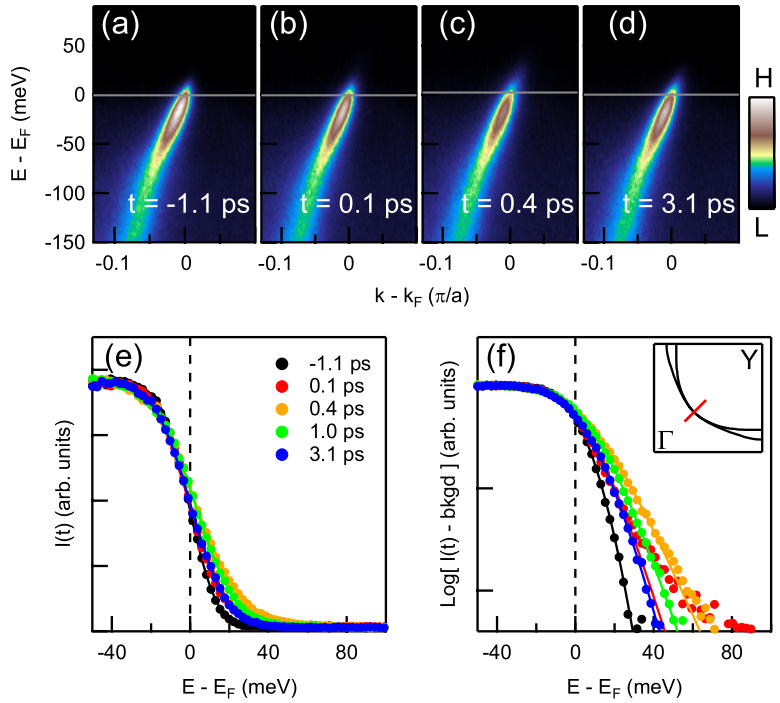

Figure 5.1. Nodal quasiparticle relaxation dynamics, characterized using a T_e and μ_e model. **(a)–(d)** Nodal time-resolved ARPES spectra at selected delay times. **(e)** Momentum-integrated EDCs (obtained by horizontally integrating the intensity for the spectra displayed in (a)–(d)) along with Fermi function fits at selected delay times. Solid curves are the result of fitting to Eq. (5.2). **(f)** Same data as in (e), but with the linear background above E_F subtracted off, and displayed on a logarithmic scale to clarify the dynamics of quasiparticles far above the Fermi energy. From Ref. 235.

As already noted above, such an analysis requires an underlying assumption of a uniformly established electronic temperature, which must ultimately break down in Bi2212 for quasiparticles to be allowed to coherently oscillate with phonons (as may become visible in the high-fluence limit),[234] or to recombine with different rates at different points in k-space.[189] However, there is precedent in the scientific literature for using a Fermi function to approximate the nonequilibrium distribution function in the cuprates,[154,187] and a Fermi fit experimentally matches transient quasiparticles at the node with reasonable accuracy. Fig. 5.1 shows that although the fits and the data do not quite agree at the shortest times, they come into better agreement after 300 fs.

Along with the increase in T_e, there is also a slight pump-induced increase[230] in the effective chemical potential μ_e (see the leading-edge shift between the data corresponding to $t = -1.1$ ps and $t = 1$ ps in Fig. 5.1(e)). Further characterization of the band structure reveals that this is a rigid upward shift in the entire band, which may be caused by a transient change in the sample work function, by pump-induced space charge, or by the fact[135] that an asymmetric density of states across E_F can result in a mismatch between μ_e and $E_F = \lim_{T\to 0}[\mu(T)]$. The shift is small compared to the gap size and dynamics; it remains less than 4 meV for a fluence of 30 μJ/cm^2, and vanishes to about 0.5 meV when

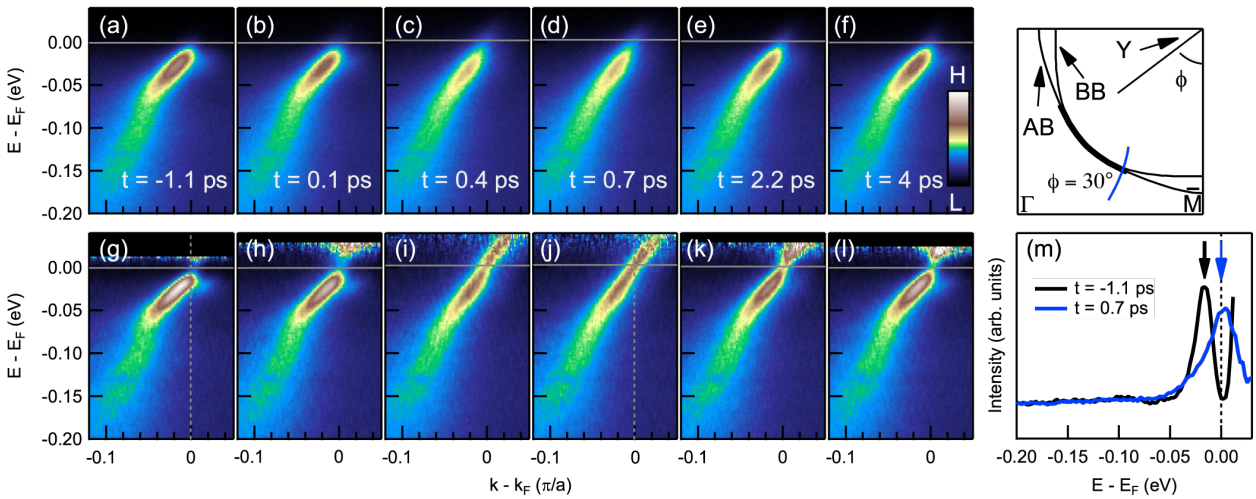

Figure 5.2. Near-nodal superconducting gap response to photoexcitation at a fluence of 23 μJ/cm^2 and an equilibrium temperature $T \ll T_c$. **(a)–(f)** Direct time-resolved ARPES intensity maps. **(g)–(l)** Intensity maps after applying a deconvolution procedure to remove the effect of the experimental resolution,[144,142] and dividing by an effective Fermi function. **(m)** EDCs at k_F extracted from panels (g) and (j). From Ref. 235.

the fluence is reduced to 4 μJ/cm^2. None of the results reported here are affected by the shift.

Figures 5.2 and 5.3 show the results of the Fermi division analysis on two gapped cuts, corresponding respectively to $\phi = 30°$ and $\phi = 21°$ (ϕ is defined from the Y point in k-space relative to Y–$\bar{M}$ as shown in the Fermi surface schematics). Prior to dividing by the Fermi function, the data have also been numerically deconvolved along the energy dimension[ii] to mitigate the impact of finite energy resolution. The equilibrium data, shown in Figs. 5.2(a), 5.2(g), and 5.3(a), exhibit several characteristic cuprate features, most prominently a gap magnitude that steadily increases between Brillouin zone diagonal and Brillouin zone face,[68] but also a well-defined dispersion kink at 70 meV that results from electron-boson coupling.[43] Distinct bilayer bonding bands (BB) and anti-bonding bands (AB)[236,237,211] are resolved in Fig. 5.3(a).

Nonequilibrium dynamics reveal that an infrared pump pulse of sufficiently high fluence dramatically affects the gap. As shown in Fig. 5.2, photoexcitation forces the near-nodal gap to completely close. This can be seen both in the dispersion map shown in Fig. 5.2(j), and in the comparison between equilibrium and transient EDCs shown in Fig. 5.2(m). The response of the gap accompanies a weakening of the 70 meV bosonic kink (compare panels (c) and (d) with panel (a)), which is discussed elsewhere.[238] Interestingly, the data also reveal that there is a slight delay between the application of the pump pulse and when the gap is maximally

[ii]Specifically, we applied 10 iterations of the Lucy-Richardson deconvolution algorithm.[144,142] Deconvolution was less effective when fewer than 10 iterations were used. Noise-induced artifacts became more prominent when more iterations were used.

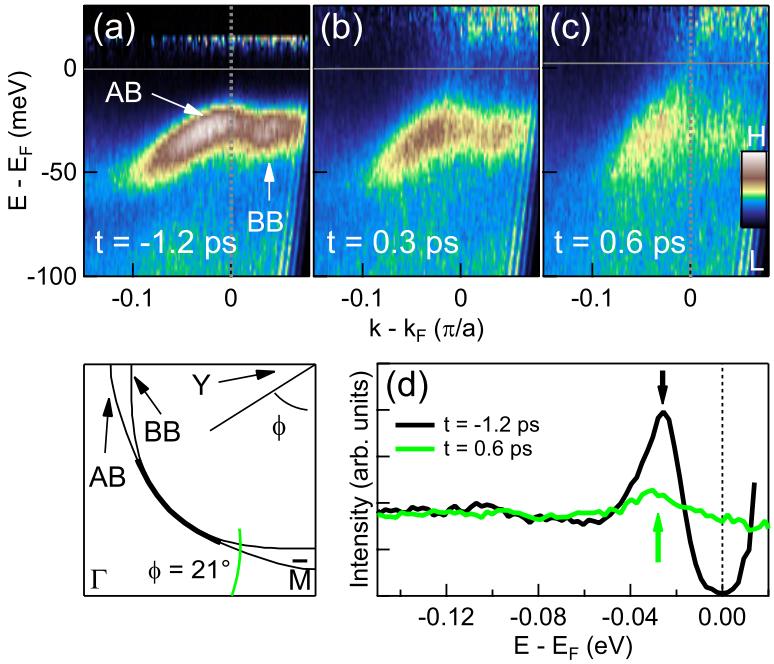

Figure 5.3. Far-off-nodal superconducting gap response to photoexcitation at a fluence of 24 μJ/cm^2 and an equilibrium temperature $T \ll T_c$. As in Fig. 5.2(g)–(l), the data have been subjected to a deconvolution procedure[144,142] and divided by an effective Fermi function. **(a)** Equilibrium spectrum. The magnitude of the energy gap is about 27 meV. Bilayer bonding bands (BB) and anti-bonding bands (AB) are visible. **(b)** and **(c)** Transient spectra. **(d)** EDCs from panels (a) and (c) at the AB Fermi wave vector (k_F).

altered from its equilibrium state. After $t = 2$ ps the gap reopens and the spectra begin to resemble those at equilibrium once again.

Figure 5.3 shows a cut far from the node ($\phi = 21°$) and reveals that the gap response is highly anisotropic. As with the near-nodal response, photoexcitation induces an increased ARPES intensity at the Fermi level, the response time is slightly delayed relative to the arrival of the pump pulse, and the dynamics are accompanied by a temporary weakening of the 70 meV bosonic kink. However, the magnitude of the far-off-nodal gap, as reflected by the peak position of the lower Bogoliubov band, is only slightly shifted (see panels (c) and (d)). As a result, the far-off-nodal gap response is more aptly characterized as filling in rather than closing.

Such dynamics could reflect a scenario where the far-off-nodal gap reflects a spatially integrated response of two coexisting forms of charge order, for example superconductivity and a competing pseudogap ordering tendency. Given that superconductivity is destroyed more easily by photoexcitation than the pseudogap, one would expect the superconducting component of the far-off-nodal gap to completely close in response to photoexcitation at 25 μJ/cm^2. The pseudogap, meanwhile, remains open at the same fluence, and the resulting sum of the two signals would be a gap that appears to fill rather than to close. Even if the far-off-nodal gap is exclusively governed by one ordering tendency, the fact that it fills rather

than closes indicates that the origin of the far-off-nodal gap may be fundamentally distinct from the origin of the near-nodal gap. A gap that fills without closing is characteristic of order being destroyed through phase fluctuations, for example, whereas a gap that closes is characteristic of the dynamics within a mean-field approximation like the Bardeen-Cooper-Schrieffer (BCS) model.[52]

5.4 Fermiology: Symmetrized EDC analysis

The results are expanded with a more detailed momentum dependence of the gap in Fig. 5.4, where EDCs at the AB Fermi wave vector (k_F) from several momentum cuts have been symmetrized.[52,189] The symmetrization procedure replaces the assumptions of a thermal analysis with an assumption of local particle-hole symmetry, and does not require line shape deconvolution,[52] complementing the Fermi-division analysis.

Interestingly, the threshold between the dynamics of the near-nodal gap, which completely closes, and the far-off-nodal gap, which does not, occurs at $\phi = 28°$. This coincides with the momentum marking the end of the normal-state Fermi arc for optimally doped Bi2212 when T is slightly greater than T_c (based on synchrotron measurements[71] as well as equilibrium measurements taken using the present setup). Inside the Fermi arc (at $\phi = 32°$ and $\phi = 29°$), the gap is fully closed by a fluence of 24 μJ/cm^2, as can be seen in the false-color symmetrized EDC intensity plots in Fig. 5.4(b)–5.4(c). The gap magnitude is less affected for cuts beyond the end of the Fermi arc ($\phi = 26°$, $\phi = 23°$, and $\phi = 21°$) at the same fluence. As shown in Fig. 5.4(d)–5.4(f), the gap remains open at all delay times although, as in Fig. 5.3(d) and 5.3(e), there is an increased intensity at the Fermi level. Such findings broadly support a coexisting-order scenario in the cuprates,[112,71,239,114] with the gap near the Brillouin zone diagonals predominantly reflecting superconductivity, and the gap near the Brillouin zone faces reflecting a distinct pseudogap order or combination of the pseudogap with superconductivity. As in Figs. 5.2(m) and 5.3(d), the failure of the gap to completely close far away from the node is accompanied by an evolution from a gap that closes in response to photoexcitation to a gap that instead fills in. Figure 5.4(g)–5.4(h) shows selected symmetrized EDCs from cuts inside and outside the Fermi arc, which particularly highlight this difference.

We note that in the present study fluences beyond 25 μJ/cm^2 are not explored, and it is likely that the antinodal gap may be destroyed in addition to the near-nodal gap at even higher fluences.

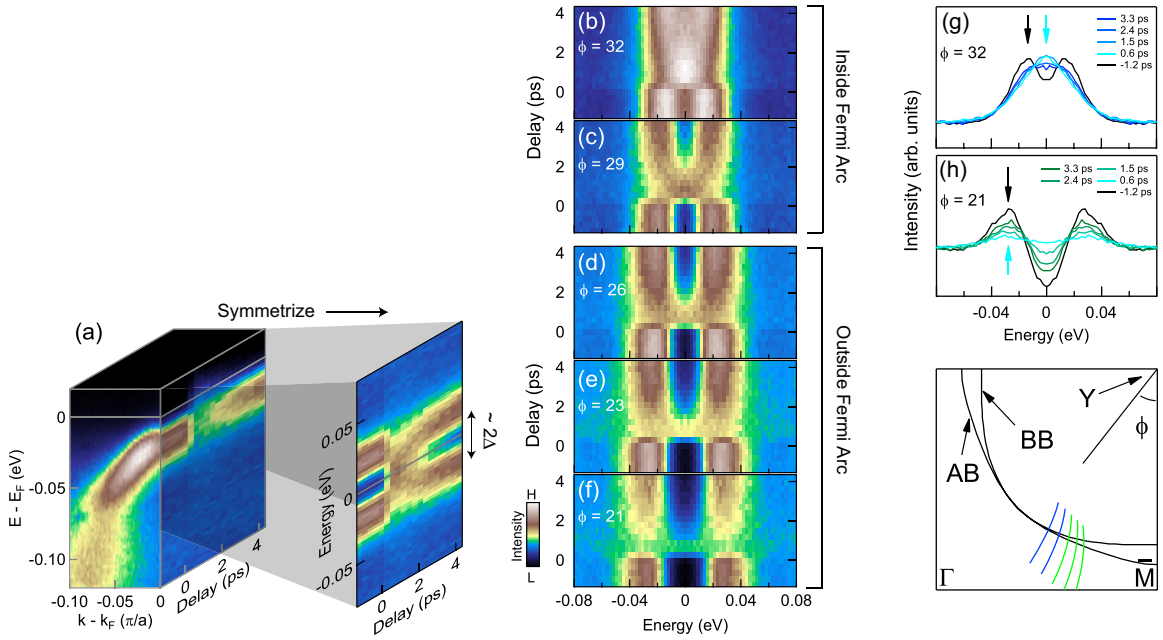

Figure 5.4. Momentum dependence of the transient superconducting gap for a pump fluence of 24 μJ/cm^2 and $T \ll T_c$, as analyzed using symmetrized energy distribution curves (EDCs). **(a)** Measurements are characterized based on EDCs at the AB Fermi wave vector (k_F), which are then symmetrized about the Fermi level to remove the effect of the electronic occupation function.[52,189] **(b)**–**(f)** False-color intensity plots of symmetrized EDC spectral weight versus energy and delay time. **(g)**–**(h)** EDCs at selected times for a representative near-nodal (g) and far-off-nodal (h) momentum cut. The black and cyan arrows highlight respective peak positions at $t = -1.2$ ps and $t = 0.6$ ps.

5.5 Quantitative dynamics

5.5.1 Near-nodal gap

In Fig. 5.5 we show the fluence dependence of the near-nodal nonequilibrium gap. The delayed gap closure noted above is especially visible here and occurs at all fluences: the gap magnitude does not drop to its minimum until 300–600 fs after the application of the pump pulse. A similar dynamic occurs in the nonequilibrium quasiparticle population,[189,229] and it is likely that the delays in the two phenomena are causally connected. Theoretical models of nonequilibrium superconductivity[240,241] predict that an increased quasiparticle population should result in a decreased gap size if it helps the system's overall free energy achieve a minimum. To characterize the gap quantitatively, we fit the data displayed in Fig. 5.5(a)–5.5(d) to the convolution of a Gaussian resolution function and the equation[52]

$$I(\omega) = C_1|\omega| + \frac{C_2\Gamma}{(\omega - \Delta_k^2/\omega)^2 + \Gamma^2}, \tag{5.3}$$

where $\Delta_k(t)$ corresponds to the energy of the gap, $\Gamma(t)$ corresponds to the peak width, and the leading term is added to account for the effects of an incoherent background. Figure 5.5(e) shows the trends in $\Delta_k(t)$, where it is clear that increasing the fluence beyond 15 μJ/cm^2 forces the near-nodal gap to completely close at 0.7 ps, in line with Figs. 5.2–5.4. The closure is closely affiliated with the destruction of superconductivity, and we note that the critical fluence here reported is in good agreement with an infrared pump and terahertz probe transmissivity study reporting that a fluence of 11 μJ/cm^2 results in a 90 percent loss of superfluid density.[242] Features near 15 μJ/cm^2 have also been reported in the initial photoexcited quasiparticle population of optimally doped and underdoped samples of Bi2212.[229]

In Fig. 5.5(f) we characterize the fluence dependence of the near-nodal nonequilibrium gap recovery rate. The gap recovery dynamics in Bi2212 are non-exponential. However, meaningful trends in gap dynamics as a function of fluence and momentum can be extracted from the instantaneous gap recovery rate $\gamma_\Delta(t) \equiv \dot{\Delta}(t)/(\Delta(t) - \Delta_{eq})$, which can be obtained from exponential fits within short time intervals. We extract γ_Δ by fitting $\Delta(t)$ to the function

$$\frac{\Delta(t)}{\Delta_{eq}} = 1 - A_0\, e^{-\gamma_\Delta (t - t_{\rm ref})} \tag{5.4}$$

between 2–4 ps, 4–6 ps, and 6–10 ps, as shown in Fig. 5.5(f). Such time intervals are chosen to be large enough to minimize statistical noise yet still small enough to return a reasonable goodness of fit. In this equation, γ_Δ is the decay rate and A_0 is an amplitude defined at the freely selected time $t_{\rm ref}$. The recovery rate of the near-nodal gap is faster at higher fluences and shorter delay times. These trends originate from a density-dependent response of the quasiparticle decay rate,[148,189] as well as from the aforementioned causal relationship between quasiparticle population and gap size, which is expected to be nonlinear. (At equilibrium, for example, the gap responds to the quasiparticle population according to the BCS gap equation.)

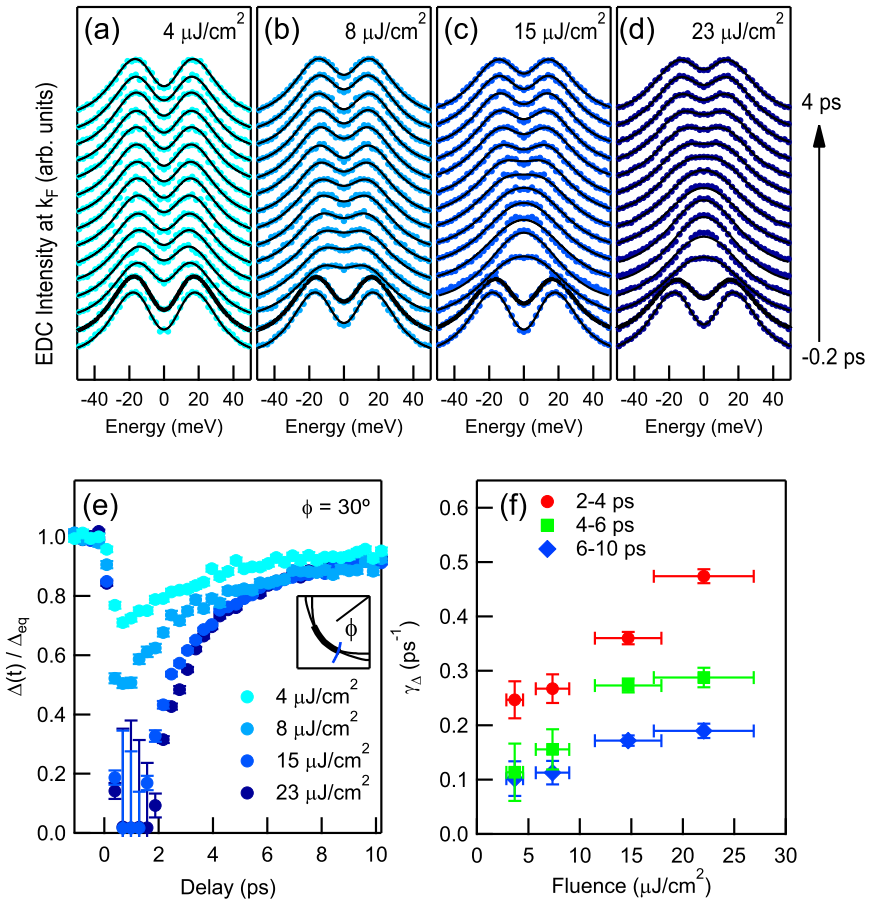

Figure 5.5. Fluence dependence of nonequilibrium gap dynamics inside the Fermi arc. **(a)**–**(d)** Symmetrized EDCs at k_F and fit curves based on Eq. (5.3), for a gapped k-space cut at $\phi = 30°$ and $T = 18$ K ($T \ll T_c$). Bold curves correspond to $t = 0$ ps. **(e)** Normalized gap magnitude versus pump-probe delay. **(f)** Gap recovery rates γ_Δ, extracted by fitting the data in (e) to Eq. (5.4) between 2–4 ps, 4–6 ps, and 6–10 ps.

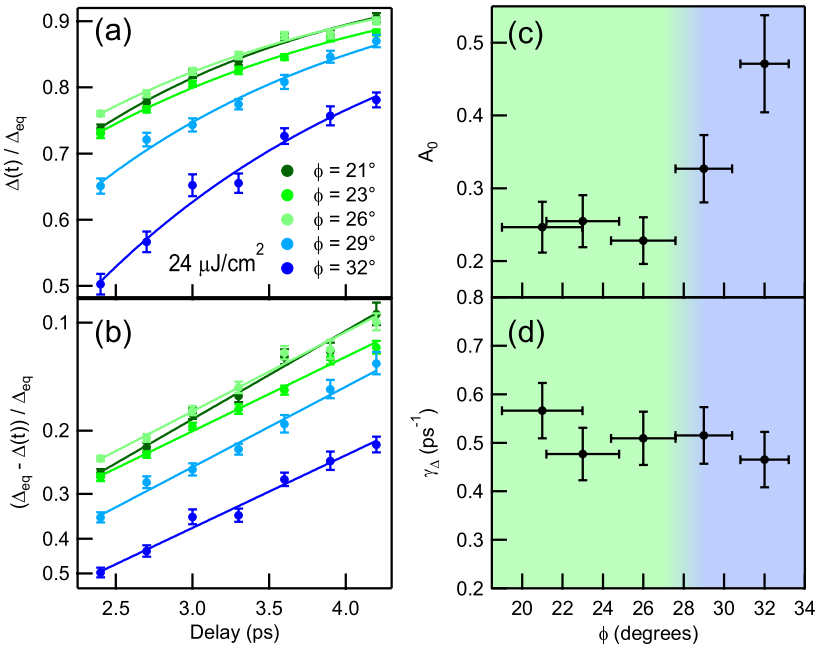

Figure 5.6. Momentum dependence of the nonequilibrium gap with a pump fluence of 24 μJ/cm^2. **(a)** Normalized gap magnitude vs. delay, and fits using Eq. (5.4), where fits are extracted between 2.5 and 4 ps. **(b)** Data and fits from (a), shown on a logarithmic scale to highlight recovery rates. **(c)** Amplitudes (A_0) and **(d)** recovery rates (γ_Δ) corresponding to the gap magnitude shifts characterized in (a) and (b). A_0 is extracted at $t_{\text{ref}} \equiv 2.5$ ps.

5.5.2 Momentum dependent gap

Figure 5.6 shows an analysis of the momentum dependence of gap recovery rates between 2.4 and 4.2 ps for a fluence of 24 μJ/cm^2, where γ_Δ is extracted from the data in Fig. 5.4 using Eqs. (5.3) and (5.4). The distinction between a gap that completely closes inside the Fermi arc and one that remains open outside the Fermi arc is clear in the amplitude dependence of the Eq. 5.4 fit parameter A_0: as shown in Fig. 5.6(c), at 2.5 ps the gap measurements at $\phi = 32°$ and $\phi = 29°$ are suppressed by 47% and 33% of their equilibrium values, respectively, while the gap measurements at $\phi = 26°$, $\phi = 23°$ and $\phi = 21°$ are only suppressed by 20–25% of their equilibrium values. However, as shown in Figs. 5.6(b) and 5.6(d), the nonequilibrium gap recovers with picosecond-scale dynamics at all probed momenta, and is independent of crystal momentum to within our uncertainty.

Figure 5.7 shows a characterization of gap rates as a simultaneous function of momentum and fluence. Recovery rates far outside the Fermi arc are more difficult to characterize than those close to the node because of the very small gap amplitude shift. However, it is clear that the far-off-nodal gap recovery rate increases with increasing fluence just as it does close to the node, and near-nodal and far-off-nodal gap recovery rates are consistent with each other at all fluences. Previously, we reported a possible gap recovery rate dependence on momentum at low fluence, though the uncertainty in recovery rates was larger than the recovery rate difference.[189] The present study disconfirms a general trend of momentum-

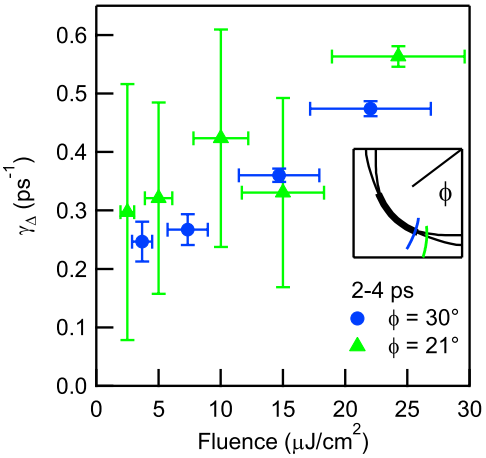

Figure 5.7. Fluence-dependent gap recovery rates for a representative cut inside ($\phi = 30°$) and outside ($\phi = 21°$) the normal-state Fermi arc. Fits are extracted between 2 and 4 ps.

dependent gap dynamics as the pump fluence is increased to higher values. These recovery rates should not be confused, however, with the dynamics of the quasiparticle population, where the recovery rates are clearly momentum-dependent.[189]

The uniformity in the gap recovery rates across the end of the normal-state Fermi arc is a puzzle, but could be explained by indications from studies using time-resolved reflectivity and transmissivity that the pseudogap state may recover as much as 10 times faster than superconductivity in Bi2212,[243,244,245] and by the fact that the magnitude of the pseudogap is largely unaffected by pumping in this fluence regime (i.e., the fractional gap magnitude shift outside the Fermi arc is small). Under these circumstances, distinct superconducting and pseudogap order parameters influence the equilibrium gap, but superconductivity dominates the gap dynamics. A cartoon depiction of the scenario is shown in Fig. 5.8, where the magnitude shift of the order parameters corresponding to the superconducting gap and a potentially competing pseudogap order (for example, a charge density wave) are displayed as a function of delay time. If superconductivity is more strongly affected by pumping than the competing order, then the signal due to superconductivity will dominate at even short times. At longer times the signal due to the competing order will be completely undetectable due to its faster recovery rate. Such a two-order-parameter scenario is generally in agreement with equilibrium ARPES measurements reporting two distinct gaps in the cuprates if the crossover between a nodal superconducting gap and anti-nodal pseudogap occurs smoothly in k-space,[71] if both superconducting and pseudogap phenomena appear on equal footing at the antinode,[114] or if superconducting and pseudogap order parameters coexist at all momenta but are spatially separated in real space.

Momentum-independent γ_Δ values are also consistent with an alternate scenario suggested by gap studies using scanning tunneling spectroscopy, which postulates that the pseudogap just beyond the end of the Fermi arc is not the result of a competing order at all, but is rather a manifestation of phase-incoherent superconductivity.[246] Though phase competition is still predicted to exist, the onset of the competing order appears not at the

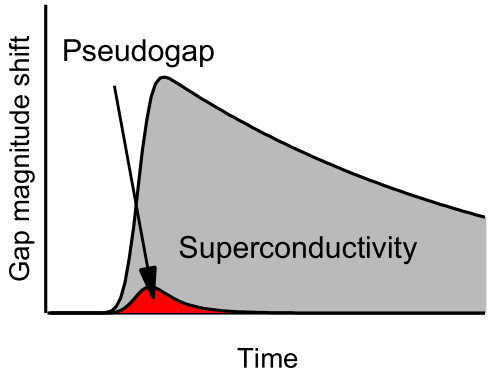

Figure 5.8. Cartoon illustration of a possible mechanism for the relatively invariant gap recovery rate. If the component of the gap magnitude corresponding to superconductivity responds more strongly to photoexcitation than the component corresponding to the pseudogap, signatures of the latter signal may be washed out by the former signal.

end of the Fermi arc, but across the intersection of the normal-state Fermi surface with the antiferromagnetic zone boundary.[247] This intersection is beyond the present study's range of accessible momenta, but would be interesting to probe using time-resolved ARPES in future studies at higher probe photon energy. Regardless of the details, it is clear under both this and the previous scenario that superconductivity plays an important role in influencing quasiparticle dynamics both inside and outside the end of the Fermi arc.

Finally, the momentum-independent gap recovery rates could indicate that thermalization between quasiparticles at different momenta occurs rapidly in the high fluence regime. The gap recovery at all momenta would be governed by a common thermal order parameter under this scenario, which gains support from the fact that the distribution of nonequilibrium quasiparticles along the node resembles a thermal distribution to a significant extent for $t > 300$ fs, and the success with which gap dynamics can be extracted given the quasi-thermal analysis employed in Figs. 5.1–5.3. However, we note that it is hard to reconcile thermal dynamics with the fluence and momentum dependencies previously reported in Bi2212 at lower fluence.[189]

5.6 Conclusions

In conclusion, we have established that infrared photoexcitation using a pump fluence beyond 15 μJ/cm^2 definitively closes the superconducting gap near the Brillouin zone diagonals, that the gap remains open beyond the end of the normal-state Fermi arc up to at least 25 μJ/cm^2, and that the gap recovers with nearly momentum-independent dynamics out to a Fermi surface angle of $\phi = 21°$ with recovery timescales on the order of picoseconds. We note that temporal onset dynamics associated with the complete quenching of the near-nodal gap provide an important benchmark for comparison with the optically induced destruction

of other forms of order in strongly correlated materials, including magnetism[248] and charge-density-wave order.[176] Beyond this, the results presented in this study have implications in the study of competing interactions in the cuprates more generally. For example, in demonstrating that photoexcitation induces a transient pseudogap, the results both add to a mounting set of experiments conducted at equilibrium supporting the existence of multiple competing phases in the cuprates, and they provide a complementary reference for ultrafast studies reporting evidence of the pseudogap in the nonequilibrium change in optical reflectivity. We hope that the dynamics and recovery trends here reported will stimulate many further discussions in the growing field of ultrafast phenomena in correlated systems.

Chapter 6

Quasiparticle dynamics in $Bi_2Sr_2CaCu_2O_{8+\delta}$ at high fluence

As increasingly powerful pump beams are applied in a time-resolved experiment, gap and quasiparticle dynamics become more intermingled. This has led to considerable interest regarding the role that the two phenomena play in relation to each other, and has prompted many questions about the degree to which signatures of the pseudogap might show up in the quasiparticle relaxation rate. In the chapter that follows, we present results of time- and angle-resolved photoemission to measure gap and quasiparticle relaxation dynamics of $Bi_2Sr_2CaCu_2O_{8+\delta}$ across the vaporization threshold for superconductivity. Whereas low-fluence measurements of quasiparticle relaxation reveal a smoothly recovering picosecond dynamics, a sharply defined femtosecond quasiparticle relaxation component emerges when the pump fluence is sufficient to close the near-nodal superconducting gap. Analyses of this connection suggest that superconducting gap dynamics dramatically influence quasiparticle relaxation rates. Intriguingly, there is no detectable connection between the fast component and the pseudogap, which dominates many features of the band structure in the normal state.

6.1 Introduction

Time-resolved reflectivity and transmissivity experiments on cuprates have revealed several differences—not apparent at equilibrium—between the dynamics of the superconducting state and those of the pseudogap state occurring at higher temperatures. Below the superconducting critical temperature (T_c) the optical response following an infrared pump pulse decays smoothly with picosecond-scale dynamics that depend on quasiparticle den-

sity, suggesting the recombination of Cooper pairs.[148,218] In the pseudogap state the signal often changes sign (depending on the pump and probe frequencies) and the recovery rate dramatically increases,[249,148,243] losing almost all population density dependence.[244] When the sample temperature is maintained below T_c and the pump intensity is increased to high values, both the pseudogap and superconducting signals become visible in the same recovery curves,[249,243,222] and recent reports have argued that these two components may even simultaneously coexist, resulting from competing charge ordering tendencies in the cuprates.[243,244,245]

In this letter, we present a complement to these studies in the form of a time- and angle-resolved photoemission (time-resolved ARPES) study of relaxation dynamics in the cuprate superconductor $Bi_2Sr_2CaCu_2O_{8+\delta}$ (Bi2212). For pump fluences exceeding the superconducting vaporization threshold, a distinctive two-component relaxation dynamic emerges, with well-defined femtosecond and picosecond recovery scales. Although in many ways the behavior resembles the findings of comparable-fluence optical studies, we show by a detailed doping and momentum dependence of recombination dynamics that—at least in this particular case—the fast component is largely *not* associated with the pseudogap. Instead, it can be understood as a consequence of dynamical changes in the superconducting gap magnitude, in the form of changing phase space restrictions on quasiparticle relaxation, and in the form of an altered recombination cross section as superconductivity is restored. Doping-dependent analyses of both components reveal that electron-boson coupling strength in Bi2212 monotonically decreases with increased hole doping, which complements and constrains the findings reported using equilibrium ARPES.[43,213] Perhaps more importantly, the results raise important questions about the origin of the pseudogap in cuprates, and how it may be connected to ultrafast optical measurements.

The experimental apparatus is as described in Ref. 190, and utilizes optical pump pulses of wavelength 836 nm ($h\nu$ = 1.48 eV) and probe pulses of wavelength 209 nm ($h\nu$ = 5.93 eV). Energy, momentum, and time resolutions are 23 meV, 0.003 Å^{-1}, and 300 fs. The pump pulse induces a time-dependent but uniform energy shift in the electronic spectrum ($\leq$ 4 meV),[235] which we have corrected before performing subsequent analyses. We have also corrected detector nonlinearity effects.[190]

6.2 Correlations between quasiparticles and the superconducting gap

We begin with a fluence-dependent analysis of correlations between quasiparticle recombination dynamics and the superconducting gap for an optimally doped sample (T_c = 91 K). Figure 6.1 shows two cuts through k-space, at $\phi = 45°$ and $\phi = 30°$ (ϕ is defined from the Y point relative to Y–$\bar{M}$ as in the panel (a) inset). The cut at $\phi = 45°$ intersects a d-wave-symmetric gap node, where quasiparticle dynamics are naturally disentangled from gap dynamics (because of the gap's absence along this direction), and can be characterized with

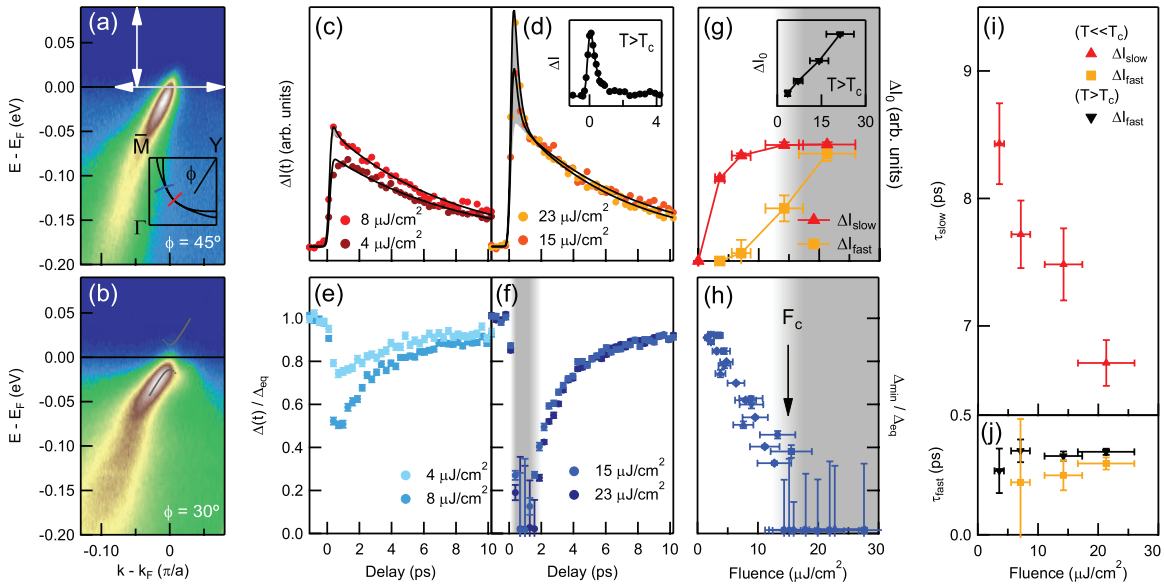

Figure 6.1. Evolution of the electronic band gap and nonequilibrium quasiparticle population in superconducting Bi2212 ($T_c = 91$ K) following a high-fluence ultrafast pump pulse. **(a)**–**(b)** Representative ARPES dispersions ($t = -1.1$ ps) for cuts at $\phi = 30°$ and $\phi = 45°$ (see panel (a) k-space schematic). **(c)**–**(d)** Nodal quasiparticle population $\Delta I(t)$, obtained by integrating ARPES intensity between the white double arrows in (a). Main panel shows data for $T \ll T_c$. Inset shows data at 23 μJ/cm^2 for $T = 100$ K ($T > T_c$). **(e)**–**(f)** Normalized gap from the cut at $\phi = 30°$, extracted by fitting symmetrized energy distribution curves at the anti-bonding band Fermi wave vector (k_F) to a broadened BCS line shape.[52] **(g)** Amplitudes $\Delta I_{0\,slow}$ and $\Delta I_{0\,fast}$, from fits to the data in (c) and (d) as described in the text. **(h)** Minimal gap from (e) and (f), versus fluence. **(i)**–**(j)** Time constants τ_{slow} and τ_{fast}, from fits to the data in (c) and (d) as described in the text.

high signal-to-noise (Figs. 6.1(c) and 6.1(d)) by integrating spectral intensity change across a large window in energy and momentum (white double arrows in Fig. 6.1(a)). Concomitant gap dynamics (Figs. 6.1(e) and 6.1(f)) are extracted using EDC symmetrization[52,189,235] from the cut at $\phi = 30°$, which has an equilibrium gap size of 14 meV (see Fig. 6.1(b)). Consistent with previous measurements,[189] at lower fluence the gap magnitude is suppressed but always finite, and the population of nonequilibrium quasiparticles decays with picosecond dynamics. As shown in Figs. 6.1(d), 6.1(f), and 6.1(h), however, beyond a critical fluence $F_c \approx 15\ \mu\text{J/cm}^2$ (defined as the fluence necessary to close the near-nodal gap), a sharp femtosecond relaxation dynamic emerges in the quasiparticle population response. The dynamic is also coupled to the near-nodal gap temporally, appearing most prominently when the gap is closed ($t < 1.5$ ps, see shaded gray regions in Figs. 6.1(d) and 6.1(f)).

Figures 6.1(g), 6.1(i), and 6.1(j) show a more detailed analysis of the quasiparticle recovery spectra, where fast and slow component amplitudes and time constants are extracted by fitting to the convolution of a Gaussian of FWHM = 300 fs and the bi-exponential decay function

$$\Delta I(t) = \Theta(t - t_0) \left[C_{fast} e^{-(t-t_0)/\tau_{fast}} + C_{slow} e^{-(t-t_0)/\tau_{slow}} \right] \tag{6.1}$$

with fit parameters τ_{fast}, τ_{slow}, C_{fast}, C_{slow}, and t_0. The quantities ΔI_{0fast} and $\Delta I_{0\,slow}$, shown in Fig. 6.1(g), correspond to the fit's resolution-convolved amplitude components. For the measurement at 4 μJ/cm^2 (where the fast component was not detected) we constrained $C_{fast} = 0$. We also measured the above-T_c response (see Fig. 6.1(g) inset), fitting to single-exponential curves and constraining $t < 0.6$ ps because C_{slow} was not apparent.

Overall, the picosecond-scale quasiparticle recovery component exhibits a variety of trends that establish a close connection to the dynamics of superconductivity. For example, it appears only in the low-temperature data, and τ_{slow} decreases with fluence,[189] as expected of quasiparticles reentering a superconducting condensate following rules of second-order kinetics.[148,218,189] The amplitude $\Delta I_{0\,slow}$ also increases rapidly with fluence in the low-fluence limit yet appears to saturate above F_c, which makes sense because the density of quasiparticles decaying into the superconducting state should not be allowed to be larger than the equilibrium superfluid density. By contrast, the femtosecond quasiparticle recovery component exhibits very different behavior. At low temperature, ΔI_{0fast} is suppressed or absent at low fluence, and only becomes substantial for $F > F_c$. At high temperature (above T_c), femtosecond dynamics dominate over all other relaxation processes. At all temperatures, the recovery timescales τ_{fast} either exhibit no detectable fluence dependence or (perhaps) even follow the opposite trend with increasing fluence as τ_{slow}.

6.3 Momentum- and energy-dependent trends

Figure 6.2 shows quasiparticle relaxation dynamics, resolved in both energy and momentum, for momentum cuts at $\phi = 26°$ (outside the pseudogap-state Fermi arc), $\phi = 37°$ (inside

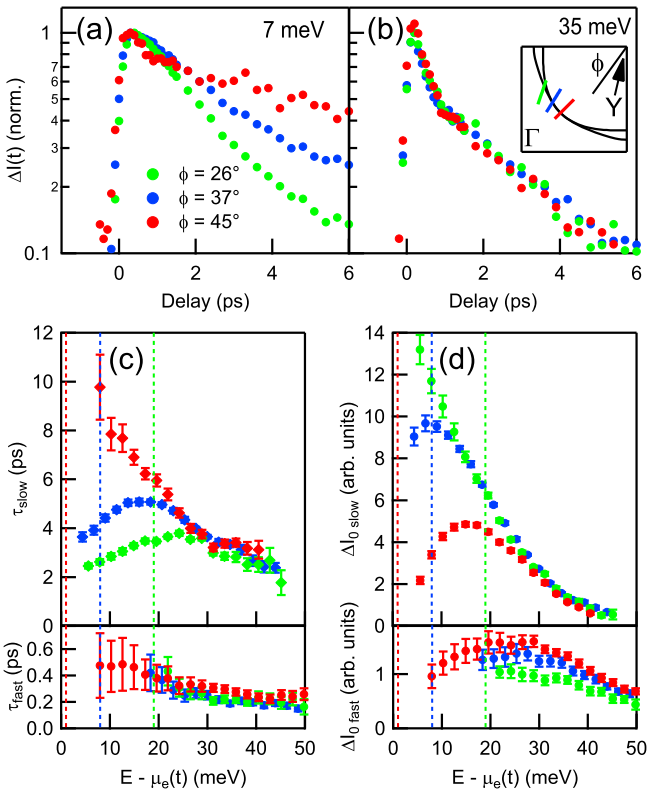

Figure 6.2. Energy and momentum dependence of quasiparticle recombination dynamics in optimally doped Bi2212 (25 μJ/cm^2 pump fluence, $T \ll T_c$, $T_c = 91$ K). **(a)** Energy-resolved ARPES intensity change $\Delta I_\omega(t)$, momentum-integrated between $|k - k_F| < 0.08\ \pi$/a (see horizontal lines in Fig. 6.1(b)), for nodal, off-nodal, and far-off-nodal cuts, at two representative energies above E_F. **(b–c)** Energy-resolved quasiparticle relaxation time constants and amplitudes. The red, blue, and green vertical dashed lines mark the gap edge at $\phi = 45°$, $\phi = 37°$, and $\phi = 26°$.

the pseudogap-state Fermi arc), and $\phi = 45°$ (the node), for a fluence of 25 μJ/cm^2 (above F_c). Such an analysis takes advantage of the full power of time-resolved ARPES, and notably demonstrates that two-component relaxation dynamics appear throughout a large portion of the Brillouin zone. As clear from Fig. 6.2(a), τ_{slow} decays more rapidly away from the node than it does at the node, in agreement with previous energy-integrated measurements at lower fluence.[189] Momentum variations in τ_{slow}[189] become largest as energies approach the superconducting gap edge, as shown in Fig. 6.2(c). This establishes further connections between superconductivity and the slow component, as low-energy quasiparticles necessarily interact more strongly with the many-body ground state than do their higher-energy counterparts.[3]

Though it is tempting, based on Fig. 6.1, to associate the fast component with a competing electronic order, Fig. 6.2 shows that the momentum- and energy-dependent trends in ΔI_{0fast} are directly at odds with the momentum dependence of the pseudogap, which is is finite for the cut at $\phi = 26°$ but absent in the cuts closer to the node. As shown in Figs. 6.2(a) and 6.2(b), off-nodal femtosecond relaxation components are visible only at

higher energies. In part, this reflects the fact that the low-energy off-nodal quasiparticle relaxation signature is overshadowed by the dynamics of the nonequilibrium gap. Even above the superconducting gap edge, however, τ_{fast} exhibits no discernible momentum dependence within experimental error (Fig. 6.2(c)), and the energy-dependent amplitudes ΔI_{0fast} do not appear to increase near the Brillouin face (Fig. 6.2(d)). Rather, they may even tend to decrease, though it is difficult to quantitatively compare quasiparticle population amplitudes among different momentum cuts.

6.4 Doping dependence

Stronger evidence differentiating the fast component from the physics of the pseudogap occurs in the doping dependence of quasiparticle relaxation. Figure 6.3 shows an analysis of nodal quasiparticle relaxation dynamics at comparable excitation densities (≈ 24 μJ/cm^2) for four different dopings of Bi2212, corresponding to critical temperatures $T_c = 78$ K (underdoped, UD78K), $T_c = 91$ K (nearly optimally doped, OP91K), $T_c = 78$ K (overdoped, OD78K), and $T_c = 59$ K (very overdoped, OD59K). For the first three dopings, both equi-

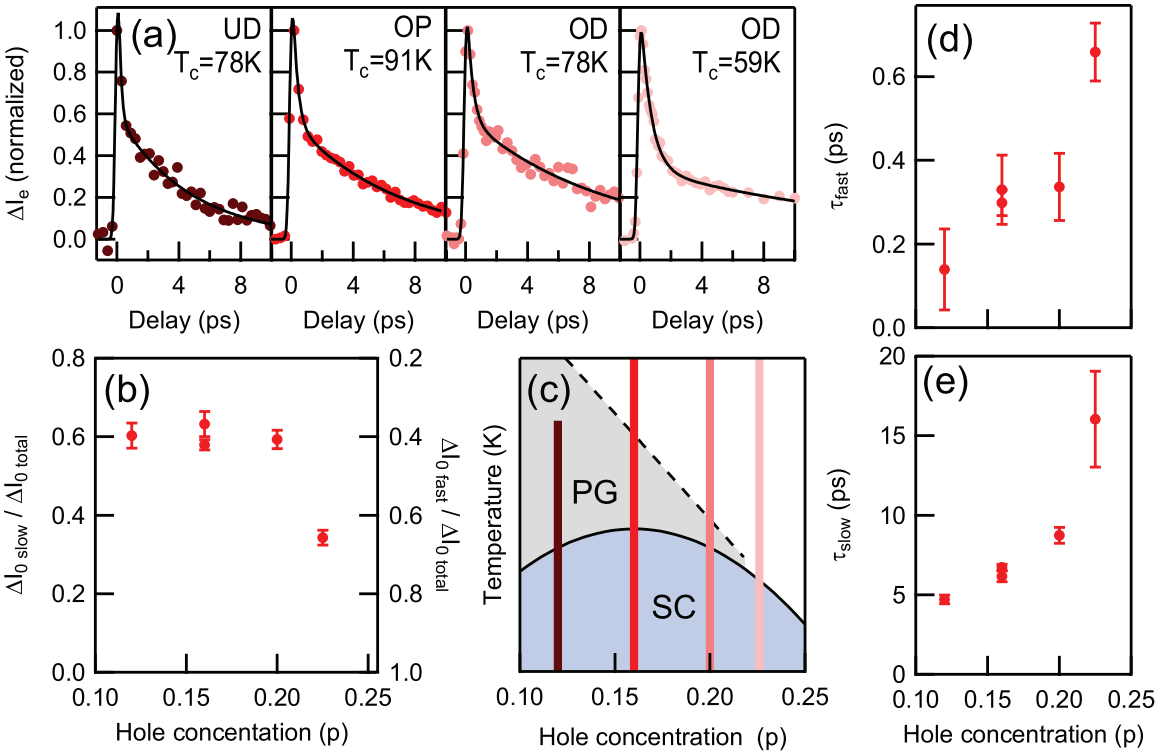

Figure 6.3. Doping dependence of quasiparticle recovery. **(a)** Nodal quasiparticle response curves, extracted as in Fig. 6.1. The fits are bi-exponential decay functions (Eq. 6.1). **(b)** Amplitude component ratios $\Delta I_{0\,slow}/(\Delta I_{0\,slow} + \Delta I_{0\,fast})$ from the fits in (a). **(c)** Bi2212 phase diagram. **(d–e)** Time constants from the fits in (a).

librium ARPES[83,73] and time-resolved ARPES[229] measurements have previously identified

distinct transition temperatures T_c and T^* for the onset of superconductivity and the pseudogap. The OD59K sample has no equilibrium pseudogap.[83,73] In spite of these differences, two-component recovery dynamics prominently appear in the time-resolved nodal quasiparticle relaxation dynamics for all four dopings (see Fig. 6.3(a)). In fact, the amplitude of the fast component for the quasiparticle relaxation in the OD59K sample is larger—by a factor of more than 1.5—than it is for the three samples of lesser doping (see Fig. 6.3(b)).

6.5 Discussion

Having ruled out the pseudogap as the primary origin of the fast component, the question remains, what mechanism does explain the onset of two-component dynamics? Insight can be gleaned from a further comparison between the component amplitudes and the equilibrium phase diagram. As can be seen in Fig. 6.3(b) and 6.3(c), while the slow-component amplitude ratios bear little relation to T^*, they do match reasonably well against the doping dependence of T_c. They match better yet against doping-dependent measurements of the equilibrium near-nodal gap magnitude, which is reported to drop off precipitously for hole concentrations $p > 0.19$ but to remain largely independent of doping for hole concentrations $0.076 < p < 0.19$.[73] We argue that the most plausible explanation for the onset of two-component dynamics is that quasiparticle relaxation dynamics are directly affected by changes in the underlying band structure that occur as the system relaxes back toward equilibrium.

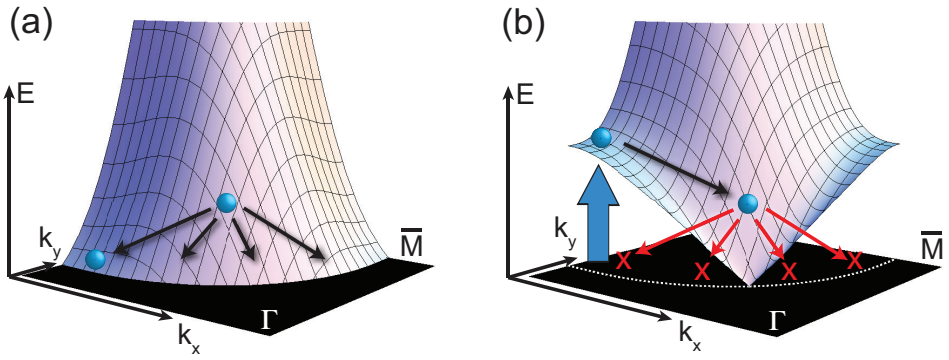

Figure 6.4. Cartoon illustration of the impact of a *d*-wave gap on quasiparticle scattering. **(a)** Scattering channels in the normal state. **(b)** Scattering channels in the superconducting state. Quasiparticle population depletion rates at low energy are additionally affected by the dynamics of antinodal states (block arrow).

Specifically, three dynamical mechanisms related to the opening of the superconducting gap are simultaneously at play. First, the opening of a gap dramatically reduces the amount of available phase space near the Fermi level. As shown by the black arrows in Fig. 6.4(a), a quasiparticle in metallic Bi2212 can relax by many channels, with a final-state phase-space density roughly proportional to the product of the Fermi surface area and the quasiparticle energy. In the presence of a *d*-wave gap, however, states near the Brillouin zone face are

transferred to higher energies, and scattering rates for lower-energy states will be sharply curtailed, as shown by the red arrows in Fig. 6.4(b). For a quasiparticle residing along the nodal direction at 15 meV in optimally doped Bi2212 ($\Delta_0 \approx 35$ meV), for example, the gap imposes an almost 80-percent phase-space reduction for relaxation via scattering (particle-conserving) interactions[i]. Momentum-conservation requirements may additionally reduce the available scattering channels,[250,251,148] although Bi2212 is highly disordered,[252] so such rules may not strictly apply.

Second, because the gap opens in the midst of the quasiparticle relaxation process, decaying quasiparticles are systematically lifted from lower energies back to higher energies on a picosecond timescale. The overall effect counterbalances quasiparticle relaxation, as illustrated by the block arrow in Fig. 6.4(b). While the effect will occur most dramatically at the Brillouin zone face, nodal and near-nodal states are also impacted because the lifting of antinodal quasiparticles from lower energies to higher energies opens a scattering channel for these quasiparticles to relax back into the nodal and near-nodal states (Fig. 6.4(b), black arrow).

Third, there is likely to be a fundamental change in electron-boson coupling matrix elements in the presence as opposed to the absence of superconductivity. The superconducting state is macroscopically coherent—with indeterminate electron occupation—muddling the impact of charge in quasiparticle scattering events. Thus, while bimolecular recombination processes are relevant to quasiparticle relaxation in both a superconductor and normal metal (in a normal metal or semiconductor, electrons recombine with holes), the recombination cross section below T_c is likely to be reduced because of a reduced Coulomb attraction.

For all of the above mechanisms both the fast and slow components encode information about electron-boson coupling at a fundamental level, and in consequence, the timescales of both effects (not just the fast component, as previously asserted[154]), can potentially be used to glean information about superconductivity. This assertion is borne out by the data. Figures 6.3(d) and 6.3(e) display time constants for the fast and slow components of the nodal quasiparticle relaxation data displayed in Fig. 6.3(a). The trends for both decay rates are in qualitative agreement with those reported for the strength of the renormalization effects in the low-energy electronic dispersion reported by equilibrium ARPES measurements,[213] and they indicate an electron-boson coupling constant that monotonically decreases with increased hole-doping.

Finally, we return in closing to the apparent contradiction between the findings of the present thesis, and an increasing number of recent works claiming to report evidence for the pseudogap in the form of time-resolved reflectivity and transmissivity data. The present study highlights the need for caution in using timescales alone to support ultrafast signatures of coexistence or competition between superconductivity and the pseudogap, but we note that some of the optical reports have reported intriguing evidence that the pseudogap may exhibit a distinct optical phase signature from that of normal-state relaxation. The ques-

[i] The d-wave gap is estimated near the node as $\Delta_k(\phi) \approx v_{gap}(\phi - 45)\pi/180$, where ϕ is the Fermi surface angle defined in the main text. Assuming a cylindrical Fermi surface, the fraction of final-state phase space (states between 0 and E) relative to ungapped final-state phase space is then given by E/v_{gap}, where E is the quasiparticle initial-state energy and $v_{gap} \approx 66$ meV/radian is estimated from the literature.[213]

tions naturally arise, can time-resolved ARPES detect a femtosecond pseudogap response of any sort that is distinct from thermal relaxation? If not, what do we make of the fact that equilibrium ARPES, as well as several other types of experiments, claim that the pseudogap corresponds to the onset of a competing electronic order that results in a gap, and yet the opening of this gap has little to no impact on relaxation rates? These questions may be important to answer in the development of a coherent unified theory of high-temperature superconductivity. We note that there does appear to be one time-resolved ARPES signature of the pseudogap, in the form of an abrupt 20-percent increase in the initially excited quasiparticle population at fixed pump fluence when the temperature is decreased below T^*.[229] Since pseudogap effects are expected to be strongest at $\bar{M}$-point, further time- and momentum-resolved studies of quasiparticle relaxation in Bi2212 at very large momenta, which are inaccessible in the present study, may provide an important clarification of pseudogap dynamics. Beyond this, a time-resolved ARPES analogue to the phase resolution available using all-optical methods would be greatly desired.

Chapter 7

Nonequilibrium cuprate phase diagram

Finally, we have used time- and angle-resolved photoemission to measure the nodal nonequilibrium electronic states in various dopings of $Bi_2Sr_2CaCu_2O_{8+\delta}$. As we show below, we find that the initial pump-induced transient signal of these ungapped states is strongly affected by the onset of the superconducting gap at T_c, superconducting pairing fluctuations at T_p, and the pseudogap at T^*. Moreover, T_p marks a suggestive threshold in the fluence-dependent transient signal, with the appearance of a critical fluence below T_p that corresponds to the energy required to break apart all Cooper pairs. These results challenge the notion of a nodal-antinodal dichotomy in cuprate superconductors by establishing a new link between nodal quasiparticles and the cuprate phase diagram.

7.1 Introduction

Cuprate superconductors are known not only for extraordinarily high critical temperatures, but also for the richness of their phase diagram, where multiple energy scales associated with different electronic orders coexist at low carrier concentration and eventually merge with the critical temperature T_c at higher carrier concentration. The conventionally held wisdom is that antinodal quasiparticles shape this phase diagram.

Indeed, in conventional superconductors the energy gap and the low-energy quasiparticle spectral weight (i.e., the area under the quasiparticle peak) are virtually isotropic around the normal state Fermi surface. In contrast, in high-T_c cuprate superconductors superconductors the gap exhibits four nodes along the Brillouin zone diagonals (nodal direction), and the quasiparticle spectral weight is strongly momentum-dependent.[253] For example, while the

quasiparticle peak in underdoped cuprates exists both above and below T_c along the nodal direction, it only appears below T_c along the antinodal direction.[93] This anisotropic character is assumed to derive from the "d-wave" symmetry of the superconducting state. Because of this sensitivity to T_c, the antinodal quasiparticle excitations have been regarded as carrying the information of superconductivity. In harmony with this notion, it has been shown that the antinodal quasiparticle spectral weight scales with the critical temperature,[254,255,256,257] and recently it has been shown that this same spectral weight is also linked to the onset of the superconducting pair fluctuations at T_p.[258] This dichotomous behavior between nodal and antinodal quasiparticles persists even above the critical temperature, in the so-called pseudogap phase, up to T^*.

Despite their central role in controlling most of the low energy properties of cuprate superconductors, the role of nodal quasiparticles in the superconducting transitions and more generally in shaping the cuprate phase diagram is still unclear and generally considered negligible.[259,260,261,239] This view has been challenged by a time- and angle-resolved photoemission experiment (time-resolved ARPES) showing that nodal quasiparticles also respond to the superconducting transition and their spectral weight scales with the superfluid density[187] and by the report of a nodeless energy gap in a very weakly doped sample.[73]

Here, we use time-resolved ARPES to investigate changes in the nodal electron dynamics across a range of dopings and temperatures in the phase diagram of $Bi_2Sr_2CaCu_2O_{8+\delta}$ (Bi2212). We found that the initial pump-induced nodal quasiparticle population exhibits sharp features reflecting the opening of the pseudogap at T^* and the onset of superconductivity at T_c, as well as an intermediate feature at T_p, between T^* and T_c. Below T_p, fluence-dependent measurements reveal a critical fluence that corresponds to the energy required to break apart all Cooper pairs, suggesting that T_p is the onset temperature below which electrons begin to pair incoherently, and that it is distinct from T^*, which marks the onset of an independent electronic order. To our knowledge, the present work is the first demonstration that all three of these characteristic temperatures affect the dynamics of nodal quasiparticles, and not just the dynamics of antinodal quasiparticles.

7.2 Experiment

Single-crystal samples from four different dopings of Bi2212 were measured: underdoped samples with $T_c = 78$ K (UD78K) and $T_c = 84$ K (UD84K); a nearly optimally doped sample with $T_c = 91$ K (OP91K); and an overdoped sample with $T_c = 84$ K (OD84K). We also measured an overdoped sample of $Bi_{1.7}Pb_{0.4}Sr_{1.6}Cu_2O_{6+\delta}$ (Bi2201) with $T_c = 32$ K. All single crystals were grown by the traveling solvent floating zone method. The underdoped samples were obtained by annealing the optimally doped sample in nitrogen. The overdoped Bi2212 sample was obtained by annealing the optimally doped sample in oxygen. All the samples were cleaved *in situ* in vacuum with a base pressure less than 5×10^{-11} Torr. In the temperature-dependent measurements the samples were cleaved at temperatures at or

above 25 K to minimize the sample surface aging effect caused by degassing of the cryostat when heated around 20 K.

7.3 Quasiparticle dynamics

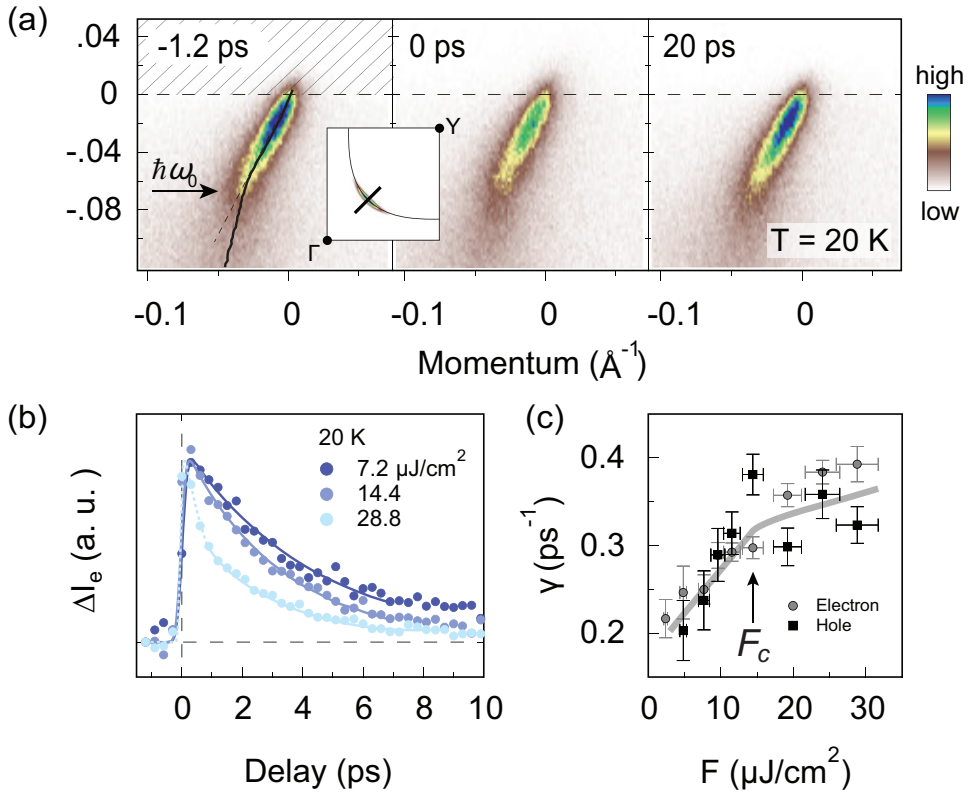

Figure 7.1. Dynamical evolution of time-resolved ARPES spectra along a nodal cut ($\Gamma(0,\ 0)$ – $Y(\pi,\ \pi)$ direction) of underdoped Bi2212 (T_c = 78 K). (a) ARPES dispersions: at delay time -1.2, 0, and 20 ps measured at 20 K with pump fluence 14.4 μJ/cm^2. The black solid curve represents the equilibrium electronic dispersion. (b) Electron-like quasiparticle recombination dynamics for different pump fluences at 20 K. The ΔI_e is obtained by integrating photoemission intensity across the hatched area shown in (a) and then subtracting the integral of the equilibrium intensity. Decay curves are normalized to the same amplitudes. (c) The non-equilibrium quasiparticle decay rate as a function of pump fluence (F) for both electron and hole parts at 20 K. From Ref. 229.

Figure 7.1 shows results for the UD78K sample. At a base temperature of 20 K, the equilibrium spectrum ($t = -1.2$ ps) shows a well-known dispersion kink at binding energy $\hbar\omega_0 \approx 70$ meV as marked by the arrow in Fig. 7.1(a).[43] As the pump pulse strikes the sample ($t = 0$ ps), the intensity of the ARPES spectrum between the Fermi level and the kink energy is suppressed. It returns to the equilibrium value after 20 ps. Such evolution of the transient

ARPES spectrum is similar to that of optimally doped Bi2212 as reported in Refs. 187 and 189. To illustrate the recovery process, Fig. 7.1(b) shows the change in integrated ARPES intensity above E_F (ΔI_e, see hatched region in Fig. 7.1(a)), with the response at different fluences normalized to the same amplitudes. In the superconducting state, the recovery rate of the non-equilibrium state increases linearly with fluence (Fig. 7.1(c)) in a manner similar to that observed in optimally doped Bi2212,[189] suggesting bimolecular recombination.[148,218] As the fluence approaches a critical fluence F_c ($\sim$13 μJ/cm^2), the decay rate undergoes a change in slope, marking the onset of different recombination processes for quasiparticles. A similar but higher critical fluence was found in a time-resolved optical reflectivity study;[220] the difference in thresholds may be because reflectivity measurements probe more of the bulk than ARPES. Such a fluence threshold is consistent with an observation of the full closure of the superconducting gap at a similar critical fluence in optimally doped Bi2212,[235] and thus we identify it as the likely fluence where all Cooper pairs have been destroyed. The identification is also consistent with a simple back-of-the-envelope calculation of the fluence needed to break apart all Copper pairs. Indeed, using a superconducting coherence length of $\sim$15 Å[262] and a penetration depth of $\sim$100 nm[151] (for 1.48 eV photons) in Bi2212, at F_c the laser deposits $\sim$0.25 meV/Å^2 of energy in the top copper oxygen plane, or $\sim$55 meV per coherence area. This is on the order of the energy gap in Bi2212. We note that a portion of the pulse energy may be transferred to phonons in the initial response, but it should not significantly affect our estimation because the initial non-thermal relaxation is dominated by electron-electron scattering.[263] Hence at the critical fluence the laser deposits just enough energy to completely break all Cooper pairs.

As the temperature increases, thermally excited quasiparticles begin to dominate the recombination dynamics,[148] making it harder to isolate the contribution of photoexcited non-equilibrium quasiparticles. This limitation can be overcome by looking at the signal at $t = 0$ (averaged over $\sim$300 fs because of time resolution), as the thermally excited quasiparticle have only negligible impact on the initial excited population. The temperature-dependent non-equilibrium quasiparticle population at $t = 0$ is studied in following section.

7.4 Fluence and temperature dependence

Figure 7.2 shows $\Delta I_e(t = 0)$ as a function of fluence and temperature for an underdoped sample. Two distinct regimes can be identified from the data: a high temperature regime, which extends from the normal state (panel (a)) well into the pseudogap state (panel (b), $T^* \approx 220$ K[88,83]), where ΔI_e is linear in fluence and extrapolates to 0 at $F = 0$ (see dashed lines)); and a low temperature regime, which sets in above T_c (panels (b) and (c)) and persists into the superconducting state (panel (d)), where ΔI_e is clearly not linear in fluence, with high-fluence values of ΔI_e extrapolating to a positive y-intercept at $F = 0$. The departure from linearity at low temperature occurs at the critical fluence ($F_c = 13 \pm 3$ μJ/cm^2) identified in Fig. 7.1(e). According to the interpretation that F_c marks the threshold above which no Cooper pairs exist, we observe a slight decrease of F_c from 13 μJ/cm^2(panels (d) and (e)) to 8 μJ/cm^2 as the temperature increases to 120 K (panel (c)). Also, in a single

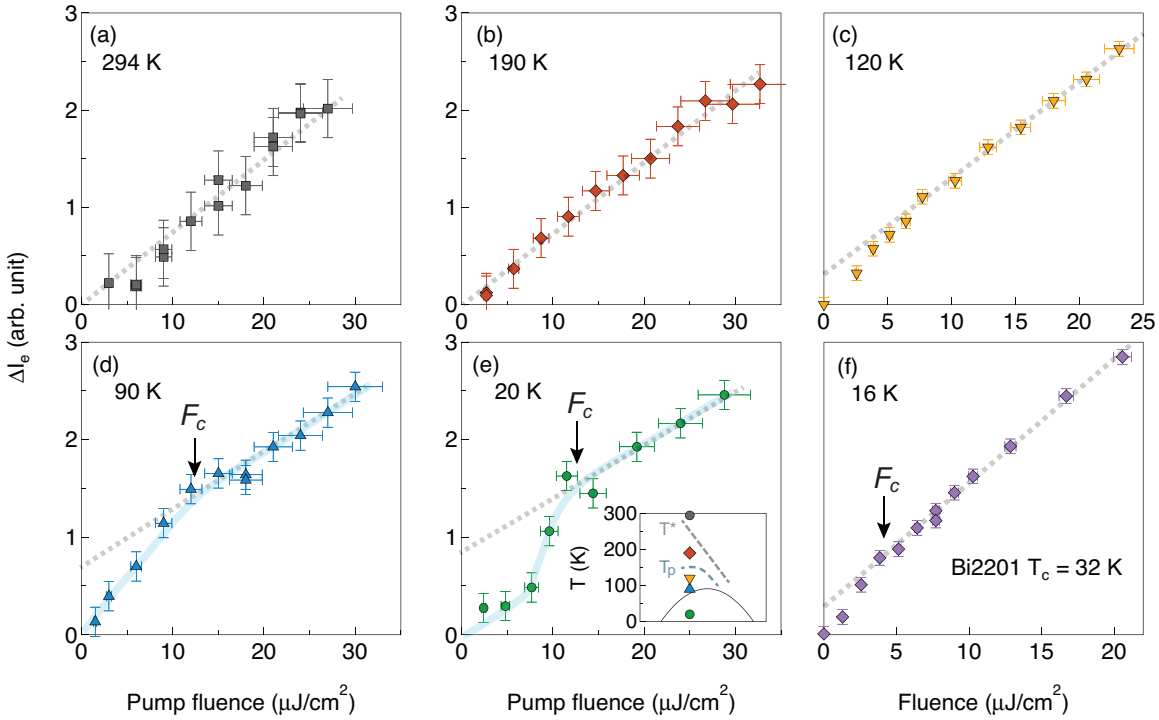

Figure 7.2. Nodal fluence dependence of the initial quasiparticle excitation density at $t = 0$ in underdoped Bi2212 ($T_c = 78$ K). (a) ΔI_e at a delay time of 0 ps measured at 294 K. (b–e) Same as (a) but measured at equilibrium temperature 190 K, 120 K, 90 K, and 20 K. As indicated in the inset of (d), the measurements correspond to equilibrium temperatures above T^* (294 K), slightly below T^* (190 K), slightly above T_c (90 K), and far below T_c (20 K). (f) Similar measurement at on an overdoped Bi2201 sample ($T_c = 32$ K) at $T = 16$ K. The bold lines are guides to the eye, and the dashed bold lines are linear fits to the high fluence data. The black arrows mark the critical fluence where the slope of the curves changes. From Ref. 229.

layer Bi2201 sample, we observe a lower F_c by a factor of 3 (panel (f)). These observations are consistent with the interpretation of F_c and the fact that it should scale with the pairing strength, which gets weaker at higher temperatures, and is weaker in Bi2201 than in Bi2212. However, the observation of two distinct temperature regimes in the UD78K sample hints at an intermediate temperature scale between T_c and T^*, which, given the similar dynamics as in the superconducting state, is likely related to the onset of superconducting fluctuations. In line with this observation, a recent ARPES experiment has shown that the antinodal spectral function is sensitive to the onset of superconducting pairing fluctuations at an intermediate temperature scale between T_c and T^*.[258]

In Fig. 7.3 we show detailed temperature and doping dependence of ΔI_e at $t = 0$ for a fixed pump fluence (14.4 μJ/cm^2, slightly above the critical fluence). We note that the reflectance of Bi2212 has little temperature dependence from 4 K to 300 K at photon energy 1.48 eV (variation is less than 1%),[195] guaranteeing that the pump fluence applied on the sample is unchanged during the temperature-dependent measurements. A common feature to all the dopings is a sharp step in ΔI_e at T^*, which coincides with the pseudogap temperature determined from transport experiments[88] and from momentum-resolved experiments looking at antinodal quasiparticles.[83,258] The sharp step is still observed above T_c for an overdoped sample (Fig. 7.3(d)), suggesting that the pseudogap temperature T^* can be defined even for this overdoped sample, consistent with recent reports by equilibrium ARPES on antinodal quasiparticles.[83,73] The step indicates that non-equilibrium electronic states below T^* result in a larger contribution to ΔI_e at the node, even though there is no gap at the node itself as generally believed.

For the underdoped and optimally doped samples (panels (a)–(c)), further cooling reveals a distinctive peak-like feature in ΔI_e centered at T_c, and a plateau in ΔI_e above T_c that is bounded on the high temperature side by T^* and on the low temperature side by a temperature T_p, defined as the temperature below which ΔI_e begins to rise. The peak-like feature at T_c is reminiscent of a variety of observables that diverge in the vicinity of T_c as a result of phase fluctuations. These include, but are not limited to, λ-shaped anomalies in the temperature dependence of thermal expansivity coefficients in YBCO,[264] and a theoretical divergence of relaxation time at the critical temperature in random-field Ising systems.[265] Thus it is reasonable to infer that the peak in ΔI_e around T_c is a measure of phase fluctuations. Further confirmation comes from the sharpening of the peak as the doping increases, reflecting a narrowing of the Ginzburg window[266] (see the width of this peak-like feature as a function of doping in the inset of Fig. 7.3(b)) . If the peak at T_c is associated with the presence of superconducting phase fluctuations, then T_p, the end of the peak feature, should be identified with the onset of such fluctuations. This scenario is further supported by the good agreement with the Nernst effect temperature,[92] identified as the onset of superconducting fluctuations in cuprate superconductors and the T_p measured in this experiment is along the nodal direction. The absence of T_p in the overdoped sample (panel (d)) implies that the superconducting transition is determined by Cooper pair formation rather than phase fluctuations. The non-equilibrium spectra in Figs. 7.3(a) and (b) do not saturate at the lowest temperature in our measurements for the two underdoped sample, indicating that fluctuating uncondensed pairs exist farther below T_c than on the overdoped side. Our result

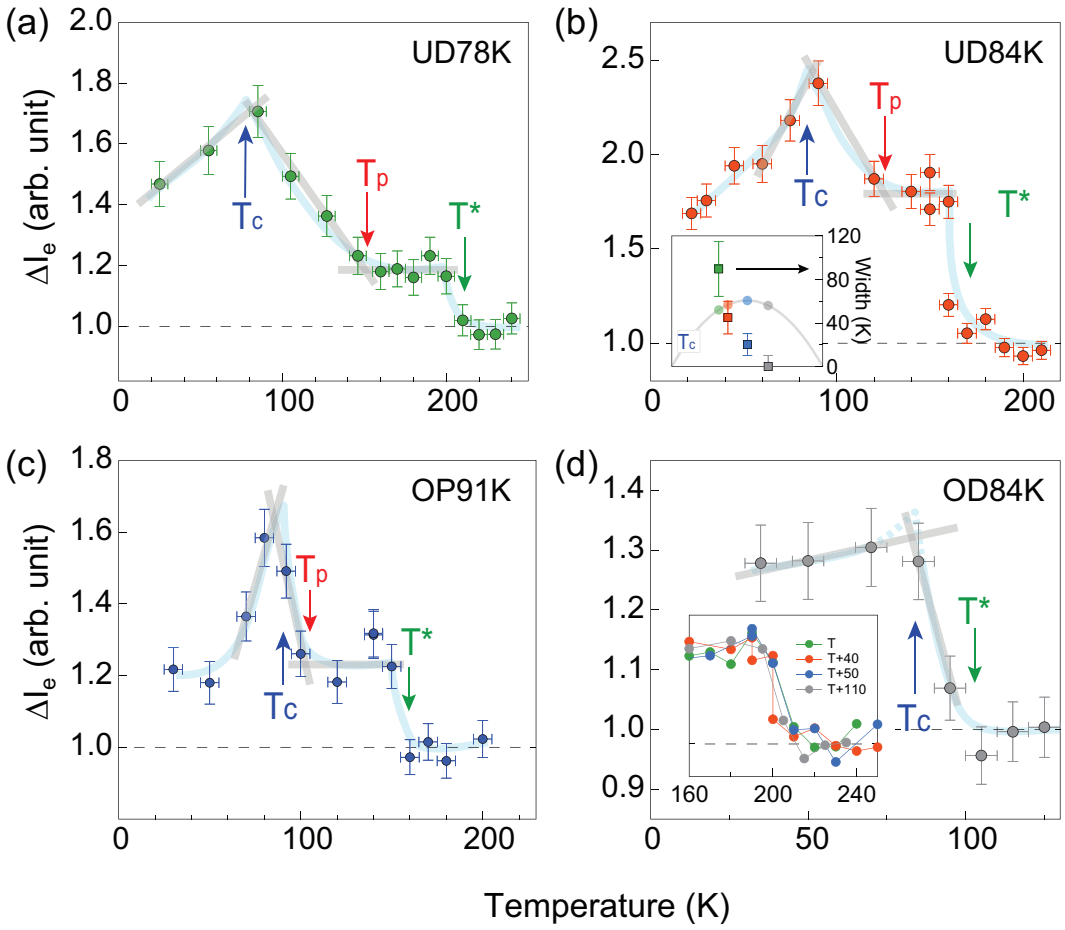

Figure 7.3. Nodal temperature dependence of the initial quasiparticle excitation density at a fixed fluence of 14.4 μJ/cm^2 for various dopings of Bi2212. (a) Underdoped ($T_c = 78$ K) sample. ΔI_e at zero delay time, defined as in Fig. 7.1, and normalized to the height above T^*. (b–d) Same as (a) for an underdoped $T_c = 84$ K sample, an optimally doped $T_c = 91$ K sample, and an overdoped $T_c = 84$ K sample. The bold cyan lines are guides to the eyes. ΔI_e at different temperature are normalized to the same probe fluence. Inset in (b) shows the width of the peak-like feature around T_c as a function of doping. Inset in (d) is the ΔI_e vs temperature for the four dopings of sample, which are scaled to the same amplitudes at T^*. Error bars are taken to be the maximum $|\Delta I(t))|$ for $t < 0$. From Ref. 229.

also demonstrates that below T_p, the breaking of uncondensed Cooper pairs by pumping dominates ΔI_e at $t = 0$.

The features at T_c, T_p, and T^* follow distinct trends as a function of doping. For all dopings, fitting the rise of the step at T^* using an error function yields a temperature smearing less than 10 K (inset of panel (d)). The abrupt onset at T^* is reminiscent of time-resolved reflectivity measurements on Bi2201, where a similar behavior was associated with T^*, marking the onset of a phase transition.[114] The fact that ΔI_e at $t = 0$ shows the same critical fluence in both the superconducting state and between T_c and T_p (Figs. 7.2(c)–(d)), demonstrates that the response of the electronic state to the pump pulse between T_p and T_c is similar to that in the superconducting state. In contrast, the absence of a critical fluence above T_p in Fig. 7.2 shows the different response between states below T_p and states below T^*, indicating the different underlying interactions of the pseudogap and the superconducting state.

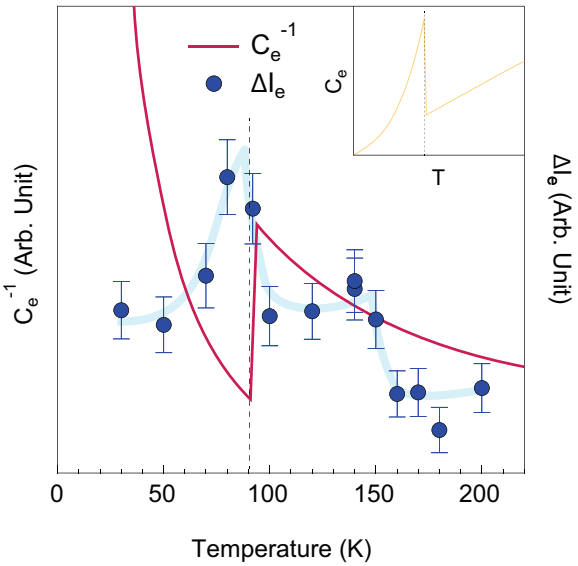

Figure 7.4. Comparison between initial nonequilibrium electrons $\Delta I_{\rm e}$ and simulated electron heat capacity $C_{\rm e}$ as a function of temperature. The inset shows the $C_{\rm e}$ as a function of temperature in a superconductor. From Ref. 229.

We note that the step at T^* and peak-like feature at T_c cannot be attributed to thermal effects. Indeed, in a thermal model the initial non-equilibrium electron population $\Delta I_{\rm e}{}^{simu}$ is proportional to the energy integral of a Fermi-Dirac distribution between the chemical potential and infinity, which is in turn proportional to the electronic temperature $T_{\rm e}$:

$$I_{\rm e}^{simu} \propto \int_0^{+\infty} \frac{1}{e^{\omega/k_B T_{\rm e}}+1} d\omega \tag{7.1}$$

$$\propto k_B T_{\rm e} \int_0^{+\infty} \frac{1}{e^{x}+1} dx \tag{7.2}$$

$$\propto T_{\rm e} \tag{7.3}$$

It immediately follows that the change in the electronic spectral weight ($\Delta I_{\rm e}$) is proportional to the change of electronic temperature $\Delta T_{\rm e}$ and independent of the equilibrium temperature.

If one assumes that the energy of the pump pulse ΔQ is mainly absorbed to heat the electrons,[263] then

$$dQ = dT_{\mathrm{e}} \cdot C_{\mathrm{e}} \tag{7.4}$$

where C_{e} is the electronic heat capacity. According then to Eqs. 7.1 to 7.3, we expect that ΔI_{e} is inversely proportional to the specific heat capacity C_{e}. In Fig. 7.4 we use a simple model to simulate the electron heat capacity C_{e} with $C_{\mathrm{e}} = AT^3$ below T_{c} and $C_{\mathrm{e}} = BT$ above T_{c} (A and B are constants). The direct comparison between C_{e} and ΔI_{e} shown in Fig. 7.4 clearly shows that the initial spectral gain above the Fermi level cannot be attributed to a simple thermal effect. Indeed, while the experimental value of $\Delta I_{\mathrm{e}}(t)$ shows a peak-like feature around T_{c}, the model predicts a dip in C_{e}^{-1} at the same temperature. The basic shape of this dip feature at T_{c} is robust, even after integrating Eq. 7.4 to account for realistically finite values of ΔI_{e} and ΔT_{e}.

7.5 Phase diagram and discussion

In Fig. 7.5, we summarize the temperatures identified for the nodal transient spectra T_c, T^*, and T_p, in the form of a phase diagram, and compare them with similar temperature scales reported in the literature. The most important implications of this comparison are (1) the position of the peak-like feature (T_c-node) in Fig. 7.3 matches the superconducting critical temperature T_c measured by SQUID; (2) T_p-node coincides with the onset temperature of superconducting phase fluctuations measured by Nernst effect;[92] and (3) T^*-node coincides with the pseudogap temperature extracted from various momentum integrated probes[88,89,87,86,85] and from ARPES along the antinodal direction (T^*-antinode).[83,258,73]

Revealing the presence of these energy scales in the spectral function of ungapped quasiparticles disrupts the conventional view that T_c, T_p, and T^* are only associated with gapped antinodal states. The signature at T^* is perhaps the most surprising of these, as the most popular explanation for the pseudogap phase at present is that it is associated with onset of charge ordering with a nesting vector along the (π,0) direction, resulting therefore in strongly suppressed antinodal electronic states.[268] The signatures of T^* and T_c in the (π,π) direction may indicate that the gapped antinodal non-equilibrium quasiparticles in both of the pseudogap and superconducting states can be scattered to nodal region via exchanging a momentum with other excitations in a very short time scale. Theoretical and experimental studies seems to argue against this possibility as this type of scattering is predicted to be pair-breaking,[251,219,188] leaving a far more exciting possibility also exists, namely, that nodal electronic states intrinsically play the same role in shaping the pseudogap and superconducting states on the phase diagram as generally believed in antinodal states.

In summary, we have revealed a strong response of non-equilibrium nodal ungapped quasiparticles to both the superconducting and pseudogap states. A new phase diagram for nodal quasiparticles results from these data, similar to the one widely discussed for gapped antinodal quasiparticles, where the pseudogap temperature T^* gradually merges with the superconducting transition temperature on the overdoped side of the phase diagram, and

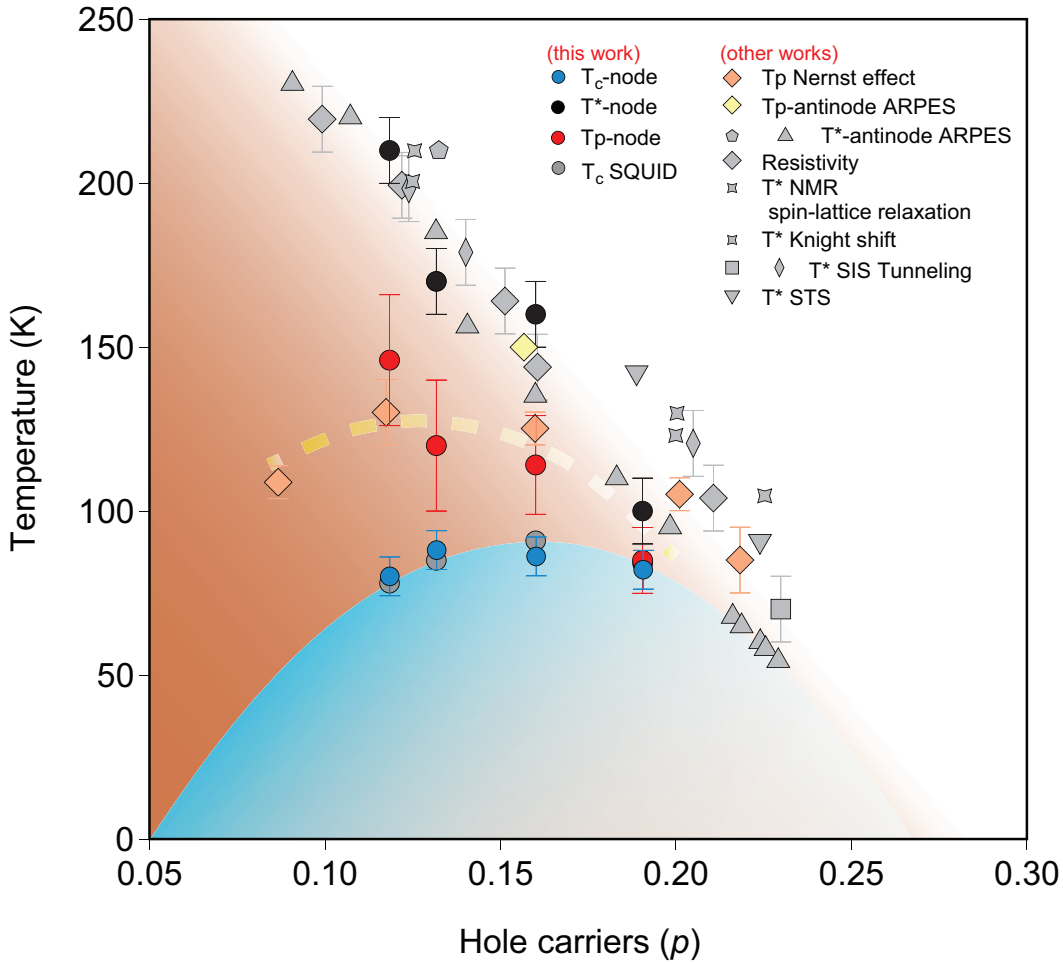

Figure 7.5. Nodal phase diagram of Bi2212. The superconducting critical temperature T_c-node, superconducting fluctuation onset temperature T_p-node and pseudogap temperature T^*-node of the four different dopings are plotted. T_c-node (blue filled circles), T^*-node (black filled circles) and T_p-node (red filled circles) are determined by the transition and onset temperature in Fig. 7.3; T_c (gray filled circles) is derived from SQUID measurements. T_p from Nernst signal measurements (pink diamonds)[92] and off-nodal ARPES measurement (yellow diamond),[258] as well as T^* (gray data points) from ARPES,[83,258] resistivity,[88] nuclear spin-lattice relaxation,[89] the Knight shift,[89] SIS tunneling[87,86] and STS[85] are also plotted. The hole carrier concentration p of each sample is calculated by the Presland-Tallon equation $T_c/T_c^{max} = 1-82.6(p-0.16)^2$.[267] From Ref. 229.

an intermediate temperature scale T_p associated with uncondensed Cooper pairs sets in between T_c and T^*. These results highlight the important role that nodal quasiparticles play for cuprate superconductivity, as well as the different electronic natures of the pseudogap and superconducting transition.

Chapter 8

Conclusions and future directions

I hope to have presented a convincing case that time-resolved ARPES has led to some important insights in the cuprate problem. Still, there is certainly much left to do. In this final chapter, I give a brief overview of some of the most interesting future directions in time-resolved spectroscopy, with special emphasis on the experiments that may be able to immediately pursued as follow-up experiments to the work thus far summarized.

Cuprate dynamics at the Brillouin zone face. As argued both in Chapters 4 and 5, there are important dynamical changes in both the superconducting quasiparticle population and dynamical gap amplitude as one begins to approach the Brillouin zone face in Bi2212. In particular, it was discussed in Chapter 4 that the increase in the recombination coefficient toward the first Brillouin zone face may reflect an increasingly well-nested resonance between superconducting quasiparticles and scattering vectors responsible for one or more phases that compete with superconductivity in cuprates. Two potential examples are shown in Fig. 8.1.

Clearly, further research into the possibility of these resonances would have a large impact in terms of helping us understand superconductivity. For the studies undertaken in the Lanzara group thus far, the only probe frequency employed has been at an energy of $h\nu = 5.93$ eV, resulting in a maximum accessible momentum, even in the unrealistic situation of photoelectrons exiting the sample at $\theta \approx 90^\circ$ from normal, of about 0.7 Å^{-1}. The Brillouin zone face, lies some ways beyond this, with the $\bar{M}$-point sitting at a wavevector of 0.82 Å^{-1}. In future experiments it may therefore be quite interesting to find ways of accessing this truly anti-nodal region of k-space. An obvious approach to doing so would consist of replacing the current system's BBO crystals with a high-harmonic generation scheme, where photon energies beyond 10 eV could be reached. Achieving this without simultaneously suffering from an unacceptable degradation in terms of energy resolution will be difficult—efforts by researchers to use high-harmonic generation techniques have thus far only been able to achieve energy resolutions in the neighborhood of 150 meV, which is several times the magnitude of the gap. Nevertheless, it may be possible to achieve energy resolutions as good

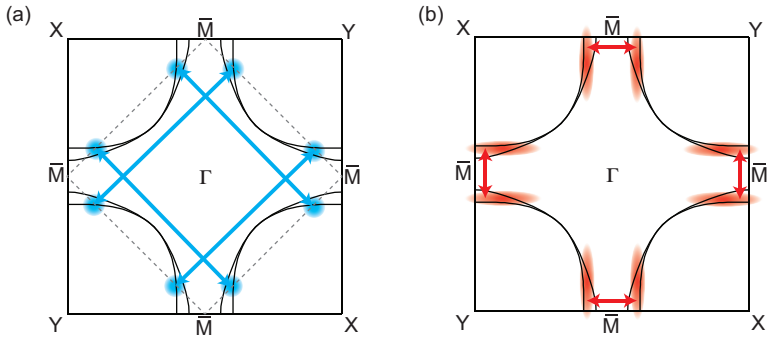

Figure 8.1. Momentum-space resonance conditions for possible interactions between the superconducting quasiparticles and competing phases. **(a)** For superconductivity to interact with antiferromagnetism, quasiparticle scattering rates may peak at eight "hot spots," occurring at the intersection between the normal-state Fermi surface (solid black lines) and the antiferromagnetic zone boundary (dashed gray lines). **(b)** For superconductivity to interact with a charge density wave, quasiparticle scattering rates may peak along extended portions of the normal-state Fermi surface near the Brillouin zone face, where the charge-density-wave scattering vector would most effectively nest.

as even 10 meV by filtering light through a monochrometer after it has been converted into the UV, or by taking advantage of resonant transitions within the noble gas the comprises the high-harmonic generation medium.

Characterization of coherent mode-coupling in cuprate superconductors. Further extensions to the present body of work may include adapting the system to make use of different and lower pump frequencies. At present, the currently employed 1.5-eV pump pulse excites quasiparticles well above the superconducting gap, and many of the relevant dynamics for superconductivity are only observed in subsequent interactions. It would, however, be very interesting to be able to tune the frequency of the pump pulse so as to resonantly excite particular phonon modes. An obvious choice of energy would be the 70-meV mode coupling so ubiquitously observed in cuprates along the nodal direction. Beyond this, it would be interesting to couple the B_{1g} "bond-buckling" phonon observed toward the Brillouin zone face, as it may play a role in facilitating interactions between superconductivity and both antiferromagnetism and charge-density-wave order. Direct resonant coupling between light and the superconducting gap may even incite coherent superconducting gap magnitude oscillations, which would be a fascinating analogue to the recently discovered Higgs boson in particle physics.

Superconductivity in places where it should normally be absent. A particularly intriguing possibility related to the above line of inquiry is is that the resonant excitation of modes not only might help us understand phenomena that are already present in cuprates, but might actually allow us to create new states of matter where none had previously existed. There are a few recent indications of this from all-optical experiments, which have

recently generated considerable excitement, and which include the enhancement of superconductivity at the expense of stripe order in $La_{1.675}Eu_{0.2}Sr_{0.125}CuO_4$,[269] and the generation of what appears to have many of the properties of a nonequilibrium superconducting state in $YBa_2Cu_3O_{7-\delta}$ at temperatures even exceeding 350 K.[270,271]

Though these studies are interesting, much controversy still surrounds the field and it would be helpful to search for alternative signatures of superconductivity using an ARPES probe, which has particular advantages in that the dynamics of the superconducting gap can be directly observed, and that the momentum resolution of the technique may help pinpoint exactly how these fascinating new sets of phenomena become manifest.

Absence of superconductivity in places where it should normally be present. Though it may perhaps seem counterintuitive, the possibility of using time-resolved ARPES to study the dynamics of states that should be superconducting, and yet are not, may be just as interesting as the converse. The reason is that the nature of the highly nonequilibrium states may be fundamentally different from the nature of non-superconducting states at equilibrium, and may help us understand how an order parameter that is not at the Free energy minimum (as it would have to be in the equilibrium case) evolves in time.

An example of one such case[272] is as depicted in Fig. 8.2, illustrated in terms of the order parameter Δ and Ginzburg-Landau free energy density f, which is expanded to fourth-order in Δ in the usual way[33] according to

$$f = f_0 + \alpha|\Delta|^2 + \frac{\beta}{2}|\Delta|^4. \tag{8.1}$$

At equilibrium, the only two qualitatively different possibilities are $\alpha > 0$, in which case

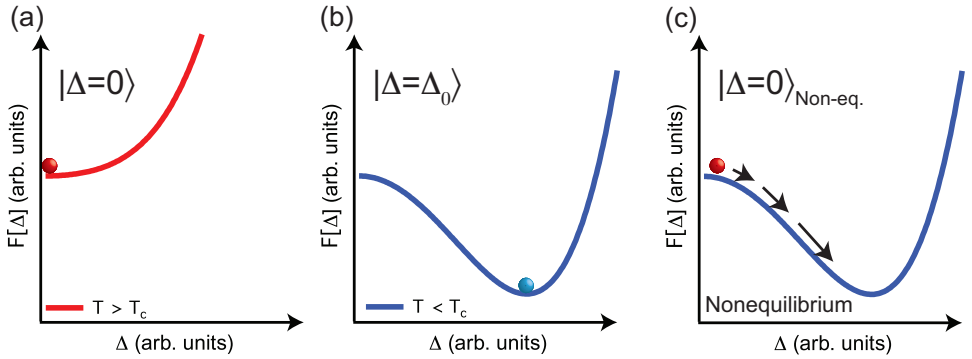

Figure 8.2. Example of a nonequilibrium state that might be uniquely accessible in a superconductor using intense optical pump pulses. In the equilibrium case, the only two physical situations are **(a)** above T_c, where the minimum in the free energy is at zero and the order parameter is zero, and **(b)** below T_c, where the minimum in the free energy is at Δ_0 and the order parameter is Δ_0. **(c)** In the nonequilibrium case, however, it may be possible to have a situation where the minimum in the free energy is at Δ_0 and yet the system has been boosted to a metastable state where the order parameter is 0.

the free energy minimum (and therefore the order parameter Δ) is zero (Fig. 8.2(a)), and $\alpha < 0$, in which case the free energy minimum and the order parameter are at $|\Delta_0|^2 = -\alpha/\beta$ (Fig. 8.2(b)). In the nonequilibrium case, an interesting third possibility also exists, however, in the form of a situation where the free energy minimum Δ_0 is at a finite value, and yet the order parameter itself has been suppressed to $\Delta = 0$ (Fig. 8.2(c)). Subsequently, the order parameter will relax toward equilibrium in time, potentially giving information about the free energy functional form.

Photon-dressed electronic states. Finally, though the discussion deviates from the study of superconductivity, some comment is warranted on the special situation in which pump and probe beams are perfectly coincident in a time-resolved ARPES experiment, where it has recently been demonstrated that the nonequilibrium interaction between the optical pump pulse and the electronic energy levels can in certain cases directly result in Floquet-Bloch states in the topological insulator Bi_2Se_3,[273] and where theoretical work has very recently been focused in graphene.[155]

Floquet-Bloch states can be understood as the generalization of Bloch's theorem, where an electron is subject not only to an electric potential that varies in space, but which also (through the oscillation of the electric field) varies periodically in time. The result is a series of states that are commensurately periodic in both momentum and energy. Perhaps a more intuitive way of understanding the generation of such states, however, is by explicitly considering the interaction between an isolated atom and an oscillating electromagnetic field. In this case, the relevant Hamiltonian[274,275]

$$H = H_{atom} + H_{rad} + H_{int} \tag{8.2}$$

includes terms not only for the atom (H_{atom}) and the atom-light interaction perturbation (H_{int}), but also for the quantized occupation of electromagnetic field itself (H_{rad}). As a result, the two-level system is replaced by an infinite ladder of dressed states, as shown in Fig. 8.3. Things can get particularly interesting in the special case where the pump frequency

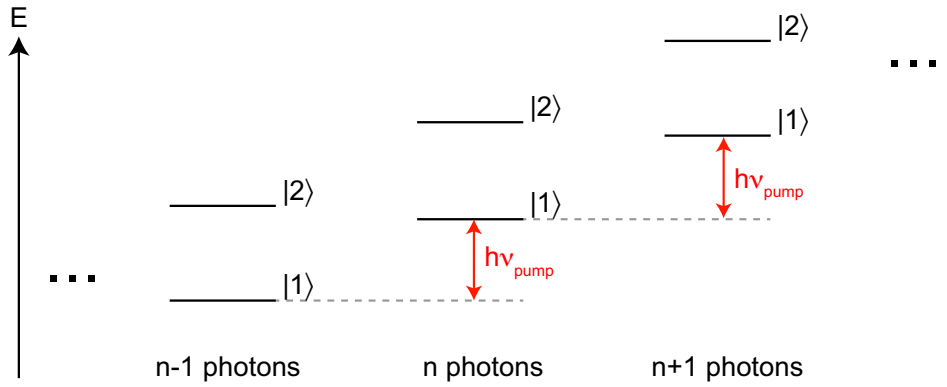

Figure 8.3. Energy-level diagram for a two-level atom interacting with an electromagnetic field of frequency ν in terms of the dressed-atom picture.

is nearly equal to the energy difference between states between the atom, for then state $|2\rangle$ of

the $n-1$ photon system becomes nearly degenerate with state $|1\rangle$ of the n photon system, and the Hamiltonian's interaction term can subsequently work to split apart this degeneracy.[275]

In the case of a solid-state system, many of the same rules apply, except that flat energy levels are replaced by dispersive bands, and perhaps most interestingly, the degeneracy-splitting effect of the interaction Hamiltonian takes the form of light-induced bandgaps. The possibility of using light to generate and manipulate such bandgaps may have important implications in semiconductor device physics, with applications ranging from transistor design to photovoltaic electricity generation.

Bibliography

1. Brewster, D. *Memoirs of the Life, Writings, and Discoveries of Sir Isaac Newton*, vol. 2 (T. Constable and Company, 1855).

2. Kamerlingh Onnes, H. Further Experiments with Liquid Helium G. On the electrical resistance of Pure Metals etc. VI. On the Sudden Change in the Rate at which the Resistance of Mercury Disappears. *Proc. K. Ned. Akad. Wet.* **14 II**, 818–821 (1912).

3. Tinkham, M. *Introduction to Superconductivity* (McGraw-Hill, New York, 1996), 2nd edn.

4. Resistance is futile. *The Economist*, Dec. 3rd (2011).

5. van Delft, D. Little cup of helium, big science. *Phys. Today* **61**, 36 (2008).

6. Shachtman, T. *Absolute Zero and the Conquest of Cold* (Houghton Mifflin Harcourt, 2000).

7. van Delft, D. & Kes, P. The discovery of superconductivity. *Phys. Today* **9**, 38–43 (2010).

8. de Bruyn Ouboter, R. Superconductivity: Discoveries during the early years of low temperature research at Leiden 1908-1914. *IEEE T. Magn.* **23**, 355–370 (1987).

9. Schmalian, J. Failed theories of superconductivity. In *BCS: 50 Years* (eds. Cooper, L. N. & Feldman, D.), chap. 4, 41–56 (World Scientific, 2011).

10. Goodstein, D. & Goodstein, J. Richard Feynman and the History of Superconductivity. *Phys. Perspect.* **2**, 30–47 (2000).

11. Meissner, W. & Ochsenfeld, R. Ein neuer Effekt bei Eintritt der Supraleitfhigkeit. *Naturwissenschaften* **21**, 787–788 (1933).

12. https://commons.wikimedia.org/wiki/File:EfektMeisnera.svg

13. http://users-phys.au.dk/philip/pictures/physicsfigures/physicsfigures.html (2007).

14. London, F. & London, H. The Electromagnetic Equations of the Supraconductor. *Proc. R. Soc. Lond. A* **149**, 71–88 (1935).

15. Bardeen, J., Cooper, L. N. & Schrieffer, J. R. Theory of Superconductivity. *Phys. Rev.* **108**, 1175–1204 (1957).

16. Cooper, L. N. Remembrance of Superconductivity Past. In *BCS: 50 Years* (eds. Cooper, L. N. & Feldman, D.), chap. 1, 3–19 (World Scientific, 2011).

17. Maxwell, E. Isotope effect in the superconductivity of mercury. *Phys. Rev.* **78**, 477 (1950).

18. Reynolds, C. A., Serin, B., Wright, W. H. & Nesbitt, L. B. Superconductivity of isotopes of mercury. *Phys. Rev.* **78**, 487 (1950).

19. Corak, W. S., Goodman, B. B., Satterthwaite, C. B. & Wexler, A. Exponential Temperature Dependence of the Electronic Specific Heat of Superconducting Vanadium. *Phys. Rev.* **96**, 1442 (1954).

20. Giaever, I. Energy Gap in Superconductors Measured by Electron Tunneling. *Phys. Rev. Lett.* **5**, 147–148 (1960).

21. Anderson, P. W. BCS: The scientific "Love of my life." In *BCS: 50 Years* (eds. Cooper, L. N. & Feldman, D.), chap. 8, 127–142 (World Scientific, 2011).

22. Josephson, B. Possible new effects in superconductive tunnelling. *Phys. Lett.* **1**, 251–253 (1962).

23. Parks, R. D. (ed.). *Superconductivity*, vol. 1 (Marcel Dekkar, 1969).

24. McMillan, W. L. Transition Temperature of Strong-Coupled Superconductors. *Phys. Rev.* **167**, 331–344 (1968).

25. Goodstein, D. *On Fact and Fraud: Cautionary Tales from the Front Lines of Science* (Princeton University Press, Princeton, 2010).

26. Bednorz, G. & Müller, K. A. Possible High-T_c Superconductivity in the Ba–La–Cu–O System. *Z. Phys. B* **64**, 189 (1986).

27. Wu, M. K. *et al.* Superconductivity at 93 K in a new mixed-phase Y-Ba-Cu-O compound system at ambient pressure. *Phys. Rev. Lett.* **58**, 908–910 (1987).

28. Schrieffer, J. R. & Brooks, J. S. *Handbook of high-temperature superconductivity: theory and experiment* (Springer, 2007).

29. Norman, M. R. Unconventional Superconductivity. In *Novel Superfluids* (eds. Bennemann, K. H. & Ketterson, J. B.), vol. 2 (Oxford University Press, 2014).

30. Kamihara, Y., Watanabe, T., Hirano, M. & Hosono, H. Iron-Based Layered Superconductor $La[O_{1-x}F_x]FeAs$ ($x = 0.05$–0.12) with $T_c = 26$ K. *J. Am. Chem. Soc.* **130**, 3296–3297 (2008).

31. http://commons.wikimedia.org/wiki/File:Sc_history.gif

32. Schrieffer, J. R. *Theory of Superconductivity* (Westview Press, Boulder, CO, 1999).

33. Annett, J. F. *Superconductivity, Superfluids, and Condensates.* Oxford Master Series in Condensed Matter Physics (Oxford University Press, Oxford, 2004).

34. Ginzburg, V. L. & Landau, L. D. On the theory of superconductivity. *Zh. Eksp. Teor. Fiz.* **20**, 1064 (1950).

35. Gor'kov, L. P. Microscopic derivation of the Ginzburg-Landau equations in the theory of superconductivity. *Sov. Phys. JETP* **36**, 1364–1367 (1959).

36. Scully, M. O. & Zubairy, S. *Quantum Optics* (Cambridge University Press, Cambridge, 1997).

37. Bogoliubov, N. N. *Nuovo Cimento* **7**, 794 (1958).

38. Valatin, J. G. *Nuovo Cimento* **7**, 843 (1958).

39. Cooper, L. N. Bound Electron Pairs in a Degenerate Fermi Gas. *Phys. Rev.* **104**, 1189–1190 (1956).

40. Valla, T., Fedorov, A. V., Johnson, P. D. & Hulbert, S. L. Many-Body Effects in Angle-Resolved Photoemission: Quasiparticle Energy and Lifetime of a Mo(110) Surface State. *Phys. Rev. Lett.* **83**, 2085–2088 (1999).

41. Zhou, S. Y., Gweon, G.-H. & Lanzara, A. Low energy excitations in graphite: The role of dimensionality and lattice defects. *Ann. Phys.* **321**, 1730–1746 (2006).

42. Siegel, D. A., Hwang, C., Fedorov, A. V. & Lanzara, A. Electron-phonon coupling and intrinsic bandgap in highly-screened graphene. *New J. Phys.* **14**, 095006 (2012).

43. Lanzara, A. *et al.* Evidence for ubiquitous strong electron-phonon coupling in high-temperature superconductors. *Nature* **412**, 510 (2001).

44. Eliashberg, G. M. Interactions between electrons and lattice vibrations in a superconductor. *Sov. Phys. JETP* **11**, 696 (1960).

45. Cohen, M. L. Predicting and explaining T_c and other properties of BCS superconductors. In *BCS: 50 Years* (eds. Cooper, L. N. & Feldman, D.), chap. 15, 375–389 (World Scientific, 2011).

46. Côté, M., Grossman, J. C., Cohen, M. L. & Louie, S. G. Electron-Phonon Interactions in Solid C_{36}. *Phys. Rev. Lett.* **81**, 697–700 (1998).

47. Moussa, J. E. & Cohen, M. L. Constraints on T_c for superconductivity in heavily boron-doped diamond. *Phys. Rev. B* **77**, 064518 (2008).

48. Moussa, J. E. & Cohen, M. L. Using molecular fragments to estimate electron-phonon coupling and possible superconductivity in covalent materials. *Phys. Rev. B* **78**, 064502 (2008).

49. Glover, R. E. & Tinkham, M. Transmission of Superconducting Films at Millimeter-Microwave and Far Infrared Frequencies. *Phys. Rev.* **104**, 844–845 (1956).

50. Schafroth, M. R., Blatt, J. M. & Butler, S. T. Quasichemical equilibrium approach to superconductivity. *Helv. Phys. Acta* **30**, 93 (1957).

51. Meservey, R. & Schwartz, B. B. Equilibrium properties: comparison of experimental results with predictions of the BCS theory. In *Superconductivity* (ed. Parks, R. D.), vol. 1, 117–192 (Marcel Dekker, New York, 1969).

52. Norman, M. R., Randeria, M., Ding, H. & Campuzano, J. C. Phenomenology of the low-energy spectral function in high-T_c superconductors. *Phys. Rev. B* **57**, R11093 (1998).

53. Leggett, A. J. What DO we know about high T_c? *Nat. Phys.* **2**, 134–136 (2006).

54. Gough, C. E. *et al.* Flux quantization in a high-T_c superconductor. *Nature* **326**, 855–855 (1987).

55. Koelle, D., Kleiner, R., Ludwig, F., Dantsker, E. & Clarke, J. High-transition-temperature superconducting quantum interference devices. *Rev. Mod. Phys.* **71**, 631–686 (1999).

56. Keene, M. N., Jackson, T. J. & Gough, C. E. Demonstration of the phase coherence of the superconducting wavefunctions between conventional and high- T_c superconductors. *Nature* **340**, 210–211 (1989).

57. Takigawa, M., Hammel, P. C., Heffner, R. H. & Fisk, Z. Spin susceptibility in superconducting $YB_2C_3O_7$ from ^{6}3Cu Knight shift. *Phys. Rev. B* **39**, 7371–7374 (1989).

58. Barrett, S. E., Durand, D. J., Pennington, C. H., Slichter, C. P., Friedmann, T. A., Rice, J. P. & Ginsberg, D. M. $YB_2C_3O_7$ from Knight shifts in the superconducting state of ^{63}Cu ($T_c = 90$ K). *Phys. Rev. B* **41**, 6283–6296 (1990).

59. Hoevers, H. F. C., Van Bentum, P. J. M., Van De Leemput, L. E. C., Van Kempen, H., Schellingerhout, A. J. G. & Van Der Marel, D. Determination of the energy gap in a thin $YBa_2Cu_3O_{7-x}$ film by Andreev reflection and by tunneling. *Physica C* **152**, 105–110 (1988).

60. Deutscher, G. Andreev–Saint-James reflections: A probe of cuprate superconductors. *Rev. Mod. Phys.* **77**, 109–135 (2005).

61. Balatsky, A. V., Lee, W. S. & Shen, Z. X. Bogoliubov angle, particle-hole mixture, and angle-resolved photoemission spectroscopy in superconductors. *Phys. Rev. B* **79**, 020505 (2009).

62. Matsui, H. *et al.* BCS-Like Bogoliubov Quasiparticles in High-T_c Superconductors Observed by Angle-Resolved Photoemission Spectroscopy. *Phys. Rev. Lett.* **90**, 217002 (2003).

63. Campuzano, J. C. *et al.* Direct observation of particle-hole mixing in the superconducting state by angle-resolved photoemission. *Phys. Rev. B* **53**, R14737–R14740 (1996).

64. Scalapino, D. J. A common thread: The pairing interaction for unconventional superconductors. *Rev. Mod. Phys.* **84**, 1383–1417 (2012).

65. Tsuei, C. C. & Kirtley, J. R. Pairing symmetry in cuprate superconductors. *Rev. Mod. Phys.* **72**, 969–1016 (2000).

66. Scalapino, D. J. The case for $d_{x^2-y^2}$ pairing in the cuprate superconductors. *Phys. Rep.* **250**, 329–365 (1995).

67. Monthoux, P., Pines, D. & Lonzarich, G. G. Superconductivity without phonons. *Nature* **450**, 1177–1183 (2007).

68. Shen, Z.-X. *et al.* Anomalously large gap anisotropy in the a-b plane of $Bi_2Sr_2CaCu_2O_{8+\delta}$. *Phys. Rev. Lett.* **70**, 1553 (1993).

69. Ding, H. *et al.* Angle-resolved photoemission spectroscopy study of the superconducting gap anisotropy in $Bi_2Sr_2CaCu_2O_{8+\delta}$. *Phys. Rev. B* **54**, R9678 (1996).

70. Meng, J. *et al.* Coexistence of Fermi arcs and Fermi pockets in a high-T_c copper oxide superconductor. *Nature* **462**, 335–338 (2009).

71. Lee, W. S. *et al.* Abrupt onset of a second energy gap at the superconducting transition of underdoped Bi2212. *Nature* **450**, 81 (2007).

72. Reber, T. J. *et al.* The origin and non-quasiparticle nature of Fermi arcs in $Bi_2Sr_2CaCu_2O_{8+\delta}$. *Nat. Phys.* **8**, 606–610 (2012).

73. Vishik, I. M. *et al.* Phase competition in trisected superconducting dome. *Proc. Natl. Acad. Sci. U.S.A.* (2012).

74. Wollman, D. A., Van Harlingen, D. J., Lee, W. C., Ginsberg, D. M. & Leggett, A. J. Experimental determination of the superconducting pairing state in YBCO from the phase coherence of YBCO-Pb dc SQUIDs. *Phys. Rev. Lett.* **71**, 2134–2137 (1993).

75. Tsuei, C. C. *et al.* Pairing Symmetry and Flux Quantization in a Tricrystal Superconducting Ring of $YBa_2Cu_3O_{7-\delta}$. *Phys. Rev. Lett.* **73**, 593–596 (1994).

76. Hanaguri, T. *et al.* Coherence Factors in a High-T_c Cuprate Probed by Quasi-Particle Scattering Off Vortices. *Science* **323**, 923–926 (2009).

77. Harter, J. W., Maritato, L., Shai, D. E., Monkman, E. J., Nie, Y., Schlom, D. G. & Shen, K. M. Nodeless Superconducting Phase Arising from a Strong (π, π) Antiferromagnetic Phase in the Infinite-Layer Electron-Doped $Sr_{1-x}La_xCuO_2$ Compound. *Phys. Rev. Lett.* **109**, 267001 (2012).

78. Peng, Y. *et al.* Disappearance of nodal gap across the insulator-superconductor transition in a copper-oxide superconductor. *Nat. Commun.* **4**, 2459 (2013).

79. Loeser, A. G., Shen, Z. X., Dessau, D. S., Marshall, D. S., Park, C. H., Fournier, P. & Kapitulnik, A. Excitation gap in the normal state of underdoped $Bi_2Sr_2CaCu_2O_{8+\delta}$. *Science* **273**, 325–329 (1996).

80. Ding, H. *et al.* Spectroscopic evidence for a pseudogap in the normal state of underdoped high-T_c superconductors. *Nature* **382**, 51 (1996).

81. Friedel, J. Quasilowdimensionality in the weak coupling limit. *Physica C* **153–155**, 1610–1616 (1988).

82. Alloul, H., Ohno, T. & Mendels, P. ^{89}Y NMR Evidence for a Fermi-Liquid Behavior in $YBa_2Cu_3O_{6+\delta}$. *Phys. Rev. Lett.* **63**, 1700–1703 (1989).

83. Chatterjee, U. *et al.* Electronic phase diagram of high-temperature copper oxide superconductors. *Proc. Natl. Acad. Sci. U.S.A.* **108**, 9346–9349 (2011).

84. Shekhter, A. *et al.* Bounding the pseudogap with a line of phase transitions in $YBa_2Cu_3O_{6+\delta}$. *Nature* **498**, 75–77 (2013).

85. Gomes, K. K., Pasupathy, A. N., Pushp, A., Ono, S., Ando, Y. & Yazdani, A. Visualizing pair formation on the atomic scale in the high-T_c superconductor $Bi_2Sr_2CaCu_2O_{8+\delta}$. *Nature* **447**, 569–572 (2007).

86. Dipasupil, R. M., Oda, M., Momono, N. & Ido, M. Energy Gap Evolution in the Tunneling Spectra of $Bi_2Sr_2CaCu_2O_{8+\delta}$. *J. Phys. Soc. Jpn.* **71**, 1535–1540 (2002).

87. Ozyuzer, L., Zasadzinski, J. F., Gray, K. E., Kendziora, C. & Miyakawa, N. Absence of pseudogap in heavily overdoped $Bi_2Sr_2CaCu_2O_{8+\delta}$ from tunneling spectroscopy of break junctions. *Europhys. Lett.* **58**, 589 (2002).

88. Oda, M., Hoya, K., Kubota, R., Manabe, C., Momono, N., Nakano, T. & Ido, M. Strong pairing interactions in the underdoped region of $Bi_2Sr_2CaCu_2O_{8+\delta}$. *Physica C* **281**, 135–142 (1997).

89. Ishida, K. *et al.* Pseudogap behavior in single-crystal $Bi_2Sr_2CaCu_2O_{8+\delta}$ probed by Cu NMR. *Phys. Rev. B* **58**, R5960–R5963 (1998).

90. Norman, M. R., Pines, D. & Kallin, C. The pseudogap: friend or foe of high T_c? *Adv. Phys.* **54**, 715–733 (2005).

91. Emery, V. J. & Kivelson, S. A. Importance of phase fluctuations in superconductors with small superfluid density. *Nature* **374**, 434–437 (1995).

92. Wang, Y., Li, L. & Ong, N. P. Nernst effect in high-T_c superconductors. *Phys. Rev. B* **73**, 024510 (2006).

93. Norman, M. R. *et al.* Destruction of the Fermi surface in underdoped high-T_c superconductors. *Nature* **392**, 157 (1998).

94. Norman, M. R., Kanigel, A., Randeria, M., Chatterjee, U. & Campuzano, J. C. Modeling the Fermi arc in underdoped cuprates. *Phys. Rev. B* **76**, 174501 (2007).

95. Hayden, S. M., Lander, G. H., Zarestky, J., Brown, P. J., Stassis, C., Metcalf, P. & Honig, J. M. Incommensurate magnetic correlations in $La_{1.8}Sr_{0.2}NiO_4$. *Phys. Rev. Lett.* **68**, 1061–1064 (1992).

96. Chen, C. H., Cheong, S.-W. & Cooper, A. S. Charge modulations in $La_{2-x}Sr_xNiO_{4+y}$: Ordering of polarons. *Phys. Rev. Lett.* **71**, 2461–2464 (1993).

97. Tranquada, J. M., Buttrey, D. J., Sachan, V. & Lorenzo, J. E. Simultaneous ordering of holes and spins in $La_2NiO_{4.125}$. *Phys. Rev. Lett.* **73**, 1003 (1994).

98. Tranquada, J. M., Sternlieb, B. J., Axe, J. D., Nakamura, Y. & Uchida, S. Evidence for stripe correlations of spins and holes in copper oxide. *Nature* **375**, 561–563 (1995).

99. Fujita, M., Goka, H., Yamada, K. & Matsuda, M. Competition between Charge- and Spin-Density-Wave Order and Superconductivity in $La_{1.875}Ba_{0.125-x}Sr_xCuO_4$. *Phys. Rev. Lett.* **88**, 167008 (2002).

100. Kivelson, S. A., Bindloss, I. P., Fradkin, E., Oganesyan, V., Tranquada, J. M., Kapitulnik, A. & Howald, C. How to detect fluctuating stripes in the high-temperature superconductors. *Rev. Mod. Phys.* **75**, 1201–41 (2003).

101. Tranquada, J. M. *et al.* Quantum magnetic excitations from stripes in copper oxide superconductors. *Nature* **429**, 534–538 (2004).

102. Wu, T. *et al.* Magnetic-field-induced charge-stripe order in the high-temperature superconductor $YBa_2Cu_3O_y$. *Nature* **477**, 191–194 (2011).

103. Ghiringhelli, G. *et al.* Long-Range Incommensurate Charge Fluctuations in $(Y,Nd)Ba_2Cu_3O_{6+x}$. *Science* **337**, 821–825 (2012).

104. Chang, J. *et al.* Direct observation of competition between superconductivity and charge density wave order in $YBa_2Cu_3O_{6.67}$. *Nat. Phys.* **8**, 871–876 (2012).

105. Wise, W. D. *et al.* Charge-density-wave origin of cuprate checkerboard visualized by scanning tunnelling microscopy. *Nat. Phys.* **4**, 696 (2008).

106. da Silva Neto, E. H. *et al.* Ubiquitous Interplay Between Charge Ordering and High-Temperature Superconductivity in Cuprates. *Science* **343**, 393–396 (2014).

107. Comin, R. *et al.* Charge Order Driven by Fermi-Arc Instability in $Bi_2Sr_{2-x}La_xCuO_{6+\delta}$. *Science* **343**, 390–392 (2014).

108. Sachdev, S. & La Placa, R. Bond Order in Two-Dimensional Metals with Antiferromagnetic Exchange Interactions. *Phys. Rev. Lett.* **111**, 027202 (2013).

109. Davis, J. C. S. & Lee, D.-H. Concepts relating magnetic interactions, intertwined electronic orders, and strongly correlated superconductivity. *Proc. Natl. Acad. Sci. U.S.A.* **110**, 17623–17630 (2013).

110. Laughlin, R. B. Hartree-Fock computation of the high-T_c cuprate phase diagram. *Phys. Rev. B* **89**, 035134 (2014).

111. Fradkin, E., Kivelson, S. A. & Tranquada, J. M. Theory of Intertwined Orders in High Temperature Superconductors. *ArXiv e-prints* arXiv:1407.4480 (2014).

112. Tanaka, K. *et al.* Distinct Fermi-Momentum-Dependent Energy Gaps in Deeply Underdoped Bi2212. *Science* **314**, 1910 (2006).

113. Hashimoto, M. *et al.* Particle-hole symmetry breaking in the pseudogap state of Bi2201. *Nat. Phys.* **6**, 414–418 (2010).

114. He, R.-H. *et al.* From a Single-Band Metal to a High-Temperature Superconductor via Two Thermal Phase Transitions. *Science* **331**, 1579–1583 (2011).

115. Damascelli, A., Hussain, Z. & Shen, Z.-X. Angle-resolved photoemission studies of the cuprate superconductors. *Rev. Mod. Phys.* **75**, 473 (2003).

116. Nandi, S. *et al.* Anomalous Suppression of the Orthorhombic Lattice Distortion in Superconducting $Ba(Fe_{1-x}Co_x)_2As_2$ Single Crystals. *Phys. Rev. Lett.* **104**, 057006 (2010).

117. Mathur, N. D., Grosche, F. M., Julian, S. R., Walker, I. R., Freye, D. M., Haselwimmer, R. K. W. & Lonzarich, G. G. Magnetically mediated superconductivity in heavy fermion compounds. *Nature* **394**, 39–43 (1998).

118. Takabayashi, Y. *et al.* The Disorder-Free Non-BCS Superconductor Cs_3C_60 Emerges from an Antiferromagnetic Insulator Parent State. *Science* **323**, 1585–1590 (2009).

119. Thomson, C. & Cardona, M. Raman Scattering in High-T_c superconductors. In *Physical Properties of High Temperature Superconductors I* (ed. Ginsberg, D. M.) (World Scientific, Singapore, 1989).

120. Tajima, S. *et al.* Optical-phonon study of single crystals of various layered cuprates and related materials: Evidence of unique electron-phonon coupling in the CuO_2 plane. *Phys. Rev. B* **43**, 10496–10507 (1991).

121. Egami, T. & Billinge, S. J. L. Lattice effects in high-T_c superconductors. In *Physical properties of high temperature superconductors V* (ed. Ginsberg, D.), chap. 5, 265 (World Scientific, Singapore, 1996).

122. Cuk, T. *et al.* Coupling of the B_{1g} Phonon to the Antinodal Electronic States of $Bi_2Sr_2Ca_{0.92}Y_{0.08}Cu_2O_{8+\delta}$. *Phys. Rev. Lett.* **93**, 117003 (2004).

123. Hüfner, S. *Photoelectron Spectroscopy: Principles and Applications* (Springer, 2003), 3rd edn.

124. Yu, P. Y. & Cardona, M. *Fundamentals of Semiconductors: Physics and Materials Properties* (Springer, Berlin, 2003), 3rd edn.

125. Campuzano, J. C., Norman, M. R. & Randeria, M. Photoemission in the High-T_c Superconductors. In *Physics of superconductors* (eds. Bennemann, K. H. & Ketterson, J. B.), vol. II, chap. 5, 167–273 (Springer, Berlin, 2004).

126. Withers, R. L., Thompson, J. G., Wallenberg, L. R., FitzGerald, J. D., Anderson, J. S. & Hyde, B. G. A transmission electron microscope and group theoretical study of the new Bi-based high-T_c superconductors and some closely related Aurivillius phases. *J. Phys. C: Solid State Phys.* **21**, 6067 (1988).

127. Siegel, D. A., Park, C.-H., Hwang, C., Deslippe, J., Fedorov, A. V., Louie, S. G. & Lanzara, A. Many-body interactions in quasi-freestanding graphene. *Proc. Natl. Acad. Sci. U.S.A.* **108**, 11365–11369 (2011).

128. Hsieh, D. *et al.* A tunable topological insulator in the spin helical Dirac transport regime. *Nature* **460**, 1101–1105 (2009).

129. Zhou, S. Y. *et al.* First direct observation of Dirac fermions in graphite. *Nat. Phys.* **2**, 595 (2006).

130. Liu, Z. K. *et al.* Discovery of a Three-Dimensional Topological Dirac Semimetal, Na_3Bi. *Science* **343**, 864–867 (2014).

131. Seah, M. P. & Dench, W. A. Quantitative electron spectroscopy of surfaces: A standard data base for electron inelastic mean free paths in solids. *Surf. Interface Anal.* **1**, 2–11 (1979).

132. Mahan, G. D. *Many-Particle Physics* (Plenum Press, New York, 1990), 2nd edn.

133. Peskin, M. E. & Schroeder, D. V. *An Introduction to Quantum Field Theory* (Addison-Wesley, Reading, MA, 1995).

134. Sakurai, J. J. & Napolitano, J. J. *Modern Quantum Mechanics* (Pearson, 2014).

135. Ashcroft, N. W. & Mermin, N. D. *Solid State Physics* (Brooks/Cole, Stamford, CT, 1976).

136. Varma, C. M., Littlewood, P. B., Schmitt-Rink, S., Abrahams, E. & Ruckenstein, A. E. Phenomenology of the normal state of Cu-O high-temperature superconductors. *Phys. Rev. Lett.* **63**, 1996–1999 (1989).

137. Gweon, G.-H. *Angle resolved photoemission study of Fermi surfaces and single-particle excitations of quasi-low dimensional materials.* Ph.D. thesis, University of Michigan (1999).

138. Siegel, D. A. *The Electronic Structure of Single-Layer Graphene.* Ph.D. thesis, University of California, Berkeley (2012).

139. Grimvall, G. *The electron-phonon interaction in metals* (North-Holland Pub. Co., 1981).

140. Smith, N. V., Thiry, P. & Petroff, Y. Photoemission linewidths and quasiparticle lifetimes. *Phys. Rev. B* **47**, 15476–15481 (1993).

141. Kanigel, A. *et al.* Evolution of the pseudogap from Fermi arcs to the nodal liquid. *Nat. Phys.* **2**, 447 (2006).

142. Yang, H.-B., Rameau, J., Johnson, P., Valla, T., Tsvelik, A. & Gu, G. Emergence of preformed Cooper pairs from the doped Mott insulating state in $Bi_2Sr_2CaCu_2O_{8+\delta}$. *Nature* **456**, 77–80 (2008).

143. Sato, T. *et al.* Evidence for a hole-like Fermi surface of $Bi_2Sr_2CuO_6$ from temperature-dependent angle-resolved photoemission spectroscopy. *Phys. Rev. B* **64**, 054502 (2001).

144. Lucy, L. B. An iterative technique for the rectification of observed distributions. *Astron. J.* **79**, 745 (1974).

145. Dynes, R. C., Narayanamurti, V. & Garno, J. P. Direct Measurement of Quasiparticle-Lifetime Broadening in a Strong-Coupled Superconductor. *Phys. Rev. Lett.* **41**, 1509–1512 (1978).

146. Okazaki, K. *et al.* Octet-Line Node Structure of Superconducting Order Parameter in KFe_2As_2. *Science* **337**, 1314–1317 (2012).

147. Rothwarf, A. & Taylor, B. N. Measurement of Recombination Lifetimes in Superconductors. *Phys. Rev. Lett.* **19**, 27–30 (1967).

148. Gedik, N., Blake, P., Spitzer, R. C., Orenstein, J., Liang, R., Bonn, D. A. & Hardy, W. N. Single-quasiparticle stability and quasiparticle-pair decay in $YBa_2Cu_3O_{6.5}$. *Phys. Rev. B* **70**, 014504 (2004).

149. Kabanov, V. V., Demsar, J. & Mihailovic, D. Kinetics of a Superconductor Excited with a Femtosecond Optical Pulse. *Phys. Rev. Lett.* **95**, 147002 (2005).

150. Atkins, P. & de Paula, J. *Physical Chemistry* (W. H. Freeman, 2010).

151. Carnahan, M. A. *Low Energy Electrodynamics of Highly Nonequilibrium Superconductors.* Ph.D. thesis, University of California, Berkeley (2004).

152. Shah, J. *Ultrafast spectroscopy of semiconductors and semiconductor nanostructures* (Springer, 1999).

153. Allen, P. B. Theory of thermal relaxation of electrons in metals. *Phys. Rev. Lett.* **59**, 1460 (1987).

154. Perfetti, L., Loukakos, P. A., Lisowski, M., Bovensiepen, U., Eisaki, H. & Wolf, M. Ultrafast Electron Relaxation in Superconducting $Bi_2Sr_2CaCu_2O_{8+\delta}$ by Time-Resolved Photoelectron Spectroscopy. *Phys. Rev. Lett.* **99**, 197001 (2007).

155. Sentef, M. A., Claassen, M., Kemper, A. F., Moritz, B., Oka, T., Freericks, J. K. & Devereaux, T. P. Theory of pump-probe photoemission in graphene and the generation of light-induced Haldane multilayers. *ArXiv e-prints* arXiv:1401.5103 (2014).

156. Kemper, A. Private communication (2014).

157. Sentef, M., Kemper, A. F., Moritz, B., Freericks, J. K., Shen, Z.-X. & Devereaux, T. P. Examining Electron-Boson Coupling Using Time-Resolved Spectroscopy. *Phys. Rev. X* **3**, 041033 (2013).

158. Koralek, J. D. *et al.* Experimental setup for low-energy laser-based angle resolved photoemission spectroscopy. *Rev. Sci. Instrum.* **78**, 053905 (2007).

159. Schmitt, F. *et al.* Transient Electronic Structure and Melting of a Charge Density Wave in $TbTe_3$. *Science* **321**, 1649 (2008).

160. Carpene, E., Mancini, E., Dallera, C., Ghiringhelli, G., Manzoni, C., Cerullo, G. & De Silvestri, S. A versatile apparatus for time-resolved photoemission spectroscopy via femtosecond pump-probe experiments. *Rev. Sci. Instrum.* **80**, 055101–8 (2009).

161. Faure, J., Mauchain, J., Papalazarou, E., Yan, W., Pinon, J., Marsi, M. & Perfetti, L. Full characterization and optimization of a femtosecond ultraviolet laser source for time and angle-resolved photoemission on solid surfaces. *Rev. Sci. Instrum.* **83**, 043109 (2012).

162. Sobota, J. A., Yang, S., Analytis, J. G., Chen, Y. L., Fisher, I. R., Kirchmann, P. S. & Shen, Z.-X. Ultrafast Optical Excitation of a Persistent Surface-State Population in the Topological Insulator Bi_2Se_3. *Phys. Rev. Lett.* **108**, 117403 (2012).

163. Koralek, J. D. *Laser Based Angle-Resolved Photoemission Spectroscopy and High T_c Superconductivity.* Ph.D. thesis, University of Colorado (2006).

164. Bauer, M., Lei, C., Read, K., Tobey, R., Gland, J., Murnane, M. M. & Kapteyn, H. C. Direct Observation of Surface Chemistry Using Ultrafast Soft-X-Ray Pulses. *Phys. Rev. Lett.* **87**, 025501 (2001).

165. Siffalovic, P. *et al.* Laser-based apparatus for extended ultraviolet femtosecond time-resolved photoemission spectroscopy. *Rev. Sci. Instrum.* **72**, 30–35 (2001).

166. Munakata, T., Masuda, T., Ueno, N., Abdureyim, A. & Sonoda, Y. Time-resolved photoemission microspectroscopy based on fs-VUV laser light. *Surf. Sci.* **507–510**, 434–440 (2002).

167. Tsilimis, G., Benesch, C., Kutzner, J. & Zacharias, H. Laser based soft-x-ray pulses for photoelectron spectroscopy of surfaces. *J. Opt. Soc. Am. B* **20**, 246–253 (2003).

168. Bauer, M. Femtosecond ultraviolet photoelectron spectroscopy of ultra-fast surface processes. *J. Phys. D: Appl. Phys.* **38**, R253– (2005).

169. Mathias, S., Miaja-Avila, L., Murnane, M. M., Kapteyn, H., Aeschlimann, M. & Bauer, M. Angle-resolved photoemission spectroscopy with a femtosecond high harmonic light source using a two-dimensional imaging electron analyzer. *Rev. Sci. Instrum.* **78**, 083105 (2007).

170. Dakovski, G. L., Li, Y., Durakiewicz, T. & Rodriguez, G. Tunable ultrafast extreme ultraviolet source for time- and angle-resolved photoemission spectroscopy. *Rev. Sci. Instrum.* **81**, 073108 (2010).

171. Christensen, B., Raarup, M. & Balling, P. Photoemission with high-order harmonics: A tool for time-resolved core-level spectroscopy. *Nucl. Instrum. Methods Phys. Res. A* **615**, 114–126 (2010).

172. Wernet, P., Gaudin, J., Godehusen, K., Schwarzkopf, O. & Eberhardt, W. Femtosecond time-resolved photoelectron spectroscopy with a vacuum-ultraviolet photon source based on laser high-order harmonic generation. *Rev. Sci. Instrum.* **82**, 063114 (2011).

173. Brabec, T. & Krausz, F. Intense few-cycle laser fields: Frontiers of nonlinear optics. *Rev. Mod. Phys.* **72**, 545–591 (2000).

174. Winterfeldt, C., Spielmann, C. & Gerber, G. Colloquium: Optimal control of high-harmonic generation. *Rev. Mod. Phys.* **80**, 117–140 (2008).

175. Tarasevitch, A., Wieczorek, J., Kohn, R., Bovensiepen, U. & von der Linde, D. Two-beam high-order harmonics from solids: Coupling mechanisms. *Phys. Rev. E* **82**, 056410 (2010).

176. Rohwer, T. *et al.* Collapse of long-range charge order tracked by time-resolved photoemission at high momenta. *Nature* **471**, 490–493 (2011).

177. Petersen, J. C. *et al.* Clocking the Melting Transition of Charge and Lattice Order in 1T-TaS_2 with Ultrafast Extreme-Ultraviolet Angle-Resolved Photoemission Spectroscopy. *Phys. Rev. Lett.* **107**, 177402 (2011).

178. Ayvazyan, V. *et al.* First operation of a free-electron laser generating GW power radiation at 32nm wavelength. *Eur. Phys. J. D* **37**, 297–303 (2006).

179. Allaria, E., Callegari, C., Cocco, D., Fawley, W. M., Kiskinova, M., Masciovecchio, C. & Parmigiani, F. The FERMI@Elettra free-electron-laser source for coherent x-ray physics: photon properties, beam transport system and applications. *New J. Phys.* **12**, 075002 (2010).

180. Hellmann, S. *et al.* Time-resolved x-ray photoelectron spectroscopy at FLASH. *New J. Phys.* **14**, 013062 (2012).

181. Zhou, X. J. *et al.* Space charge effect and mirror charge effect in photoemission spectroscopy. *J. Electron Spectrosc. Relat. Phenom.* **142**, 27–38 (2005).

182. Passlack, S., Mathias, S., Andreyev, O., Mittnacht, D., Aeschlimann, M. & Bauer, M. Space charge effects in photoemission with a low repetition, high intensity femtosecond laser source. *J. Appl. Phys.* **100**, 024912 (2006).

183. Graf, J. *et al.* Vacuum space charge effect in laser-based solid-state photoemission spectroscopy. *J. Appl. Phys.* **107**, 014912 (2010).

184. Hellmann, S., Ott, T., Kipp, L. & Rossnagel, K. Vacuum space-charge effects in nano-ARPES. *Phys. Rev. B* **85**, 075109 (2012).

185. Leuenberger, D., Yanagisawa, H., Roth, S., Osterwalder, J. & Hengsberger, M. Disentanglement of electron dynamics and space-charge effects in time-resolved photoemission from h-BN/Ni(111). *Phys. Rev. B* **84**, 125107 (2011).

186. Krishana, K., Ong, N. P., Li, Q., Gu, G. D. & Koshizuka, N. Plateaus Observed in the Field Profile of Thermal Conductivity in the Superconductor $Bi_2Sr_2CaCu_2O_8$. *Science* **277**, 83–85 (1997).

187. Graf, J., Jozwiak, C., Smallwood, C. L., Eisaki, H., Kaindl, R. A., Lee, D.-H. & Lanzara, A. Nodal quasiparticle meltdown in ultrahigh-resolution pump-probe angle-resolved photoemission. *Nat. Phys.* **7**, 805–809 (2011).

188. Cortés, R., Rettig, L., Yoshida, Y., Eisaki, H., Wolf, M. & Bovensiepen, U. Momentum-Resolved Ultrafast Electron Dynamics in Superconducting $Bi_2Sr_2CaCu_2O_{8+\delta}$. *Phys. Rev. Lett.* **107**, 097002 (2011).

189. Smallwood, C. L. *et al.* Tracking Cooper Pairs in a Cuprate Superconductor by Ultrafast Angle-Resolved Photoemission. *Science* **336**, 1137–1139 (2012).

190. Smallwood, C. L., Jozwiak, C., Zhang, W. & Lanzara, A. An ultrafast angle-resolved photoemission apparatus for measuring complex materials. *Rev. Sci. Instrum.* **83**, 123904 (2012).

191. Jozwiak, C. *et al.* A high-efficiency spin-resolved photoemission spectrometer combining time-of-flight spectroscopy with exchange-scattering polarimetry. *Rev. Sci. Instrum.* **81**, 053904 (2010).

192. Kirchmann, P., Rettig, L., Nandi, D., Lipowski, U., Wolf, M. & Bovensiepen, U. A time-of-flight spectrometer for angle-resolved detection of low energy electrons in two dimensions. *Appl. Phys. A* **91**, 211–217 (2008).

193. Öhrwall, G. *et al.* A new energy and angle resolving electron spectrometer—First results. *J. Electron Spectrosc. Relat. Phenom.* **183**, 125–131 (2011).

194. Taylor, J. R. *An Introduction to Error Analysis: The Study of Uncertainties in Physical Measurements* (University Science Books, 1997).

195. Tanaka, J., Tanaka, C., Takada, K. & Mori, W. Infrared Spectra of Single Crystals of Underdoped $Bi_2Sr_2CaCu_2O_{8+\delta}$. *Phys. Stat. Sol. (B)* **215**, 541–546 (1999).

196. Quijada, M. A., Tanner, D. B., Kelley, R. J., Onellion, M., Berger, H. & Margaritondo, G. Anisotropy in the ab-plane optical properties of $Bi_2Sr_2CaCu_2O_8$ single-domain crystals. *Phys. Rev. B* **60**, 14917–14934 (1999).

197. Jackson, J. D. *Classical Electrodynamics* (Wiley, 1998), 3rd edn.

198. Diels, J.-C. & Rudolph, W. *Ultrashort Laser Pulse Phenomena* (Elsevier, Amsterdam, 2006), 2nd edn.

199. SNLO nonlinear optics code available from A. V. Smith, AS-Photonics, Albuquerque, NM.

200. Moore, J. H., Davis, C. C. & Coplan, M. A. *Building Scientific Apparatus: A Practical Guide to Design and Construction* (Westview Press, 2003), 3rd edn.

201. Imhof, R. E., Adams, A. & King, G. C. Energy and time resolution of the 180 degrees hemispherical electrostatic analyser. *J. Phys. E. Sci. Instrum.* **9**, 138 (1976).

202. Kevan, S. D. Design of a high-resolution angle-resolving electron energy analyzer. *Rev. Sci. Instrum.* **54**, 1441–1445 (1983).

203. VG Scienta R4000 Data Sheet (2011).

204. Kay, A. W. *et al.* Multiatom resonant photoemission. *Phys. Rev. B* **63**, 115119 (2001).

205. Mannella, N. *et al.* Correction of non-linearity effects in detectors for electron spectroscopy. *J. Electron Spectrosc. Relat. Phenom.* **141**, 45–59 (2004).

206. Wicks, R. C. & Ingle, N. J. C. Characterizing the detection system nonlinearity, internal inelastic background, and transmission function of an electron spectrometer for use in x-ray photoelectron spectroscopy. *Rev. Sci. Instrum.* **80**, 053108 (2009).

207. Reber, T. J., Plumb, N. C., Waugh, J. A. & Dessau, D. S. Effects, determination, and correction of count rate nonlinearity in multi-channel analog electron detectors. *Rev. Sci. Instrum.* **85**, 043907 (2014).

208. Fero, A., Smallwood, C. L., Affeldt, G. & Lanzara, A. Impact of Work Function Induced Electric Fields on Laser-based Angle-resolved Photoemission Spectroscopy. *J. Electron Spectrosc. Relat. Phenom.* (2014), http://dx.doi.org/10.1016/j.elspec.2014.01.008

209. Haynes, W. M. (ed.). *CRC Handbook of Chemistry and Physics 2014–2015* (CRC Press, 2014), 95th edn.

210. Chuang, Y.-D., Gromko, A. D., Dessau, D. S., Kimura, T. & Tokura, Y. Fermi Surface Nesting and Nanoscale Fluctuating Charge/Orbital Ordering in Colossal Magnetoresistive Oxides. *Science* **292**, 1509–1513 (2001).

211. Bogdanov, P. V. *et al.* Photoemission study of Pb doped $Bi_2Sr_2CaCu_2O_8$: A Fermi surface picture. *Phys. Rev. B* **64**, 180505 (2001).

212. Kordyuk, A. A. *et al.* Doping dependence of the Fermi surface in $(Bi,Pb)_2Sr_2CaCu_2O_{8+\delta}$. *Phys. Rev. B* **66**, 014502 (2002).

213. Vishik, I. M. *et al.* Doping-Dependent Nodal Fermi Velocity of the High-Temperature Superconductor $Bi_2Sr_2CaCu_2O_{8+\delta}$ Revealed Using High-Resolution Angle-Resolved Photoemission Spectroscopy. *Phys. Rev. Lett.* **104**, 207002 (2010).

214. Crommie, M. F. & Zettl, A. Thermal-conductivity anisotropy of single-crystal $Bi_2Sr_2CaCu_2O_8$. *Phys. Rev. B* **43**, 408–412 (1991).

215. Kaplan, S. B., Chi, C. C., Langenberg, D. N., Chang, J. J., Jafarey, S. & Scalapino, D. J. Quasiparticle and phonon lifetimes in superconductors. *Phys. Rev. B* **14**, 4854–4873 (1976).

216. Rettig, L. *et al.* Ultrafast Momentum-Dependent Response of Electrons in Antiferromagnetic $EuFe_2As_2$ Driven by Optical Excitation. *Phys. Rev. Lett.* **108**, 097002 (2012).

217. Segre, G. P., Gedik, N., Orenstein, J., Bonn, D. A., Liang, R. & Hardy, W. N. Photoinduced Changes of Reflectivity in Single Crystals of $YBa_2Cu_3O_{6.5}$ (Ortho II). *Phys. Rev. Lett.* **88**, 137001 (2002).

218. Kaindl, R. A., Carnahan, M. A., Chemla, D. S., Oh, S. & Eckstein, J. N. Dynamics of Cooper pair formation in $Bi_2Sr_2CaCu_2O_{8+\delta}$. *Phys. Rev. B* **72**, 060510 (2005).

219. Gedik, N., Langner, M., Orenstein, J., Ono, S., Abe, Y. & Ando, Y. Abrupt Transition in Quasiparticle Dynamics at Optimal Doping in a Cuprate Superconductor System. *Phys. Rev. Lett.* **95**, 117005 (2005).

220. Coslovich, G. *et al.* Evidence for a photoinduced nonthermal superconducting-to-normal-state phase transition in overdoped $Bi_2Sr_2Ca_{0.92}Y_{0.08}Cu_2O_{8+\delta}$. *Phys. Rev. B* **83**, 064519 (2011).

221. Demsar, J. *et al.* Pair-Breaking and Superconducting State Recovery Dynamics in MgB_2. *Phys. Rev. Lett.* **91**, 267002 (2003).

222. Kusar, P., Kabanov, V. V., Demsar, J., Mertelj, T., Sugai, S. & Mihailovic, D. Controlled Vaporization of the Superconducting Condensate in Cuprate Superconductors by Femtosecond Photoexcitation. *Phys. Rev. Lett.* **101**, 227001 (2008).

223. Giannetti, C. *et al.* Discontinuity of the ultrafast electronic response of underdoped superconducting $Bi_2Sr_2CaCu_2O_{8+\delta}$ strongly excited by ultrashort light pulses. *Phys. Rev. B* **79**, 224502 (2009).

224. Torchinsky, D. H., Chen, G. F., Luo, J. L., Wang, N. L. & Gedik, N. Band-dependent Quasiparticle Dynamics in Single Crystals of the $Ba_{0.6}K_{0.4}Fe_2As_2$ Superconductor Revealed by Pump-Probe Spectroscopy. *Phys. Rev. Lett.* **105**, 027005 (2010).

225. Torchinsky, D. H., McIver, J. W., Hsieh, D., Chen, G. F., Luo, J. L., Wang, N. L. & Gedik, N. Nonequilibrium quasiparticle relaxation dynamics in single crystals of hole- and electron-doped $BaFe_2As_2$. *Phys. Rev. B* **84**, 104518 (2011).

226. Beck, M., Klammer, M., Lang, S., Leiderer, P., Kabanov, V. V., Goltsman, G. N. & Demsar, J. Energy-Gap Dynamics of Superconducting NbN Thin Films Studied by Time-Resolved Terahertz Spectroscopy. *Phys. Rev. Lett.* **107**, 177007 (2011).

227. Fong, H. F. *et al.* Neutron scattering from magnetic excitations in $Bi_2Sr_2CaCu_2O_{8+\delta}$. *Nature* **398**, 588–591 (1999).

228. Marshall, D. S. *et al.* Unconventional Electronic Structure Evolution with Hole Doping in $Bi_2Sr_2CaCu_2O_{8+\delta}$: Angle-Resolved Photoemission Results. *Phys. Rev. Lett.* **76**, 4841–4844 (1996).

229. Zhang, W. *et al.* Signatures of superconductivity and pseudogap formation in nonequilibrium nodal quasiparticles revealed by ultrafast angle-resolved photoemission. *Phys. Rev. B* **88**, 245132 (2013).

230. Rameau, J. D. *et al.* Photoinduced changes in the cuprate electronic structure revealed by femtosecond time- and angle-resolved photoemission. *Phys. Rev. B* **89**, 115115 (2014).

231. Randeria, M. *et al.* Momentum Distribution Sum Rule for Angle-Resolved Photoemission. *Phys. Rev. Lett.* **74**, 4951 (1995).

232. Freericks, J. K., Krishnamurthy, H. R. & Pruschke, T. Theoretical Description of Time-Resolved Photoemission Spectroscopy: Application to Pump-Probe Experiments. *Phys. Rev. Lett.* **102**, 136401 (2009).

233. Moritz, B., Kemper, A. F., Sentef, M., Devereaux, T. P. & Freericks, J. K. Electron-Mediated Relaxation Following Ultrafast Pumping of Strongly Correlated Materials: Model Evidence of a Correlation-Tuned Crossover between Thermal and Nonthermal States. *Phys. Rev. Lett.* **111**, 077401 (2013).

234. Kirchmann, P. Private communication (2014).

235. Smallwood, C. L., Zhang, W., Miller, T. L., Jozwiak, C., Eisaki, H., Lee, D.-H. & Lanzara, A. Time- and momentum-resolved gap dynamics in $Bi_2Sr_2CaCu_2O_{8+\delta}$. *Phys. Rev. B* **89**, 115126 (2014).

236. Feng, D. L. *et al.* Bilayer Splitting in the Electronic Structure of Heavily Overdoped $Bi_2Sr_2CaCu_2O_{8+\delta}$. *Phys. Rev. Lett.* **86**, 5550–5553 (2001).

237. Chuang, Y.-D. *et al.* Doubling of the Bands in Overdoped $Bi_2Sr_2CaCu_2O_{8+\delta}$: Evidence for c-Axis Bilayer Coupling. *Phys. Rev. Lett.* **87**, 117002 (2001).

238. Zhang, W. *et al.* Simultaneous quench of electron-boson interaction and superconducting gap in photo-stimulated Bi2212. *Submitted* (2014).

239. Kondo, T., Khasanov, R., Takeuchi, T., Schmalian, J. & Kaminski, A. Competition between the pseudogap and superconductivity in the high-T_c copper oxides. *Nature* **457**, 296 (2009).

240. Owen, C. S. & Scalapino, D. J. Superconducting State under the Influence of External Dynamic Pair Breaking. *Phys. Rev. Lett.* **28**, 1559– (1972).

241. Parker, W. H. Modified heating theory of nonequilibrium superconductors. *Phys. Rev. B* **12**, 3667– (1975).

242. Carnahan, M. A., Kaindl, R. A., Orenstein, J., Chemla, D. S., Oh, S. & Eckstein, J. N. Nonequilibrium THz conductivity of $Bi_2Sr_2CaCu_2O_{8+\delta}$. *Physica C* **408**, 729–730 (2004).

243. Liu, Y. H., Toda, Y., Shimatake, K., Momono, N., Oda, M. & Ido, M. Direct Observation of the Coexistence of the Pseudogap and Superconducting Quasiparticles in $Bi_2Sr_2CaCu_2O_{8+y}$ by Time-Resolved Optical Spectroscopy. *Phys. Rev. Lett.* **101**, 137003 (2008).

244. Toda, Y., Mertelj, T., Kusar, P., Kurosawa, T., Oda, M., Ido, M. & Mihailovic, D. Quasiparticle relaxation dynamics in underdoped $Bi_2Sr_2CaCu_2O_{8+\delta}$ by two-color pump-probe spectroscopy. *Phys. Rev. B* **84**, 174516 (2011).

245. Coslovich, G. *et al.* Competition Between the Pseudogap and Superconducting States of $Bi_2Sr_2Ca_{0.92}Y_{0.08}Cu_2O_{8+\delta}$ Single Crystals Revealed by Ultrafast Broadband Optical Reflectivity. *Phys. Rev. Lett.* **110**, 107003 (2013).

246. Lee, J., Fujita, K., Schmidt, A. R., Kim, C. K., Eisaki, H., Uchida, S. & Davis, J. C. Spectroscopic Fingerprint of Phase-Incoherent Superconductivity in the Underdoped $Bi_2Sr_2CaCu_2O_{8+\delta}$. *Science* **325**, 1099–1103 (2009).

247. Kohsaka, Y. *et al.* How Cooper pairs vanish approaching the Mott insulator in $Bi_2Sr_2CaCu_2O_{8+\delta}$. *Nature* **454**, 1072 (2008).

248. Beaurepaire, E., Merle, J.-C., Daunois, A. & Bigot, J.-Y. Ultrafast Spin Dynamics in Ferromagnetic Nickel. *Phys. Rev. Lett.* **76**, 4250–4253 (1996).

249. Kaindl, R. A. *et al.* Ultrafast Mid-Infrared Response of $YBa_2Cu_3O_{7-\delta}$. *Science* **287**, 470–473 (2000).

250. Feenstra, B. J. *Low Energy Electrodynamics of High T_c Superconductors.* Ph.D. thesis, University of Groningen (1997).

251. Howell, P. C., Rosch, A. & Hirschfeld, P. J. Relaxation of Hot Quasiparticles in a d-Wave Superconductor. *Phys. Rev. Lett.* **92**, 037003 (2004).

252. McElroy, K., Lee, J., Slezak, J. A., Lee, D.-H., Eisaki, H., Uchida, S. & Davis, J. C. Atomic-Scale Sources and Mechanism of Nanoscale Electronic Disorder in $Bi_2Sr_2CaCu_2O_{8+\delta}$. *Science* **309**, 1048 (2005).

253. Shen, Z.-X. & Schrieffer, J. R. Momentum, Temperature, and Doping Dependence of Photoemission Lineshape and Implications for the Nature of the Pairing Potential in High- T_c Superconducting Materials. *Phys. Rev. Lett.* **78**, 1771–1774 (1997).

254. Loeser, A. G., Shen, Z.-X., Schabel, M. C., Kim, C., Zhang, M., Kapitulnik, A. & Fournier, P. Temperature and doping dependence of the Bi-Sr-Ca-Cu-O electronic structure and fluctuation effects. *Phys. Rev. B* **56**, 14185 (1997).

255. Fedorov, A. V., Valla, T., Johnson, P. D., Li, Q., Gu, G. D. & Koshizuka, N. Temperature Dependent Photoemission Studies of Optimally Doped Bi2Sr2CaCu2O8. *Phys. Rev. Lett.* **82**, 2179 (1999).

256. Feng, D. L. *et al.* Signature of Superfluid Density in the Single-Particle Excitation Spectrum of $Bi_2Sr_2CaCu_2O_{8+\delta}$. *Science* **289**, 277 (2000).

257. Ding, H. *et al.* Coherent Quasiparticle Weight and Its Connection to High-T_c Superconductivity from Angle-Resolved Photoemission. *Phys. Rev. Lett.* **87**, 227001 (2001).

258. Kondo, T. *et al.* Disentangling Cooper-pair formation above the transition temperature from the pseudogap state in the cuprates. *Nat. Phys.* **7**, 21–25 (2011).

259. Valla, T. *et al.* Evidence for Quantum Critical Behavior in the Optimally Doped Cuprate $Bi_2Sr_2CaCu_2O_{8+\delta}$. *Science* **285**, 2110 (1999).

260. Kordyuk, A. A. *et al.* Constituents of the Quasiparticle Spectrum Along the Nodal Direction of High-T_c Cuprates. *Phys. Rev. Lett.* **97**, 017002 (2006).

261. Lee, W. S. *et al.* Superconductivity-induced self-energy evolution of the nodal electron of optimally doped $Bi_2Sr_2Ca_{0.92}Y_{0.08}Cu_2O_{8+\delta}$. *Phys. Rev. B* **77**, 140504 (2008).

262. Mourachkine, A. *High-Temperature Superconductivity in Cuprates: The Nonlinear Mechanism and Tunneling Measurements* (Springer, 2002).

263. Basov, D. N., Averitt, R. D., van der Marel, D., Dressel, M. & Haule, K. Electrodynamics of correlated electron materials. *Rev. Mod. Phys.* **83**, 471–541 (2011).

264. Meingast, C., Pasler, V., Nagel, P., Rykov, A., Tajima, S. & Olsson, P. Phase Fluctuations and the Pseudogap in $YBa_2Cu_3O_x$. *Phys. Rev. Lett.* **86**, 1606–1609 (2001).

265. Fisher, D. S. Scaling and critical slowing down in random-field Ising systems. *Phys. Rev. Lett.* **56**, 416–419 (1986).

266. Ginzburg, V. L. Certain theoretical aspects of radiation due to superluminal motion in a medium. *Sov. Phys. Usp.* **2**, 874 (1960).

267. Presland, M. R., Tallon, J. L., Buckley, R. G., Liu, R. S. & Flower, N. E. General trends in oxygen stoichiometry effects on T_c in Bi and Tl superconductors. *Physica C* **176**, 95–105 (1991).

268. Fu, H. & Lee, D.-H. Dichotomy between the nodal and antinodal excitations in high-temperature superconductors. *Phys. Rev. B* **74**, 174513 (2006).

269. Fausti, D. *et al.* Light-Induced Superconductivity in a Stripe-Ordered Cuprate. *Science* **331**, 189–191 (2011).

270. Hu, W. *et al.* Optically enhanced coherent transport in $YBa_2Cu_3O_{6.5}$ by ultrafast redistribution of interlayer coupling. *Nat. Mater.* **13**, 705–711 (2014).

271. Kaiser, S. *et al.* Optically induced coherent transport far above T_c in underdoped $YBa_2Cu_3O_{6+\delta}$. *Phys. Rev. B* **89**, 184516 (2014).

272. Lee, D.-H. Private communication (2014).

273. Wang, Y. H., Steinberg, H., Jarillo-Herrero, P. & Gedik, N. Observation of Floquet-Bloch States on the Surface of a Topological Insulator. *Science* **342**, 453–457 (2013).

274. Cohen-Tannoudji, C., Dupont-Roc, J. & Grynberg, G. *Atom-Photon Interactions: Basic Processes and Applications* (Wiley, New York, 1998).

275. Metcalf, H. J. & van der Straten, P. *Laser Cooling and Trapping* (Springer New York, 1999).